UNIVERSITA' DI PADOVA
FACOLTA' DI INGEGNERIA

SCUOLA DI DOTTORATO DI RICERCA IN
INGEGNERIA INDUSTRIALE

INDIRIZZO IN
INGEGNERIA ELETTROTECNICA

CICLO:XXI

MEASUREMENT AND TRANSMISSION OF ELECTRICAL AND MAGNETIC QUANTITIES IN MAGNETIC CONFINEMENT FUSION DEVICES

DIRETTORE DELLA SCUOLA:
Ch.mo Prof. Paolo Bariani

SUPERVISORE:
Ch.mo Prof. Ing. Giuseepe Chitarin

DOTTORANDO: Ing. Edoardo Alessi

31 gennaio 2009

DIPARTIMENTO DI INGEGNERIA ELETTRICA

UNIVERSITA' DEGLI STUDI DI PADOVA

Dipartimento di Ingegneria Elettrica

Scuola di Dottorato di Ricerca in Ingegneria Industriale

Indirizzo in Ingegneria Elettrotecnica

Ciclo XXI

Measurement and transmission of electrical and magnetic quantities in magnetic confinement fusion devices

Direttore della Scuola: Ch.mo Prof. Paolo F. Bariani

Supervisore: Ch.mo Prof. Ing. Giuseppe Chitarin

Dottorando: Ing. Edoardo Alessi

31 gennaio 2009

Contents

CHAPTER II

Definition of a Reconstruction procedure

CHAPTER III

Part II

CHAPTER IV

CHAPTER V

CHAPTER VI

Introduzione

In questo lavoro vengono illustrate le due principali attività svolte durante il mio periodo di dottorato: una concernente le correnti di Halo che attraversano il Vacuum Vessel di una macchina sperimentale per la fusione termonucleare, e l'altra la trasmissione via radio-frequenza della misura della corrente del magnetizzante di RFX. Le due attività si sono svillupate separatamente anche se tutte e due riguardano l'utilizzo di misure elettriche e/o magnetiche. Per questo motivo la presente tesi è sviluppata in due parti distinte.

L'attività di ricerca per il mio dottorato è cominciata nel Gennaio del 2006. Mi sono inizialmente dedicato al progetto ed alla realizzazione di uno schermo attivo per la compensazione del campo magnetico indotto dagli avvolgimenti del magnetizzante di RFX su uno spettrrometro a Risonanza Magnetica Nucleare (NMR) presente nell'Istituto ICIS a 150m di distanza dall'esperimento RFX. Lo schermo attivo è controllato in catena aperta. Le spire, atte alla compensazione del disturbo magnetico vicino allo spettrometro, sono pilotate attraverso un segnale proporzionale alla corrente del magnetizzante di RFX. Questa attività ha comportato anche la realizzazione di un collegamento wireless adatto allo scopo di trasmettere il segnale da RFX all'Istituto ICIS.
Successivamente ho continuato a seguire questa attività fino ai test sperimentali del sistema nell'istituto ICIS, avvenuti nel Luglio 2008.
Il disegno, la realizzazione, ed i successivi test di ogni parte del sistema componente lo schermo magnetico attivo costituiscono la parte pratica della mia attività di ricerca durante il dottorato, che mi ha fornito l'esperienza pratica sui problemi che si possono incontrare durante la realizzazione di un dispositivo così complesso.

Nel Novembre 2006, ho cominciato una attività più teorica nell'ambito delle collaborazioni con l'esperimento ITER. Questa seconda attività ha riguardato lo sviluppo di una procedura di ricostruzione per la distribuzioni delle correnti di Halo in ITER.
Questa attività si è inizialmente sviluppata lavorando sulle basi dei risultati ottenuti attraverso un semplice modello di un Tokamak, allo scopo di individuare una strategia o una procedura appropriata per un futuro utilizzo su ITER. Tale procedura di ricostruzione è stata sviluppata e, come naturale prosecuzione di questa attività, ho proceduto allo sviluppo di alcuni codici per la simulazione delle correnti di Halo su un modello accurato delle prima parete di ITER.

Durante l'ultimo anno, lo sviluppo della procedura di ricostruzione è diventata la mia attività principale. Per questo motivo la prima parte di questa tesi riguarda lo sviluppo di una tale procedura mentre la seconda parte illustra il progetto e la realizzazione dello schermo magnetico attivo.

Le due parti che compongono la presente tesi sono ambedue provviste di un riassunto sulla attività discussa al loro interno.

Introduction

Two main activities have been carried out during my PhD: one concerning the measurement of the Halo current flowing through the vacuum vessel of a magnetic confinement fusion device which occurs during disruptive events and the other concerning the transmission by Radio Frequency of the magnetizing current measurement in the RFX experiment. Even though both activities are concerning the electrical measurements, they have been carried out separately. Therefore, the present thesis is divided in two parts, each concerning one of these two activities.

The research activity for my PhD began in 2006, the January. My first activity involved the design of an active shield for the magnetic field induced by the Magnetizing winding of RFX on a Nuclear Magnetic Resonance (NMR) spectrometer housed at ICIS institute, 150m far from the RFX experiment. The active shield is feed-forward, since the coils aimed to create the compensating magnetic field near to the spectrometer are driven by signal proportional to the current flowing through the magnetizing winding of RFX. Then, this activity involved also the realization of a suitable Radio Frequency system to transmit the signal from RFX to the ICIS institute.
Afterward, I continued this activity until the experimental tests of the equipment in the ICIS Institute performed in the 2008, the July.
The design, the realization, and the testing of each part of the equipment making up the magnetic active shield constitutes the practical activity I have carried out during my PhD, which allows me to experience the practical issues that can arise during the realization of a so complex device.

In the November, 2006, I began a more theoretical application in the framework of the collaboration with the ITER experiment. This second activity concerned the development of a reconstruction procedure for the Halo current distributions in ITER. It was not foreseen that such activity could be settled with the effective realization and testing of the reconstruction procedure.
I started this activity working on the basis of the results given out by a simple model of a Tokamak with the aims of individuating a strategy or a suitable reconstruction procedure to be applied in ITER. Such a reconstruction procedure was developed, and as a natural carrying on, I started working to develop some algorithm able to evaluate the Halo current distribution on a model of the ITER first wall.

During the last year, the development of the reconstruction procedure became my main activity. This is the reason for the first part of this thesis is concerning the development of a reconstruction procedure for the Halo current, and the second part is concerning the design and the realization of the active magnetic shield.

The two parts in which the thesis is divided are both provided of a summary regarding the activity discussed therein.

PART I

Development of a reconstruction procedure for the Halo current distributions on the ITER plasma facing components

In magnetic-confinement toroidal machines, Halo currents mainly occur in case of Vertical Displacement Events (VDEs), following a loss of control or an unrecoverable MHD instability, when the hot plasma region "hits" the First Wall protective Modules at some locations. In these cases, the First Wall Modules act as a plasma "limiter" dragging the current of the "Halo" region of the plasma into the Vacuum Vessel. This "Halo" current can flow across the Vessel Structure and its Supports giving rise to considerable JxB Electromagnetic Loads.
The evaluation of these loads under various operational conditions is essential for the prevention of mechanical failures and for this reason the Halo currents are routinely measured in all present large-scale experimental machines. However, in practice only a limited number of First Wall modules can be equipped with Halo current sensors, giving incomplete information about the real distribution of the Halo current. The reconstruction of the complete pattern of the Halo Current flowing across all the First Wall modules into the vessel surface is therefore a necessary step to evaluate the electrodynamic loads JxB exerted on the vessel structure.
The contact areas of the plasma with the wall are spatially discontinuous during disruptions. So, the resulting Halo current distribution is a discontinuous function of the toroidal and poloidal coordinates which cannot be efficiently fitted using harmonic or other continuous basis functions. For this reason a reconstruction procedure shall use some "*a priori*" information and two separate problems have to be solved. The first problem is the determination of a complete set of patterns of Halo Currents, which could theoretically be "injected" on the vessel by several kinds of MHD instabilities. The second problem consists in the determination of the amplitude and phase of the MHD instabilities which actually can produce a pattern of injected current most similar to the measured one.
The first problem is a direct problem which requires developing 3-dimensional codes and computing realistic distributions of the Halo currents.
In the present experiments (such as JT60-U, JET, AUG, DIIID [1,2,3,4]) the vacuum vessel includes bellows or other resistive sections which produce a strong anisotropy of the poloidal and toroidal resistance. For this reason, in these machines the Halo Currents "injected" in the vessel structure tend to flow along poloidal paths, independently of the pre-disruption configuration, and the phenomenon can sufficiently be described using a simple poloidal distribution and a Toroidal Peaking Factor (TPF) representing the degree of asymmetry of the poloidal Halo Current along the toroidal direction, it is defined as the ratio of the maximum to the average poloidal HC [4]. On the other hand, the ITER vacuum vessel resistance will be almost symmetric having a resistance of 7.9 μΩ along the toroidal direction and 4.1 μΩ along the poloidal direction.

During the VDE, the plasma loses the elongation and some MHD modes can be destabilized. The perturbation of the plasma surface due to the MHD modes can modify the "footprint" of the Halo Currents in the Vessel. The loss of the toroidal symmetry (related with the destabilized MHD modes) together with a quite isotropic vessel resistance should cause a not negligible toroidal component of the vessel current. So, the description of Halo current based on the TPF could be not sufficient to describe the overall amount of current flowing into the Vessel and a more complex description shall be taken into account to relate the asymmetric VDEs and the asymmetric Halo Current patterns with the presence of some destabilized MHD modes [5].
Moreover, results from these codes might be used as inputs for 3D electrodynamic models of the ITER Vessel to evaluate the JxB loads on the vessel structure.
With these aims, many models for the computation of the Halo currents injected into the vessel were developed.
The second problem is an inverse problem. It requires developing an algorithm able to recognize the actual MHD perturbing modes and fill in the Halo Current measurements with the estimated values of Halo Currents for the no equipped modules.

Chapter I is aimed to giving the basis underlying this work to the reader. A brief introduction on ITER is presented. The equilibrium issue for magnetically confined plasma is discussed to give a theoretical basis to the quasi equilibrium models developed on the next chapter. On the other hand, the MHD stability is treated in order to introduce the main phenomena causing the Halo currents: Major disruption and vertical displacement events. At the end of this chapter (section 6), the Halo current phenomena are deeply exposed together with the description commonly used at present in plasma researcher's world.
In chapter II, a first simple code has been developed for the solution of the direct problem on the basis of an "interference" function, to evaluate Halo current density patterns and then the Halo current distributions on an ideal first wall surface with circular cross section. Results from this code allowed a first review of typical three dimensional Halo Currents distributions.
Then, a procedure for the solution of the inverse problem has been developed which estimates the Halo currents flowing across the remaining part of the First wall on the basis of a limited number of available measurements.
In chapter III, more advanced codes are described for the solution of the direct problem with a realistic ITER first wall geometry. Actually, three different codes have been developed with the purpose of determining the Halo current distribution starting from the First wall geometry and plasma perturbation parameters. The performances of the three options are also compared in this chapter.

CHAPTER I

Halo currents in ITER

ITER experiment is presented in sections 1 and 2, firstly introducing the last important results found in fusion research and highlighting the main issues ITER should give an answer.
The bases of the ideal MHD equilibrium are shown in section 3. MHD equilibrium is useful to introduce the study of the instabilities of fusion plasma. Moreover, some solutions of the MHD equilibrium equations are used in chapter II and III to develop a simple model of the Halo plasma.
The linearised equations underlying the study of the instability of the plasma are discussed in section 4. The vertical instabilities is briefly treated in section 4.2.
Halo currents phenomena can appear after some abnormal events as major disruption and/or Vertical Displacement Events (VDE). A discussion about these events and their occurrence in ITER is reported in section 5. Halo currents are finally introduced in section 6. Present status of the foreseen layout for Halo current diagnostics is also reported.

1. Fusion basics

1.1 From renewable to nuclear power

The increase in energy needs has led to the use of energy sources able to supply a larger quantity of energy for a given mass of matter (in terms of energetic density, Figure 1). The chemical reactions involve phenomena that take place at the level of electrons. The chemical energy is then millions of times lower than that involved in reactions involving the kernel of the atom.

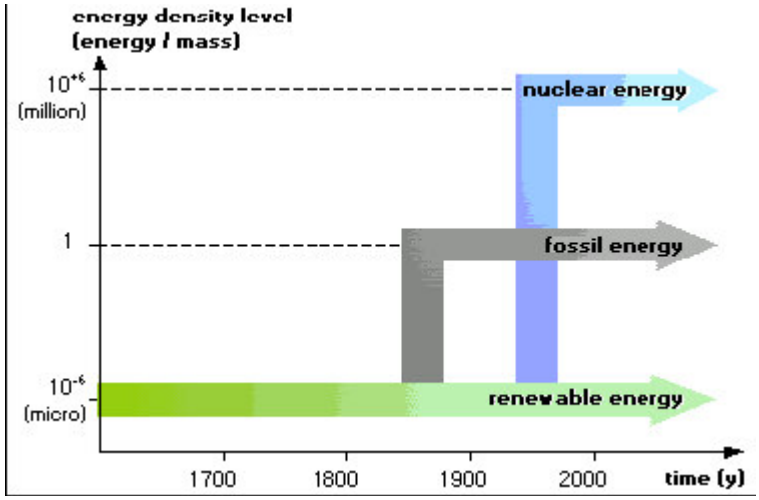

Figure 1. Classification of energy sources by energy density levels.

To produce energy, it is necessary to carry out a transformation in which, between the initial and final state, a small proportion of the body mass involved disappears. This mass defect may then be found in the form of energy through the well-known Einstein's formula $E=mc^2$, where E is the energy produced, m the mass that has disappeared and c the speed of light. Two main types of nuclear reactions, which lower mass and therefore release energy, are possible:

- From joining very light atomic nuclei (examples; deuterium and tritium) to build heavier atoms through the process called fusion (Figure 2-a).
- From splitting the nucleus of a sufficiently heavy atom (such as the uranium atom) to make lighter atoms, through the process called fission (Figure 2-b).

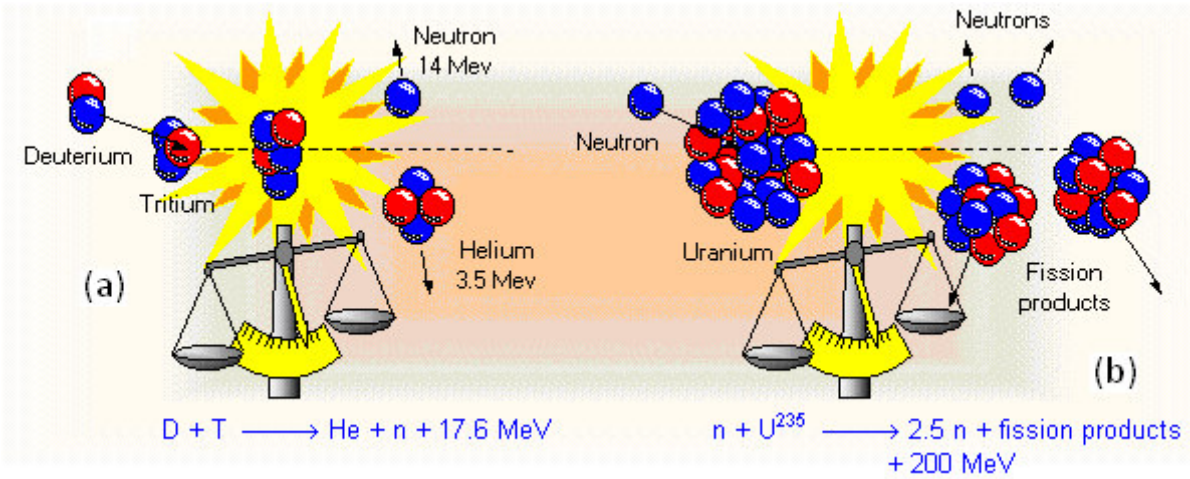

Figure 2 Fusion of two light nuclei (a) and fission of a heavy nucleus (b)

1.2 Fusion reactions

To obtain a fusion reaction, we must bring two nuclei sufficiently close together for them to overcome electrostatic repulsion, as they are both charged positively. A certain amount of energy is therefore vital to cross this barrier and arrive in the zone, extremely close to the nucleus, where the weak nuclear forces exceed the electrostatic repulsion. The probability of crossing this barrier may be quantified by the "effective cross section". The dependence of effective cross sections of several fusion reactions on interaction energy expressed in keV (thousand of electronvolts [eV], 1eV= 11600 K) is shown in Figure 3.

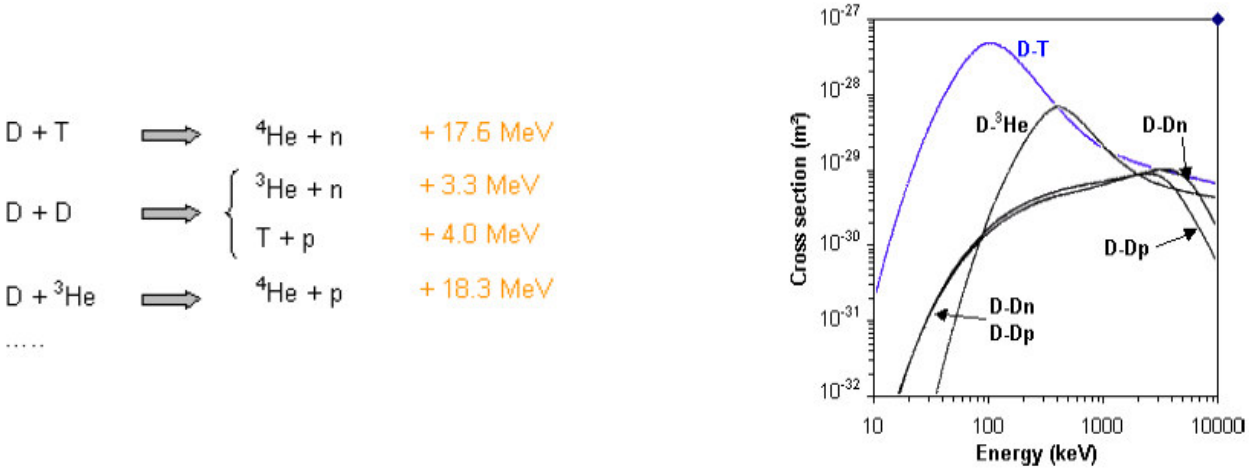

Figure 3. Most important types of fusion reactions.

The most accessible fusion reaction is the reaction involving two isotopes of hydrogen, deuterium (a neutron plus a proton) and tritium (two neutrons plus a proton) and on this reaction most research on controlled fusion is conducted.
The temperatures (which measure interaction energy) required for thermonuclear fusion are greater than a hundred million degrees. At such temperatures, the matter presents as a plasma. A plasma is a gaseous assembly of electrons, ions and neutral molecules residing in electric and magnetic field. Plasma exists in the universe in various forms and with very variable characteristics. Thus temperatures go from one to 10000keV and densities range even more widely, going from a few particles per m^3 in interstellar gas, up to 10^{30} particles per m^3 in the centre of certain stars. Plasma is by far the most widespread form of matter in the universe.
Fusion is the source of energy in the sun and other stars. A star starts to shine when, under the force of gravity, the matter in its very heart attains sufficiently high densities and temperatures to set off thermonuclear reactions, which then release energy. Plasma's tendency of dispersing, and therefore cooling down, is balanced out by gravitational force. On Earth, gravitational confinement is impossible.
Two paths have been studied to reproduce these reactions:

- Raising a small volume of matter for a very short time to very high pressure and temperature, described as inertial confinement. These experiments seek to obtain the greatest possible number of fusion reactions before the plasma disperses.
- Trapping and maintaining plasma at very high temperature. This plasma is confined in an intangible torus-shaped bottle created by magnetic fields, described as magnetic confinement.

1.3 Magnetic Confinement

In order for the fuel in the form of plasma to produce enough thermonuclear reactions, it must be maintained in a limited volume and kept away from any solid material in order to maintain its high temperature. This is called confinement.
In the free state of plasma, the particles' trajectory is random and the particles can easily escape, Figure 4 -a.
As the plasma is made up of charged particles, the magnetic fields may act on them. If the plasma is subjected to a rectilinear magnetic field, the particles wind around the field lines and will no longer touch the side walls, Figure 4-b.
So as to avoid losses from the edges, we close off the magnetic bottle by creating a torus, Figure 4-c. The magnetic field thus created by a series of magnets surrounding the plasma is called a toroidal magnetic field. The magnets generating this field are the toroidal magnets.
To minimize particle leakage even more, the field lines must be helicoidal, Figure 4-d. This is achieved by adding another magnetic field to the toroidal field, which is perpendicular to it (the poloidal field). The method used to produce these helicoidal field lines has given birth to two types of machines (Figure 5).

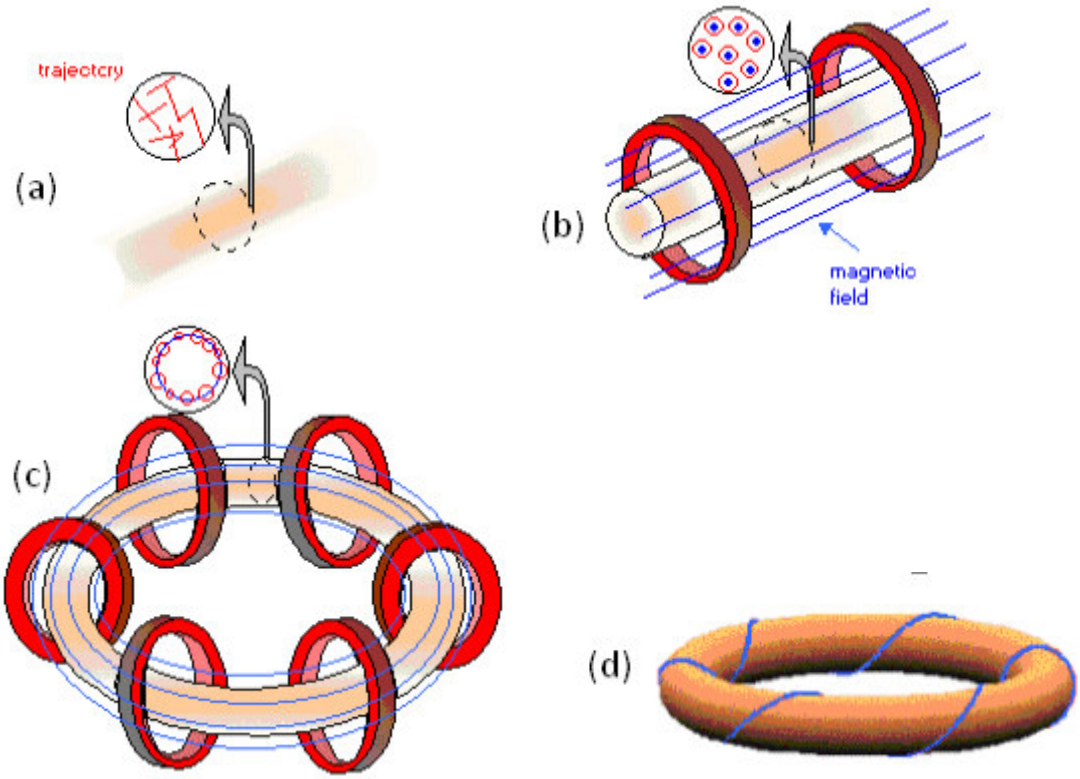

Figure 4. a): a not confined plasma; b): sketch of a magnetic bottle configuration; c): close loop confinement; c): needs of a configuration with helicoidal magnetic field lines.

In a "tokamak", an assembly of coils produces a magnetic field in the direction of the torus, to which the magnetic field created by an intense axial current flowing in the plasma itself is added. The two fields generate the helicoidal structure of the field lines, Figure 5-a. In a

"stellarator", the magnetic configuration is entirely based on currents flowing in helicoidal coils, Figure 5-b.

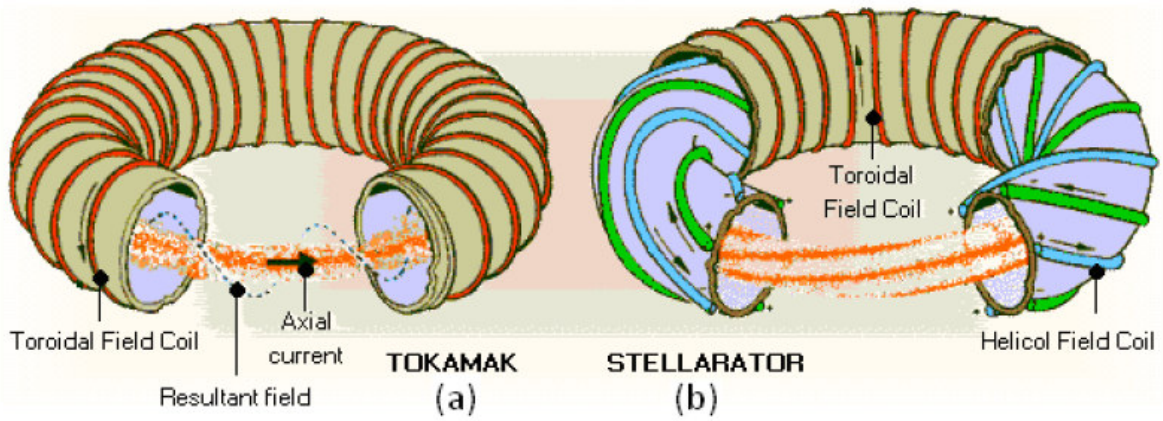

Figure 5. Types of machine. The coils producing the main field are shown.

There are many other kinds of fusion experiments whose magnetic configuration differ from those before presented. The Reverse Field Pinch (**RFP**) is a fusion experiment similar to the Tokamak, but where the poloidal field has the same order of magnitude of the toroidal field. One of the most important RFP experiment around the world is the RFX experiment installed in Padua.

1.4 Tokamak

The Tokamak is an axisimmetric torus with a large toroidal magnetic field, a moderate plasma pressure and a relatively small toroidal current. The basic means of producing the plasma current consists in generating it by magnetic induction. Plasma current is created by induction exactly like in an electric transformer. A coil made up of horizontal layers can be placed in the middle of the torus (Figure 6-a) or connected to the centre of the torus by a iron core (Figure 6-b). When the current flowing through the coil is varied, the gas in the Vacuum Chamber senses a voltage due to the transformer effect and the breakdown and the Ohmic Heating is achieved.

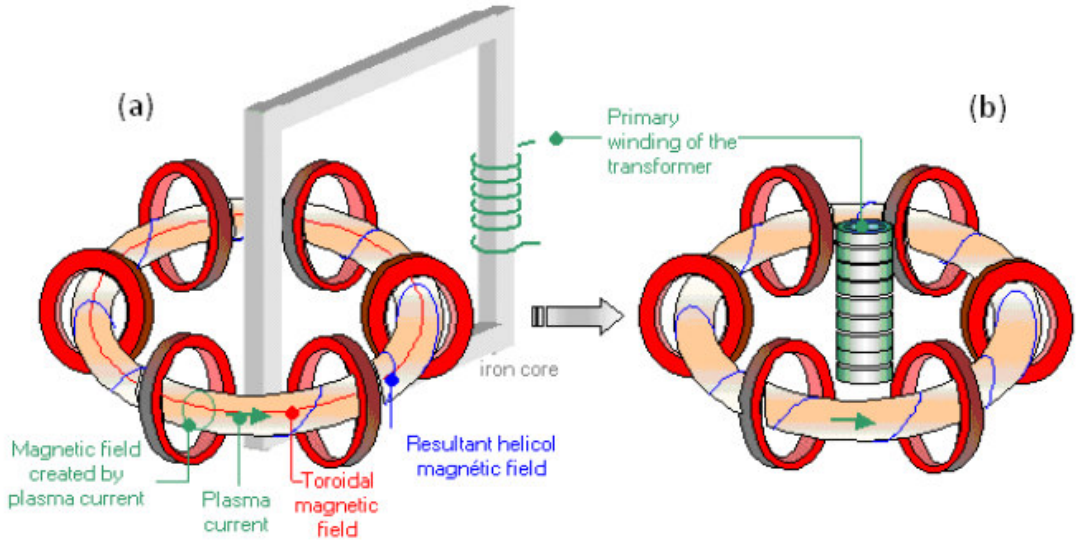

Figure 6. Generating Plasma current with (a) and without (b) iron core.

The equilibrium of the plasma, its position, its shape and the control of the current are taken care of by the group of horizontal magnets called poloidal field coils, Figure 7.

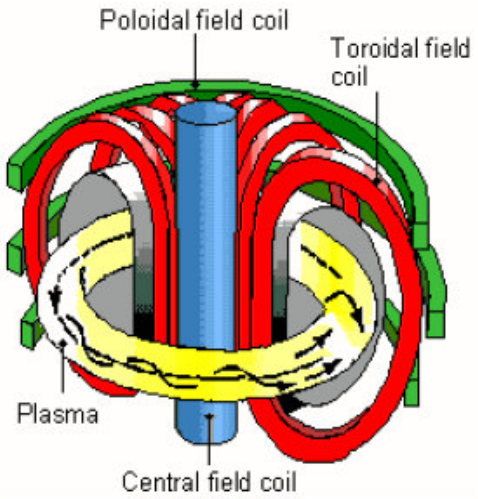

Figure 7. Plasma equilibrium by Poloidal Coils (green).

Whatever the way in which the plasma was created inside the confinement structure, it never initially has the temperature required for fusion. Three methods are possible to heat the plasma up:

- The current flowing in the plasma is used to heat the plasma by Joule effect (ohmic heating). The latter is effective up to a temperature around 10 million degrees. Beyond that, plasma resistivity becomes too weak and effectiveness of this method decreases.
- Heating by injection of neutral particles consists in creating and accelerating a beam of ions, outside the confinement machine. This beam is then neutralised before entering the plasma where the particles are ionised and confined by the magnetic field. The collisions redistribute energy and the temperature of the plasma rises.
- The plasma can absorb energy from electromagnetic waves at frequencies characteristic of its particles. This heating by electromagnetic waves is transmitted to the plasma by antennas covering part of the confinement area. The frequency has to be chosen according to the type of particles (ions or electrons) that shall be heated up and the area through which the wave and thus the heating will be absorbed.

1.5 Ignition and break even criteria

In a thermonuclear fusion reactor by magnetic confinement, the temperature of the plasma may be raised to a suitable level by a combination of the methods presented above. When there is a large number of a fusion reaction, the energy carried by the helium nuclei remains confined in the plasma and contributes to heating it. If this contribution becomes equal to the energy lost by the plasma, then the heating methods above are no longer necessary. The thermonuclear plasma is thus self-maintained, and we say that it is ignited (**criteria of ignition**). If we define the **amplification factor Q** as being the ratio between the total power generated by the plasma and the heating power injected into the plasma, then this amplification factor is infinite ($Q \rightarrow \infty$) if the plasma is self-maintained. When this factor is equal to one ($Q=1$), the plasma supplies as much energy as is injected into it. This last condition is called "**break even**".

1.6 The main results

Since the invention of the tokamak T1 in 1958, plasma fusion power generated by various installations throughout the world has increased as shown in Figure 8. Many significant results have been obtained in all fields, whether in physics or in the technologies used.

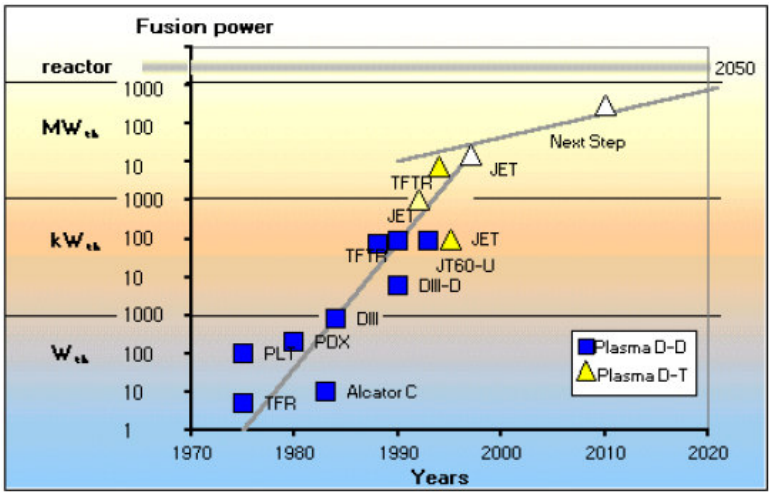

Figure 8. The progress in fusion power through the years.

The highest fusion power plasmas was obtained in 1997 in the Joint European Torus (**JET** at Culham, UK), Figure 9.

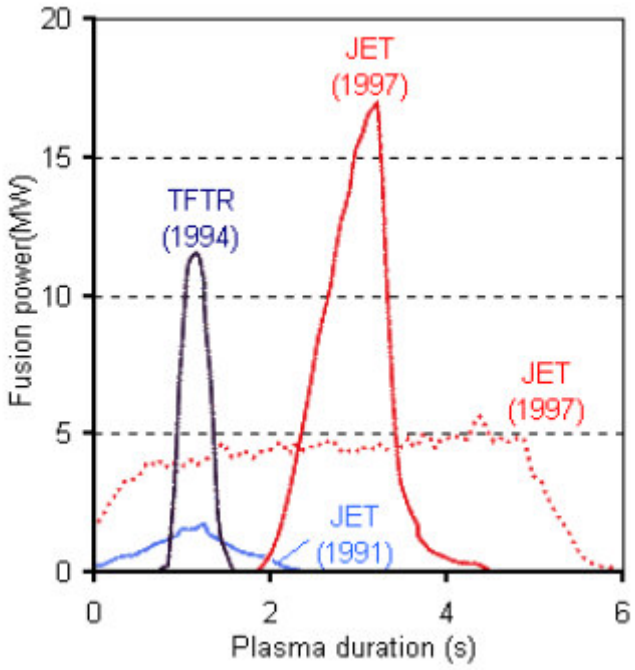

Figure 9. Important fusion results.

To obtain a high performance plasma, it must meet criteria of density (there must be enough pressure) and of temperature (these nuclei must be at temperatures of several million degrees). The energy carried by the helium nuclei must also remain confined in the plasma for a sufficient time. The period during which the energy stays confined inside the plasma is called the **energy confinement time** and this varies according to the square of the major radius of the plasma. This size effect is one of the (intrinsic) features of fusion installations. High performance plasmas are obtained in large-scale installations.
The criteria above have been obtained independently for density, temperature and confinement time in the various current experimental installations. The next step is to demonstrate control of sustained combustion of deuterium-tritium plasma at high power levels and over long durations. This will be the main goal of the next international experimental machine ITER, presented in section 2.

1.8 From experimental devices to reactor

Future electricity generating fusion reactor will have a nominal power of above 1GW. The plasma confinement in this reactor has to be only 4 or 5 times higher than in the nominal performance of the ITER project. It is difficult to define what the future current generating fusion reactor might be like. If we exclude all the components dealing with energy production, a reactor will look much like what an experimental installation of the next generation like ITER. What the diagram of the principle of the electro-generating reactor could be as shown in Figure 10.

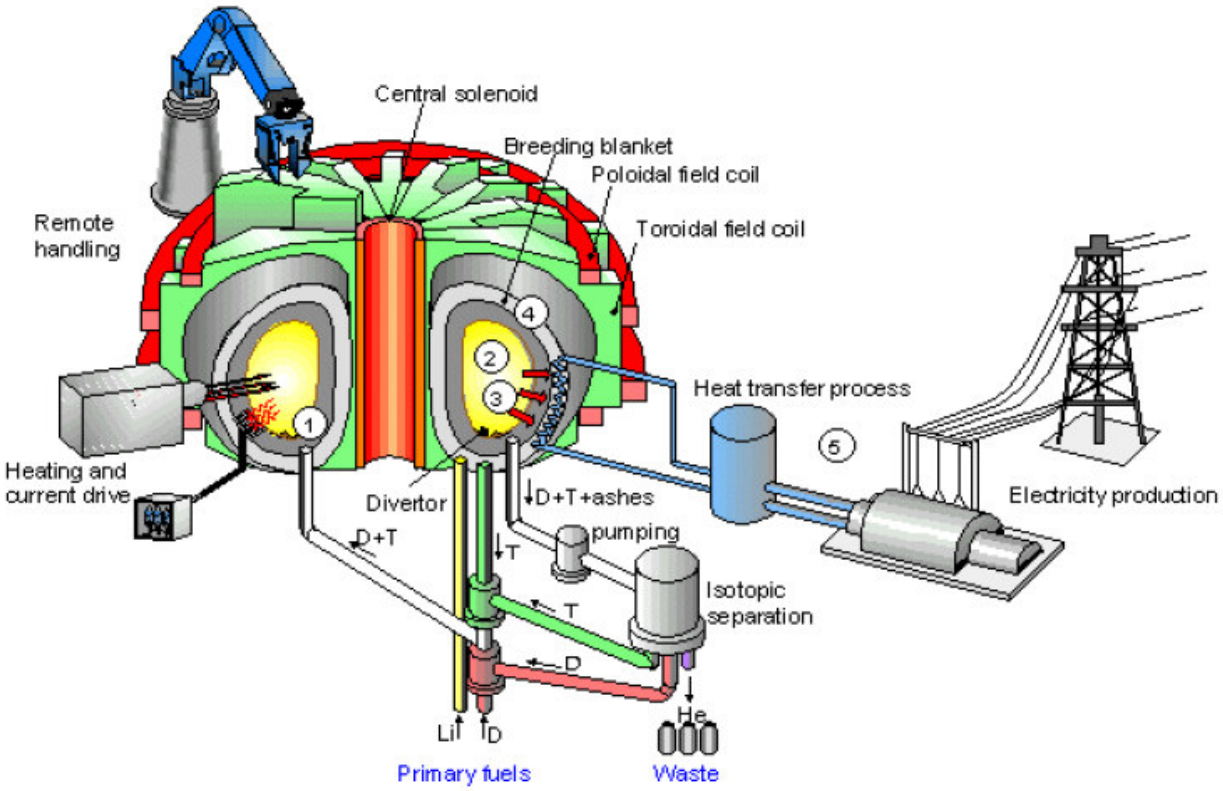

Figure 10. Schema of a future electrical power generating fusion reactor.

The deuterium-tritium fuel mixture is injected **(1)** into a chamber, where, thanks to a system of confinement it goes into a plasma state and burns **(2)**. In doing so, the reactor produces ash (helium atoms) and energy in the form of fast particles or radiance **(3)**. The energy produced in the form of charged particles and radiance, is absorbed in a special component, the "first wall" which, as its name illustrates, is the first material element encountered by the plasma. The energy, which appears in the form of kinetic energy in neutrons, is, for its part, converted into heat in the breeding blanket **(4)**: which is the element beyond the first wall, but nevertheless inside the vacuum chamber. The breeding blanket is Tokamak structure where tritium is bred by neutron capture in lithium in the blankets. To determine the best combination for tritium and power production, a number of different combinations of tritium breeding material, neutron multiplier, structural material, and coolant will be tried out on ITER to determine the best combination. Each one of these solutions is referred to as a “breeding technology”. The vacuum chamber itself is the component enclosing the area where the fusion reaction takes place. The first wall, blanket and vacuum chamber are obviously cooled down by a heat extraction system. The heat is used to produce steam and supply a conventional turbine and alternator electricity producing system **(5)**.

2. ITER [7]

The International Thermonuclear Experimental Reactor (ITER) is the previous step to build the demonstrative nuclear fusion power plant (DEMO). The goals of the ITER experiment are to address several plasma physics and fusion technology issues. ITER thus has the crucial role of being the flagship facility for the world's fusion program for the next two decades. The project is enormously important in that progress towards a fusion reactor will be directly tied to the physics and technological performance of ITER.
At present seven parties are participating to the project: the European Union (EU), India, Japan, Republic of China, Russia, South Korea, and the USA. After long negotiations, an international agreement was finally reached (in July 2005) to construct the new ITER at the French site in Cadarache.
After several proposal, from the 1985 to today, it was decided to build a cost-limited version of ITER called Fusion Energy Advanced Tokamak (FEAT). This version is aimed to achieve a finite value of the gain power Q=10 (against the initial goal of achieve the ignition conditions –Q=∞-). The main parameters are shown in Table 1 [8].

Table 1. Parameters for base operation of ITER experiments [8].

Parameters	**Symbol**	**Units**	**ITER**
Major radius	R_0	m	6.2
Minor radius	a	m	2.0
Aspect ratio	$\varepsilon=R_0/a$		3.1
Elongation	κ		1.7
Plasma Volume	V_P	m^3	837
Plasma surface area	A_P	m^2	678
Toroidal Magnetic field	$B_0=B_t(R_0)$	T	5.3
Plasma current	I_P	MA	15
Kink safety factor	q_*		1.94
Safety factor	q_{95}		3.0
Average temperature	$T_e \approx T_i = T_k$	keV	11.2
Temperature peaking factor	$T(0)/T_k$		1.7
Average electron density	n_{20}	$10^{20}m^{-3}$	0.91
Density Peaking factor	$n(0)/n_{20}$		1.1
Density/Greenwald Density	n_{20}/n_G		0.85
Energy Confinement time	τ_E	s	3.7
Performance parameter	$p\tau_E$	atm*s	6.4
Power gain	$Q=P_f/P_H$		10
Neutral Beam power	P_{NBI}	MW	33
ICH power	P_{ICH}	MW	20
ECH power	P_{ECH}	MW	20
Ohmic pulse length	τ_{pulse}	s	400
Toroidal beta	β		0.026

2.1 The Project

The primary physics mission of ITER is to produce a stable, well-confined, Q=10 plasma lasting for a sufficiently long duration to reach quasi-steady-state operation. A second physics mission is to achieve steady state operation using non-inductive current drive at Q>5.
With respect to technology, the construction of ITER would demonstrate the viability of large superconducting magnets, various plasma facing materials, and large-scale remote handling. It would also test the effectiveness of the divertor design and begin to explore tritium breeding.

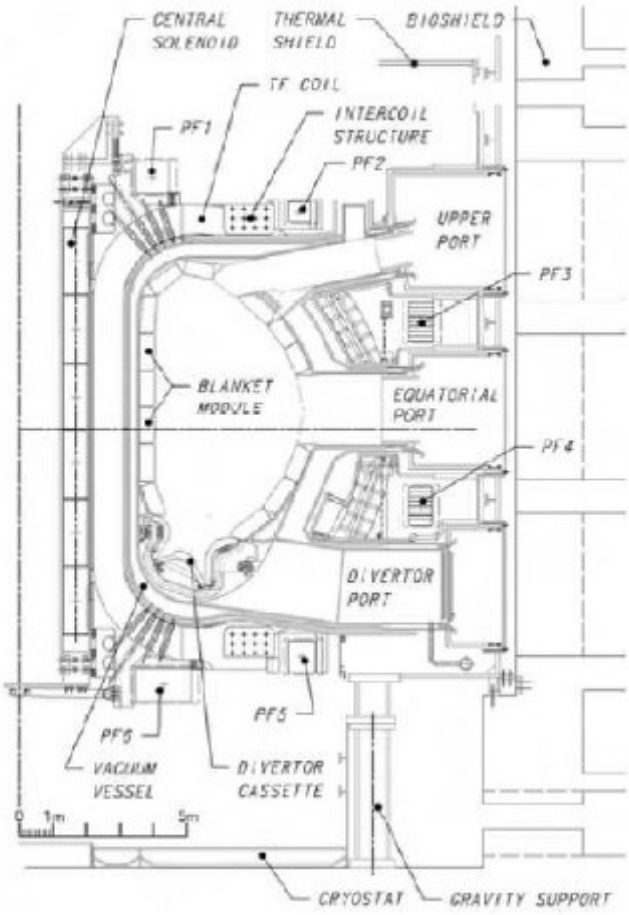

Figure 11. Cutaway drawing of the ITER design. ITER Final Design Report (2001).

The actual ITER design is illustrated in a cutaway view in Figure 11 and a possible structure of the device is shown in Figure 12. Note that ITER has a single null divertor and superconducting magnets constructed of NbTi and Nb_3Sn. The magnetic field at the center of the plasma is B_0 = 5.3 T. The size of the machine has been designed subject to the constraints of achieving Q=10 operation with H-mode scaling in a plasma which is MHD stable without a conducting wall. This leads to a major radius R_0 = 6.2 m, a minor radius a = 2 m, and an aspect ratio R_0/a = 3.1. The current required to achieve the necessary confinement time is I =15 MA. At Q = 10 operation the average density and temperature are $n_{20} = 0.9*10^{20}$ m^{-3} and T_k = 11keV.

For base operation, ITER will have three sources of auxiliary power: 33 MW of negative ion-driven neutral beams, 20 MW of ICRH (Ion Cyclotron Resonance Heating), and 20 MW of ECRH (Electron Cyclotron Resonance Heating). The neutral beams and ICRH will be used primarily for heating. The ECRH will be used, at least initially, to stabilize a localized resistive MHD instability known as the neoclassical tearing mode (NTM). This instability should limit the achievable value of β, see section 3.

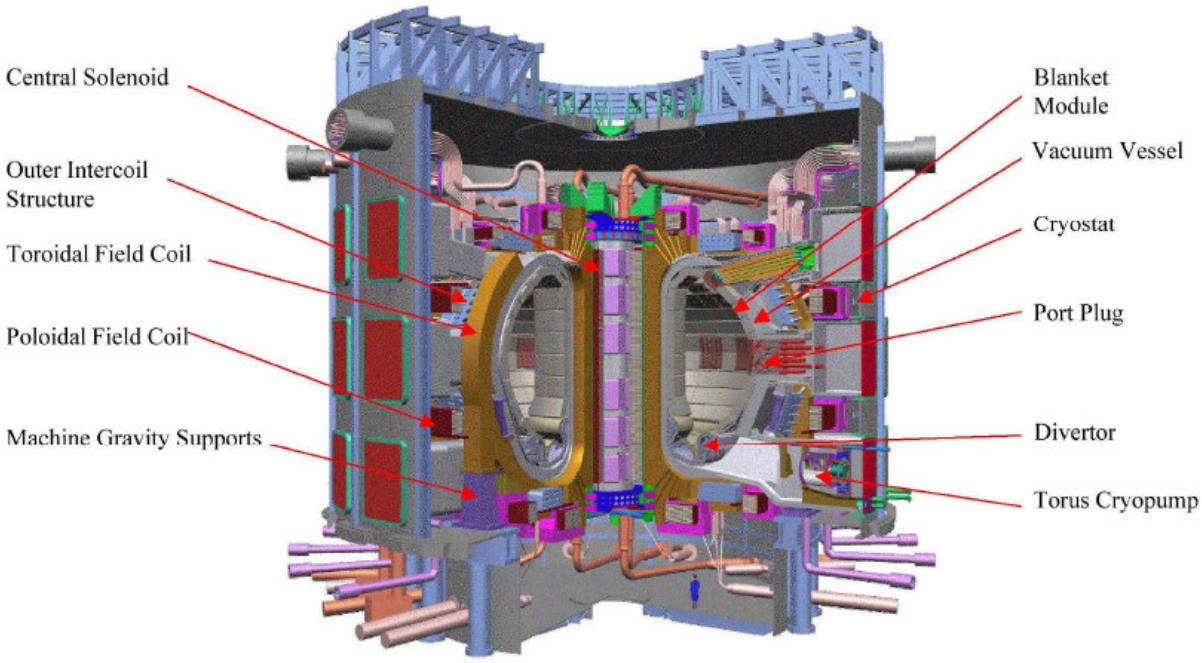

Figure 12. Cutaway of ITER Tokamak inside the Cryostat/Biological Shield.

ITER will operate for pulse durations of about $\tau_{pulse} \approx 400$s, driven entirely by the ohmic transformer. No current drive is planned for base operation. If successful, ITER should produce a Q=10 plasma corresponding to a fusion performance factor of $p\tau_E = 6.4$ atm s.
ITER is close to being a full-scale prototype fusion reactor in terms of size and performance. The main difference is that ITER is still largely an experimental facility and therefore has not been designed to have the very high duty factor associated with a steady state power producing reactor.

2.2 Design

Beyond the extrapolation still in plasma physics, the major technical challenges of building and operating ITER are the large size of the superconducting magnets, structures and reaction chamber, the high heat and neutron fluxes on plasma-facing in-vessel components, and the ability to rapidly and remotely repair and maintain in-vessel components. The overall philosophy of the ITER design has been to use advanced but proven technological approaches, verifying their application to ITER through detailed analysis, and validating them through technology R&D.
Such activities included development and qualification of the applicable technologies by testing at different scales, development and verification of industrial techniques. Testing programs determine the operating margins in performance of hardware, to optimise the flexibility in operation.

2.2.1 Magnets and structures

The superconducting magnet system is composed of three main subsystems. 18 toroidal field (TF) coils (Figure 13, left) which produce the confining and stabilizing toroidal field. 6 poloidal field (PF) coils which contribute to the plasma positioning and shaping and central solenoid (CS) coil which provides the main contribution to inducing current in the plasma. The magnet system weighs, in total, about 8700 t.
The CS and TF coils use Nb_3Sn as superconductor, and the technology of "wind, react and transfer", whereas the PF and correction coils use NbTi. All coils are cooled by supercritical helium at ~ 4.5K.

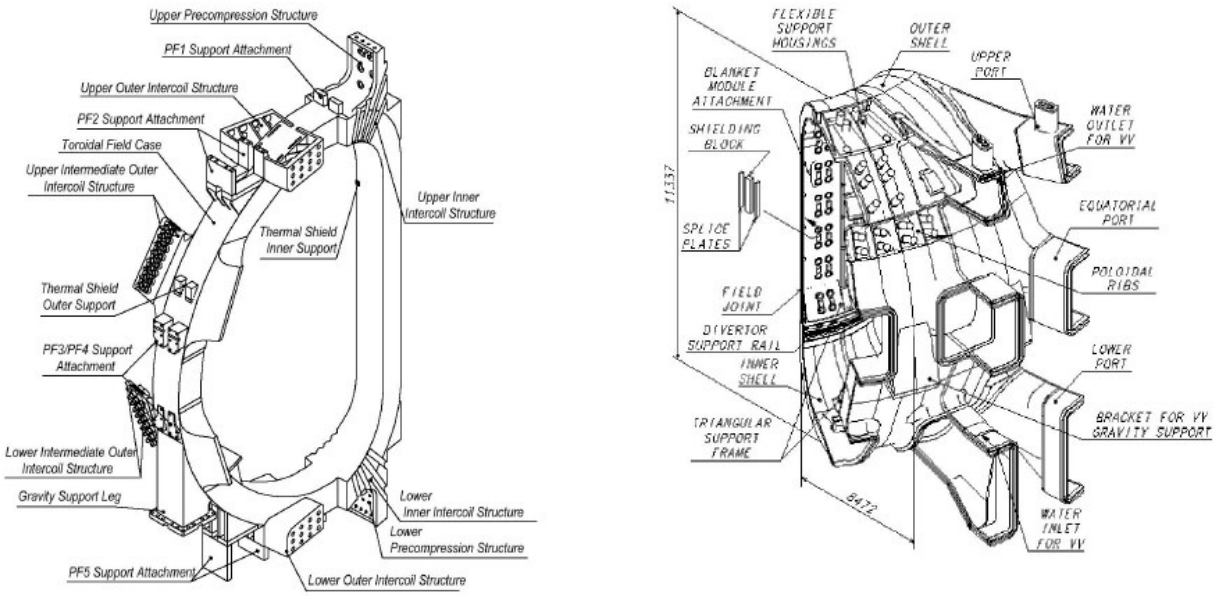

Figure 13. TF coil structure (left) and main vessel (right).

The TF coil case is the main structural component of the magnet system and the machine core. The PF coils and vacuum vessel are linked to the TF coils such that all interaction

forces are resisted internally in the system. The TF coils are wedged to resist at toroidal compression and local de-wedging forces.

2.2.2. Vessel, Blanket and Divertor

The double-walled vacuum vessel (VV; Figure 13, right) is lined by modular removable components, including blanket modules (Figure 14, left) composed of a separate first wall mounted on a shield block, divertor cassettes (Figure 14, right), and diagnostics sensors, as well as port plugs such as the limiter, heating antennae, and test blanket modules.
All these removable components are mechanically attached to the VV.
These vessel and internal components absorb most of the radiated heat from the plasma and protect the magnet coils from excessive nuclear radiation. This shielding is accomplished by a combination of steel and water, the latter providing the necessary removal of heat from absorbed neutrons. A tight fitting configuration of the VV to the plasma aids the passive plasma vertical stability, and ferromagnetic material in the VV located under the TF coils reduces the TF ripple and its associated particle losses.

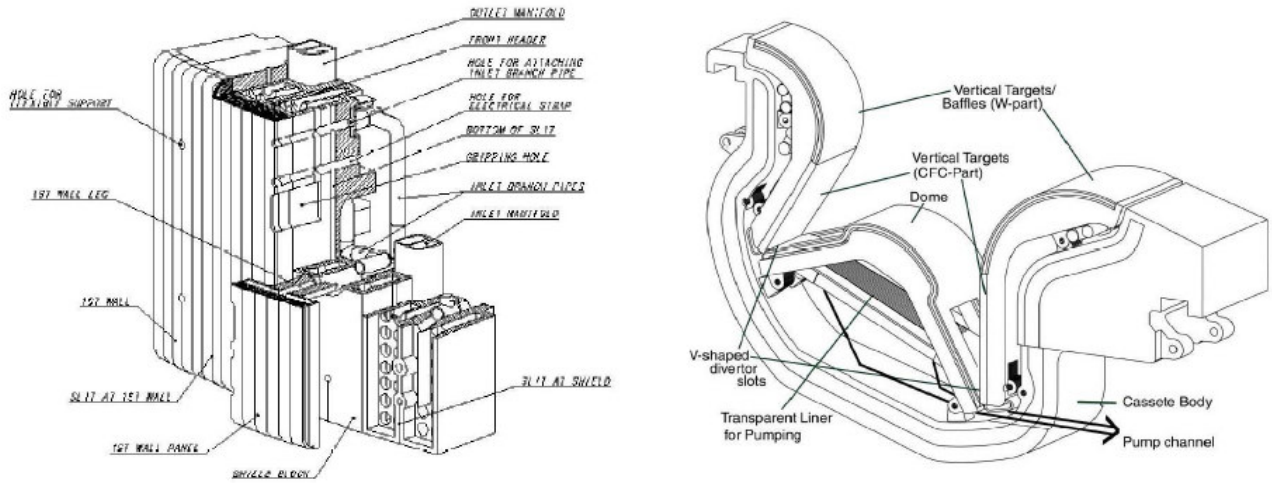

Figure 14. (left) Blanket module and (right) Divertor cassette.

The initial blanket acts solely as a neutron shield, and tritium breeding experiments are confined to test blanket modules which can be inserted and withdrawn at radial equatorial ports. The blanket module design consists of a separate faceted first wall (FW) built with a Beryllium (Be) armour and a water cooled copper heat sink attached to a stainless steal (SS) shielding block. This minimizes radioactive waste and simplifies manufacture.
The blanket is cooled by channels mounted on the vessel.
The divertor is made up of 54 cassettes. The target and divertor floor form a W-shape and the large opening between the inner and outer divertor legs allows an efficient exchange of neutral particles. These choices provide a large reduction in the target peak heat load, without adversely affecting helium removal.
The current design uses carbon at the vertical target strike points. Tungsten is being considered as a backup, and both materials have their advantages and disadvantages. Carbon has the best behaviour to withstand large power density pulses (ELMs, disruptions), but

gives rise to tritiated dust. Procedures for the removal of tritium are under consideration and need further development. Presently, a removal of all carbon components is foreseen before initiating the D-T phase in ITER.

2.3.3. In-Vessel Remote Handling.

Systems near the plasma will become radioactive and will require remote maintenance, with special remote handling equipment. An in-vessel transporter system is used for the removal and reinstallation of blanket modules, multifunction manipulators for divertor cassette removal, and specialised manipulators to handle vacuum vessel port plugs. Special casks, which dock horizontally to the access ports of the vacuum vessel, are designed to house such equipment and to transport radioactive items from the tokamak to the hot-cell where refurbishment or waste disposal operations can be carried out. Docking of these casks to the vessel and the hot cell flanges is tight, to avoid spreading of contamination. Hands-on assisted maintenance is used wherever justifiable, following the ALARA principles.

3. MagnetoHydroDynamic Model for a confined plasma

In magnetic confinement fusion experiments is necessary to know how a magnetic field can produce forces to hold a plasma in order to achieve a stable, macroscopic equilibrium.
The analysis of macroscopic equilibrium and stability is based on a single-fluid description [10] called MHD. In this model the separate identities of the ions and electrons do not appear.
MHD takes into account the following principles making up a closed set of equations (where the number of the equations is equal to the number of the unknowns) [9]:

- Conservation of mass, expressed by the continuity equation;
- Conservation of momentum, expressed by the equation of motion;
- Conservation of Energy, expressed by the energy or entropy equation;
- The Ohm's law;
- The Faraday's law;
- The Ampere's law.

The requirement $\nabla\cdot\mathbf{B}=0$ is necessary as initial condition; it will then hold for later times by Faraday's law.
One particular point worth noting in the derivation is the transformation of the electron momentum equation into a single-fluid Ohm's law, which relates the electric field to the current density. There are actually three forms of Ohm's law depending upon how many terms are maintained. Consequently, there are three corresponding forms of the MHD model. The most inclusive form is usually referred to as the "generalized" Ohm's law. Neglecting certain terms in this relation leads to a reduced form, known as the "resistive" Ohm's law. Lastly, if the resistivity itself is neglected, one obtains the "ideal" Ohm's law, which corresponds to plasma with perfect conductivity. Interestingly, for all three forms of Ohm's law, the equilibrium force balance relation is identical.
With the help of the Ideal MHD model, the main aspects regarding the Tokamak equilibrium and stability are discussed as follows.
The Ideal MHD model equations [JF, PH] are as follows:

(1)	$\frac{d\rho}{dt}+\rho\cdot\nabla\cdot\mathbf{v}=0$	Continuity equation
(2)	$\rho\frac{d\mathbf{v}}{dt}=\mathbf{J}\times\mathbf{B}-\nabla p$	Equation of motion
(3)	$\mathbf{E}+\mathbf{v}\times\mathbf{B}=\mathbf{0}$	Ideal Ohm's law
(4)	$\frac{d}{dt}\left(\frac{p}{\rho^{\gamma}}\right)=0$	Entropy equation
(5)	$\nabla\times\mathbf{E}=-\frac{\partial\mathbf{B}}{\partial t}$	Farady's law
(6)	$\nabla\times\mathbf{B}=\mu_0\mathbf{J}$	Ampere's law
(7)	$\nabla\cdot\mathbf{B}=0$	

3.1 Tokamak equilibrium

The subject of Tokamak equilibrium has two basic aspects. Firstly there is the internal balance between the pressure of the plasma and the forces due to the magnetic field. Secondly there is the shape and position of the plasma, these being determined and controlled by currents in external coils.
A fusion plasma must be in the shape of a torus in order to avoid end losses. Here, two qualitatively different types of forces are involved in producing an MHD equilibrium. First there are radial expansion forces due to the natural tendency of a hot gas to expand. Both toroidal and poloidal magnetic fields are capable of balancing the radial expansion force. Second, there are toroidal forces, arising from the toroidal geometry, that tend to make the plasma "ring" expand to a larger and larger major radius. Bending a straight cylinder into a torus results in the generation of three new toroidal forces all directed outwardly along the direction of the major radius (i.e., along R). These forces are as follows:

a: the hoop force;
b: the tire tube force;
c: the 1/R force.

These kinds of forces are due to the toroidal geometry. Both poloidal and toroidal magnetic field approximately behave as 1/R. Such a behavior produces that the poloidal field causes an outward force acting on the inner surface of the torus, close to the symmetry axis, greater then the inward force acting on the outer plasma surface. The net results is an outward force: the hoop force. A sketch is presented in Figure 15.

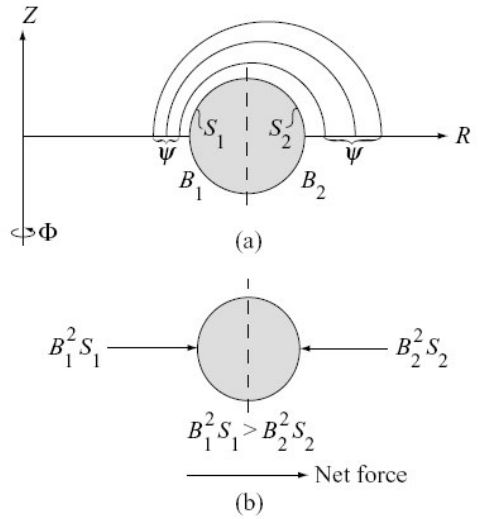

Figure 15 Qualitative picture of the hoop force: (a) conservation of flux showing that $B_1 > B_2$; (b) toroidal force balance showing a net outward force along R.

Pressure is a constant on the edge of the plasma. On the S_1 surface, Figure 15, the pressure generates an inward force which is overcome by the outward force exerted on the S_2 surface. This is called tire-tube force.
Finally, the 1/R force is due to the magnetic field. In case of diamagnetic plasma, it generates a net outward force, while in case of paramagnetic plasma it generates a net inward force.

3.2 Equilibrium equation

The study of the equilibrium condition is carried out considering the absence of any flows. That means as follows:

$$\frac{\partial}{\partial t} = 0, \quad \mathbf{v} = \mathbf{0} \tag{8}$$

In this case the equation of motion becomes:

$$\mathbf{J} \times \mathbf{B} = \nabla p \tag{9}$$

Equation (9) is the basic condition for equilibrium. This requires that the magnetic force balance the force due to the plasma pressure, that is the force on the plasma be zero at all points.
From this equation, it can be deduced that there is no pressure gradient along the magnetic field lines and the magnetic surfaces are surfaces of constant pressure. Current lines lie on the magnetic surfaces, as shown in Figure 16. That means the current flow between two flux surfaces and not across them.

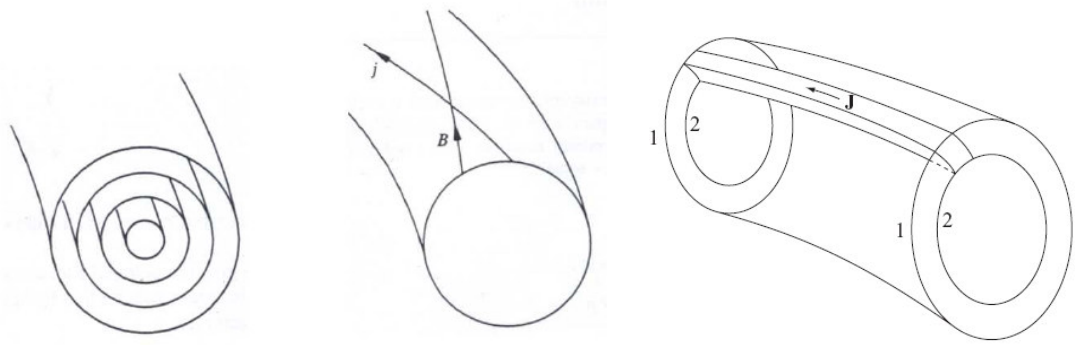

Figure 16 (left) The magnetic field lines lie in nested toroidal magnetic surfaces. They are also surfaces of constant pressure. (middle) Both current lines and magnetic lines lie on magnetic surfaces. (right) Two flux surfaces, 1 and 2, at two different toroidal locations showing that the current flows between and not across them.

Finally, reordering the MHD equation under the present conditions, one can find:

$$\nabla \cdot \left(\frac{B^2}{2\mu_0} - p \right) = 0 \tag{10}$$

Considering, the ideal case of a perfectly diamagnetic plasma with uniform pressure and toroidal shape with a minor radius r. The magnetic field is zero into the plasma volume and equal to B_a at the edge. In this ideal case we have

$$\frac{B_a^{\,2}}{2\mu_0} = p \tag{11}$$

It is common to use in plasma physics a parameter which represents the efficiency of confinement of plasma pressure by the magnetic field:

(12) $$\beta = \frac{p}{B^2 / 2\mu_0}.$$

3.3 Magnetic coordinates

To describe the equilibrium is useful to introduce a cylindrical coordinate system based on the major axis R of the torus, as shown in Figure 17.

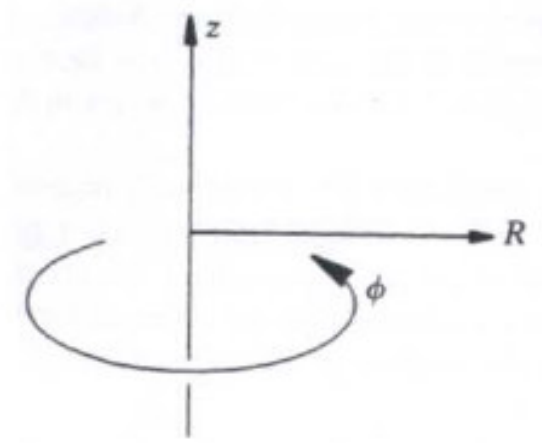

Figure 17 Cylindrical coordinate system.

In studying tokamak equilibrium it is convenient to define the poloidal magnetic flux function ψ. This function is determined by the poloidal flux lying within each magnetic surface and is therefore a constant on that surface.
Let ψ be the pololoidal flux per radian in φ, the poloidal magnetic field is related to ψ by

(13) $$B_R = -\frac{1}{R}\frac{\partial \psi}{\partial z} \quad B_z = \frac{1}{R}\frac{\partial \psi}{\partial R}.$$

The flux function is arbitrary to an additive constant which may be chosen for convenience.
A total poloidal Ψ flux function can be defined as the magnetic flux linked with the circumference passing across point P(R,z) and having its center on the z axis (Figure 18). It is related with the poloidal magnetic flux function by $\Psi = 2\pi\,\psi$.

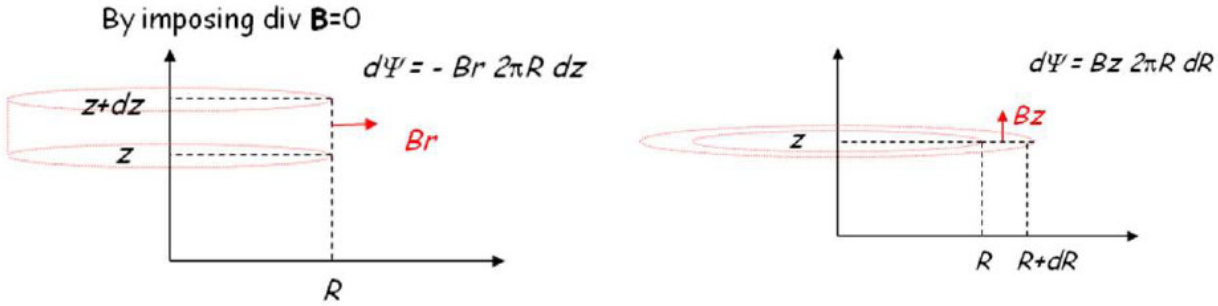

Figure 18 Elementary considerations about the poloidal flux function.

For the same geometry of J and B, a poloidal current function f can be defined as the current per unit of toroidal angle φ, so that the total current function $I_{pol}=2\pi$ f and it is related to the poloidal current density by

(14) $$J_R = -\frac{1}{R}\frac{\partial f}{\partial z} \quad J_z = \frac{1}{R}\frac{\partial f}{\partial R}$$

It is possible to show that $\nabla f \times \nabla p = 0$ and $\nabla \psi \times \nabla p = 0$ so f is a function of p and both are functions of the poloidal flux function ψ. The poloidal magnetic flux is normally used as a label for the magnetic surfaces.

3.4 Grad-Shafranov Equation

The equilibrium equation for an axisymmetric system such as a tokamak can be written as a differential equation for the poloidal flux function ψ. This equation which has two independent functions, p(ψ) and f(ψ), is usually called the Grad-Shafranov equation.
The Grad-Shafranov equation can be found after some mathematics [10] by means of the equilibrium equation (9) and of equations (13) and (14):

(15) $$R\frac{\partial}{\partial R}\left(\frac{1}{R}\frac{\partial \psi}{\partial R}\right) + \frac{\partial^2 \psi}{\partial z^2} = -\mu_0 R^2 \frac{\partial p}{\partial \psi} - \mu_0{}^2 f \frac{\partial f}{\partial \psi}$$

Figure 19 shows the flux surfaces and profiles of j_φ, p and B_φ obtained by numerical solution of the equation for a typical case.

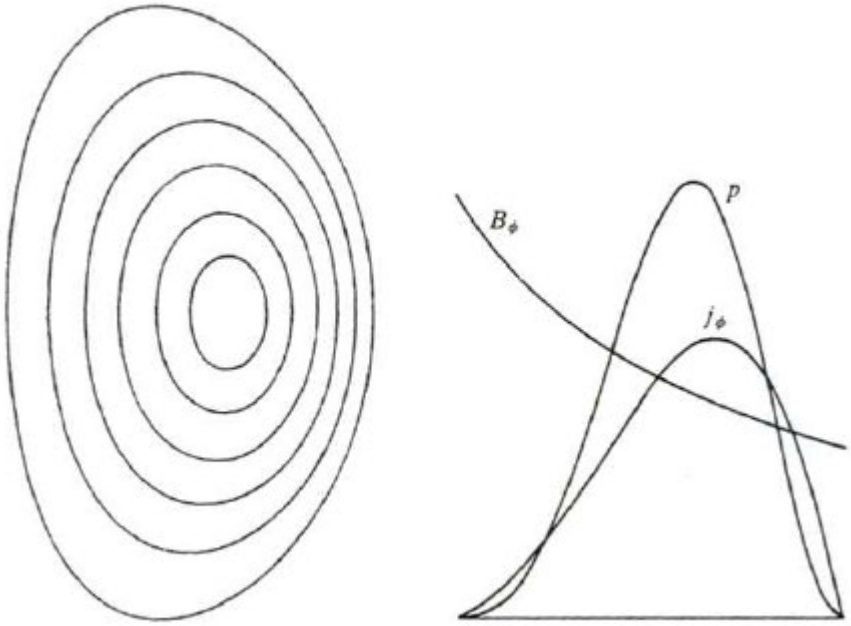

Figure 19 Equilibrium flux surfaces and plots of toroidal current density, plasma pressure and toroidal magnetic field across the midplane.

Each field line follows a helical path as it goes round the torus on its associated magnetic surface. If at some toroidal angle, φ, the field line has certain position in the poloidal plane, it will return to that position in the poloidal plane after change of toroidal angle Δφ. The **Safety Factor** value is defined as

$$q = \frac{\Delta\varphi}{2\pi} \tag{16}$$

It is so called because of the role it plays in determining stability.
If q=m/n, where m and n are integers, the field line joins up on itself after m toroidal and poloidal rotations round the torus. Rational value of q play an important role in stability, a brief discussion is reported in section 4.1. It can be also seen as the pitch of the field line twisted round the torus.

3.5 Analytical solution for large aspect ratio

The aspect ratio of a Tokamak is given by the ratio:

$$\varepsilon^{-1} = \frac{R_0}{a} \tag{17}$$

Where R_0 is the major radius (coordinate of the magnetic axis along the major radius R), and a is the minor radius of the edge of the plasma.

In case of plasma with circular cross section and large aspect ratio (the inverse aspect ratio ε is a small quantity), the q Safety Factor can be approximated as:

$$q = \frac{rB_\varphi}{R_0 B_\vartheta} \tag{18}$$

Where B_ϑ is the poloidal magnetic field and r is the minor radius of a given flux surface.
Moreover, the Tokamak equilibrium takes a simple approximated form:

$$\begin{aligned} B_\varphi &= B_{\varphi 0}\frac{R_0}{R} \qquad B_\vartheta \cong \varepsilon B_\varphi \\ J_\varphi &\cong \frac{\varepsilon B_\varphi}{\mu_0 a} \qquad J_\vartheta \cong \frac{\varepsilon^2 B_\varphi}{\mu_0 a} \end{aligned} \tag{19}$$

The form for the Tokamak equilibrium presented in equations (19) can be considered as a first order solution of the Grad-Shafranov equation, where the effects due to the toroidal geometry are not included.
When toroidal effects are included, the flux surfaces form non-concentric circles The flux surface center moves outwards as the minor radius decreases. This corresponds to a condition where B_ϑ is higher on the outside of the torus, to counteract the tendency of plasma to expand under the kinetic pressure. At the equilibrium, the poloidal field at the edge of the plasma is:

$$B_\vartheta(a,\vartheta) = -\frac{\mu_0 I}{2\pi a}\left(1+\frac{a}{R_0}\Lambda\cos(\vartheta)\right) \tag{20}$$

Λ is called the "asymmetry factor", it depends upon integral parameters (as the internal inductance and the poloidal beta [10]) and not on the detailed distribution of p and **J**.

3.6 The Virial's Theorem

From a mathematical point of view, it says that there is no time-independent solutions to the MHD equations with the property that p=0 and **J=0**.
It merely states that a equilibrium will not be generated by the plasma alone. Unfortunately, the field has to be imposed from the outside. The use of external field coils is then necessary in experiments on Earth, while the gravitational force keeps plasma together in space.
From Grad-Shafranov's equation, it is found that the following field is necessary to the equilibrium:

$$B_z = -\frac{\mu_0 I}{4\pi R_0}\left(\ln\frac{8R_0}{a}+\Lambda-\frac{1}{2}\right) \tag{21}$$

This is the vertical magnetic field necessary to maintain the plasma in equilibrium, its effect being to provide an inward force to balance the outward hoop force on the plasma.

4. MHD stability

The stability of the equilibrium can be explained as the ability of the given equilibrium to maintain its characteristics. In Figure 20 is shown a mechanical example of this concept.

Figure 20 (left) stable configuration; (right) unstable configuration.

In Figure 20 (left), the system is considered to be in stable equilibrium. Any perturbation of the ball away from its equilibrium position causes it to oscillate about this position. Moreover, any perturbation causes a shift to states with higher potential energy ($\delta W>0$). In Figure 20 (right), the ball is in an unstable equilibrium since any small perturbation causes it to continuously mover further and further away from its equilibrium position. Any perturbation causes with lower potential energy ($\delta W<0$).
Stability is determined by examining the time evolution of the MHD solutions and seeing whether or not the long-time behavior corresponds to a steady state solution exhibiting good confinement.
This requires the mathematical solution of a set of coupled, non-linear 3-D partial differential equations in which the unknowns are functions of R, φ, Z, t.
The mathematics is greatly simplified by separating the problem into two parts: equilibrium and linear stability. Specifically, all dependent variables are written as $Q(r, t) = Q_0(r) + Q_1(r, t)$. The quantity $Q_0(r)$ represents the equilibrium contribution to the total solution. It is an exact solution of the MHD equilibrium equations and therefore, by definition, is not a function of t.
From this consideration, the study of stability is carried out considering at a first step an equilibrium state solving the MHD equations.
The quantity $Q_1(r, t)$ represents the perturbation away from equilibrium. The perturbation is assumed to be small in amplitude implying that $|Q_1(r, t)| << |Q_0(r)|$. It is, in general, a function of all the independent variables R, φ, Z, t in order to allow for all possible unstable motions. The small-amplitude assumption simplifies the analysis as the product of two perturbed unknown (B_1 and J_1) are kept small with respect to the order of magnitude of the product of an equilibrium values (B_0) with a perturbed one (J_1).
The stability problem has thus been reduced to examining the time evolution of the small amplitude perturbations. Since the relevant equations are linear, this represents an enormous simplification of the problem. This is the primary reason why most MHD stability studies focus on linear stability.
This approach allows us to write two systems of equations:

Equilibrium

$$\begin{aligned} \mathbf{J}_0 \times \mathbf{B}_0 &= \nabla p_0 \\ \nabla \times \mathbf{B}_0 &= \mu_0 \mathbf{J}_0 \\ \nabla \cdot \mathbf{B}_0 &= 0 \end{aligned} \tag{22}$$

Linear stability

$$\begin{aligned} \frac{\partial \rho_1}{\partial t} + \nabla \cdot (\rho_0 \mathbf{v_1}) &= 0 \\ \rho_0 \frac{\partial \mathbf{v_1}}{\partial t} &= \mathbf{J_1} \times \mathbf{B_0} + \mathbf{J_0} \times \mathbf{B_1} - \nabla p_1 \\ \frac{\partial p_1}{\partial t} + \mathbf{v_1} \cdot \nabla p_0 + \frac{\gamma p_0}{\rho_0} \left(\frac{\partial \rho_1}{\partial t} + \mathbf{v_1} \cdot \nabla \rho_0 \right) &= 0 \\ \frac{\partial \mathbf{B_1}}{\partial t} &= \nabla \times (\mathbf{v_1} \times \mathbf{B_0}) \\ \nabla \times \mathbf{B_1} &= \mu_0 \mathbf{J_1} \\ \nabla \cdot \mathbf{B_1} &= 0 \end{aligned} \tag{23}$$

The time dependence of the perturbations can be explicitly extracted by means of a normal mode expansion. This is possible since the equilibrium quantities are independent of time, and the stability equations are linear. All perturbed quantities can thus be written as

$$\mathbf{Q_1}(\mathbf{r}, t) = \mathbf{Q_1}(\mathbf{r}) \exp\{-j\omega t\} \tag{24}$$

The frequency ω, which may be complex, appears as an eigenvalue in the problem. In general, the plasma supports a large, sometimes infinite, number of normal modes, each with its own eigenvalue. Once the normal mode equations are solved and the eigenvalues determined, stability is ascertained by examining the imaginary part of $\omega = \omega_r + j\omega_i$ (i.e., ω_i is the growth rate) for each mode. If any eigenvalue has $\omega_i > 0$, the system is unstable since the perturbations grow exponentially in time: Q1~exp ($\omega_i t$). If all eigenvalues have $\omega_i \leq 0$, the system is stable as the perturbation either decays to zero or at worst oscillates about the equilibrium position. Note that when introducing the normal mode expansion into the linear stability equations the factor exp (−jωt) cancels in each and every term.
A perturbed displacement vector $\boldsymbol{\xi}$ is introduced as follows:

$$\mathbf{v_1} = \frac{\partial \xi}{\partial t} = -j\omega\xi(r) \exp\{-j\omega t\} \tag{25}$$

the vector ξ represents the perturbed displacement of the plasma away from its equilibrium position.
The final linearized MHD stability equations are most easily obtained by eliminating all perturbed quantities in terms of ξ.
The perturbed quantities are substituted into the linearized momentum equation. The result is a vector equation for the three components of ξ given by

(26) $$-\omega^2 \rho \xi = F(\xi)$$

And a force operator **F** is defined.
To complete the formulation of the linear MHD stability problem one must specify boundary conditions. There are two cases of interest corresponding to internal modes and external modes.
This distinction is based on whether or not the surface of the plasma moves as the instability grows. For an internal mode the plasma surface remains fixed in place. These instabilities occur purely within the plasma and place constraints on the shape of the pressure and current profiles. Often they do not lead to catastrophic loss of plasma but can result in important experimental operational limits or enhanced transport. External modes, on the other hand, involve motion of the plasma surface, and hence the entire plasma. Since it is this motion that leads to plasma striking the first wall, external modes are particularly dangerous in fusion plasma and must, in general, be avoided.
Finally, from equation (26), an expression for the conservation of energy can be evaluated:

(27) $$\omega^2 \int \rho |\xi|^2 \, dr = -\int \xi^* \cdot \mathbf{F}(\xi) \, dr$$

On the basis of equations (26) and (27), the study on the stability of a given equilibrium can be done, and equilibrium criterions have been carried out. As an example, in the next section the external kink instabilities are discussed.

4.1 External Kink instability

The external kink modes are called current-driven instabilities because they are excited by a large value of the toroidal current. The case shown in Figure 21 can be considered as a Z-pinch [8] with a strong internal axial field. Although the current still flows primarily in the axial direction, this now corresponds to the parallel direction. The instability mechanism is similar to that of the pure Z-pinch. However, the toroidal magnetic field lines, which behave somewhat like rubber bands, become bent as the perturbation grows. The tension in the lines tries to restraighten them and this corresponds to a stabilizing force. Instability can still persist if the toroidal field is too small.

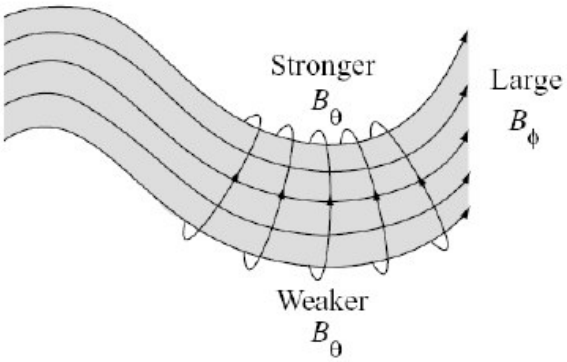

Figure 21 Kink instability in a screw pinch with a large toroidal field. Note that J is quite parallel with the toroidal magnetic field.

If the maximum achievable toroidal magnetic field is determined by magnet engineering considerations, then this sets a limit on the maximum toroidal current that can flow. Specifically, if the current becomes too large with respect to the maximum toroidal field, then the stabilizing effect of toroidal field-line bending is not large enough to stabilize the mode.
With the help of the linearised MHD equation, a stability criterion can be found. The vector displacement is written as [9]:

(28) $$\xi(r,\vartheta,\varphi,t) = e^{-j\omega t} \cdot e^{j(m\vartheta+n\varphi)} \cdot \xi_0(r).$$

Equation (28) has been evaluated applying the Fourier Transform along the ϑ and φ angles.The periodicity of the modes are defined by the **poloidal oder number m** and the **toroidal order number n**.
It is found that external kink modes (i.e., modes with $\xi(a) \neq 0$) are stable if the safety factor at the wall q(a) satisfies the equation:

(29) $$q(a) > m/n$$

but can be unstable otherwise. In particular, the m = 1 mode is unstable if

(30) $$q(a) < 1.$$

This so-called Kruskal-Shafranov criterion –q(a)>1→stable- limits the total current I_P that can be carried by the plasma. Since

(31) $$B_{pol}(a) = \frac{\mu_0 I_p}{2\pi \cdot a}$$

This current is limited by

(32) $$I_p < \frac{2\pi \cdot a^2 B_0}{\mu_0 R_0}$$

4.2 Vertical instability of Elongated plasmas

Elongated cross sections are used for tokamaks to improve the MHD stability limits and alleviate plasma-wall interaction problems. Moreover, D-shaped toroidal field coils experience a lower stress for the same field intensity. The non circular plasma section is produced by the shaping coils.
A crucial feature for the stability behavior is the safety factor q(r) defined as the number of large toroidal turns necessary to complete one poloidal turn of the helix on each magnetic surface and so it is a fraction of two natural numbers q=m/n. For a tokamak it is an increasing function of radius $q(r) \approx r\, B\varphi/R_0 \cdot B_\vartheta$ and, most importantly, is always large: q(r) > 1 over almost the entire plasma, a consequence of the large toroidal magnetic field.

The large toroidal field and correspondingly large edge safety factor lead to finite values of MHD stable β without a conducting wall and to reasonably high experimental values of the energy confinement time τ_E. Good confinement allows the plasma to heat up to high temperatures using only a moderate amount of external heating. In addition the resulting values of β lie in the regime of reactor interest. The parameters β and I set the equilibrium limits. First, there is a limit set by the maximum value of β/I^2. Second, as $\beta \rightarrow 0$ there is a stability limit that sets the maximum value of I due to low n number kink modes. Third, there is a stability limit due to low-n ballooning-kink modes that sets a limit on the maximum allowable β at a corresponding optimized value of I. The strictest β limit results from the ballooning-kink mode. These modes must be avoided in large experiments and reactors since the large transient forces developed can cause actual physical damage to the structure.
A combination of elongation and triangularity of the plasma cross section increases the β limit against low n ballooning-kink modes. There is, however, a practical limit to the maximum achievable elongation due to the excitation of an n = 0 axisymmetric mode. Typically, it is very difficult to achieve elongations greater than a factor of height/width ≈ 2.
In Figure 22 is shown a simple configuration to keep the plasma elongation by a couple of wire posed on the top and on the bottom of the plasma column.

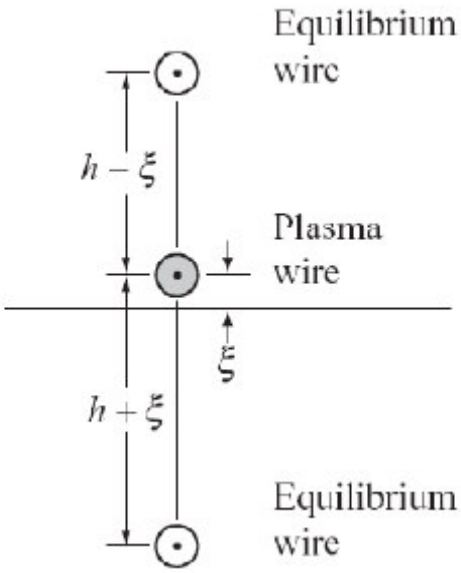

Figure 22 Simple wire model showing the vertical instability.

A plasma column elongated vertically tends to be unstable and so the elongated cross section introduces a instability. Assume the plasma wire is held in equilibrium by two equally spaced wires as shown in the diagram.
To elongate the plasma vertically the currents must flow in the same direction as the plasma current. The resulting attractive force due to each equilibrium wire "pulls" on the top and bottom of the plasma causing it to become elongated.
Now assume the plasma wire undergoes a small vertical displacement ξ towards the upper wire, Figure 22. The force of the upper wire on the plasma wire is inversely proportional to the distance separating them. Thus, the upward pulling force is increased since the wires are slightly closer to each other. Similarly the pulling force of the lower wire is decreased since it is now slightly further away from the plasma. The conclusion is that there is a net force

acting on the wire pointing in the upward direction. The direction of this force is to move the plasma wire even further away from its equilibrium position. This clearly corresponds to an unstable situation.
In an axisymmetric machine the vertical stability condition is given by the same field which determines the shape of the plasma cross-section. This implies that if the field is vertically stabilizing the plasma column is elongated horizontally and vice versa. In an experimental tokamak or reactor, the plasma shape should be elongated vertically and the plasma column tends to be unstable.
To improve the vertical stability behavior every modern tokamak uses passive conductors and a feedback system. The passive conductors are the vacuum vessel, blanket, and mechanical structure where currents are induced which helps to counteract the vertical displacement. This passive system is important because its respond instantaneously by plasma movement. The feedback system is a fast active control system of the vertical position of the plasma. It is composed by equilibrium windings which produce an adjustable radial magnetic field, while the control is made by electronics. A reliable magnetic diagnostic, data handling and power amplifier system is needed to accurately control the plasma shape and to stabilize the plasma column.
Together they are capable of producing elongations up to about $\kappa=1.8$.

5. Disruptive events in ITER [11]

Modern tokamaks, like ITER, have complex cross section, which combines ellipticity, triangularity, and a divertor. In Figure 23 is shown the ITER cross section, it is a configuration with a Single Null (SN) X-point near to divertor. The study of this plasma equilibrium and stability is much more difficult and always solved by numerical algorithms. Also these devices suffer the basic instabilities and, having elongated cross section, also the vertical instability.
Disruptive events in tokamaks generally involve the growth of some plasma instability which eventually results in a loss of thermal energy, or "thermal quench". This energy loss can be partial and recoverable, producing a "minor" disruption, or nearly total and unrecoverable, resulting in a plasma-terminating disruption.

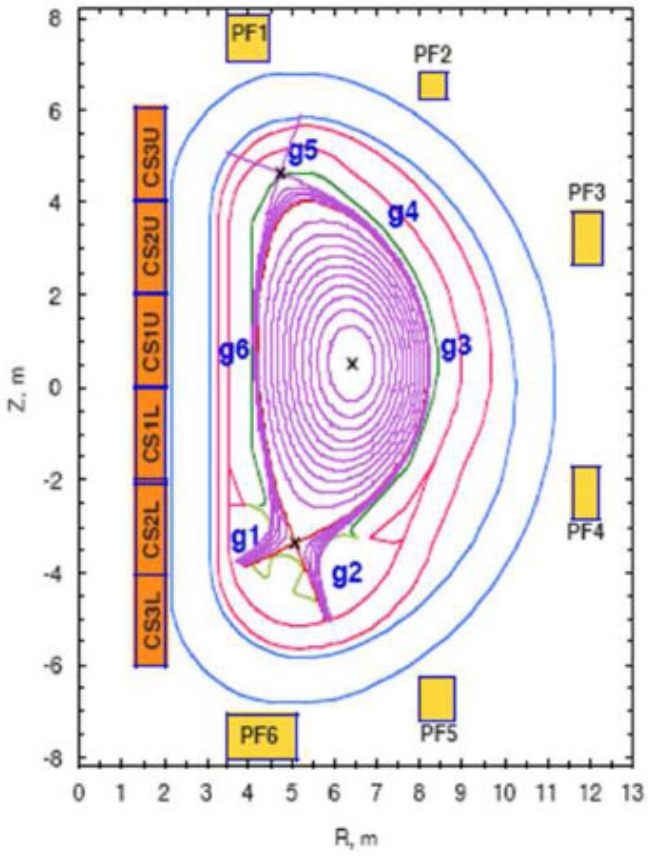

Figure 23 ITER cross section.

We shall distinguish between two common and important kinds of disruptions in which vertical stability is lost at some point during the event. We shall define **major disruption** as a plasma-terminating event in which the thermal quench occurs before loss of vertical stability (if any). By contrast, a **Vertical Displacement Event** (VDE) will be understood to be a plasma-terminating disruption in which vertical stability is lost first, and the thermal and current quenches occur well after the plasma becomes wall limited by moving vertically [3].

5.1 Major disruptions

Disruptions [IPB2007] and their consequences pose significant design and plasma operation challenges for reactor-regime tokamaks in general and for ITER in particular. The magnitude and scope of these challenges arise from a combination of physics, structural and thermal engineering considerations and from inherent limits on the thermal energy handling capabilities of materials available for plasma-facing component (PFC) surfaces.
It is well known that stable sustainable (disruption-free) operation in a tokamak system is limited with regard to maximum plasma current, maximum electron density and maximum total normalized plasma pressure (β) by three basic 'operational limit' considerations:

- Current 'limit': set by a requirement for a plasma edge safety factor, $q_{95} \geq \sim 2$ – see equation (32)-.
- Density 'limit': set by a requirement that the plasma density should not appreciably exceed the empirical 'Greenwald' density limit $n_{GW}[10^{20}\ m^{-3}] = I\ [MA]/\pi a^2[m^2]$.
- Pressure 'limit': set by a requirement that the normalized volume-average toroidal beta, $\beta_N = \langle\beta_{\%}\rangle/(I[MA]/a[m]\ B[T])$, should not exceed the 'Troyon' ideal MHD betalimit of approximately 3.5% $MAm^{-1}\ T^{-1}$.

Attempting plasma operation that approaches or exceeds the limiting values of any of these three operational boundary 'limits' typically initiates an increase in MHD activity that eventually results in a major disruption, wherein the tokamak magnetic configuration becomes globally unstable to helical perturbations of the form $\boldsymbol{\xi}(\mathbf{r}) = \boldsymbol{\xi}(\mathbf{r})\ \exp\{i(m\vartheta - n\varphi)\}$, where ϑ and φ are the poloidal and toroidal angles and m and n are the corresponding poloidal and toroidal integer mode numbers.
Major disruptions terminate the plasma discharge by expelling almost all of the thermal energy suddenly as a result of rapid MHD instability growth.
The **thermal quench** is a phenomenon in which most of the plasma thermal energy is lost by the plasma and is subsequently deposited, by conduction or/and convection and radiation, on the limiter and divertor surfaces. The thermal quench is typically followed by a redistribution of current which "flattens" the current density profile, decreasing the normalized internal inductance per unit length l_i. In order to conserve flux, the plasma current typically increases slightly at this point, producing a characteristic "current bump." In a single null (SN) discharge, this flattening produces a shift of the current centroid toward the X point simply as a consequence of the SN field geometry. This shift can initiate uncontrollable unstable vertical motion. Loss in β_p is accompanied by a sudden radial shift [Humphreys].
The ensuing increase in plasma resistivity that this thermal quench cooling produces then precipitates a rapid decay of the plasma current (typically described as a **current quench**) and, in a vertically elongated tokamak, simultaneous development of vertical instability, typically described as vertical displacement event (**VDE**) and sometimes also as a vertical disruption or Vertically Unstable Disruption (**VUD**).
During the current quench phase of a disruption in a vertically elongated plasma, the decay of the plasma current and the ensuing motion of the plasma column induce toroidal currents in the nearby toroidally conducting structures (e.g. the ITER torus vacuum vessel) and also drive force-free helical current flow in the wall-contacting ex-plasma 'halo' region that lies beyond the last closed plasma flux surface. Both the toroidal current and the ex-plasma halo current flow act to mediate the dynamic evolution of the current channel during the current

decay phase. The components of the ex-plasma halo current that reconnect through the vessel and the in-vessel conducting structures (e.g. the ITER shield blanket modules, the divertor baffle and cassette modules) give rise to in-vessel halo currents that produce forces on these structures.
In addition, the plasma current I_p decay and motion induce locally circulating 'eddy currents' in nearby plasma-facing conducting structures (e.g. the ITER first-wall and shield blanket modules), and the interaction of these induced circulating currents with the toroidal and poloidal fields gives rise to localized torques and overturning forces on these PFC structures.
Plasma, whose initial position is vertically "balanced" so that no currents are induced in the wall during the I_p decay, will experience no increased destabilization and may move primarily radially during the current decay. A major disruption which ends with primarily radial plasma motion is a "radial disruption."

5.2 VERTICAL DISPLACEMENT EVENTS

Since plasmas in typical elongated cross-section tokamaks are inherently unstable against vertical displacements, a sufficiently large and fast change in plasma parameters can cause the loss of the vertical position control, leading to an uncontrolled upward or downward excursion of the plasma column. A true vertical displacement event (VDE) begins with a loss of vertical stability that develops before any appreciable cooling of the plasma centre occurs. Such events are typically described as a 'hot-plasma' VDE. The plasma current centroid moves vertically away from its equilibrium position and the moving plasma column eventually contacts a limiting surface. The direction of initial movement, even in single-null plasmas, can be either towards or away from the X-point, depending on the changes in the plasma current and pressure profiles as well as the initial location of the plasma current centroid.
In a VDE, the plasma continues to move into the wall, reducing the plasma area, typically with little change in the total plasma current, thus reducing the edge safety factor. A pronounced ex-plasma halo current flow also develops, as shown in Figure 24, and the 'halo' currents flowing in the wall-contacting ex-plasma region reconnect through the structures that the plasma comes in contact with. The resulting in-vessel currents, which typically flow mostly in a poloidal direction, are commonly called **halo currents**.

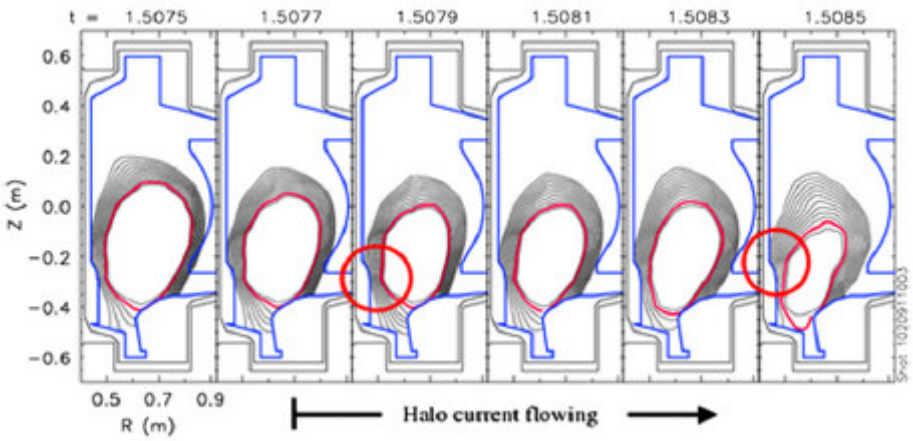

Figure 24 Plasma configuration evolution and halo current region development in a typical Alcator C-Mod disruption. The data shows that much of the ex-plasma halo current region

(inferred from magnetic reconstruction data) now misses the new, less-protruding inboard divertor [11].

The evolution of a VDE is illustrated in Figure 24. The plasma current centroid moves vertically downward from its initial equilibrium position and the plasma eventually strikes a limiting surface. The plasma continues to move into the first wall, reducing the plasma cross section with essentially no change in the plasma current, thus reducing the edge safety factor, q(a) (=q_{95}). The plasma current is approximately fixed during this "hot plasma wall-contact" phase because the resistive decay time of the core plasma is extremely long compared to the vertical motion timescale, and current scraped away at the edge of the plasma is essentially reinduced in the plasma core. When q(a) reaches a sufficiently low value, rapid growth of MHD activity produces a thermal quench similar to those observed in major disruptions.
Because the VDE thermal quench typically occurs with the plasma shifted significantly off the machine axis, in contact with the wall, and with the plasma current largely intact (Figure 25), VDEs potentially produce the maximum heat loads and plasma facing component (PFC) forces.

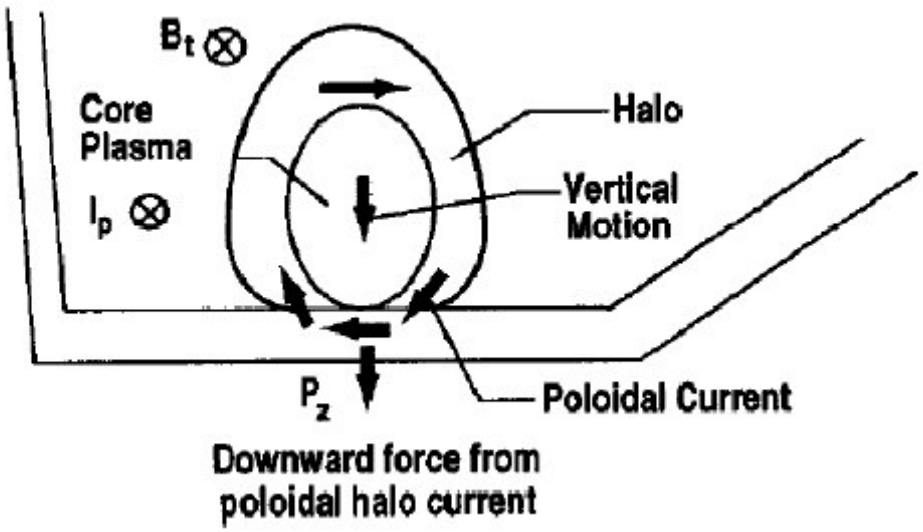

Figure 25 Geometry of the post-thermal quench, wall-limited plasma, and associated halo region. The limiting surface illustrated corresponds to a flat wall consistent with an open divertor. [3]

6. Halo currents phenomena

When the plasma is in contact with the wall, in-vessel halo currents are also driven to compensate for the plasma toroidal flux lost because of the plasma area reduction. The plasma current stays approximately fixed during the hot plasma–wall contact phase because the resistive decay time of the still hot core plasma is long compared with the vertical motion timescale. When the boundary safety factor decreases to a sufficiently low value (typically less than 2), rapid growth of MHD activity (n = 1) produces a fast thermal quench similar to

those observed in major disruptions. As the plasma current starts to decay, toroidal currents are induced in the halo region to conserve the poloidal flux.
Vertical instability can also occur following the onset of a disruptive thermal quench. In this case, the resulting vertical evolution can be described as a vertical disruption, or more correctly, as a vertically unstable-disruption (VUD) current quench. The resulting 'cold-plasma' current decay phase shares the most of the attributes—including the generation of in-vessel halo currents and large transient vertical forces on the vacuum vessel—of a 'hot-plasma' VDE.
The most important considerations for halo currents are (1) the magnitude of the in-vessel halo currents, (2) the toroidal asymmetry of these in-vessel halo currents and (3) the resulting $\mathbf{j}_{\text{in-vessel}} \times \mathbf{B}$ forces that act on the vessel components. It is the sum of these local forces (plus the global vertical forces that are directly generated by induced toroidal vessel currents) that gives rise to the large vertical vacuum-vessel forces that are observed in present tokamaks during VDEs and VUDs. Toroidal asymmetry in the halo current distribution can also give rise to an asymmetric radial de-centering and/or tilting forces on vacuum vessel systems. Finally, the magnitude and spatial (radial) extent of the ex-plasma halo current flow becomes the dominant factor (especially in the end phase of the current decay) in determining the equilibrium dynamics of both hot-plasma VDEs and cold-plasma VUDs. More simply put, in this end phase, most of the remaining plasma current flows in the halo region. The presence and dynamics of this ex-plasma halo current must be self-consistently taken into account in calculations of the plasma equilibrium evolution and the resulting vacuum vessel and in-vessel-component toroidal eddy currents, and forces on these component systems.
In actual experimental reactors, the halo currents I_h have mainly measured along the poloidal direction. Usually, I_h refers to the poloidal component of the halo current.
From the measurement of I_h values at different toroidal locations, two main parameters are defined as follows.
The **Normalized Halo Current fraction** f is defined as the average of the halo current $I_{h,av}$ divided by I_{p0}, the plasma current before disruption.

$$f = \frac{I_{h,av}}{I_{p0}} \tag{33}$$

The **Toroidal Peaking Factor** TPF is defined as the ratio of maximum value of halo current measured $I_{h,max}$ against the averaged one $I_{h,av}$.

$$TPF = \frac{I_{h,max}}{I_{h,av}} \tag{34}$$

When discussing the ITER case it is of course important to consider also the results given by present experiments. In particular the parameter usually shown to summarise the different measurement is the product f*TPF, normalized Halo fraction times toroidal peaking factor. In Figure 26, experimental points from many tokamaks are presented together. This product should be less than 0.7 (black dashed lines in Figure 26).

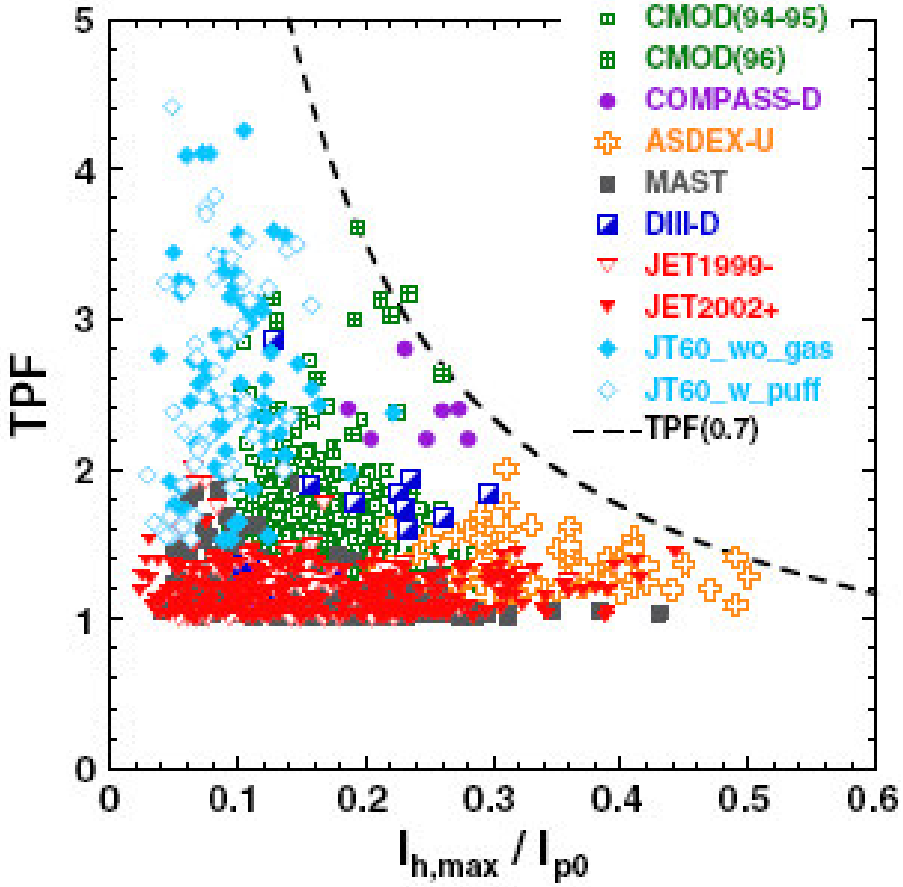

Figure 26 f*TPF product by experimental data from different experiments. [11]

It should be noted that in almost all experiments the TPF can reach values higher than 2.0, suggesting that strong asymmetries could develop also in ITER.

During the vertical displacement events [12], in the areas where a plasma-wall interaction takes place, the current lines in the plasma Halo region, which are interrupted by the first wall, constitute the sources and the sinks of the Halo current distribution in the Vessel structure. It is reasonable to assume that the current density distribution in the plasma, just before the interaction with the wall, is still characterized by current lines practically parallel to the magnetic field lines, which thus have a helical pattern with a substantial toroidal component.

It is also worth noticing that present experiments, as JET, ASDEX UpGrade and others (where the halo current have been measured), are characterized by a strong anisotropy of the Vessel resistance, which is much larger along the toroidal direction than along the poloidal direction, due to the presence of metallic bellows or other separations.

In these cases, due to the high resistance values along the toroidal direction, it is commonly accepted that the halo currents “injected” in the structure are forced to flow along a purely poloidal path, independently of the pre-disruption configuration.

In JET and ASDEX-UpGrade, the Halo current patterns in the structures are in practice considered to be always following the shortest path between the sources and the sinks, along poloidal direction only. The sudden cancellation of the toroidal component of the pre-existing current induces an electrical field on the high-resistance section of the structure and produces a considerable Eddy Current distribution on the remaining part of the structure.

On the other hand, the ITER Vacuum Vessel will have a resistance of 7.9μΩ along the toroidal direction and 4.1 μΩ along the poloidal direction and therefore the circulation of the current along the toroidal direction in the ITER Vessel should not be hindered.
Therefore the initial distribution of the Halo currents between the "sources" and "sinks" in the ITER vessel should maintain a poloidal and toroidal component similar to that existing in the plasma just before the VDE.
This initial current distribution in the vessel structure, having an helical pattern with the same pitch as the Magnetic field lines, will obviously evolve towards the lowest resistance (i.e. the shortest path) distribution with the vessel time constant. The shortest path usually being oriented along the poloidal direction, the Halo currents will produce electrodynamic loads on the structure as soon as they are not parallel to the magnetic field lines any more.
Another way of interpreting the situation is to assume that the Halo currents in the structure still have not toroidal component, but that the termination of the Plasma toroidal current produces an increment of the toroidal loop voltage and consequently induces a substantial increase of the toroidal current in the vessel.
For these reasons, a 3D representation of the Halo current should be necessary in order to better understand the most likely Halo current pattern in ITER, and a great number (with respect to present experiments) of Halo Rogowski coils are foreseen to measure the Halo currents injected on the first wall. In Figure 27 is shown the layout of the Halo sensors, which are posed behind the Blanket modules.

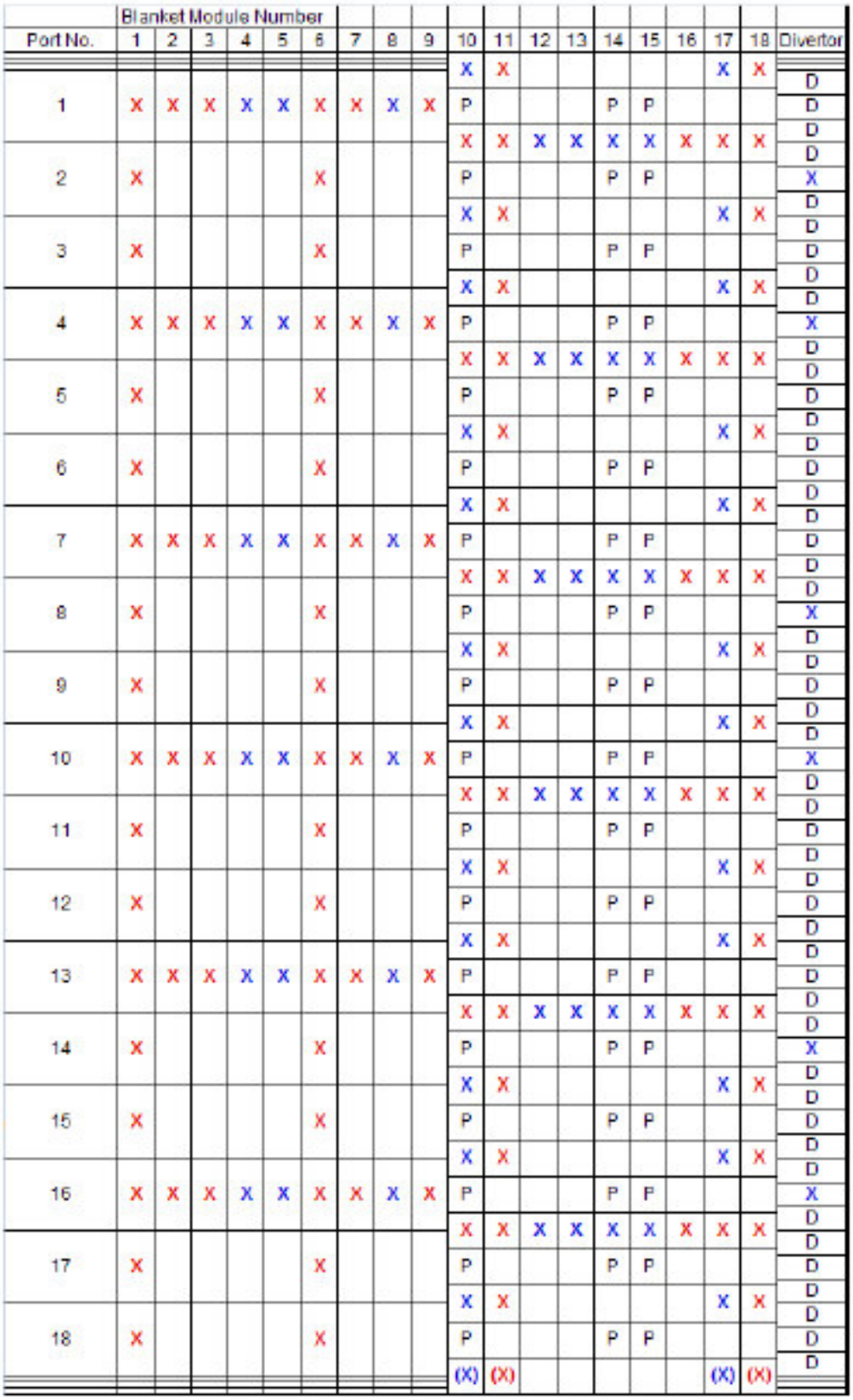

Figure 27. Present layout of the Blanket modules. Modules ticked by 'X' will be equipped with Halo Rogoswki sensors. 'D' refers to standard Divertor modules without instrumentation. 'P' refers to ports. [12]

The Blanket Modules are electrically connected to the Vessel, but insulated from one another. The Halo Current picked-up by the surface of one module can enter or exit the vessel only through two electrical straps connecting the rear of the Blanket module with the vessel. Thus, the discretization of the Blanket modules determines a physical discretization of the distribution of the Halo current sources and sinks on the vessel.
The larger number of Halo diagnostics foreseen for ITER does not directly provide the measure of the complete Halo current distribution. A reconstruction procedure is therefore needed to estimate the values of Halo current entering or exiting in the not equipped Blanket modules.
The development of such a procedure is described in the next chapter.

7. SUMMARY

A power fusion of about 15MW has been achieved during experiments with Deuterium and Tritium at JET (section 1). The next step of fusion research, toward the realization of an electrical power generating fusion reactor, is ITER. This experiment involves seven countries in the world: the European Union (EU), USA, Republic of China, South Korea, Russia, Japan and India. ITER should get answer about technological issues as well as it should operate with considerable power gain of Q=10 (section 2).
Last generation of experimental Tokamaks works with elongated plasma to achieve higher value of β, as well as ITER will do. Confined elongated plasma suffers of the typical instabilities which can be studied with the helps of the MHD equation; such an example is given by the external kink modes modifying the shape of plasma. This kind of instabilities cans growth in plasma if the safety factor q decreases under certain values (section 4). Moreover, elongated plasma also suffers of vertical instability.
The study of the plasma stability starts from an initial condition found solving the MHD equations under equilibrium conditions. The MHD equations for the equilibrium can be solved analytically for plasma with large aspect ratio and low pressure (section 3).
The instabilities above recalled can occur also in ITER, leading to major disruption or Vertical Displacement Events (section 5). In both cases, the plasma can hit the wall producing Halo currents phenomena.
Halo currents phenomena are discussed in section 6, together with the layout foreseen for the Halo diagnostics in ITER. Few blanket modules will be equipped with Halo sensors, behind each equipped modules a Rogowski coil will be posed to measure the current flowing through the electrical connection between the blanket modules and the vacuum vessel. In order to evaluate the mechanical loads produced on the vessel by the interaction of the Halo current with the pre-existing magnetic field, a reconstruction procedure should be developed. This activity requires developing some codes to evaluate the Halo current distributions in ITER, then, on the basis of these “virtual” measurements, a reconstruction procedure can be developed.
A strategy to reconstruct the Halo current distribution starting from few “virtual” measurements has been individuated, as reported in chapter V, for a simple geometry of the first wall. In chapter VI, the further step of developing one or more code to evaluate the Halo currents in ITER is described.

Chapter II

Definition of a Reconstruction procedure

In a first phase a solution to the direct problem has been developed in order to evaluate the Halo current distributions assuming an ideal model of the first wall. On the basis of the results of this code, a preliminary analysis has been carried out. Results from analysis were useful to define the most promising and successful strategy to reconstruct the Halo current distributions in ITER. A reconstruction procedure has been developed and several numerical tests carried out. The models of the first wall and of the plasma are described in section 1. In section 2 the results of the preliminary analysis are reported. The reconstruction procedure is discussed in section 3, and its results are reported in section 4.

1. A simple 3D code for the simulation of the Halo current distributions (Direct problem)

A simplified analytical model has been developed in order to obtain the possible distribution of the Halo current on the Blanket modules. The model here presented has been developed with Matlab, and has been used to realize and test the reconstruction procedure.
The first wall model assumes a circular cross-section.
The plasma model also has a circular cross section concentric with the cross section of the First wall at equilibrium. It is assumed that Halo Currents are driven by a MHD perturbation which modifies the plasma surface causing the contact between plasma and First Wall.
On this basis, a code has been developed to determine the "footprint" of the Halo current on the machine First Wall, i.e. the position and the shape of the sources and sinks of the Halo current on the Vessel structure.

1.1 First wall model

The first wall model is an ideal torus of major radius R and minor radius b. Each point on the first wall surface is easily defined in a toroidal coordinate system by the (ϑ, φ) angles varying from 0 to 2π. So, the "footprint" of Halo currents will be a function of the (ϑ, φ) angles. The first wall can be also described in a usual Cartesian coordinate system, as follows:

$$(1)\qquad \begin{cases} x_{wall}(\vartheta,\varphi) = [R + b\cdot\cos\vartheta]\cdot\cos\varphi \\ y_{wall}(\vartheta,\varphi) = [R + b\cdot\cos\vartheta]\cdot\sin\varphi \\ z_{wall}(\vartheta,\varphi) = b\cdot\sin\vartheta \end{cases}$$

The Halo current patterns can be represented as surfaces depending on two coordinates.
The first wall model has been divided in a 2D array of 18x18 blanket modules. The modules are all equally spaced along ϑ and φ. Only few modules are equipped with Halo sensors. The model takes into account this information, and a layout similar to that of ITER (Figure 27, chapter I) has been utilized. The present layout is shown in Figure 1

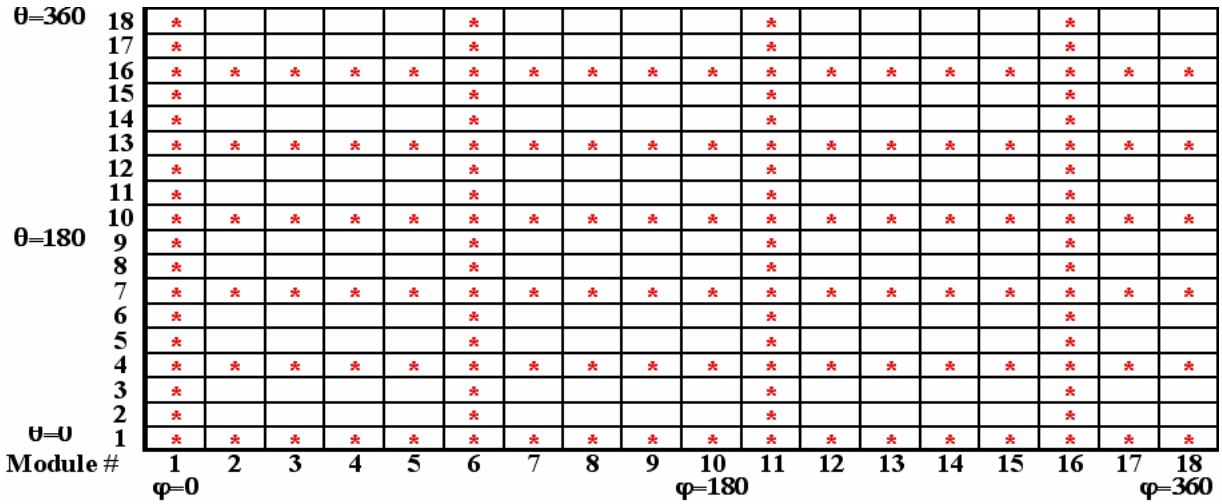

Figure 1 Layout of blanket modules equipped with Halo sensors, similar to that proposed for ITER and used in simulations, ticked squares indicate the equipped modules. Starting from the Halo current values measured on equipped modules the procedure must reconstruct the unknown values of halo current.

1.2 Plasma model

The Halo region involves the external surfaces of the plasma. Therefore, the plasma has been modeled as a set of concentric nested surfaces. In present application, only the external plasma surface has been considered. The external plasma surface is an ideal torus with major radius R and minor radius a (≤ b). This surface is perturbed by some MHD instabilities deforming the shape of the plasma surface, as the external kink modes described in section 4.1, chapter I. The local displacement of the plasma surface given by the MHD perturbations is a function of the (ϑ, φ) angles. Therefore, the external plasma surface can be described as:

$$(2)\qquad \begin{cases} x(\vartheta,\varphi) = \left[R + r_{m,n}(\vartheta,\varphi)\cdot\cos\vartheta\right]\cdot\cos\varphi \\ y(\vartheta,\varphi) = \left[R + r_{m,n}(\vartheta,\varphi)\cdot\cos\vartheta\right]\cdot\sin\varphi \\ z(\vartheta,\varphi) = r_{m,n}(\vartheta,\varphi)\cdot\sin\vartheta \end{cases}$$

The perturbed minor radius $r_{m,n}$ depends on the normalized amplitude of the MHD perturbation components $\Delta_{m,n}$ and the initial phases $\beta_{m,n}$:

(3) $$r_{m,n} = a \cdot \left(1 + \sum_{m,n} \Delta_{m,n} \sin\left(m\vartheta + n\varphi + \beta_{m,n} \right) \right)$$

The periodicity of each MHD mode is defined by the couple of (m,n) order numbers along the poloidal and the toroidal directions respectively (see section 4.1, chapter I).
The minor radius a can be considered as an equilibrium minor radius or an average minor radius.
In order to evaluate the Halo current density injected on the first wall, the plasma density current is evaluated as follows:

(4) $$J_{plasma}(\vartheta) = \frac{J_0 \cdot R}{R + a \cdot \cos(\vartheta)}$$

The formula above is a rough approximation of J_{plasma} on the Halo region that works properly for the purposes of the calculations shown in this chapter. This approximation can be justified by the analytical solution of the MHD equilibrium shown in section 3.5, chapter I, and from the following considerations. Force-free conditions are assumed, that is:

(5) $$\overline{J} = \mu \cdot \overline{B}$$

On a Tokamak (as ITER) $B_\varphi >> B_\theta$, so we can not overlook the spatial variations of B_θ compared with those of B_φ in order to estimate the variations of J_{plasma}, where B_φ varies inversely as $(R + a \cdot \cos(\vartheta))$.
For a given angle ϑ, a flat distribution of the plasma current density in the Halo region was assumed.
The plasma current density becomes a function of the (ϑ, φ) angles if the plasma surface is perturbed by a MHD instabilities. In fact, the unperturbed minor radius a is replaced by the perturbed minor radius $r_{m,n}$.
An example of a plasma perturbed surface is shown in Figure 2. A sketch of the first wall model (blue surface) and the current density lines (red lines) entering and exiting to the first wall is shown in Figure 3.

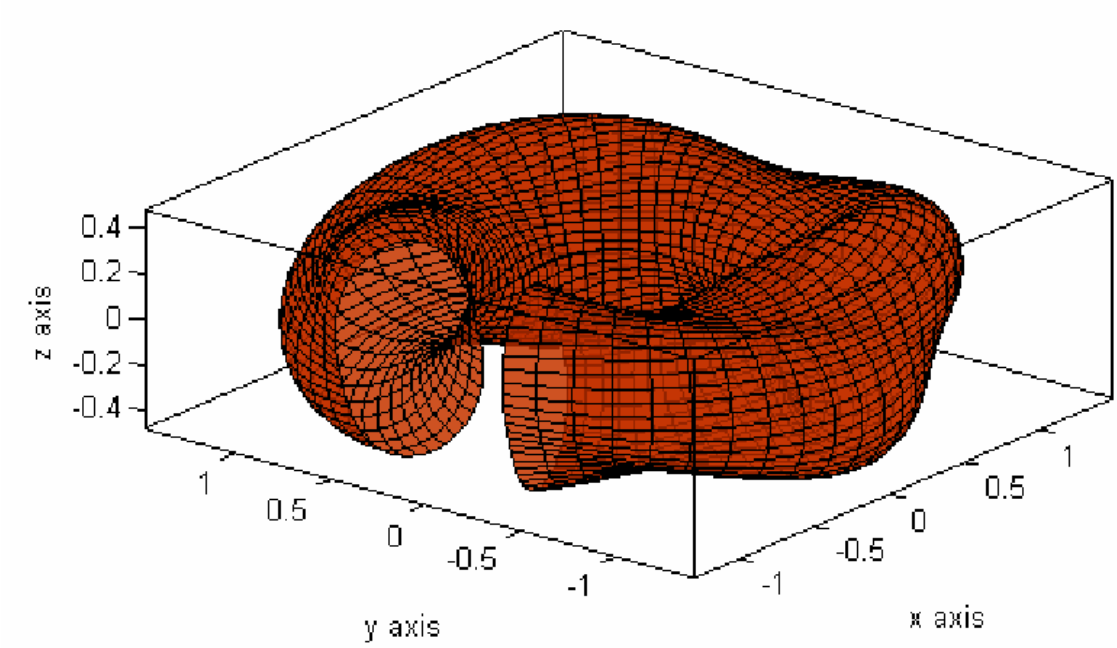

Figure 2. Surface perturbed by a (m=2, n=3) MHD mode.

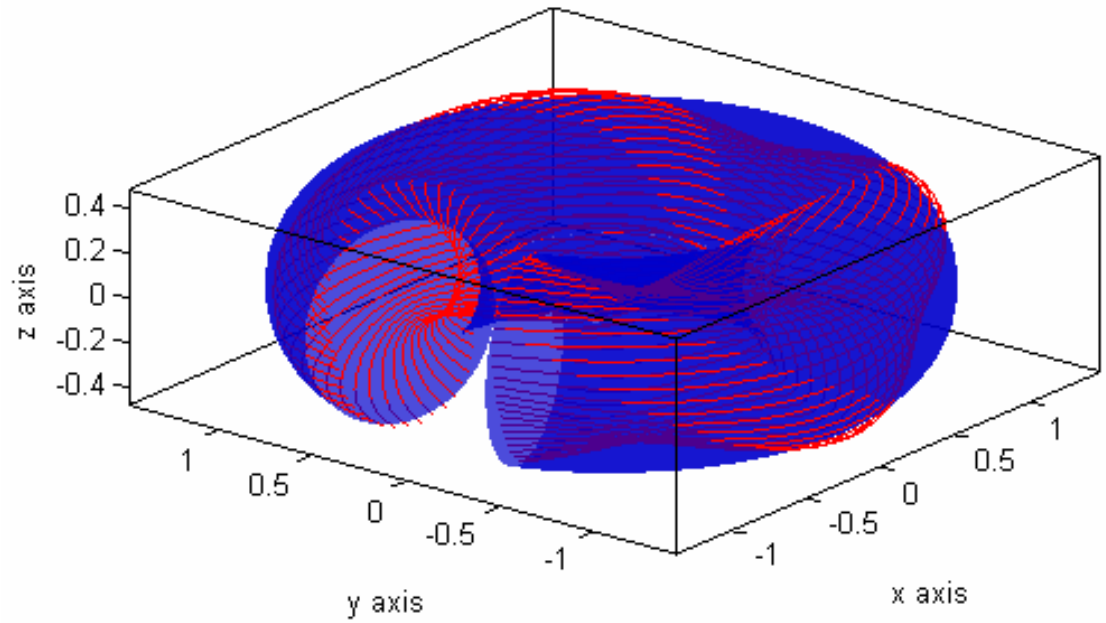

Figure 3. Blue surface corresponding to the first wall and red lines corresponding to field lines of a plasma subjected to a perturbation with periodicity order (m=2, n=3) and normalized amplitude $\Delta_{2,3}$= 20%;

1.3 Evaluation of the Halo current density injected on the first wall

Figure 4 shows the current injection into the First Wall and the Vessel. The current density injected on each first wall modules is drained to the vessel through the electrical connection between the vessel and the modules. The picture plane is parallel to the magnetic field and current density lines in the plasma-wall interaction area. The pattern of the current density injected into the first wall can be determined observing that the density of the Halo Current entering or exiting the Vessel Structure $J_{\perp}$ is related to the modulus of the Plasma Current density J_{plasma} by the relation:

$$J_{\perp} = J_{plasma}(\vartheta)\sin(\alpha). \tag{6}$$

α is the angle of incidence of the current against the first wall, as shown in Figure 4.

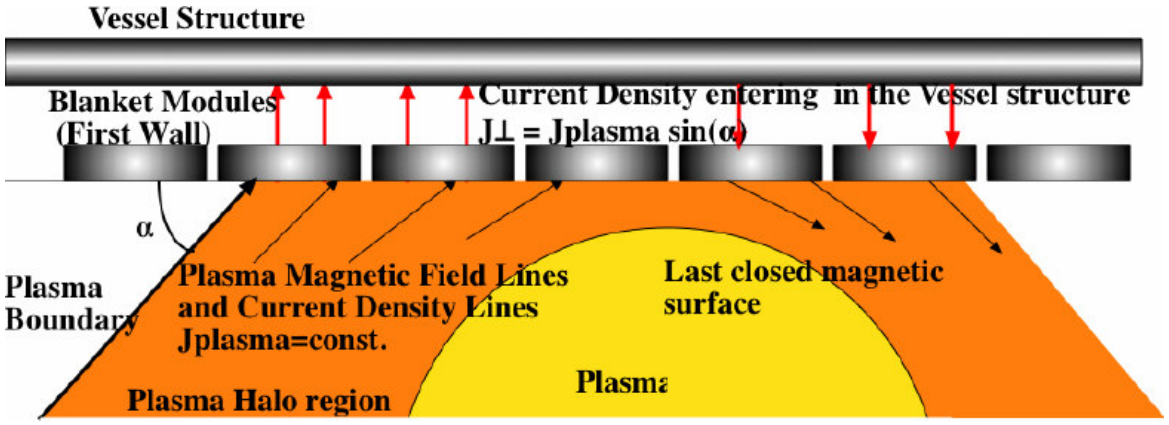

Figure 4. The Halo Currents entering the vessel structure $J_{\perp}$ is directly related to the plasma current density J_{plasma}.

In order to evaluate the angle of incidence α, a first order calculation has been implemented neglecting the change of the shape of the plasma due to the contact between the first wall and the plasma. So, the external plasma surface can be ideally extended over the first wall, and an **Interference function** is defined as:

$$\begin{aligned} &\delta(\vartheta,\varphi) = r(\vartheta,\varphi) - b \text{ if } r_{m,n}(\vartheta,\varphi) > b \\ &\delta(\vartheta,\varphi) = 0 \qquad\qquad \text{if } r_{m,n}(\vartheta,\varphi) \le b \end{aligned} \tag{7}$$

The angle of incidence α is related to the interference function by:

$$\begin{aligned} \tan(\alpha) &= \frac{d\delta(\vartheta,\varphi)}{ds} \\ \frac{d\delta(\vartheta,\varphi)}{ds} &= \frac{\partial\delta(\vartheta,\varphi)}{\partial\vartheta}\frac{d\vartheta}{ds} + \frac{\partial\delta(\vartheta,\varphi)}{\partial\varphi}\frac{d\varphi}{ds} \end{aligned} \tag{8}$$

In Figure 5 are shown a distribution of the interference function (left) and the related Halo current density distribution (right).

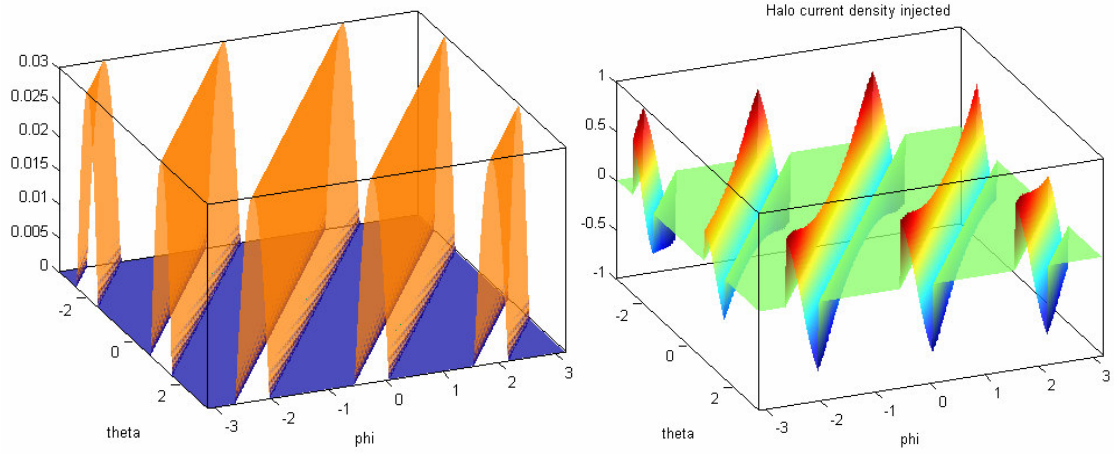

Figure 5. (left): geometrical interference function $\delta(\theta, \varphi)$ for the case considered in Figure 4, plotted as a function of the toroidal and poloidal angle; (right): Pattern of the current density $J_\perp$ evaluated by the interference pattern shown at left. The positive values correspond to the current sources for the Vessel and negative correspond to the current sinks.

The current density $J_\perp$ injected on the first wall can have positive or negative values. The positive values of $J_\perp$ can be considered as the *sources* of the Halo currents flowing in the vessel structure, while the negative ones can be considered as the *sinks*.

1.4 Modeling of Halo current distributions on blanket modules

The model described in section 1.3 allows the calculation of realistic Halo current density patterns on the first wall surface. As shown in section 1.1, the first wall has been divided in 18x18 modules equally spaced along the ϑ and φ angles. A set of Halo current measurements can be evaluated by integrating the $J_\perp$ pattern on each module:

$$I_{i,j} = \iint_{\substack{\text{module} \\ i,j}} J_\perp(\vartheta,\varphi)\cdot(R + b\cdot\cos(\vartheta))\cdot b \quad d\vartheta d\varphi \tag{9}$$

Considering a machine equipped with 18x18 First Wall modules, any Halo Current pattern can be described by a 18x18 **V** matrix whose elements are the currents $I_{i,j}$.
V matrices describe Halo current patterns as evaluated by the code. Actually, only few values are experimentally available since only few elements are equipped with Halo sensors as shown in figure 1. From each **V** matrix, a matrix $\mathbf{V_D}$ of 18x18 elements can be extracted zeroing those elements of **V** corresponding to not equipped modules.

$$(10) \qquad (V_D)_{i,j} = \begin{cases} (V)_{i,j} & \text{if the (i, j) module has an Halo sensor} \\ 0 & \text{elsewhere} \end{cases}$$

Measurements are affected by noise, in ITER a noise of the 20% on each Halo sensor [14] is foreseen. Adding a random noise to a $\mathbf{V_D}$ matrix, a realistic simulation of "virtual" measurements is obtained.

$$(11) \qquad \mathbf{A} = \mathbf{V_D} + \mathbf{noise}$$

We define **A** the matrix of "virtual" measurements. In order to simplify the calculations both **A, V,** and $\mathbf{V_D}$ are modeled by 18x18 matrices.
Figure 6, Figure 7, and Figure 8 shows some results of the code evaluating the halo current patterns. Figure 6 shows the "virtual" Halo current values **V** and the measurable, or available values $\mathbf{V_D}$ for plasma affected by a single perturbing mode (1,1) with an amplitude of $\Delta_{1,1}$=15%. Figure 7 shows the same patterns in figure 6 in case of a (2,3) single perturbing mode with an amplitude of $\Delta_{2,3}$=20%. Figure 8 shows the **V** and $\mathbf{V_D}$ patterns for plasma affected by two modes. Plasma in Figure 8 is affected by the sum of the perturbations affecting the plasma in Figure 6 and Figure 7.

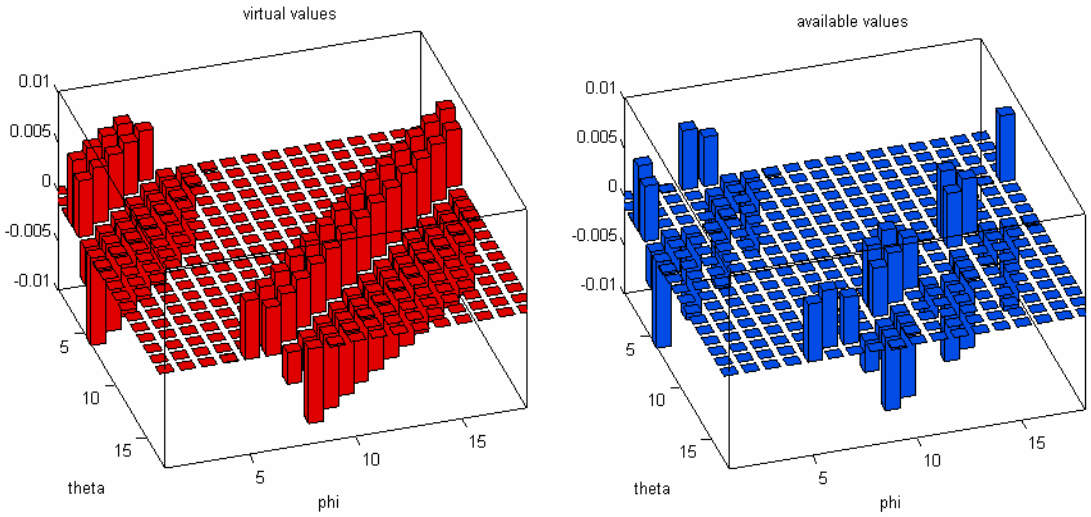

Figure 6. V (left) and $\mathbf{V_D}$ (right) matrices for a (1,1) perturbation representing the values of injected Halo Current in the First Wall modules.

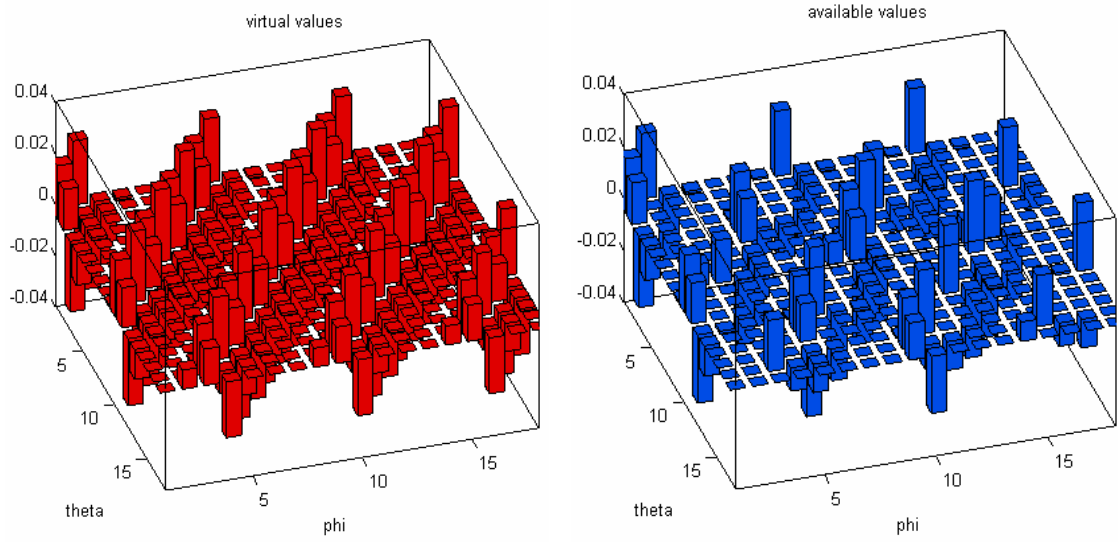

Figure 7. V (left) and $\mathbf{V_D}$ (right) matrices for a (2,3) perturbation representing the values of injected Halo Current in the First Wall modules.

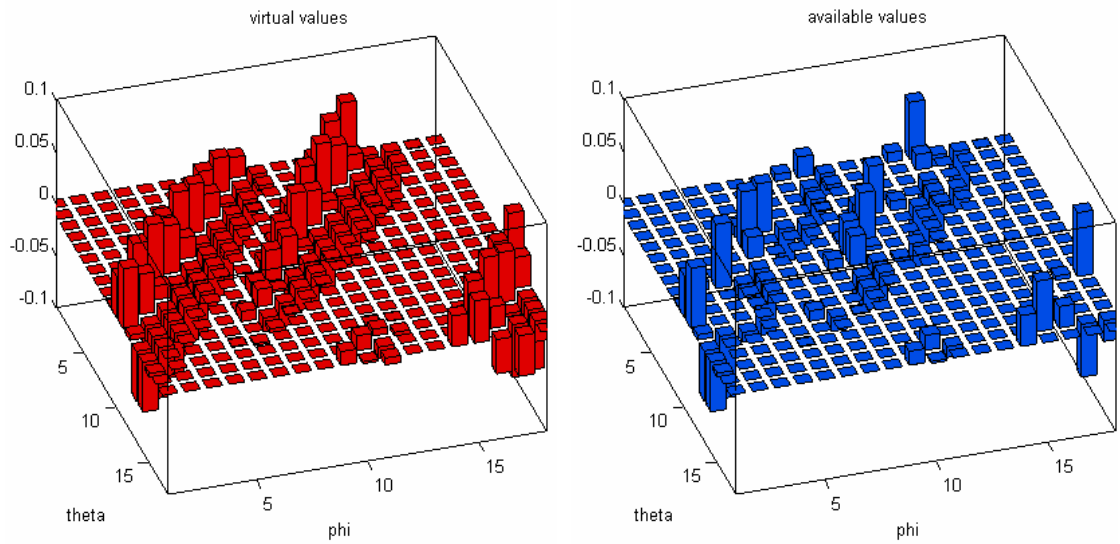

Figure 8. V (left) and $\mathbf{V_D}$ (right) matrices for a perturbation composed by the sum of a (1,1) mode plus a (2,3) mode representing the values of injected Halo Current in the First Wall modules.

2. Preliminary analysis

The model presented in section 1 has been developed with Matlab in order to find and to test a suitable reconstruction procedure. Starting from the same equations presented in section 1, a preliminary analysis was carried out reducing the dimensions of the problem. In fact, the patterns shown in section are depending on two variables, the ϑ and φ angles. In order to highlight the main challenges that a reconstruction procedure has to overcome, the φ angle has been neglected in all equations presented in section 1. For little angle of incidence α, $\tan(\alpha) \cong \sin(\alpha) \cong \alpha$, then the value of the Halo current density injected can be write as:

$$J_{\perp}(\vartheta) = \frac{d}{d\vartheta}\delta(\vartheta) \tag{12}$$

In equation (12) J_{plasma} has kept as constant and equal to1, and also $\frac{d\vartheta}{ds} = 1$.
The interference function defined in equation (7) can be rewritten as:

$$\delta(\vartheta) = f(\vartheta) \cdot u(f(\vartheta)) \tag{13}$$

Introducing a function $f(\vartheta) = r_m(\vartheta) - b$ (here, only the poloidal order number m is taken into account), and the usual step function

$$u(x) = \begin{cases} 1 & \text{if} \quad x \geq 0 \\ 0 & \text{elsewhere} \end{cases} \tag{14}$$

So, u(f(ϑ)) is a function equal to 1 in case of contact between the plasma and the first wall surface. It is 0, otherwise.
Also equation (12) can be rewritten as:

$$J_{\perp}(\vartheta) = \frac{df(\vartheta)}{d\vartheta} \cdot u(f(\vartheta)) \tag{15}$$

In equation (15) the main difficulty that a reconstruction procedure for Halo current meets is highlighted. The major difficulty is found in the no-linear behaviour of the contact areas between plasma and first wall –represented by the function u(f(ϑ)) -, this non-linear behaviour is present also in the Halo density current pattern, producing discontinuous patterns.
This non-linear behavior is shown in Figure 6, Figure 7, and Figure 8. In fact, the perturbation affecting the plasma in Figure 8 is the sum of the perturbations affecting the plasma in Figure 6 and Figure 7, but the Halo current pattern shown in Figure 8 can not be thought as the sum of the patterns shown in Figure 6 and Figure 7.
On the basis of the simplified equations here presented, a code has been developed in MathCad to carry out a preliminary analysis through the Discrete Fourier Transform (DFT).

2.1 DFT analysis

The angle ϑ ranges within (0, 2π)., The range of ϑ has been divided both in 16 intervals, related to the actual number of modules in ITER, and in 64 intervals, in order to enhance all the harmonic contents of a Halo current distribution. Each interval in both the models (with 64 and with 16 intervals) corresponds to a first wall module. So, we distinguish one as the 16 modules model and the other one as the 64 modules model. The Halo current density pattern in equation (15) is integrated along the angle ϑ:

$$I_k = \int_{\text{module k}} J_{\perp}(\vartheta)\, d\vartheta \tag{16}$$

The dependence of the Halo current distribution spectra on the order number of the perturbing mode has firstly investigated. The spectra for three different cases of Halo current distributions due to a plasma affected by a single perturbing mode with poloidal order number m=1,2,and 3 are shown in Figure 9 and Figure 10, using the models with 16 and 64 modules respectively. The three perturbing modes have the same amplitude Δ_m=15%.

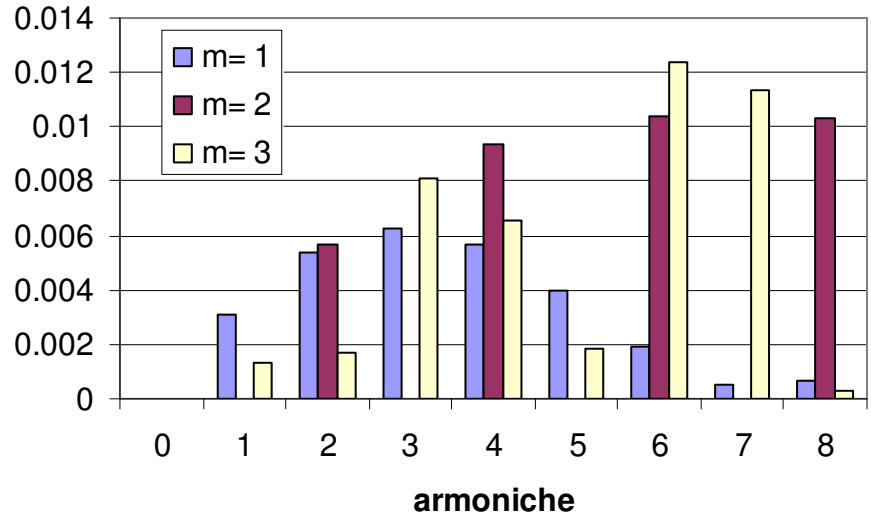

Figure 9 16 modules model. Spectra for m=1,2, and 3 perturbing modes with same amplitude Δ_m=15%.

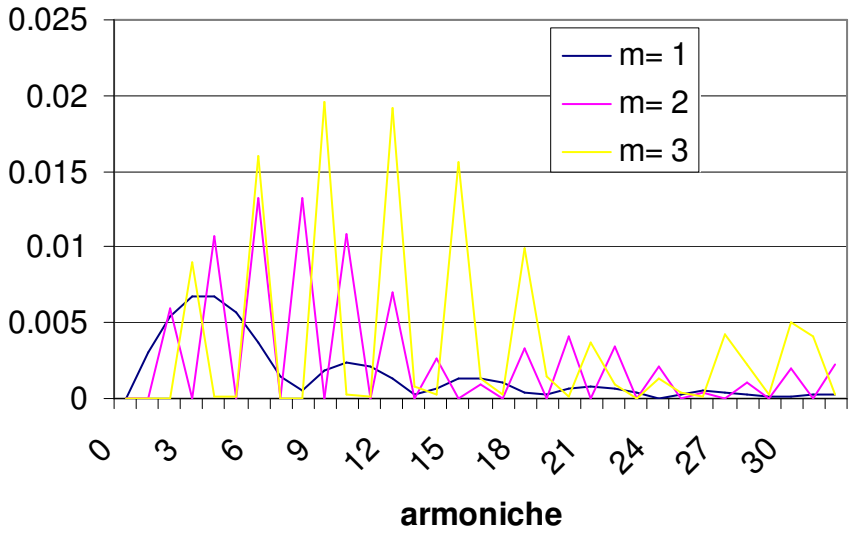

Figure 10 64 modules model. Spectra for m=1,2, and 3 perturbing modes with same amplitude Δ_m=15%.

The comparison between Figure 9 and Figure 10 shows that the spectra of an Halo current distribution has an harmonic content higher than the harmonic content appreciable using a small number of modules as that foreseen in ITER. Therefore, aliasing errors might pose additional challenges to a reconstruction procedure based on the Fourier Transform.
It is worth noticing that the spectra obtained for different values of m are different one from another, these differences could be an advantage for a reconstruction procedure. It means that each Halo current contains some information about its causes, and is strictly related to the order number of the plasma perturbing mode.
The effects of change in amplitude of the perturbing mode have been investigated. In Figure 11 is reported the comparison between two spectra due to a single mode with m=1, but with different amplitudes (Δ_1=15%, blue bars; and Δ_1=25%, red bars).

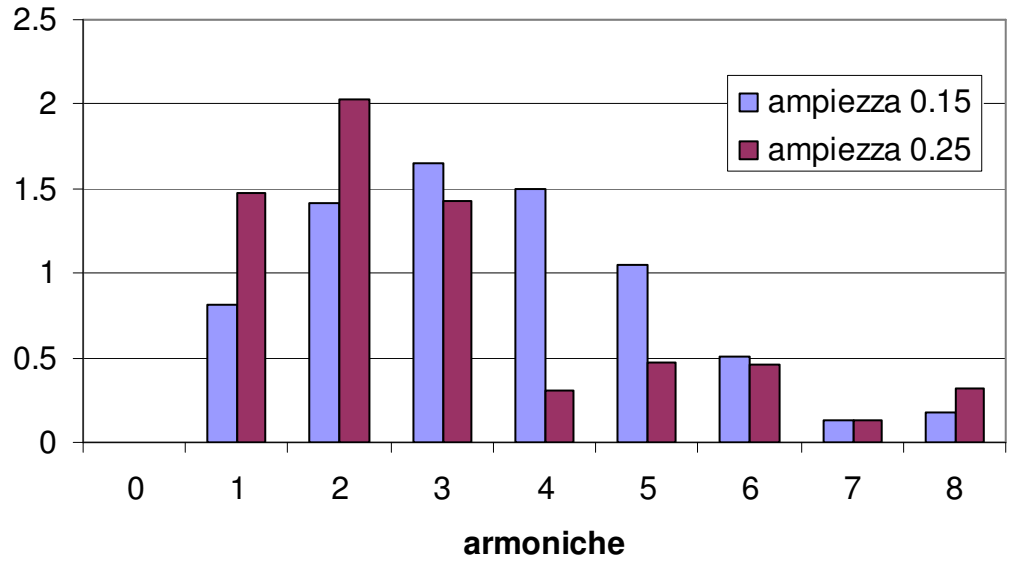

Figure 11 Comparison between two spectra obtained by the 16 modules model. Blue bars refer to a plasma affected by m=1 mode with Δ_1=15%; red bars refer to a plasma affected by a m=1 mode with Δ_1=25%.

The ratio between each pair of harmonics depends upon the amplitude, as shown in Figure 11. Therefore, the analysis of the spectrum of a Halo current distribution can give out information about the amplitude of the perturbing mode. On the other hand, this information is necessary to correctly fit the Halo current measurements and to find the missing values.
The aims of developing a reconstruction procedure has general purposes, that is to say the reconstruction procedure should be extended in a latter step to more realistic case involving a complex geometry of the first wall. The wall geometry will add its harmonic content to the poloidal spatial spectrum of a given Halo current distribution. In order to take into account such an effect, it is therefore necessary to develop an algorithm able to reconstruct Halo current distribution due to a superposition of perturbing modes. This case is more complicated than single mode cases, since it involves more unknowns related to the parameters defining each perturbing mode. Moreover, as previously noticed discussing the results reported in Figure 6, Figure 7, and Figure 8, it is not possible to reduce such a distribution to the sum of few distributions due to a single perturbing mode.
Several numerical simulations have been carried out in case of more than one perturbing modes. Here, some cases are compared. The plasma is affected by two perturbing modes of order m=1 and m=2, and have equal amplitudes Δ_m=15%. Varying the spatial phases β_m of the two perturbing modes, also the spectrum of the Halo current distribution varies. Two cases are taken into account. In the **first case**, the spatial phases of perturbing modes with order number m=1 and m=2 are of β_1=1.2radians and β_2=3.7radians respectively.
In the **second case**, the spatial phases of perturbing modes with order number m=1 and m=2 are of β_1=1.1radians and β_2=6.2radians respectively.
The Halo current distributions (red lines)are shown in Figure 12 and Figure 13 for the first case and the second case respectively. The halo current density distributions (blue lines) are also reported.

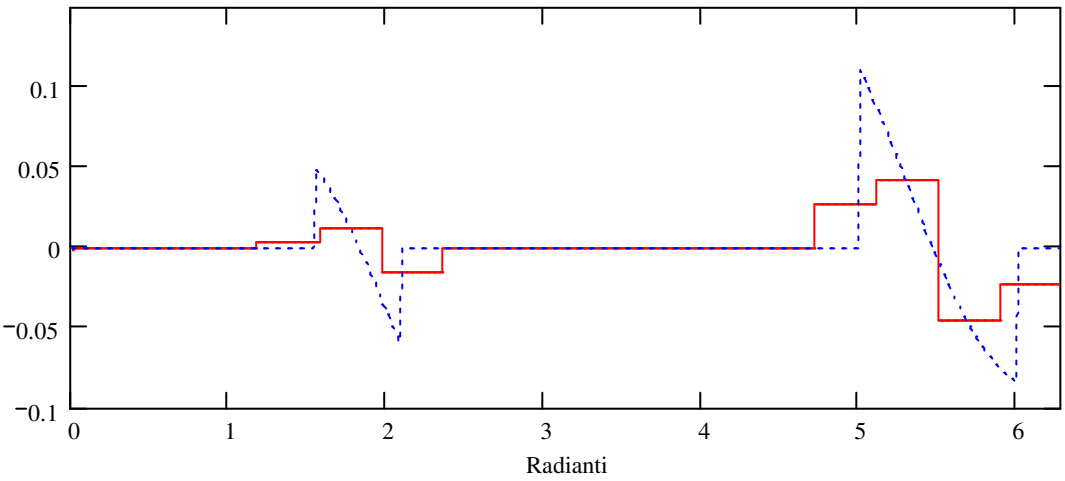

Figure 12 Halo current (red line) and Halo current density (blue line) distributions for a plasma affected by two perturbing modes with order number m=1 and m=2. The perturbing modes have equal amplitudes Δ_k=15%, and spatial phases equal to β_1=1.2radians and β_2=3.7radians. (First case)

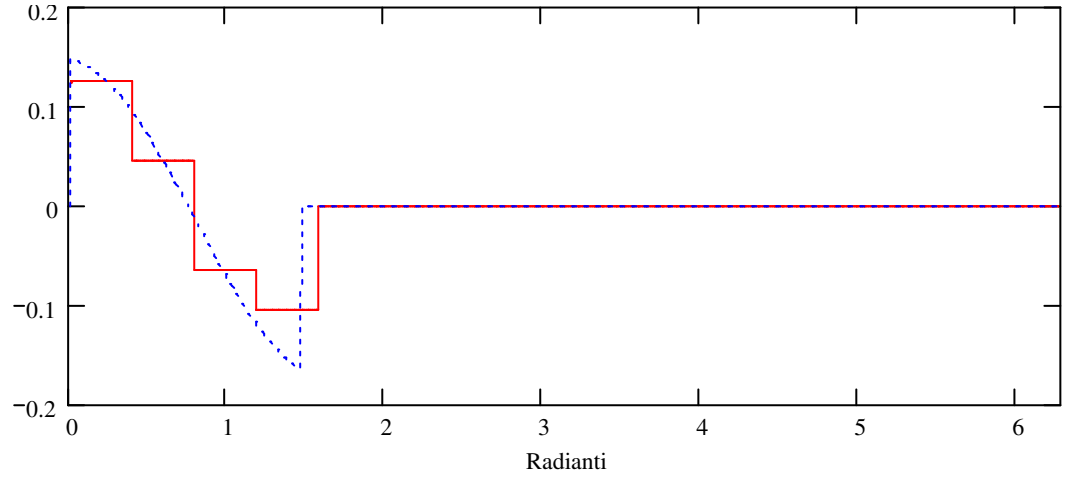

Figure 13 Halo current (red line) and Halo current density (blue line) distributions for a plasma affected by two perturbing modes with order number m=1 and m=2. The perturbing modes have equal amplitudes Δ_k=15%, and spatial phases equal to β_1=1.1radians and β_2=6.2radians. (Second case)

The spectra obtained for the two Halo current distributions shown in Figure 12 and Figure 13 are shown in Figure 14. Blue bars refer to the spectrum for the **first case**, and red bars refer to the spectrum for the **second case**.

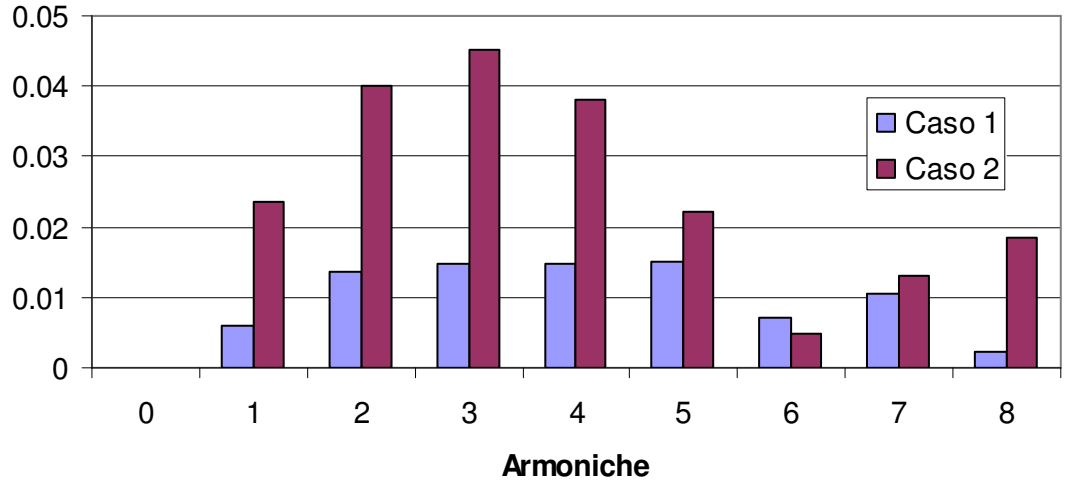

Figure 14 Spectra of the Halo current distributions shown in Figure 12 (blue bars) and Figure 13 (red bars).

In case of a superposition of perturbing modes, the spectrum of the Halo current distribution depends on the difference between the spatial phases ($\Delta\beta=\beta_1-\beta_2$) of each mode. Moreover, the Halo current distributions are discontinuous function of the phase, since the value of Halo current injected in a given module depends upon the overlap of the discontinuous $u(f(\vartheta))$ function, defined in equation (13), with the module surface.
The last example concerns the case of a superposition of modes. Fixing the spatial phase equal to β_1=1.1radians and β_2=6.2radians, the amplitudes of the two modes are varied. Three cases are taken into account:

1>2	Δ_1= 0.25	Δ_2= 0.15
1=2	Δ_1= 0.15	Δ_2= 0.15
1<2	Δ_1= 0.15	Δ_2= 0.25

The spectra related to these three cases are shown in Figure 15.

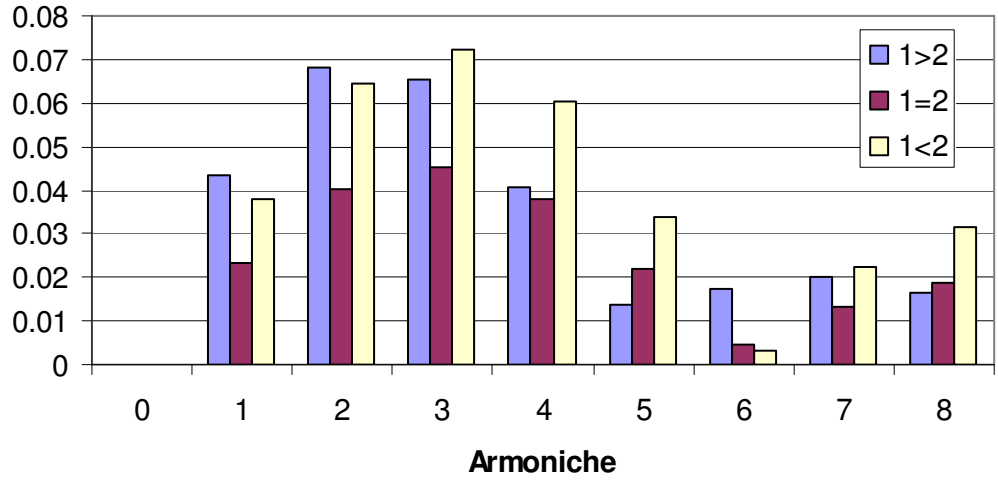

Figure 15 Comparison of the three spectra evaluated for the three cases above reported.

Figure 15 shows that in case of superposition of modes, the spectrum of the Halo current distribution depend also on the amplitudes of each mode.

2.2 Algorithms for Halo currents distribution reconstruction

The results obtained by the preliminary analysis reported in section 2.1 show that a halo current distribution strongly depends on the perturbing modes causing the contact between plasma and the first wall.
The Halo current distributions are characterized by a kind of periodicity which is strictly related with the periodicity order numbers (m,n) of the perturbing mode, but the harmonic contents of the halo current distribution is no directly related to (m,n), especially in case of two or more perturbing modes. The spectra are also depending on the amplitudes $\Delta_{m,n}$ and the spatial phases $\beta_{m,n}$ of the perturbing mode. Hence, these parameters strongly affect the halo current distribution.
This preliminary analysis has shown that the use of a Fourier transform does not give any advantage in reconstructing the Halo current distribution. However, in earlier phase of my activity in this framework, some algorithms using Fourier Transform have been developed. Some results have been obtained in single mode cases using procedures based on the Fourier transform, but these procedures were not able to reconstruct the Halo current distributions due to a superposition of perturbing modes.
Figure 6, Figure 7, and Figure 8 show that the Halo current distributions have a quite planar shape. A reconstruction procedure has been developed which extrapolates the unknown virtual values of Halo currents starting from the measured values, by a planar extrapolation.

This reconstruction procedure gave out considerable errors (of about the 200%) due to the extrapolation of Halo current values in modules where Halo currents are not injected.
The main purpose of a reconstruction procedure is to estimate the position of sources and sinks of the Halo currents flowing through the vacuum vessel. Such a result seems achievable only by an algorithm which uses some a priori information on the shape of the Halo currents distribution injected on the first wall.
The strong dependence of the Halo current distributions on the parameters defining the perturbing modes means that a procedure reconstructing the Halo current distributions is able to recognize, at the same time in an implicit or explicit way, the parameters describing the perturbing modes. Therefore, it was decided to develop a procedure which works on the basis of a predefined set of Halo current distributions. The Halo current measurements are compared with each predefined Halo current distribution, and the estimate of the actual Halo current distribution is taken as that predefined pattern which best fits the current data.
Some mathematics is required to develop such a reconstruction procedure. The reconstruction procedure and the underlying mathematics are reported in section 3. The results obtained by this procedure are reported in section 4.

3. Reconstruction procedure

The reconstruction procedure works on the basis of a pre-defined set of Halo current distributions. Few measurements of Halo current are available. Each distribution belonging to the predefined set is compared with the available measurements in order to individuate the predefined distributions which best fits the data and extrapolate the unknown values of Halo current.
The Halo current values are arranged in a matrix **V** of 18x18 real numbers, as described in section 1. Also the $\mathbf{V_D}$ (measurable values of Halo current) and **A** (virtual measurements of Halo current) matrices are arranged as matrices of 18x18 real numbers, even if they contains less useful information than the **V** matrices. In fact, the elements (i,j)of the $\mathbf{V_D}$ and **A** matrices are zero if they corresponds to no equipped modules (i,j). The **V** matrices could be arranged also in other way. In each case, the **V** matrices belong to a vectorial space. With the actual arrangement, the set {**V**} of all the possible Halo current patterns belongs to the space *H* of real 18x18 matrices. *H* is a vectorial space once the canonical scalar product for tensor is defined as:

$$\langle \mathbf{X} | \mathbf{Y} \rangle = \sum_{i,j} X_{i,j} \cdot Y_{i,j} \tag{17}$$

$\mathbf{V_D}$ and **A** matrices belong to a subspace *D* of *H*. It is worth noticing that the set {**V**} of all possible halo current distributions does not coincide with the *H* vectorial space, i.e. a given matrix **K** of *H* can be not representing an Halo current distribution. As an example, it is clear that the sum of all elements of the **V** matrix should result zero:

$$\sum_{i,j} (V)_{i,j} = 0 \tag{18}$$

In fact, the first wall surface is a quite close surface and $\nabla \cdot J = 0$ leads to equation (18). Only few matrices of *H* suit this constraint.
The explanation of the algorithm underlying the reconstruction procedure needs of some mathematic definitions which are given in section 3.1.

3.1 Projection [15]

Let *H* be a general vectorial space. Let **A** and **B** be two vectors belonging to *H*. The projection of the **A** vector on the vector **B** (or in the direction pointed by **B**) is a vector **C** belonging to *H*:

$$\mathbf{C} = \mathbf{A} \rightarrow \mathbf{B} = \frac{\langle \mathbf{A} | \mathbf{B} \rangle}{\langle \mathbf{B} | \mathbf{B} \rangle} \mathbf{B} \tag{19}$$

Let D be a subspace of H. The projection of the vector $\mathbf{A}$ on the subspace D is a vector called $\mathbf{A_D}$ belonging to D:

$$\mathbf{A_D} = \left\{ \frac{\langle \mathbf{A} | \mathbf{B} \rangle}{\langle \mathbf{B} | \mathbf{B} \rangle} \mathbf{B} : \| \mathbf{A_D} - \mathbf{B} \| = \min \{ \| \mathbf{A} \to \mathbf{C} \|, \forall \mathbf{C} \in D \} \right\} \tag{20}$$

The norm ||·|| is defined as $\|\mathbf{K}\| = \sqrt{\langle \mathbf{K} | \mathbf{K} \rangle}$.

The vector of the available measurements $\mathbf{V_D}$ is so defined as the projection of $\mathbf{V}$ in the subspace H.

3.2 Overprojection [13, 16]

Being H a vectorial space and D a subspace of H, for a given matrix $\mathbf{A}$ of D and a matrix $\mathbf{B}$ of H, we define the overprojection O[$\mathbf{A}$, $\mathbf{B}$; D] of $\mathbf{A}$ in $\mathbf{B}$ through D as:

$$O[\mathbf{A}, \mathbf{B}; D] = \frac{\langle \mathbf{A} | \mathbf{B_D} \rangle}{\langle \mathbf{B_D} | \mathbf{B_D} \rangle} \mathbf{B} = \mathbf{E} \tag{21}$$

where $\mathbf{B_D}$ is the matrix obtained projecting $\mathbf{B}$ in D. The result of this operation is a matrix $\mathbf{E}$ which belongs to H and lies along the "direction" indicated by $\mathbf{B}$. A vectorial representation of $\mathbf{E}$ is given in Figure 16, where $H = R^{3x1}$ = {(x, y, z)} and D={(x, y, 0)} is defined as the z = 0 plane.

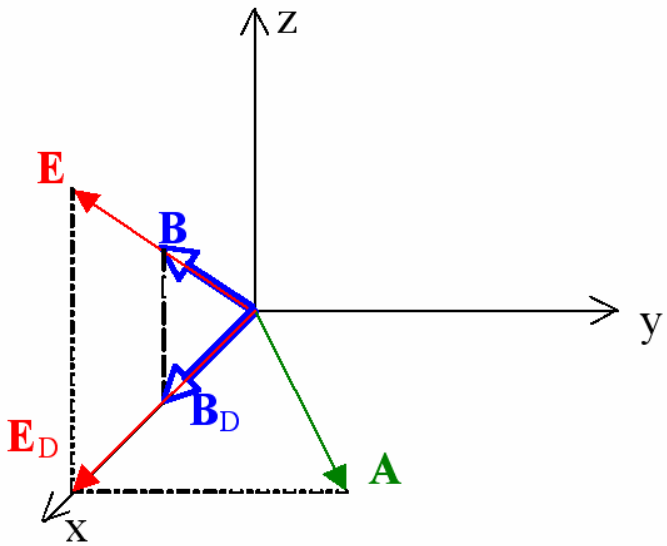

Figure 16 Representation of the overprojection in the R^{3x1}. $\mathbf{A}$ is overprojected in $\mathbf{B}$ through the z = 0 plane, where $\mathbf{A}$ and $\mathbf{B_D}$ lie. $\mathbf{E}$ is evaluated in such a way its projection on the z=0 plane equals the projection of $\mathbf{A}$ in $\mathbf{B_D}$.

The result of projecting the matrix **E** again on *D* is equal to:

$$\mathbf{E}_D = \frac{\langle \mathbf{A} | \mathbf{B}_D \rangle}{\langle \mathbf{B}_D | \mathbf{B}_D \rangle} \mathbf{B}_D \tag{22}$$

$\mathbf{E}_D$ is equal to the projection of **A** along the direction of $\mathbf{B}_D$, as shown in fig. 6. If **A** is a matrix of "virtual measurements", $\mathbf{A} = \mathbf{V}_D$ + **noise**, the matrix **E** resulting from **E** = O[**A**, **B**; *D*] can be considered as an estimation of the Halo current pattern **V**.
To evaluate the quality of the estimation in case of unknown Halo current pattern **V** and in presence of noise, we define the mean square error in the equipped modules (or relative error):

$$\varepsilon_D = \sqrt{\|\mathbf{A} - \mathbf{E}_D\|^2 / \|\mathbf{A}\|^2} \qquad [\%] \tag{23}$$

And the mean square error (or total error):

$$\varepsilon = \sqrt{\|\mathbf{V} - \mathbf{E}\|^2 / \|\mathbf{V}\|^2} \qquad [\%] \tag{24}$$

Ideally, the reconstruction procedure is provided of all the necessary information to reconstruct a given pattern **V** from $\mathbf{V_D}$, and the measurements are not affected by the noise. Therefore the ideal case is represented by the following condition:

$$\mathbf{noise} = \mathbf{0} \tag{25}$$

In the ideal case, the reconstruction procedure can work comparing the $\mathbf{V_D}$ matrix with a basis pattern $\mathbf{B}^* = \|\mathbf{V}\|^{-1}\mathbf{V}$, which contains all the necessary information to reconstruct **V**. In this case, the errors found by the procedure should be as little as possible. The overprojection operation is able to evaluate an exact estimation **E*** = [**A** , **B***; *D*] of **V** with negligible total and relative errors. The overprojection operation has been tested in the three cases shown in Figure 6, Figure 7, and Figure 8. The total and relative errors are reported in Table 1.

Table 1 Errors found in the ideal reconstruction of the Halo current distributions shown in Figure 6, Figure 7, and Figure 8.

	(1,1)	(2,3)	(1,1) + (2,3)
ε_D [%]	$2.6 \cdot 10^{-14}$	$1.9 \cdot 10^{-14}$	$1.2 \cdot 10^{-14}$
ε [%]	$2.5 \cdot 10^{-14}$	$1.9 \cdot 10^{-14}$	$1.1 \cdot 10^{-14}$

The estimate obtained overprojecting $\mathbf{V_D}$ in **B*** is an exact reconstruction of V in each case reported in Table 1. So, the overprojection operation can be considered the basis operation that a reconstruction procedure shall perform in order to compare the data ($\mathbf{V_D}$) with a given basis pattern (**B**) and to extrapolate the unknown values of Halo current by the above distributions.

3.3 Halo patterns basis set [16]

The simple code described in section 1 takes into account some first order approximations. Therefore, the actual Halo current distributions might differ from the estimation carried out by the code. In general, any code takes into account some approximations neglecting effects considered of the second order. In the present framework, these little differences can affect the performance of the reconstruction, because an additional error is found from the basis distribution and the actual one. I called these differences as "error of knowledge", because it is an error due to a lack of the knowledge of the code.
In order to have realistic simulation of how the reconstruction procedure should actually work with experimental data, the basis set of Halo current distribution has been created using rough approximations of the Halo current density patterns. Afterward, the reconstruction procedure has been tested reconstructing Halo current distributions given out by the code described in section 1.
Let **B** be a 18x18 matrix representing an Halo current distribution for a given perturbing mode, and $\mathbf{B_D}$ the projection of the **B** matrix on the *D* subspace. A $\{\mathbf{B^i}\}$ set representing Halo current distributions in case of a single perturbing mode has been built using rough approximations of the Halo current density patterns, as shown in Figure 17 using a simple ramp function.

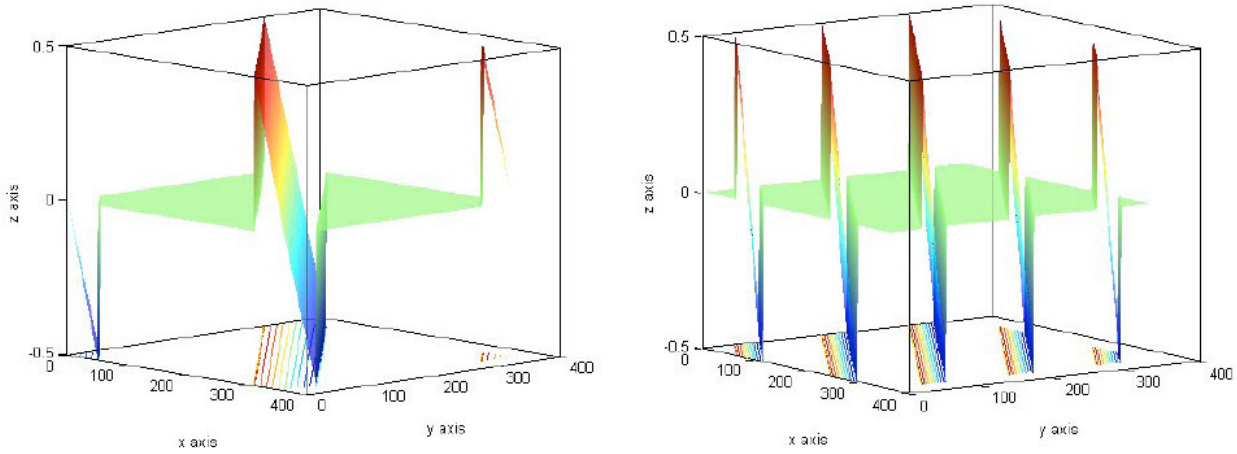

Figure 17 . Basic functions corresponding to a (1,1) mode (left), and to a (2,3) mode (right).

Note that functions $f(\vartheta,\varphi)$ in figure are similar to the pattern of $J_{\perp}(\vartheta,\varphi)\cdot(R+b\cdot\cos\vartheta)$. From these patterns, the elements of each basic matrices **B** were evaluated through the following integration:

$$(26) \qquad (\mathbf{B})_{i,j} = \iint_{\substack{\text{module} \\ i,j}} f(\vartheta,\varphi)\cdot b \; d\vartheta \; d\varphi$$

Each **B** matrix of the $\{\mathbf{B}^i\}$ set is defined varying the periodicity of the pattern, as shown in Figure 17, the amplitude and the spatial phase. The corresponding values of these parameters for the estimate **E** found by the reconstruction procedure can be thought as estimates of the corresponding parameters of the Halo current patterns. In the following, the order number M, N of the periodicity along the poloidal angle and the toroidal angle respectively are taken into account.
Each matrix in $\{\mathbf{B}^i\}$ set corresponds to a particular case of a single mode perturbation. The $\{\mathbf{B}^i\}$ set was calculated for M= 1, 2 and 3; N= 1, 2 and 3; for 36 values of the spatial phase β; and 8 values of amplitude resulting in a set of 2592 matrices.

3.4 Outline of the Reconstruction procedure

Let $\{\mathbf{B}^i\}$ be a limited set of pre-determined Halo current patterns. For a given set of virtual measurements **A,** a set $\{\mathbf{E}^i = O[\mathbf{A}, \mathbf{B}^i ; D] \; ; \; \mathbf{B}^i \in \{\mathbf{B}\}\}$ of possible estimates of **V** is found, together with the corresponding set of mean square errors $\{\varepsilon_D\}$. At this point the reconstruction procedure simply consists on choosing the best estimate **E***on the basis of the mean square error ε_D.
The reliability of such a procedure depends on the hypothesis that smallest total error ε is related to the smallest relative error ε_D found by the procedure. The truth of this hypothesis depends on the positioning of the sensors and on the "nature" of the patterns. Moreover, the performances of the procedure depend also on the completeness of the predetermined set of basis patterns $\{\mathbf{B}\}$ and on the noise level, as described in section 4 where the results of numerical tests are discussed.

4. Numerical validation tests [13, 16]

The reconstruction procedure described in section 3 has been implemented in Matlab on the basis of simple model shown in section 1. The outline of the numerical tests is as follows. An evaluation of the Halo current distribution **V** is given out by the simple model of section 1. Then, **V** is projected in *D* resulting in a $\mathbf{V_D}$ matrix, as also described by equation (10). Afterward, the $\mathbf{V_D}$ matrix can be added to a random noise in order to evaluate the virtual measurements matrix **A**, and then the reconstruction procedure is applied to the **A** matrices or to the $\mathbf{V_D}$ matrices.
As a first example, the reconstruction procedure has been applied to the $\mathbf{V_D}$ matrices evaluated shown in Figure 6, Figure 7, and Figure 8.
The estimation **E** matrices found by the reconstruction procedure are shown in Figure 18, Figure 19, and Figure 20, the errors are reported in Table 2.

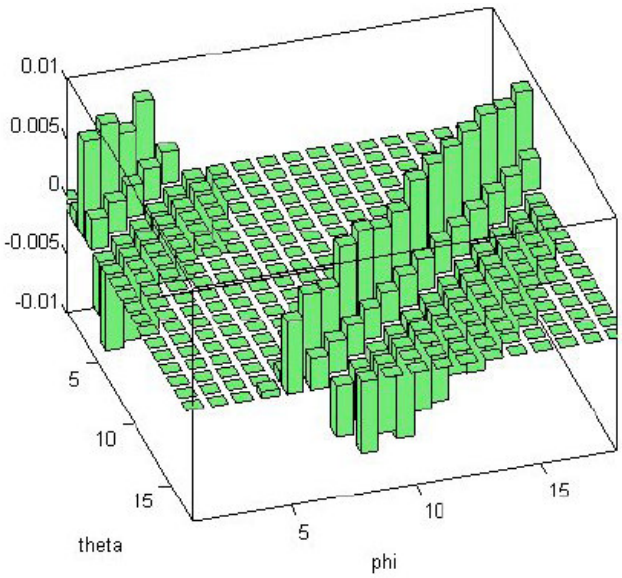

Figure 18 Matrix **E** of the "virtual" Halo current measurements estimated by the reconstruction procedure from the Halo currents measurements $\mathbf{V_D}$ matrix shown in Figure 6.

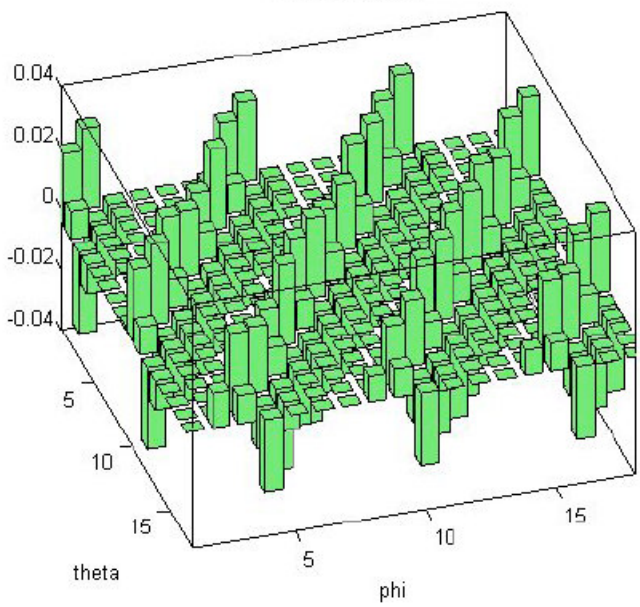

Figure 19 Matrix **E** of the "virtual" Halo current measurements estimated by the reconstruction procedure from the Halo currents measurements $\mathbf{V_D}$ matrix shown in Figure 7.

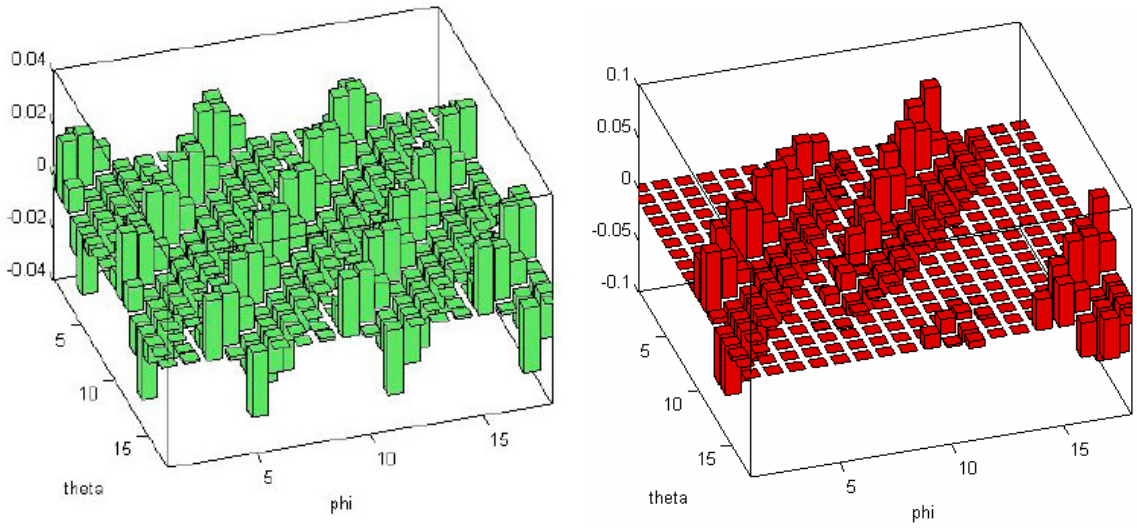

Figure 20 (left) Matrix **E** of the "virtual" Halo current measurements estimated by the reconstruction procedure from the Halo currents measurements $\mathbf{V_D}$ matrix shown in figure 8. (right)The **V** matrix evaluated from the model that the procedure should reconstruct.

Table 2 Errors produced by the reconstruction procedure for the cases shown in Figure 6, Figure 7, and Figure 8.

	(1,1)	(2,3)	(1,1) + (2,3)
ε_D [%]	28.8	19.6	79.8
ε [%]	30.3	20.4	78.5
M	1	2	2
N	1	3	3

As shown in the two first columns of Table 2, the reconstruction procedure is able to reconstruct the distribution related to a single perturbing mode with acceptable errors ($\leq$ 30%), and also to correctly estimate the periodicity order numbers of the perturbing mode.
Right column (superposition of perturbing modes) in Table 2 has more severe errors than the other columns (single perturbing mode). In Figure 20 are shown both the **E** estimate than the input pattern **V**. Some differences occur between the shape of **V** and **E**, the reconstruction procedure fit the current pattern with a pattern representing a Halo current distribution due to a single perturbing mode with order numbers (2, 3), filling in some modules, which are not in contact with the plasma, with no zero values of Halo current.
Nevertheless, it is worth noticing that the $\{\mathbf{B}^i\}$ set does not include a matrix able to describe the case of a multiple modes perturbation. If **B** matrices describing superposition of modes are included in the $\{\mathbf{B}^i\}$ set, the results shown in Table 1 and in Table 2 mean that the algorithm can identify the overprojection on one of these **B** matrices as its estimation of **V**. In fact, the relative error ε_D evaluated by the procedure (Table 2) is larger than the 70%, and from the results shown in Table 1 we can expect that the reconstruction procedure should find smaller relative errors ε_D comparing the $\mathbf{V_D}$ matrix representing a superposition of modes with matrices representing the same case. Comparing the relative errors the procedure will choice that estimate having the smaller error, that is to say an estimate related to a case of a superposition of perturbing modes.
Moreover, Table 2 shows also that the relative errors ε_D are close to the total errors ε, i.e. the main hypothesis, (section 3.4) underlying such a reconstruction procedure, is well found.
So, a reconstruction algorithm based on the overprojection should give adequate estimations both in case of a single perturbing mode and in case of a superposition of perturbing modes.
Last two rows in Table 2 show the values of M and N, the periodicity order numbers of the basis pattern approximating the **V** matrix. In single mode cases, these values correspond to the value m and n of the order of the perturbation producing the Halo current pattern **V**. Therefore, the reconstruction procedure is able to recognize the periodicity order numbers (m,n) of the perturbing mode. In case of a superposition of modes, these values correspond to the values of one of the perturbing modes. This is another important outcome of the algorithm, useful to extend it to cases of multiple modes perturbations
Afterwards, several numerical tests have been carried out in order to test the robustness of the reconstruction procedure against the noise.
For each test pattern **V**, a first test was carried out assuming zero noise (using the $\mathbf{V_D}$ matrix as input test pattern), and a second test was carried out using the **A** matrix as input test pattern, that is to say assuming a random noise level of 20%, corresponding to that expected in ITER [14]. The reconstruction errors were evaluated according to equations (23) and (24) for test patterns due to single perturbing mode with periodicity order numbers of (1, 1) and for single (2, 1) mode. In absence of noise, the errors are typically in the 5-30% range (Figure 21) and the total and the relative errors ε and ε_D are almost identical. In all these

cases, the reconstructed periodicity, amplitude and initial angle are in good agreement with respect to the corresponding input Halo current pattern used for the tests. When the noise is considered, a negligible increment in total error is found, confirming the robustness of the reconstruction and indicating that the most significant source of error is most likely the rough discretization of the set of basis patterns {**B**}. However, the presence of noise enhances the difference between total and relative errors (Figure 22).

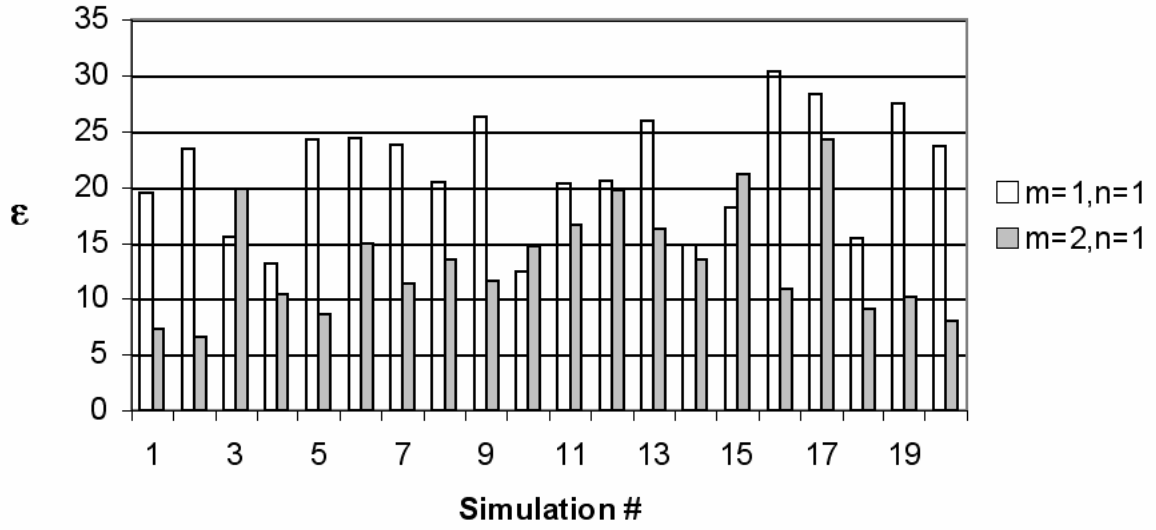

Figure 21 Total reconstruction error ε for (m=1,n=1) test pattern (white bars) and for (m=2, n=1) (gray bars).

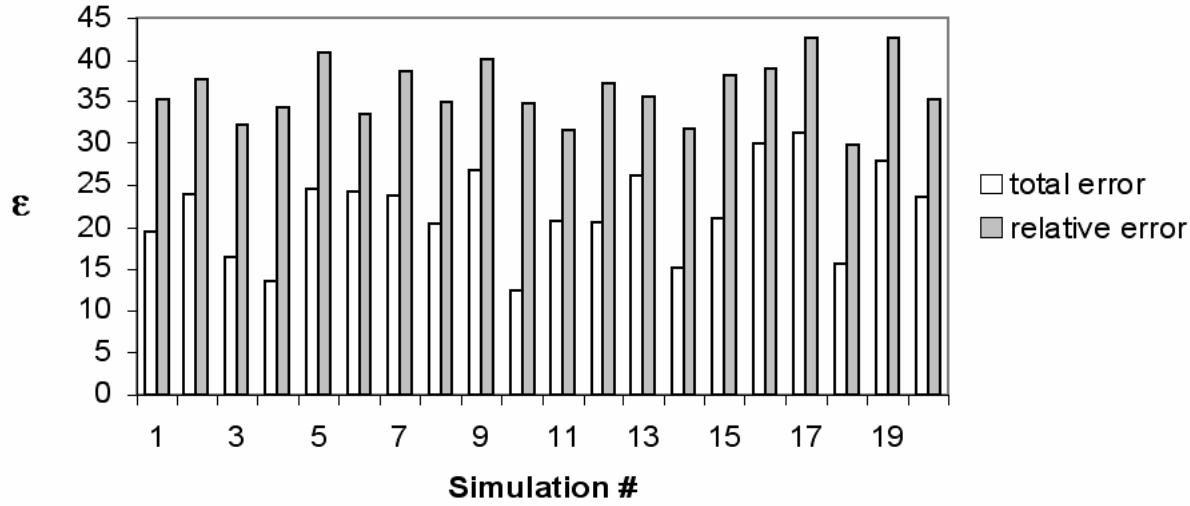

Figure 22 Comparison of total and relative errors for the (m=1,n=1) patterns with noise.

The results reported in Figure 21 and Figure 22 are in agreement with the previous results reported in Table 2. Further numerical experiments have been carried out considering randomly generated Halo current patterns in case of superposition of modes. The spatial phase of each pair of modes generating an input test pattern were calculated by a random function, also the amplitudes were calculated randomly but considering a main mode having an amplitude larger than the other one. The secondary mode can be considered as a perturbation of a single mode case, having amplitude of one tenth of the amplitude of the main mode. In these cases, the reconstruction procedure produced estimates with errors as large as the 70%, but recognizing the periodicity order number of the main mode. Also these results are in good agreement with the results shown in Table 2.
The reconstruction procedure has been assessed by means of the numerical tests here reported. A reconstruction procedure seems to be reliable also in case of fusion reactor with more complex geometry of the first wall. In fact, the algorithm here adopted seems to be the most promising in reconstruct 2D distributions with complex spatial spectra and a strongly dependence on a large number of parameters, as the collection of the amplitudes and the spatial phases of each mode which could affect the shape of the plasma.
The present implementation of the reconstruction procedure is aimed at reconstructing Halo current patterns due to a single perturbing mode. The assessment of the errors show that in case of a single perturbing mode, the reconstruction procedure works well evaluating estimate with acceptable errors, less than the 30%.
Also the robustness of the reconstruction procedure has verified for the level of noise foreseen in ITER. The performances of the procedure are not affected by the noise.
From the good results here obtained, it was decided to continue this activity applying a similar reconstruction procedure to simulation of Halo current distributions in ITER. However, a suitable model able to evaluate such a distribution in ITER was not still present. So, it was decided to develop few suitable codes able to evaluate the Halo current distributions in ITER. Three codes have been evaluated, as described in chapter III.

5. Summary

A simple model of an ideal tokamak has been utilized to carry out realistic simulation of Halo currents. The first wall is here modeled as an ideal torus with circular cross section. A model of a plasma has been developed. The plasma hits the wall when it is perturbed by one or more MHD instabilities. If contact between the plasma and the first wall occurs, Halo currents are injected on the first wall. A code has been developed to evaluate the Halo current density pattern on the overall first wall. Then, the first wall has been discretized in a number of blanket modules close to the number of blanket modules foreseen in ITER, and virtual measurements of Halo currents have been evaluated by integrating the Halo current density distribution on each module.
A preliminary analysis has been carried out lowering the dimensions from 3 to 2 and taking little approximation. This preliminary analysis allows highlighting the non-linearity occurring in Halo current patterns. Due to this non linearity, a reconstruction procedure needs to compare the data to reconstruct with a $\{\mathbf{B}\}$ set of pre-defined basis patterns. Such a comparison is achieved by the definition of suitable errors and the reconstruction is based on the operation of overprojection.
Then, an algorithm has been developed and tested for the estimation of the Halo currents injected in all the blanket modules, on the basis of the values measured on the instrumented modules (really or virtually).
The algorithm is essentially an "extrapolation" algorithm, based on the operation of "Overprojection". The reliability of this algorithm was assessed by means of numerical experiments, using "virtual" measurements, under the following conditions:

- single-mode perturbation;
- first wall with circular cross-section.

In the case of single-mode perturbation, the error of the algorithm was found to be acceptable ($\leq 30\%$) for the purpose of electromagnetic load estimation. The results obtained in presence of noise were also acceptable, showing the robustness of the method.
It is worth noting that, exploiting the periodicity of the configuration provided by the particular conditions above mentioned, several other algorithms could be applied, such as algorithms based on the Discrete Fourier Transform (DFT), or on an inspection of data plus some simple algebraic calculations.
Nevertheless, the algorithm based on the Overprojection seems to be the most appropriate to be applied to more general geometrical conditions, i.e. to the ITER first wall cross-section. Even though the algorithm has been developed for single-mode perturbation, tests have been carried out also assuming multiple-mode perturbations, demonstrating that the method is able to recognize the order number (m,n) of the periodicity of the main perturbing mode. The occurrence of larger errors, as in case of 2-mode plasma perturbations, is due to the absence in the $\{\mathbf{B}\}$ set of suitable basis patterns to represent these cases. The algorithm seems to be able to reconstruct also pattern produced by a superposition of modes, if corresponding predefined patterns are inserted into the $\{\mathbf{B}\}$ set.
In fact, the reliability of such an algorithm does not depend on the particular conditions, but only on the occurrence of some kind of correlation among the data. Moreover, the efficiency and reliability of the algorithm strongly depends on the choice of the basis set.
The nest step shall be the application of the Overprojection algorithm to more realistic geometrical "ITER-like" conditions. This will require the use of suitable models for the

computation of 3D Halo current patterns in generic geometry to define the "basis set" to be used for the Overprojection. The development of similar codes is discussed in chapter III.

CHAPTER III

Three dimensional models for the simulation of the Halo current distribution in ITER

Due to the symmetric Vessel resistance of ITER, the description of the Halo Current by the Toroidal Peaking Factor could be not sufficient to describe the Halo Current phenomenon. In fact, especially in case of asymmetric VDEs, the toroidal component of the Halo Current can be not negligible in ITER. Some 3-dimensional codes have been developed to simulate more realistic Halo Current distributions on the First Wall surface of ITER.
These codes are made up of a suitable numerical model of the First Wall and an analytical model of the plasma surface.
The model of the First Wall is described in section 1. The model of the plasma has been developed taking into account the hypothesis of a quasi-equilibrium, as discussed in section 2. Three different codes have been developed as discussed in section 3.
Finally, the consistency between these codes is discussed in section 4.

1. Numerical model of the ITER First Wall [17]

On the basis of the technical design of the ITER First Wall, shown in Figure 1 [14], a suitable 3D model has been developed with Matlab.
ITER First wall is made up of several modules and ports. The overall model of the First Wall is a collection of several sub-models describing a part of a Toroidal surface. Each sub-model contains different field. The minimum number of information needed to describe the surface of a given Plasma Facing Component is stored in the sub-model. During simulation a numerical model of each plasma facing component is taken into account. Each surface is meshed in a number of point depending on the resolution Δs. The resolution Δs of the mesh is defined as the greater spacing between each point of the mesh with the next. It is a value variable from the user, its default value is of 10cm. The coordinates of each point in 3D Cartesian system are stored in a 3D array contained on each sub-model. The sub-model contains in an apposite field the information on Plasma Facing Component considered. A plasma facing component can be the surface of a module or of a port. Moreover, the module can be equipped with Halo sensor or not. In this way, when a simulation starts, the user can decide if mesh all of the plasma facing component or mesh only the surfaces corresponding to modules or just the surfaces corresponding to the equipped modules. Afterward, the evaluation of the Halo current will be carried out only on the meshed surfaces.
The Halo current simulation codes perform their calculation on the sub-models which have been meshed. The results of the simulation codes is recorded in an appropriate field of the sub-model.
When the Halo current evaluation are performed on all of the first wall, the user is ever able to select only the values of Halo current corresponding to the modules or only to the equipped modules.

The position of each port and module is defined in the 3D space with respect to the proposal design of the ITER first wall, shown in Figure 1 [14].
In Figure 2 is shown the mesh of the ITER First Wall computed taking into account only the equipped modules, the resolution is of Δs=10 cm, that is the spacing between each point of the mesh with the next (both along s and along φ) is less than Δs.

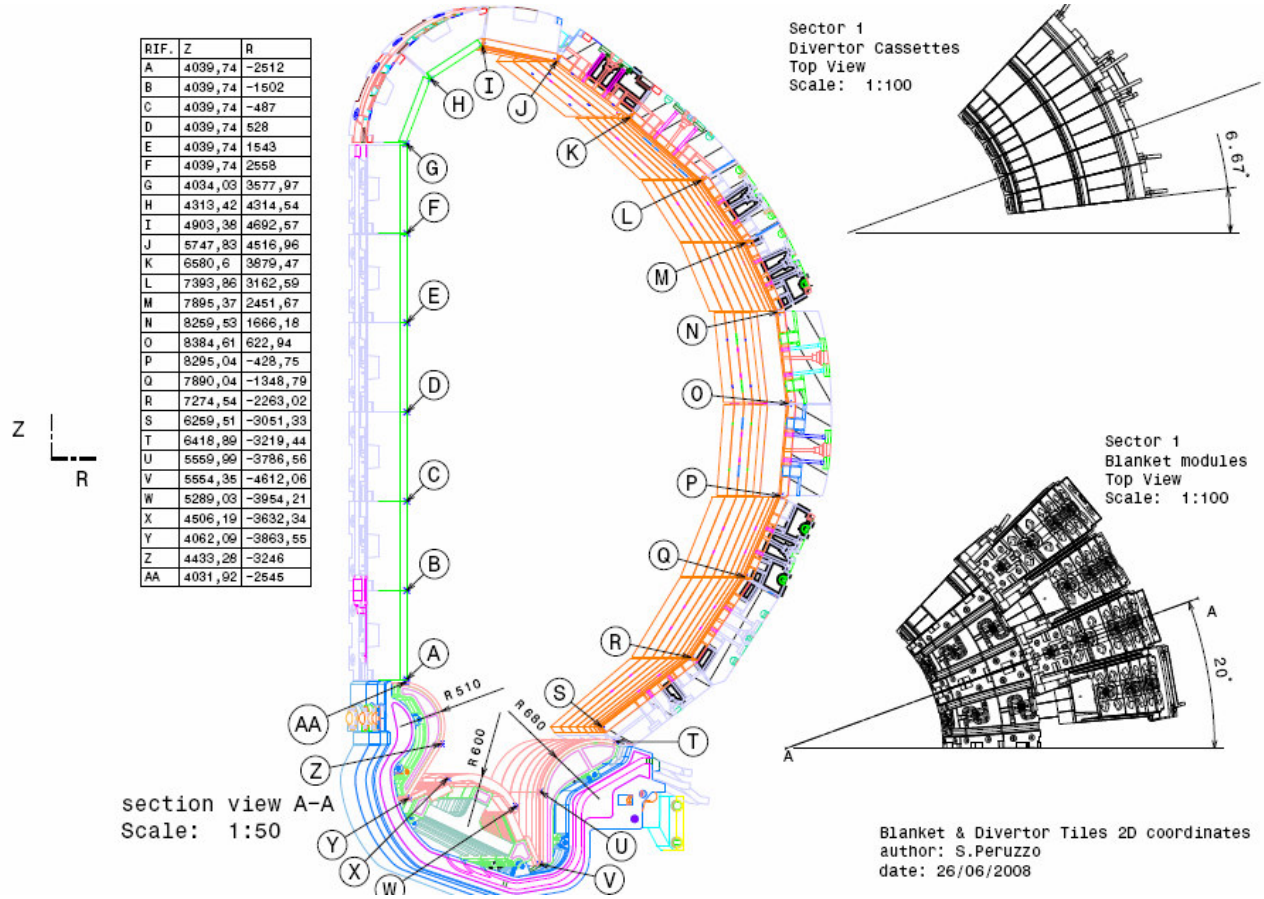

Figure 1. Technical Drawing used to define the model of the cross section [14].

Each point of the First wall is defined in the 3D Cartesian reference system, and in a 2D system (s, φ). The φ coordinate corresponds to the toroidal angle. The s coordinate is a curvilinear coordinate defined along the cross section, it starts from the point A in Figure 1 (s=0) and goes around the perimeter of the first wall to the point S, along the clock wise direction. Finally, it goes around the divertor cross section from the point T to the point AA.

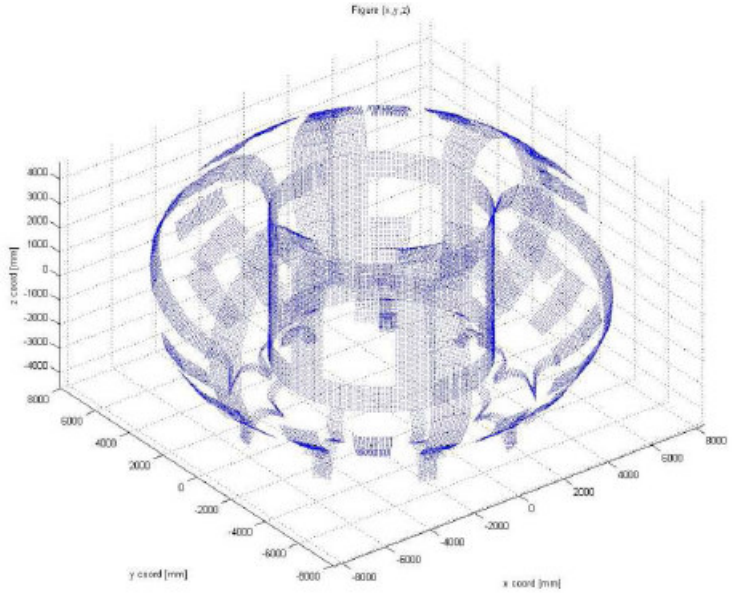

Figure 2. Numerical model of the ITER First Wall. Only the equipped modules are reported. [17]

2. Analytical model of the plasma surfaces

Three codes for the computation of the pattern of Halo currents injected into the vessel from the halo region are described in section 3. These codes are based on the model of the First wall, described in section 1 and on the following model of the plasma surfaces and current density distribution.
The main approximation of the plasma model lies in assuming a circular plasma cross section before the growth of the MHD modes and it is based on experimental observation and on the results of two dimensional simulations of Vertical Displacement Events (VDE) performed by means of the MAXFEA [18] and DINA [19] finite elements codes. Halo currents mainly occur in the Case of VDEs following a loss of control or an unrecoverable disturbance. In both cases, during the first phase, the plasma shrinks and loses its elongation. When the plasma hits the wall and the halo phenomenon starts, the plasma cross section is reasonably approximated by a circular geometry as visible in Figure 3.
With the aims of modelling the Halo currents phenomena with a 3D description, plasma in an equilibrium state with a circular cross-section can be the starting point in order to develop a model suitable to describe the plasma affected by some MHD perturbations and Vertical Displacement Events.

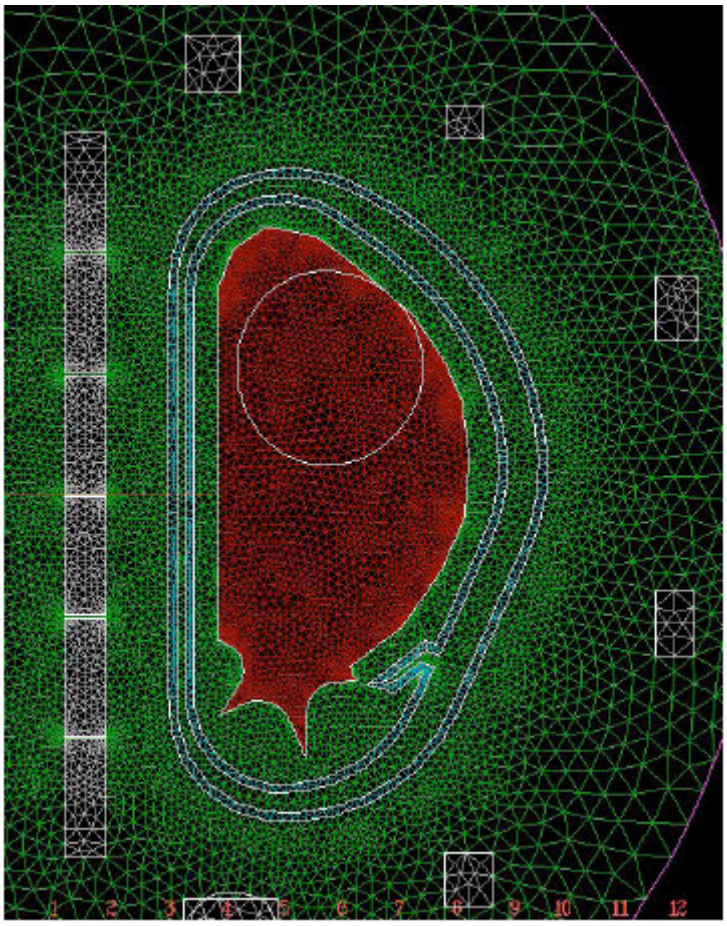

Figure 3. ITER plasma shape in the late VDE phase from MAXFEA simulation [18].

A simple VDE, not affected by MHD instabilities, causes a deposition of Halo current symmetric along φ. The effect of a VDE can be easily described with two shifts, one along the radial direction and the other along the vertical direction, of the plasma centre.
Superposition of one or few MHD modes modifies the shape of the plasma, causing asymmetric deposition of Halo current. The plasma is seen as an uncompressible fluid. The MHD perturbing modes modify the spatial distribution of the density current. In fact, the shape of each plasma surface is modified by the MHD modes tilting the direction of the density current vectors which belong on the given plasma surface. On the other hand, the module of the vectors as well as the total amount of the current flowing through two plasma surfaces retains its value at equilibrium.
So, the calculation of the current flowing through two different plasma surfaces can be carried out considering the initial unperturbed plasma.
Plasma surfaces can be labelled by their minor radius r_s at equilibrium. The minor radius r_s is strictly related with the value of the poloidal flux function ψ discussed in section 3.3, chapter IV. Points lying on a given plasma surface r_s are positioned in the 3D Cartesian system depending on the ϑ, φ coordinates defined in a quasi-toroidal system. The quasi-toroidal system (r_s, ϑ, φ) of coordinates is defined with respect to the position of the plasma axis on a cross section (R_{maj}, z_0).

As a starting position, at equilibrium the plasma axis is located at the centre of the ITER cross section: R_{eq}= 6,2 m and z_{eq}= 0 m.
A VDE is simply represented adding the radial ΔR and the vertical Δz displacements. So, the actual plasma axis position is evaluated by:

(1) $$R_{maj} = R_{eq} + \Delta R \quad z_0 = z_{eq} + \Delta z$$

The deformations due to some MHD perturbations are modelled modifying the value of the effective minor radius r corresponding to the minor radius coordinate of a Toroidal system as a function of ϑ and φ:

(2) $$r(r_s, \vartheta, \varphi) = r_s \cdot \left(1 + \sum_{m,n} \Delta_{m,n} \cdot \sin(m \cdot \vartheta + n \cdot \varphi + \beta_{m,n})\right)$$

It is similar to equation (2) in section 1.2, chapter V, with the same significance of the symbols. Here, r_s is the minor radius at equilibrium of a given plasma surface, this parameter ranges from 0 to r_{min}, the minor radius of the outer plasma surface. This last quantity is evaluated as

(3) $$r_{min} = r_{close}(1 + Hw)$$

Where r_{close} is the minor radius of the last close plasma surface, and Hw is a measure of the Halo width.
The relationships between the coordinates in a Cartesian system with the coordinates defining a given point on a plasma surface r_s are:

(4) $$\mathbf{S}(r_s, \vartheta, \varphi) = \begin{bmatrix} x = (R_{maj} + r(r_s, \vartheta, \varphi) \cdot \cos(\vartheta)) \cdot \cos(\varphi) \\ y = (R_{maj} + r(r_s, \vartheta, \varphi) \cdot \cos(\vartheta)) \cdot \sin(\varphi) \\ z = z_0 + r(r_s, \vartheta, \varphi) \cdot \sin(\vartheta) \end{bmatrix}$$

2.1 Model of the plasma current density

In order to describe the spatial distribution of the density plasma current, a simple model of the plasma surfaces at equilibrium is taken into account. The aim of the model is to describe with sufficient accuracy the spatial distribution of the current flowing in the Halo region, that is to say the surfaces close to the edge of plasma.
In this region, the plasma surfaces can be considered as approximately concentric with circular cross-section and can be defined (labelled) by the minor radius r_s. A constant value of the safety factor q and force-free condition [5] are assumed, in such a way J~B~1/R. The modules of the poloidal and toroidal component of the density current are related with the Safety Factor by:

$$q = \frac{r_{min} \cdot B_\varphi}{R_{maj} \cdot B_\vartheta} = \frac{r_{min}}{R_{maj}} \cdot \frac{J_\varphi}{J_\vartheta} \tag{5}$$

In the following, it is assumed that J_φ and J_ϑ are flowing towards the counter clock wise direction along φ and ϑ respectively, kept as the positive directions.
The plasma current density $\mathbf{J_{plasma}}$ distribution is represented as the product of the module J_p and a unit vector **j**.
The current density vector is always tangential to the plasma surface, and it can be evaluated considering two unit vectors **t** and **p**. For a given point $(r_s, \vartheta, \varphi)$ **t** and **p** can be evaluated by the relationships in eq. (4):

$$\begin{aligned} \mathbf{t} &= \frac{\partial \mathbf{S}}{\partial \varphi} \\ \mathbf{p} &= \frac{\partial \mathbf{S}}{\partial \vartheta} \end{aligned} \tag{6}$$

In a general case **t** and **p** vectors have a little component along the direction of the minor radius. When the plasma is not affected by any MHD perturbation, it can be found:

$$\begin{aligned} \mathbf{t} &= \nabla \varphi \\ \mathbf{p} &= \nabla \vartheta \end{aligned} \tag{7}$$

Under this quasi-equilibrium condition, the pitch of the current density line is related to the safety factor q, as described in equation (5). Therefore, it can be found:

$$\mathbf{j} \propto q \frac{R_{maj}}{r_{min}} \cdot \mathbf{t} + \mathbf{p} \tag{8}$$

The quantities above described are related with the plasma current density distribution by:

$$\mathbf{J_{plasma}} = J_p \mathbf{j} = J_\varphi \mathbf{t} + J_\vartheta \mathbf{p} \tag{9}$$

J_p, J_φ and J_ϑ are evaluated without taking into account the effect of MHD perturbations, so they depend on the r_s plasma surface where the density current vector lies and on the ϑ angle, in order to satisfy the free-force condition [5] and $\nabla \cdot \mathbf{J} = 0$:

$$J_p(r_s, \vartheta) = J_0 \frac{R_{maj}}{R_{maj} + r_s \cdot \cos\vartheta} \tag{10}$$

Where J_0 is the estimate of the plasma current density at the plasma axis, $r_s=0$.
Under quasi-equilibrium conditions, that is for plasma affected by a pure VDE, we can calculate the amount of current flowing through the infinitesimal poloidal and toroidal surfaces between the plasma surface r_s and the outer plasma surface r_{min}. These values are evaluated for circular plasma in a quasi-equilibrium state, but since MHD modes are seen as rigid displacement of the plasma, present calculations can be used also in case of perturbed plasma.

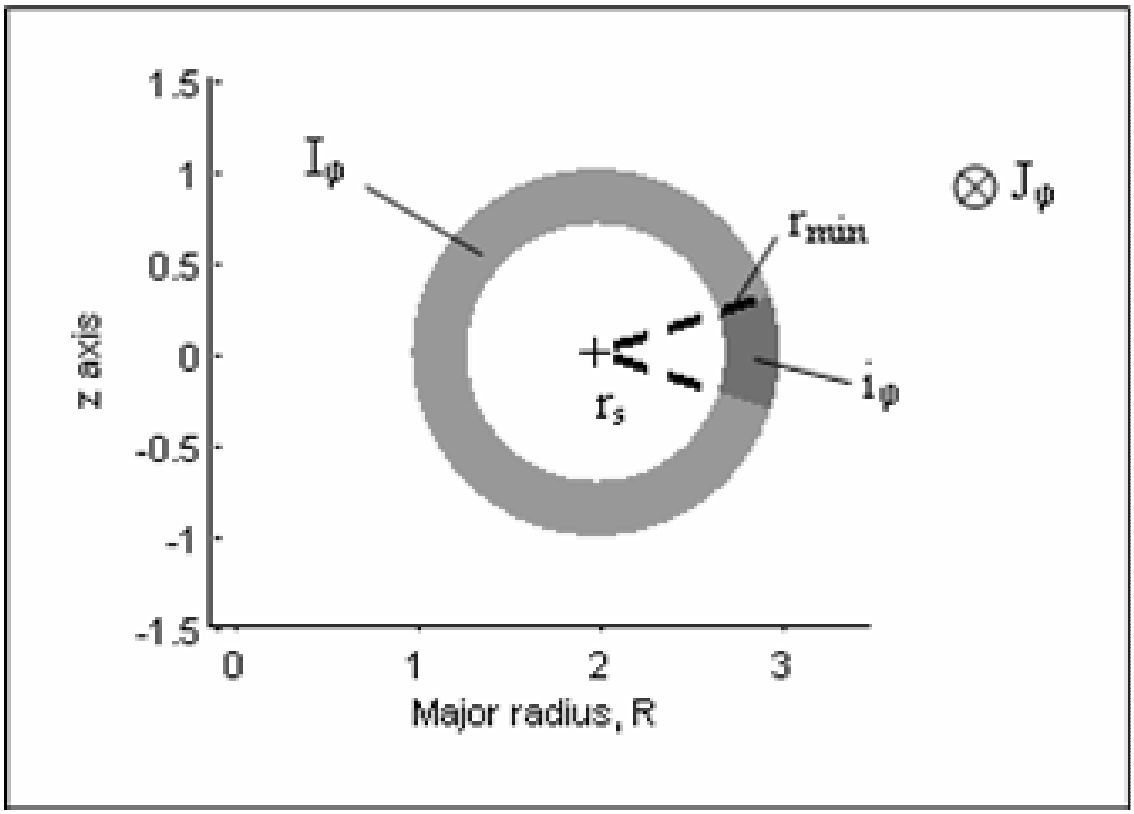

Figure 4. Sketch of a plasma cross section (grey) between a plasma surface with minor radius r_s and the outer plasma surface r_{min}. The toroidal current flux I_φ is evaluated integrating the toroidal component of the current density on this area. Infinitesimal values of I_φ are evaluated for infinitesimal value of the angle ϑ, as an example, on the dark grey area.

Figure 4 shows the toroidal section defined between the r_s plasma surface and the r_{min} outer surface. At the equilibrium, the toroidal component of the density current J_φ is orthogonal to this surface. The value I_φ of the current flowing through the toroidal section coloured in grey is evaluated as follows:

$$J_\varphi = \frac{J_{\varphi 0} R_{maj}}{R_{maj} + r \cdot \cos\vartheta} \tag{11}$$

$$\begin{aligned} I_\varphi &= \int_0^{2\pi} d\vartheta \int_{r_S}^{r_{min}} r dr \frac{J_{\varphi 0} R_{maj}}{R_{maj} + r \cdot \cos\vartheta} = J_{\varphi 0} \int_0^{2\pi} d\vartheta \int_{r_S}^{r_{min}} r dr \frac{1}{1 + r/R_{maj} \cdot \cos\vartheta} \\ &\cong J_{\varphi 0} \int_0^{2\pi} d\vartheta \int_{r_S}^{r_{min}} r dr \left(1 - r/R_{maj} \cdot \cos\vartheta\right) = J_{\varphi 0} 2\pi \left(\frac{r_{min}^2 - r_s^2}{2}\right) = 2\pi J_{\varphi 0} \cdot \delta \cdot r_M \end{aligned} \tag{12}$$

$\delta = r_{min} - r_s$ is an "interference" value and $r_M = (r_s + r_{min})/2$.
$J_{\varphi 0}$ is the toroidal component of the plasma current density at the plasma axis.
In Figure 4 the dark grey area is seen from the plasma axis with an angle of $d\vartheta$. The infinitesimal value of current i_φ flowing through this infinitesimal area is interesting and it can be evaluated as follows:

$$\begin{aligned} \frac{dI_\varphi}{r_s d\vartheta} &\cong \frac{J_{\varphi 0}}{r_s} \int_{r_S}^{r_{min}} r\left(1 - r/R_{maj} \cdot \cos\vartheta\right) dr \\ &= \frac{J_{\varphi 0}}{r_s} \cdot \left[\frac{r_{min}^2 - r_s^2}{2} - \frac{1}{3}(r_{min} - r_s) \frac{r_{min}^2 + r_s^2 + r_{min} r_s}{R_{maj}} \cdot \cos\vartheta \right] \\ &= \frac{J_{\varphi 0}}{r_s} \cdot \delta \cdot \left[r_M - \frac{r_M^2 + \delta^2/12}{R_{maj}} \cdot \cos\vartheta \right] \end{aligned} \tag{13}$$

For small values of $\delta/r_M \cong 0$, $r_s \cong r_M$, it can be approximated as:

$$i_\varphi = \frac{dI_\varphi}{r_s d\vartheta} \cong J_{\varphi 0} \cdot \delta \cdot \left[1 - \frac{r_M}{R_{maj}} \cdot \cos\vartheta\right] \cong \frac{J_{\varphi 0} R_{maj}}{R_{eff}} \cdot \delta \tag{14}$$

Where $R_{eff} = R_{maj} + r_M \cos\vartheta$ is an effective radius.

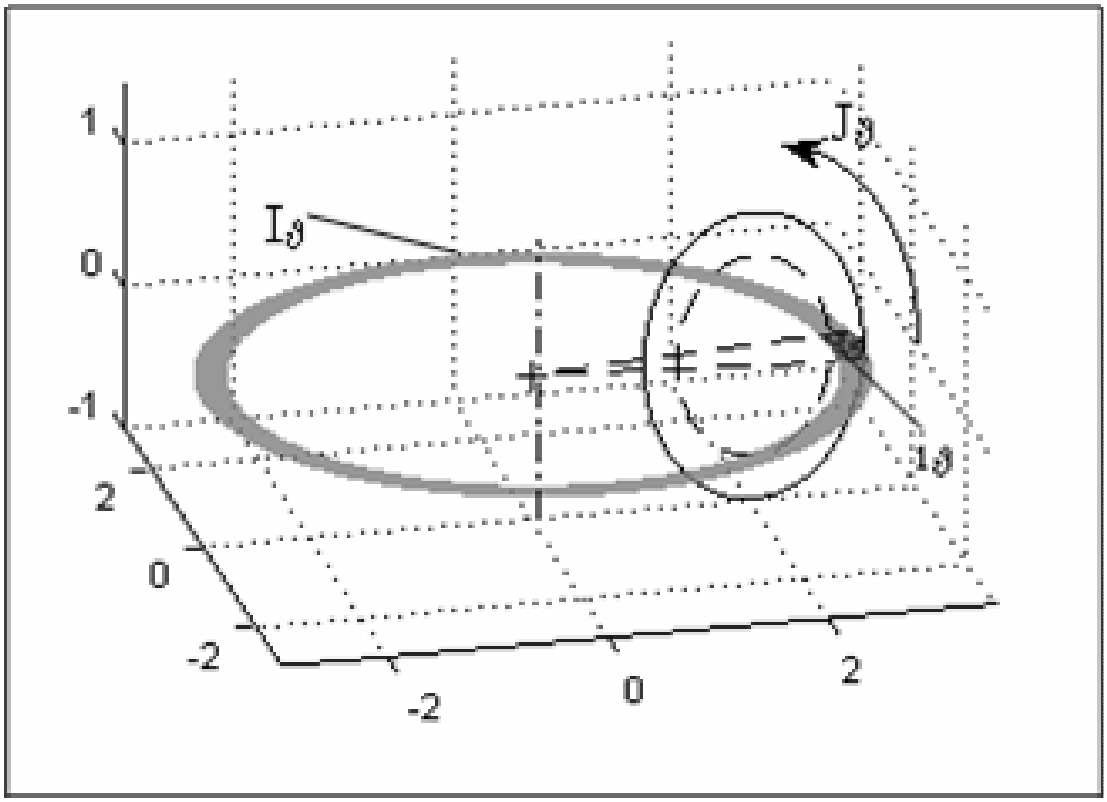

Figure 5. Sketch of the area for the evaluation of the poloidal current flux I_ϑ.

In Figure 5 is shown the grey area where the poloidal current flux is evaluated. For given angles ϑ and φ, the line to the plasma surface r_s from the outer surface r_{min} is rotated along the axis of symmetry. In such a way an area is defined which is orthogonal to the poloidal component of the density current J_ϑ, at the equilibrium. The value I_ϑ of the current flowing through this poloidal section is evaluated as follows:

(15) $$J_\vartheta = \frac{J_{\vartheta 0} R_{maj}}{R_{maj} + r \cdot \cos\vartheta}$$

(16) $$I_\vartheta = \int_0^{2\pi} \left(R_{maj} + r \cdot \cos\vartheta\right) d\varphi \int_{r_S}^{r_{min}} dr \frac{J_{\vartheta 0} R_{maj}}{R_{maj} + r \cdot \cos\vartheta} = 2\pi J_{\vartheta 0} \cdot \delta \cdot R_{maj}$$

$J_{\vartheta 0}$ is the poloidal component of the plasma current density at the plasma axis. The poloidal current flux does not depend on the angle ϑ.
The infinitesimal value of the Poloidal current i_ϑ flowing through an infinitesimal section defined by $d\varphi$ is evaluated as follows:

(17) $$i_\vartheta = \frac{dI_\vartheta}{\left(R_{maj} + r_S \cos\vartheta\right) d\varphi} = \frac{J_{\vartheta 0} R_{maj}}{R_{maj} + r_S \cdot \cos\vartheta} \int_{r_S}^{r_{min}} dr \cong \frac{J_{\vartheta 0} R_{maj}}{R_{eff}} \delta$$

For small values of δ.

In case of a simple VDE, the model of the plasma does not vary its shape and the spatial distribution of the plasma current density is similar to that described above. The MHD modes are seen as rigid displacement of the plasma, and the poloidal and the toroidal current flowing through two plasma surfaces are kept constant. So, when some MHD modes are unstable the spatial distribution of the density current can be modified, but the infinitesimal values of the poloidal i_ϑ and toroidal current fluxes can be evaluated with the (14) and (17) formulae. The functions i_ϑ and i_φ here presented are similar to the poloidal and toroidal current flux function discussed in section 3.3, chapter V; even though they are defined having a zero value at the edge of the plasma and not at the plasma axis.
In the following, several simulations will be presented with a safety factor q= 1,5 and a plasma current density J_0= 1,38 A/mm^2 . The value of J_0 has been evaluated by eq. (12), imposing an overall plasma current I_p= 10 MA, and a uniform current density profile. The plasma current is evaluated as the maximum value of the toroidal current flux. It is worth noticing also that the corresponding value of poloidal current I_ϑ is almost larger than the plasma current I_p reported before. In fact, I_ϑ can be evaluated by eq. (16) considering $I_p = I_\varphi$, so by the eq. (5) it can be found that

(18) $$\frac{I_\vartheta}{I_\varphi} = \frac{2\pi \cdot J_{\vartheta 0} \cdot r_{min} \cdot R_{maj}}{\pi \cdot J_{\varphi 0} \cdot r_{min}^{\ 2}} = \frac{2}{q} = 1{,}25$$

The maximum amount of the poloidal current flux is equal to $I_{\vartheta,M}$=12,5 MA.
We consider two case. In the first case a pure VDE occur whose radial and vertical displacements are described in Table 1. In the second case, a (2,3) MHD perturbing mode with amplitude $\Delta_{2,3}$= 25 % is superimposed to the VDE, as described in Table 1.

Table 1. Parameters considered for the VDE and the MHD mode.

ΔR [m]	**Δz [m]**	**r_{close} [m]**	**Halo width [%]**	**$\Delta_{2,3}$ [%]**
-0.4	**3.2**	**1.014**	**50**	**25**

In Figure 6, the cross section of the First wall (blue lines) is shown together with the cross section of the last close plasma surface (green line) and finally the cross section of the outer plasma surface hitting the First wall (red line). In order to show the effects of a perturbation the last closed plasma surface has been represented without adding the effects of a perturbation, while these effects have been added drawing the outer plasma surface.

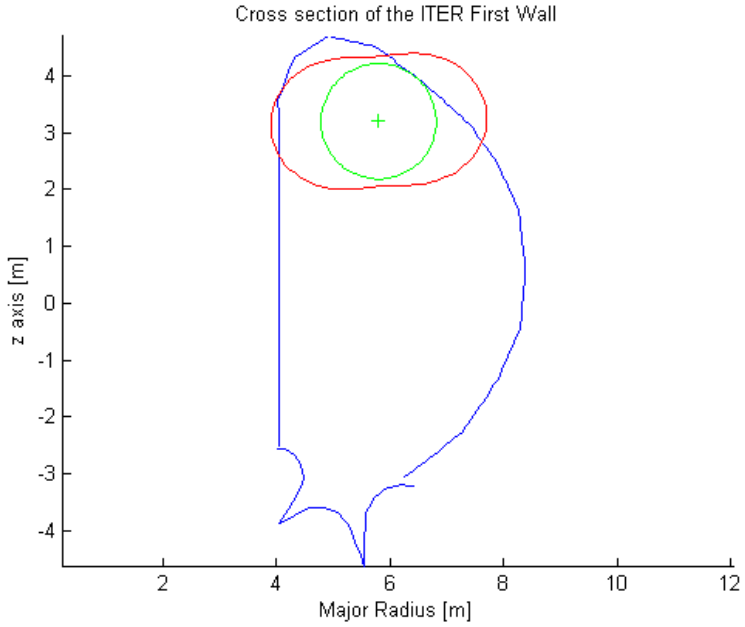

Figure 6. Cross section of the ITER First wall. The green circle represents the unperturbed last close plasma surface. The red line represents the outer plasma surface hitting the wall affected by a (2,3) mode of magnitude $\Delta_{2,3}$= 25 %.

3. Three codes calculating the Halo current distributions

Three codes are here presented which evaluate the Halo Current distribution in ITER.
The first code is named as the Geometrical code; it calculates the actual distribution of the plasma current density to evaluate the Halo density current injected on the first wall and, after an integral, the total amount of Halo Current injected on each module of the First Wall. The second code evaluates directly the Halo Current injected on each module using the poloidal i_ϑ and toroidal i_φ current flux functions defined in section 2.1. This code performs the calculation in shorter time than the first and we can refer to it as the Fast code. The last code evaluates the Halo current distribution under the condition of a pure VDE, when the plasma is not affected by any MHD perturbing mode and the Halo current distribution enjoys the toroidal symmetry. In this case the calculations are performed in a very short time and we can name it as the Ultra-fast code.

3.1 Geometrical Code

For each point of the First wall module, the toroidal coordinates $(r_p,\vartheta_p,\varphi_p)$ are evaluated with respect to the plasma axis. The value of r_p is compared with $r(r_{min}, \vartheta_p,\varphi_p)$, see eq. (2).
If $r_p > r(r_{min}, \vartheta_p,\varphi_p)$, there is no contact between the plasma and the First wall in the present point. Elsewhere the value of r_s' which satisfies $r_p = r(r_s',\vartheta_p,\varphi_p)$ is evaluated.
Finally, the plasma density current vector $\mathbf{J_{plasma}}$ entering or exiting the First wall in the present point is evaluated using the $(r_s',\vartheta_p,\varphi_p)$ coordinates.

The unit vector **n** orthogonal to the first wall in the point under consideration is evaluated. The amount of Halo current density injected $J_\perp$ on the present point is:

(19) $$J_\perp = \mathbf{J}_{plasma} \cdot \mathbf{n}$$

The scalar product of the vectors above defined.
Finally, the overall amount of the Halo Current injected in a module is evaluated integrating the values of $J_\perp$ in all points of the module, as in eq. (9) in section 1.4, chapter V.
The overall structure of the ITER first wall together with the perturbed plasma surface is shown in Figure 7.

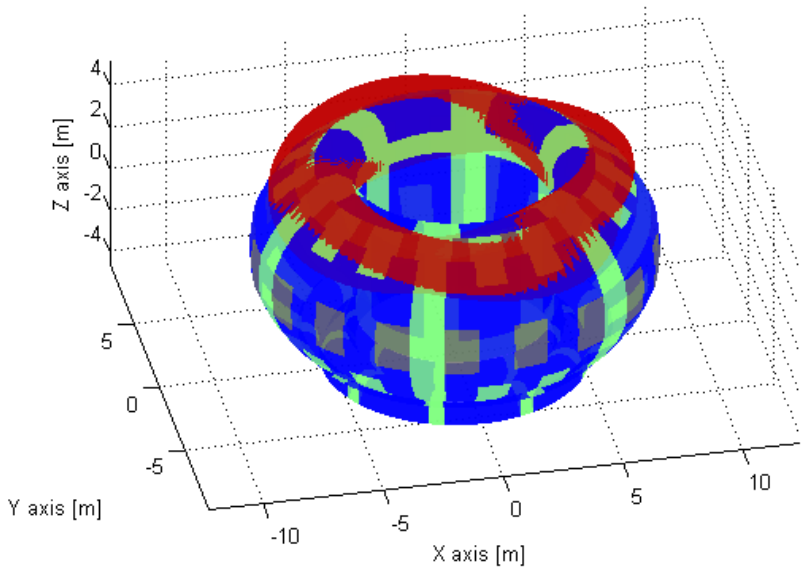

Figure 7. ITER first wall and perturbed plasma surface (red surface). The port surfaces are depicted in black, the modules equipped with Halo sensors are depicted in green, the modules without Halo sensors are depicted in blue.

In Figure 7 all First wall is shown where ports, modules with or without equipment are drawn with different colours. The equipped modules are depicted in green, the ports are depicted in black and the modules without equipment are depicted in blue.
Results from the present code are here discussed for the asymmetric VDE case reported in Table 1. The Halo currents injected on the modules are reported in Figure 8. The Halo current values range from -470 kA to 320 kA. Negative signs refer to Halo currents exiting from the First Wall while the positive values refer to Halo currents entering in the First wall. In such a way, the entering and the exiting values constitute the sources and the sinks of the Halo currents flowing through the Vacuum Vessel structure.
The overall amount of Halo current injected is equal to 9.96 MA.
The ITER first wall can be thought as a close surface and the current distribution should satisfy $\nabla \cdot \mathbf{J} = 0$. The algebraic sum of all values of Halo currents injected, either on the ports and on the modules, is less than 1% of the plasma current. This error is probably due to the resolution of the First Wall mesh, and can be considered as acceptable.

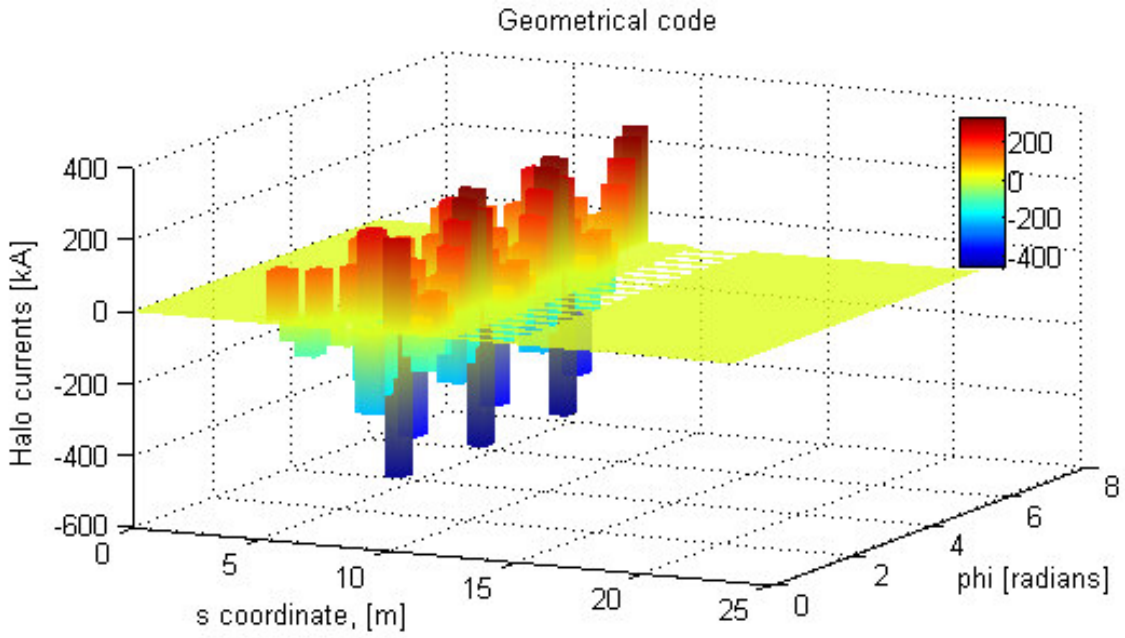

Figure 8. Halo currents injected in all modules. Colours are related with the amplitude of the Halo current injected on each module. The Halo current values range from -467.1 kA to 321.5 kA.

3.2 Fast code

A Fast code able to evaluate the Halo currents injected on each module has been implemented. It does not need to evaluate the Halo current density on the overall First Wall but a model of the plasma current density satisfying $\nabla \cdot \mathbf{J} = 0$ is necessary.
The model of the plasma hitting the wall is a first order model because it does not take into account the deformation of the shape due to the contact of the plasma with the wall. Therefore, the outer plasma surface can be ideally extended over the First Wall, as shown in Figure 7. It is an isoflux surface and the current flowing through it is zero. For each module, two poloidal sections and two toroidal sections can be built from the horizontal and the vertical borders of the module surface respectively to the outer plasma surface. So, a volume is defined into the two poloidal and the two toroidal surfaces, the module surface and a part of the outer plasma surface, a sketch of this volume with its six faces is shown in Figure 9. The blue surface represents the module surface and the red surface is the interested part of the outer plasma surface. The green surfaces represent the two toroidal sections lying on two planes with φ constant and intersecting the vertical borders of the module. The toroidal plasma current fluxes $I_{\varphi,1}$ and $I_{\varphi,2}$ entering and exiting in this volume are evaluated on these surfaces. The two surfaces representing two poloidal sections are not represented in Figure 9, in order to make the figure readable. The poloidal plasma current fluxes $I_{\vartheta,1}$ and $I_{\vartheta,2}$ entering and entering in the volume are evaluated on these surfaces.
Since $\nabla \cdot \mathbf{J} = 0$, the current injected on the module can be evaluated by the balance of the currents entering and exiting in this volume:

(20) $$I_{HC} + I_{\vartheta,1} + I_{\varphi,1} = I_{\vartheta,2} + I_{\varphi,2}$$

The amount of the currents flowing through the poloidal and the toroidal surfaces can be evaluated integrating on each border of the module surface the infinitesimal value i_ϑ and i_φ of the poloidal and the toroidal current fluxes, as defined in eqs. (17) and (14) respectively.

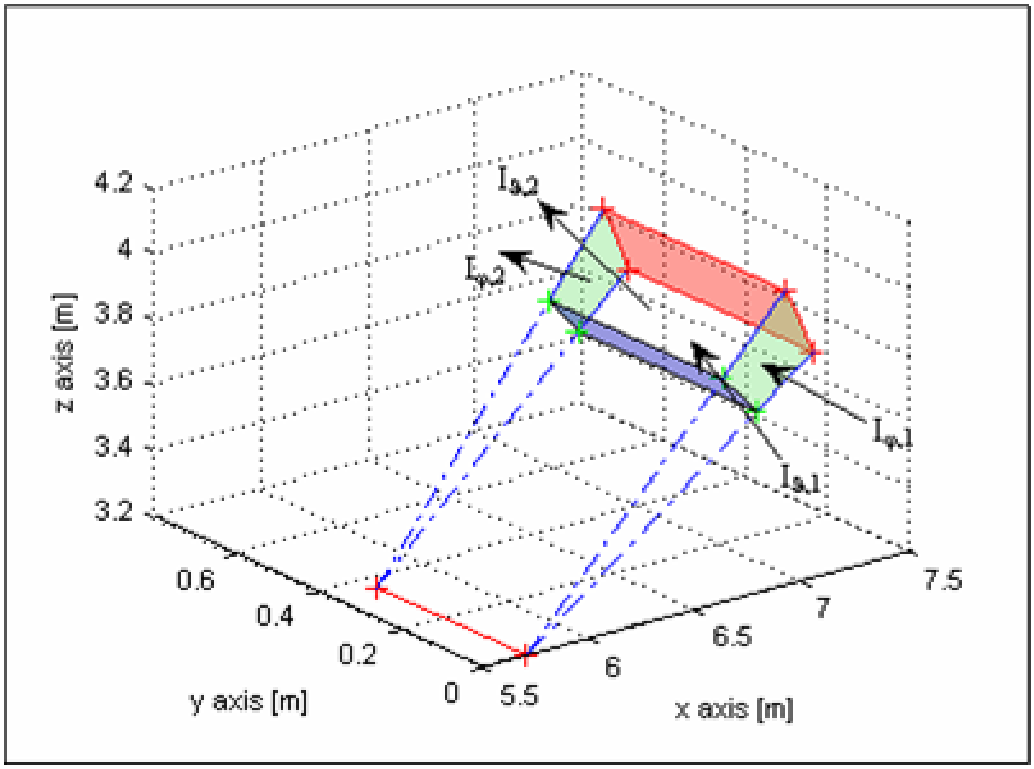

Figure 9. Sketch of the volume built around the border of a module (black lines). Red surface represents a part of the outer plasma surface, no current is flowing through this surface. The green surfaces represent the toroidal sections where the toroidal current fluxes $I_{\varphi,1}$ and $I_{\varphi,2}$ are evaluated. The poloidal sections where the poloidal current fluxes $I_{\vartheta,1}$ and $I_{\vartheta,2}$ are evaluated are not represented here. The amount of current flowing through the module surface can be evaluated by the balance of the currents entering or exiting from the volume, eq. (20).

In Figure 9, the black lines represent the border of the module surface. These lines are meshed. For each point on the border it is evaluated if the plasma hits the wall in this point, as described for the Geometrical code in section 3.1. The value of r_s' is evaluated for each point on the border, and if $r_s' < r_{min}$ the value of i_ϑ or i_φ is evaluated by eq. (17) or (14) if the point lies on a horizontal or on a vertical border respectively. Toroidal and poloidal current fluxes are evaluated on each border by integration.

Vertical borders of the module lie on a plane with constant φ. Each point on the vertical border can be labelled by the coordinate s, and it is seen by an angle ϑ'(s) from the plasma

axis. Each point intersects a different plasma surfaces $r_s'(s)$. So, the infinitesimal toroidal current flux depends on the s coordinate: $i_\varphi(s)$. The toroidal current I_φ flowing through each toroidal section is evaluated by the following integral:

$$I_\varphi = \int_{s_1}^{s_2} i_\varphi(s) \cdot ds \tag{21}$$

In equation (21) it is approximated $ds \approx r_s d\vartheta$.
The two poloidal surfaces lying on the planes with ϑ constant and intersecting the horizontal borders of the module are not represented in Figure 9. The poloidal plasma current fluxes $I_{\vartheta,1}$ and $I_{\vartheta,2}$ are evaluated on these surfaces.
Horizontal borders of a module lye on a plane with ϑ, s and the major radius R constants. Each point on the horizontal border can be labelled by the angle φ, and the infinitesimal poloidal current flux generally depends on φ: $i_\vartheta(\varphi)$. So, the poloidal current I_ϑ flowing through this section is evaluated by integrating:

$$I_\vartheta = \int_{\varphi_1}^{\varphi_2} i_\vartheta(\varphi) \cdot R d\varphi \tag{22}$$

Finally, the code evaluates the amount of Halo Current injected on the module by eq. (20).
For the asymmetric VDE case reported in Table 1, the results from the Fast code are here discussed. The Halo current values range from -3890 kA to 280 kA. The overall amount of Halo current injected is equal to 8.9 MA. The algebraic sum of all values of Halo currents injected, either on the ports and on the modules, is -2.2 A. The percentile of this residual value with respect to the overall amount of Halo current injected can be neglected.
In Figure 10, the results from the Fast code are reported only for the equipped modules.

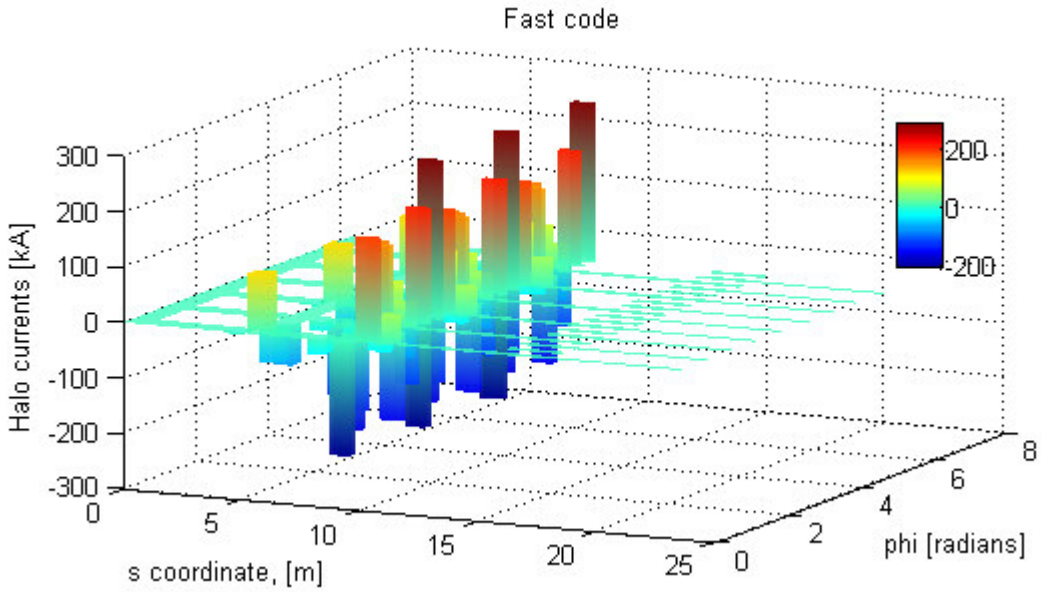

Figure 10. Results from the Fast code. Halo Current values injected on the equipped modules. Note that these values range from – 207.9 kA to 283.4 kA, but the minimum value of current injected when all modules are taken under consideration is -387.8 kA.

3.3 Ultra Fast code

In case of a plasma affected by a symmetric VDE, that is without any destabilized MHD mode, the Halo Current distribution does not depend on φ, since the toroidal symmetry. The values of $I_{\varphi,1} = I_{\varphi,2}$ are equal one another, and their contribution can be neglected in eq. (20). Moreover, from the toroidal symmetry the infinitesimal values of Poloidal current fluxes i_ϑ do not depend on φ and are constant on each horizontal border of the module. So, the I_ϑ values can be easily evaluated considering only few points on a cross section of the ITER first wall. In Figure 11 is reported the ITER cross section. The crossed points are the border of each module. For the m-th module, i_ϑ is calculated on the two border points of each module. The Halo Current injected in the module is easily evaluated as:

$$I_{HC,m} = \left[i_{\vartheta,2} \cdot R(2) - i_{\vartheta,1} \cdot R(1) \right] \cdot \Delta\varphi \tag{23}$$

In equation (23), R(i) is the major radius coordinate of the i-th point and Δφ is the spacing along φ of the module. Moreover, $i_{\vartheta,2} \cdot R(2) - i_{\vartheta,1} \cdot R(1)$ is equal for each module on a horizontal line.

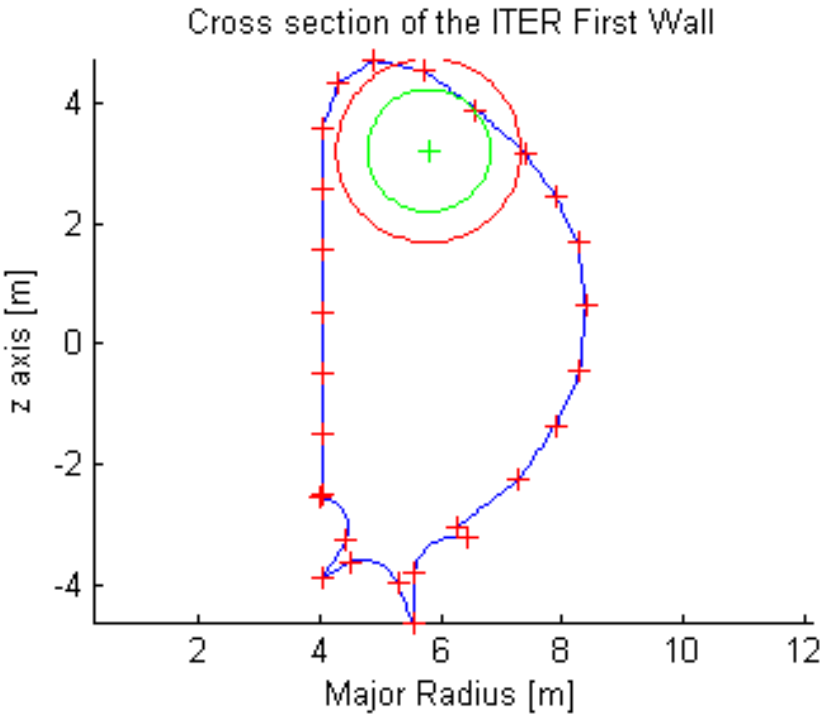

Figure 11. Cross section of the ITER First wall and of a plasma affected by a symmetric VDE. Crossed points are the border points of the cross section of each line of modules. Ultra Fast Code evaluates the Halo Currents injected on the First Wall taking under consideration only the ticked points.

This code has been tested for a symmetric VDE, whose displacement values and the Halo width are reported in Table 1. Moreover, it has been tested also in case of the asymmetric

VDE to compare its results with results from 3D codes. The comparison of the results is reported on the next sections.
For the symmetric VDE the Halo current injected on the First wall range from -97 kA to 113 kA. The overall amount of Halo current injected is equal to 4.1 MA, this value is in good agreement with the one third of the maximum Poloidal current flux (12.5 MA), that is in good agreement with an evaluation of the Halo current on the basis of the Halo width. The sum of all values of Halo currents injected, both on the ports and on the modules, is almost zero (on the order of nA). The percentile of this residual value with respect to the overall amount of Halo current injected is about 10^{-13} %, that is on the order of numerical errors.
In Figure 12 the results from the Ultra Fast code are reported on the First Wall modules.

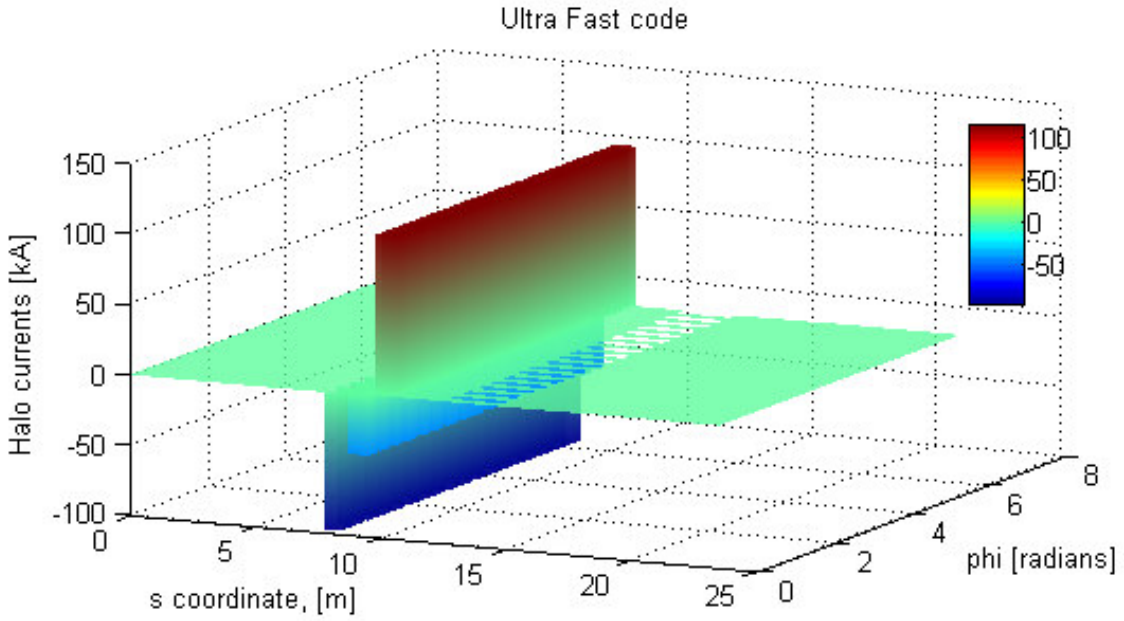

Figure 12. Results from the Ultra Fast code for a pure VDE, as depicted in Figure 10. Results for the modules are here reported.

4. Comparison between the codes

The three codes above presented spend different computational time to get out their estimations since the different computational strategies. The Geometrical code performs its calculation for each point on the overall mesh of the ITER First Wall. Each module is meshed in a matrix of points. Let N be the number of points in each border of the module, after the mesh of module. Therefore, the module is meshed with N^2 points. Consider that all points are meshed with an equal number of points. Therefore, the number of the calculations growth as N^2. Generally, the number N depends on the resolution of the mesh and can differ module by module.
The Fast code performs its calculations only for the points lying on the border of the modules. So, the complexity of the algorithm depends on the mesh of the module perimeter and it growths as $2 \cdot N$.
In present simulations the mesh of the First wall is given with a resolution of $\Delta s = 10$ cm. In this case, N=10 is the average number of points lying on a border of all modules, so the Fast code should be about five time faster than the Geometrical code.
Performing the two codes on the same machine, the Geometrical code spends about two minutes and the Fast code spends half a minute to carry out the same results, that is to say the Fast code is about four times faster than the Geometrical code.
Finally, the Ultra Fast code works on the basis of a cross section taking into account only the border points of each module, as shown in Figure 11. So, it evaluates the Halo current injected on the overall First Wall taking into account only 19 points (for Blanket modules) plus 8 points (for the Divertor). Its computational time is really little taking less than half a second.
Nevertheless, it has to be noted that the use of the Ultra Fast code is restricted to the pure symmetric VDE cases. Moreover, it shall be noted that the Geometrical code is able to get out also the patterns of Halo current density injected on each module surface, while the Fast code can evaluate only the overall Halo current injected on the module. The Fast code can be made able to evaluate also the Halo Current density distribution, but its computational time should become greater than the computational time of the Geometrical code (considering the same resolution of the mesh).
The Ultra Fast code performs its calculations using the same equations of the Fast code; it differs from the Fast code because it performs the calculations in a limited case and on the basis of a little number of points.
These three codes have been tested in the asymmetric VDE case reported in Table 1. Moreover, they have been tested also in a pure VDE case with the same vertical and radial displacements and the same Halo width of the asymmetric VDE case, but the amplitude of the (2,3) MHD perturbing mode is here reduced to zero. The results obtained by the three codes on these two cases are reported in Table 2.

Table 2. Results from the codes in case of both a pure VDE and an asymmetric VDE. The maximum and minimum values (max and min respectively), the Overall amount of Halo current entering or exiting from the First wall (Overall) and the residual evaluated summing all evaluations of Halo currents injected (Residual) are reported.

Codes	PURE VDE				ASYMMETRIC VDE			
	max	min	Overall	Residual	max	min	Overall	Residual
Geometrical	**129,7 kA**	**-104,7 kA**	**4,81 MA**	**-284,4 kA**	**321,4 kA**	**-467,1 kA**	**9,96 MA**	**38,34 kA**
Fast	**113,4 kA**	**-97,4 kA**	**4,08 MA**	**≈ nA**	**283,4 kA**	**-387,7 kA**	**8,9 MA**	**-2,2 A**
Ultra Fast	**113,4 kA**	**-97,4 kA**	**4,08 MA**	**≈ nA**	**163,2 kA**	**- 84,7 kA**	**5,9 MA**	**≈ nA**

With the aims to compare the codes, each Halo current distribution evaluated by a code has been collected in an array. It is convenient to introduce the following symbols:

G array of the values of Halo currents calculated by the Geometrical code;
F array of the values calculated by the Fast code;
U array of the values calculated by the Ultra Fast code.

Moreover, in order to compare the coherence between the patterns evaluated by the Geometrical and the Fast codes, the **F** array has been resized with an overprojection operation. On the basis of the values calculated for the equipped modules, shown in Figure 10, the **F** array has been "overprojected" on **G**, and the results is called as **F***.
The arrays are built in such a way to provide a one to one relationship between the terms of the array and the values calculated for a given module of the First Wall. So, the difference between the results from the codes can be evaluated as the total error ε defined in equation (24), section 3.2, chapter V. The total error $\varepsilon_{I,J}$ is defined as follows:

(24) $$\varepsilon_{I,J} = \sqrt{\|I - J\|^2 / \|I\|^2}$$

The results of these comparisons are reported in Table 3.

Table 3. Comparison of the Halo Currents evaluation carried out by the different codes.

Total errors	PURE VDE [%]	ASYMMETRIC VDE [%]
$\varepsilon_{G,F}$	**13,7**	**26,9**
ε_{G,F^*}	**5,9**	**13,0**
$\varepsilon_{F,U}$	**$\approx 10^{-13}$**	**98**

The comparison between the results of the Geometrical and the Fast code shows that the two codes give almost the same value of Halo Current injected on each module with a average error of about the 20%. These errors are strongly reduced after the overprojection of **F** on **G**, showing that the patterns are similar one another with a medium error of the 10%. So, a Reconstruction procedure can be tested using these two codes, how has been carried out in the simple case reported on the first section.
The comparison between the Fast and the Ultra Fast codes shows that they evaluate the same value of Halo currents injected on each module in case of a pure VDE. In fact, only numerical errors occur in this case. In case of asymmetric VDE, strong differences between the codes rise up to errors equal to the 98%. That is the single values of Halo current injected on each module as well as the overall Halo current distribution estimated by the codes are strongly different. This value can be thought as an estimate of the error occurring when the Halo current distribution due to an asymmetric VDE is approximated with one due to a pure VDE.

5. SUMMARY

A numerical model of the ITER First Wall has been developed. Afterward, three different codes evaluating the Halo current distributions have been designed and the results have been compared.
The model of the plasma is analytical. At beginning, the plasma is in a condition of quasi equilibrium having a circular cross section (i.e., without any elongation), whose centre is located at the centre of the cross section of the ITER first wall. Afterward, the plasma can suffer of a simple Vertical Displacement Event, i.e., it is shifted of a radial and vertical displacement, or of a VDE plus an MHD instability deforming the external plasma surfaces.
All of the plasma surfaces intersecting the First wall are taken into account in the Geometrical code. The Geometrical code (section 3.1) evaluates the plasma current density vector in a point of the first wall, and then, through purely geometrical consideration, the value of the Halo current density injected in the point. The Halo current distribution is evaluated by integrating the Halo current density pattern on each module.
The Fast code (section 3.2) takes into account only the points lying in the borders of the module, reducing the number of calculations to carry out and improving the speed of the algorithm.
The Ultra Fast code (section 3.3) performs the same algorithm of the Fast code, but in case of a symmetric VDE. So, the Ultra Fast code takes into account only few points belonging to a cross section. It spends about half a second against the computational time of few minutes spent by the Geometrical and the Fast code.
The results from different codes have been compared showing a good agreement between the codes. In fact, the results from the Fast code and the Geometrical code differ less than the 30%. The difference between the patterns has been estimated to be less than the 15%.
The estimate of the Halo Current injected scale as a function of the Halo width in case of a pure VDE. In case of asymmetric VDE the dependence of the Halo current on the Halo width and on the amplitude of the perturbing MHD modes should be investigated, because the overall amount of halo current injected in this case is about two times those in the case of a pure VDE with same Halo width, radial and vertical displacements.
In case of an asymmetric VDE, the comparison between the results from the Fast code and the Ultra Fast code highlights the large error occurring when one Halo current distribution due to an asymmetric VDE is approximated with one distribution due to a pure VDE (errors of about the 98%).

CONCLUSIONS

In the framework of a study aimed at assessing the ITER diagnostic system ability to reconstruct the Halo current distribution in the vessel, my PhD research activity was initially aimed to define a reconstruction procedure for the Halo current distributions on the basis of a simple model. This activity reached its aims, as discussed in chapter II. The development of the 3D models presented in chapter III is a carrying on of this activity, necessary for a further development of the reconstruction procedure on the basis of realistic simulations of the Halo current distributions in ITER.

The development of a reconstruction procedure for the Halo current distributions in ITER requires several steps. During this path, I obtained the results here reported.
The first result was the development of a reconstruction procedure for the Halo current distribution in an ideal Tokamak. The development of this procedure is presented in chapter II. An algorithm has been developed on the basis of an operation called "overprojection". This algorithm compares the Halo current data with a set of predefined Halo current patterns, and evaluates an estimate of the distribution of Halo current injected in all the first wall modules "overprojecting" the data on that predefined pattern which best fits the data themselves.
This reconstruction procedure has been tested under the following conditions:

- single-mode perturbation;
- first wall with circular cross-section.

The error of the algorithm was found acceptable (<30%). Moreover, the procedure works well also in presence of a noise having the same amplitude of the noise foreseen for the Halo diagnostics in ITER.
In spite of its operational limits, the algorithm seems to be the most appropriate for a further application to more general conditions, in particular to ITER-like data.

So, the second part was aimed to develop some 3D models able to calculate the Halo current distribution on an accurate model of the ITER first wall, since similar algorithms were not yet available. At present, the predictions of the mechanical loads induced by the Halo currents are based on the results of 2D simulation codes as MAXFEA [18] or DINA [19].
Three codes working on the basis of a numerical model of the ITER first wall have been developed as reported in chapter III. These codes showed to be in good agreement one another, and are suitable to further developments of a reconstruction procedure in ITER.
Nevertheless, these 3D models can be used also to develop a procedure able to evaluate the diffusive paths of Halo current into the vacuum vessel of ITER. Such a procedure shall include a model of the ITER vacuum vessel, and requires as inputs the knowledge of the time history of the magnetic field (provided by the magnetic diagnostics located in and out the vessel) surrounding the structure as well as the time history of the Halo current injected in all the blanket modules. With the aims of developing such a procedure, simulations can be carried out using the Halo current distributions provided by the three codes. In fusion experiments, the actual Halo current distribution has to be estimated by a reconstruction procedure.

PART II

REALIZATION OF AN ACTIVE MAGNETIC SHIELD IN OPEN LOOP

The RFX experiment, a magnetic confinement fusion device operating in Padua since 1991, is located in the building of the IGI (Istituto Gas Ionizzati) in the Research area of the CNR. In the same area, about 150 meters far from the IGI, are installed (at present) two Nuclear Magnetic Resonance spectrometers at the ICIS (Istituto di Chimica Inorganica e delle Superfici) institute.
Already in 1998, when the current in the RFX experiment was increased over 25kA, a peculiar electromagnetic compatibility problem was found with the NMR spectrometer. The anomalies were correlated to the presence of the magnetic field created by the RFX main windings, necessary to initiate the hot plasma discharge, which is lower than 3 μT (less than one tenth of the hearth magnetic field), owing to the distance between the two premises, and it is slowly varying with characteristic times of 100 ms – 1s.
A careful investigation was undertaken in order to identify the interference mechanism. Several experiments on the susceptibility of different NMR spectrometer have been done in the 1998 and 1999. In spite of the difference in compensating an external stray magnetic field - all of the NMR spectrometer showed that an extremely low field (a sensibility threshold could be 0.1 μT) and slowly varying (0.1 to 3 Hz) is enough to corrupt the measurements-, it has been concluded that such type of spectrometer is unable to compensate for external field interferences if they have significant harmonics in a well-defined range, spanning from 0.1 and 3 Hz. Pulsed magnetic confinement fusion experiments, as RFX, emit a field to which spectrometer are very sensitive, especially when the perturbing field is present during the critical phases of the measurement cycle.

In 1999, the project of an active shield has been individuated as the best mitigating measure (other mitigating measures could be the installation of a passive shield or to move away the NMR spectrometer further than 500 meters from RFX). So, a prototype shield has been realized [20] and tested. The prototype was driven by a feedback system based on a localsensor, in which a measurement probe is present near the spectrometer and senses the perturbing field. Tests with this prototype on a CRT monitor, a device that is typically disturbed by the RFX pulses, showed the effectiveness of this mitigating measure as well as the main issues related to this solution. In fact, a similar solution required a very sensitive probe, able to select the RFX field signal among all the other fields of various origins always present but not affecting the spectrometer. Tests showed the main drawbacks of such a control, shifting the initial choice to an “open loop” configuration.
In 1999, a large fire stopped the experiments of RFX as the project here presented.
At the end of 2004 RFX came back in operation, and during 2005 the pulses energy has been increased. As a consequence, the interferences were observed again raising the needs of a definitive solution.
In the 2005, I was following the one year Master in “Ingegneria e Fisica dei Plasmi” at the University of Padua. Prof. Giuseppe Chitarin proposed me to find a transmission system

suitable to send a control signal from RFX to the spectrometer as final work for the stage related to the Master [21].
In the following years, I worked as PhD student on the design of the definitive system, its realization, and test.

In this part of my PhD thesis, the main concepts underlying the project are briefly reported in chapter IV together with brief review on the NMR spectroscopy and on the RFX experiment. Moreover, the results of the susceptibility test on a NMR spectrometer are reported. Finally, different strategies to compensate a stray magnetic field are discussed.
In chapter V, I present the block-scheme of the compensation system based on an active magnetic shield, discussing the design and the realization of each block.
In chapter VI, I report the results of all the tests carried out, starting from preliminary tests done at RFX using the prototype shield [20], up to the definitive tests in situ near and on the NMR device.

CHAPTER IV

Magnetic disturbance induced by RFX on a NMR instrumentation

In this chapter the principles of the NMR spectroscopy are reviewed in section 1. A quick overview of the RFX experiment is presented in section 2 aimed to introduce the magnet system of the machine. Section 3 summarizes the main results of an intense experimental activity carried out during the 1998 to the 1999, aimed to characterize the susceptibility of a typical NMR instrumentation. The strategies suitable to compensate the magnetic disturbance induced by RFX are discussed in section 4. In section 5, a summary of the present chapter is reported.

1. Nuclear Magnetic Resonance (NMR) Spectroscopy [22]

NMR Spectroscopy is an experimental method which exploits the Nuclear Magnetic Resonance Phenomenon to study the interaction of electromagnetic radiation with matter and obtain information on physical, chemical, and biological properties of matter.

1.1 Nuclear Magnetic Resonance

The Nuclear Magnetic Resonance phenomenon is based on the property of some particles, from protons to more complex molecules like organic compounds, to possess a magnetic spin of the nuclei. When subjected to a strong magnetic field, spins are oriented towards a preferential direction, and a discretization of energy levels is observed.

1.2 Spin and Energy levels splitting by a magnetic field

The spin of the particle can be considered as a magnetic moment vector. When the particle is placed in an external magnetic field of strength B, the spin vector of the particle align itself with the external field, just like a magnet would. In a similar way, a low energy configuration or state can be distinguished from a high energy state depending on the alignment of the spin with the external field.
The energy gap E between these two states is directly proportional to B, as shown in Figure 1.

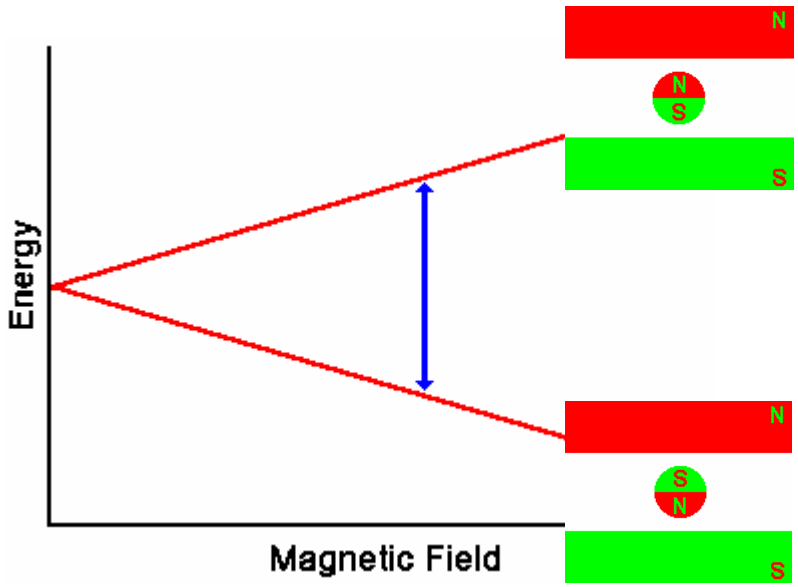

Figure 1 Energy levels splitting by a magnetic field. The splitting is directly proportional to the strength of the magnetic field.

When a group of spins is placed in a magnetic field, each spin aligns to one of the two possible orientations. The number of spins in the lower energy, N^+, outnumbers the number in the upper level, N^-, coherently with the Boltzmann statistics:

(1) $$\frac{N^-}{N^+} = e^{-\frac{E}{KT}}$$

Where k= 1.3805×10^{-23} J/Kelvin is the Boltzmann's constant and T is the temperature in Kelvin.
The signal in NMR spectroscopy is proportional to the population difference between the states. Note that at room temperature there are very small population differences. It is the resonance which makes NMR able to detect these small quantities.
When placed in a magnetic field, a molecule can undergo a transition between the two energy states by the absorption of a photon. A particle in the lower energy state absorbs a photon and ends up in the upper energy state. The energy of a photon is related to its frequency, ν, by Planck's constant (h = 6.626×10^{-34} J s) and must exactly match the energy difference between the two states to be absorbed. So, the frequency of the photon is related to the strength B of the external magnetic field by:

(2) $$\nu = \gamma B$$

where **γ** is the **gyromagnetic ratio** of the molecule, and characterizes a given molecule. For hydrogen, γ = 42.58 MHz/T.

1.2.1 Magnetization Vector

A spin packet is a group of spins experiencing the same magnetic field strength. At any instant in time, the magnetic field due to the spins in each spin packet can be represented by a magnetization vector. The size of each vector is proportional to $(N^+ - N^-)$. The vector sum of the magnetization vectors from all of the spin packets is the net magnetization. In order to describe pulsed NMR is necessary from here on to talk in terms of the net magnetization.
Adopting the conventional coordinate system, the external magnetic field B_0 is along the Z axis. At equilibrium the net magnetization vector, called the equilibrium magnetization M_0, is along the Z axis. So, there is no transverse (M_X or M_Y) magnetization here and the longitudinal magnetization (the Z component of the magnetization) M_Z equals M_0. It is possible to change the net magnetization by exposing the nuclear spin system to energy of a frequency equal to the energy difference between the spin states. If enough energy is put into the system, it is possible to saturate the spin system and make $M_Z=0$.
M_Z returns to its equilibrium with a time constant T_1 called the **spin lattice relaxation time**. T_1 constant can be defined as the time to reduce the difference between M_Z and M_0 by a factor of e.
If the net magnetization is placed in the XY plane it will rotate about the Z axis at a frequency equal to the frequency of the photon which would cause a transition between the two energy levels of the spin. This frequency is called the Larmor frequency.
The transverse magnetization M_{XY} returns to zero (its equilibrium value) with a time constant T_2 called the **spin-spin relaxation time**.
Both processes, described above, occur simultaneously with the only restriction being that $T_2 \leq T_1$.

1.2.2 Pulsed Magnetic Field

An alternate current being passed through a coil of wire placed around the X axis produces a magnetic field B_1 which alternates its direction along the X axis. In a rotating frame of reference travelling clockwise about Z at the same frequency ν_0 the B_1 field appears stationary with that, because the component of B_1 rotating counter clockwise at $2*\nu_0$ can be neglected. If ν_0 equals the Larmor frequency and the alternating current through the coil is turned on and off, it creates a pulsed B_1 magnetic field rotating around the Z axis. The spins respond to this pulse in such a way as to cause the net magnetization vector about the direction of the applied B_1 field. The rotation angle depends on the length of time the field is on and its magnitude B_1. Spectroscopic measurement is based on this response phenomenon.

1.3 NMR Spectroscopy

1.3.1 Chemical shift

When an atom is placed in a magnetic field, its electrons circulate about the direction of the applied magnetic field. This circulation causes a small magnetic field at the nucleus which opposes the externally applied field. The effective magnetic field B at the nucleus is therefore less than the applied field B_0 by a fraction σ.

$B = B_0 (1-\sigma)$

In some cases, such as the benzene molecule, the circulation of electron can enhance the B_0 field (deshielding). The electron density around each nucleus in a molecule varies according to the types of nuclei and bonds in the molecule. The opposing field and therefore the effective field at each nucleus will vary. This is called the **chemical shift phenomenon**.
Consider a molecule with different types of nuclei. Each type has its own resonance frequency which depends on the strength of the magnetic field B_0 and on the other nuclei forming the molecule. The resonance frequencies of two types of nuclei differ. This difference is proportional to B_0. This relationship could make it difficult to compare NMR spectra taken on spectrometers operating at different field strengths. The term chemical shift was developed to avoid this problem. The chemical shift of a nucleus is the difference between the resonance frequency of the nucleus and a standard. This quantity is reported in ppm and given the symbol δ:

(3) $$\delta = \frac{\nu - \nu_{REF}}{\nu_{REF}} 10^6$$

In NMR spectroscopy, this standard is often tetramethylsilane, $Si(CH_3)_4$, abbreviated TMS. The chemical shift is a very precise metric of the chemical environment around a nucleus. For example, the hydrogen chemical shift of CH_2 hydrogen next to a Cl (in a CH_2Cl molecule) will be different than that of a CH_3 next to the same Cl (in a CH_3Cl molecule).
Nuclei experiencing the same chemical environment or chemical shift are called equivalent, nonequivalent otherwise. Nuclei which are close to one another exert an influence on each other's effective magnetic field. This effect shows up in the NMR spectrum when the nuclei are nonequivalent. If the distance between nonequivalent nuclei is less than or equal to three bond lengths, this effect is observable in the NMR spectrum. This effect is called spin-spin coupling or J coupling.
Such an example, consider two nuclei, A and B, three bond lengths away from one another in a molecule. The spin of each nucleus can be either aligned with the external field or opposed to the external field. The magnetic field at the nucleus A will be greater than B_0 or less than B_0 by a constant amount due to the influence of nucleus B. There are a total of four configurations for the two nuclei in a magnetic field. In NMR, an allowed transition is one where the spin of one nucleus changes from spin up to spin down, or from spin down to spin up. Absorptions of energy where two or more nuclei change spin at the same time are not allowed. Arranging these configurations in order of increasing energy gives the diagram in Figure 2.

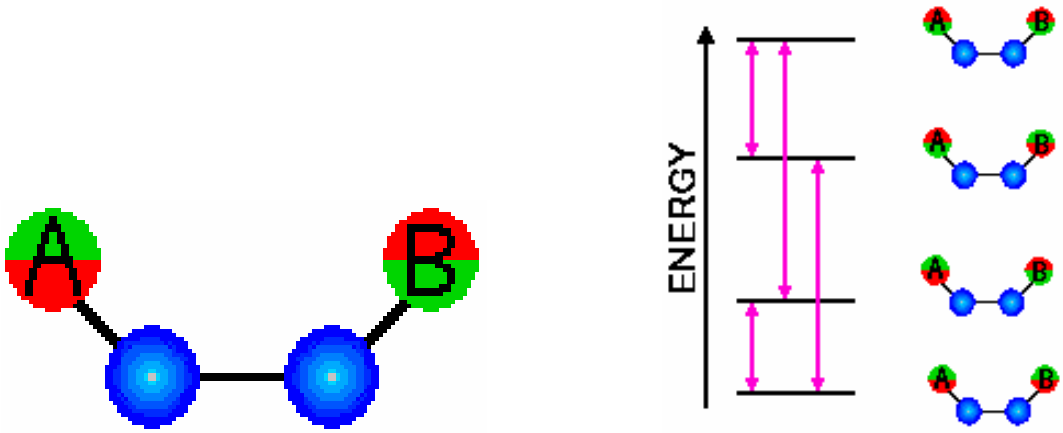

Figure 2 Left, a molecule with two nuclei far three bond lengths from one another. Right, allowed spin configurations for the molecule at left, the B field is oriented as in Figure 1.

In Figure 2, vertical lines between the energy levels represent the absorption frequencies allowed for the transitions.

1.3.2 FREE INDUCTION DECAY

An NMR sample may contain many different magnetization components, each with its own Larmor frequency. Based on the number of allowed absorptions due to chemical shifts and J couplings of the different nuclei in a molecule, an NMR spectrum may contain many different frequency lines.
Once a magnetization vector is in the XY plane it rotates about the direction of the B_0 field, the +Z axis. This rotation induces a current in a coil of wire located around the X axis. This signal has a time behavior similar to a sine wave decaying with a time constant T_2*. The decay is due to dephasing of the spin packets. This signal is called **free induction decay** (FID).
Figure 3 shows the magnetization vector M_{XY} rotating on the XY plane, and the time behavior of the signal induced on the coil.
The NMR spectrum is the Fourier Transform of this signal.

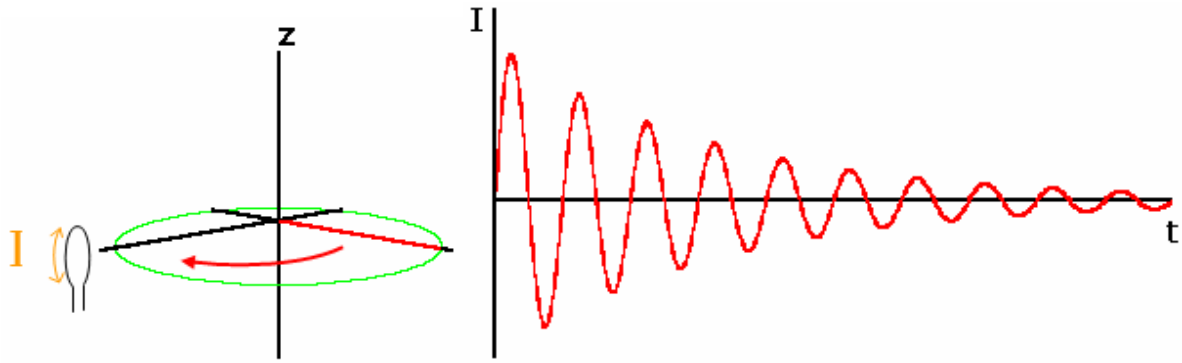

Figure 3 Left, M_{xy} rotation and current induced on the coil. Right, time behavior of the current signal in the coil (FID signal).

1.4 Layout of a typical NMR device

In Figure 4 is shown a schematic representation of the major systems of a nuclear magnetic resonance spectrometer and a few of the major interconnections. This overview briefly states the function of each component.

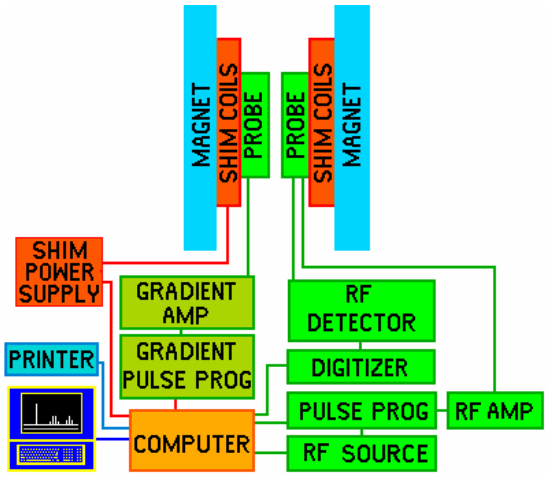

Figure 4 Main systems of a NMR instrument.

The superconducting magnet is shown at the top of the schematic representation, it produces the B_0 field. Immediately within the bore of the magnet are the shim coils for homogenizing the B_0 field. Within the shim coils is the probe.
The probe contains the RF coils for producing the B_1 magnetic field necessary to rotate the spins by 90^o or 180^o. The RF coils also detect the signal from the spins within the sample. The sample is positioned within the RF coil of the probe. Some probes also contain a set of gradient coils. These coils produce a gradient in B_0 along the X, Y or Z axis.
The heart of the spectrometer is the computer. It controls all of the components of the spectrometer. The RF components under control of the computer are the RF frequency source and pulse programmer. The source produces a sine wave of the desired frequency. The pulse programmer sets the width and in some cases the shape, of the RF pulses. The RF amplifier increases the pulses power from milliWatts to tens or hundreds of Watts. The computer also controls the gradient pulse programmer which sets the shape and amplitude of gradient fields. The gradient amplifier increases the power of the gradient pulses to a level sufficient to drive the gradient coils.
Next sections go into more detail concerning each system of a NMR spectrometer.

1.4.1 Magnet

The NMR magnet is one of the most expensive components of the nuclear magnetic resonance spectrometer system. Most magnets are of the superconducting type. A superconducting magnet is made of superconducting wire, which has a resistance

approximately equal to zero when it is cooled by liquid helium (4.2 K). Once the coil is energized, the current will continue to flow for as long as the coil is kept at liquid helium temperatures.
The coil and the liquid helium are kept in a large dewar. This dewar is typically surrounded by a liquid nitrogen (77.4 K) dewar, which acts as a thermal buffer between the room temperature air (293 K) and the liquid helium.

1.4.2 Field lock

In order to produce a high resolution NMR spectrum of a sample, especially one which requires signal averaging or phase cycling, a temporally constant and spatial homogeneous magnetic field is needed. A careful passive magnetic shield is aimed to protect the NMR spectrometer from typical AC fields at power line frequency and above. On the other side, the field strength B_0 might vary over time due to aging of the magnet, movement of metal objects near the magnet and temperature fluctuations. The field lock is aimed to compensate these slowly variations.
The field lock is a NMR spectrometer tuned to the deuterium NMR resonance frequency, within the main NMR spectrometer. It constantly monitors the resonance frequency of the deuterium signal coming from the deuterium solvent used to prepare the sample. It makes minor changes in the B_0 magnetic field to keep the resonance frequency constant, as a results B_0 is kept to a constant value.

1.4.3 Shim coils

The purpose of shim coils on a spectrometer is to correct minor spatial variations in B_0 magnetic field. These variations could be caused by the magnet design, materials in the probe, variations in the thickness of the sample tube, sample permeability and ferromagnetic materials around the magnet. A shim coil is designed to create a small magnetic field which will oppose and cancel out the small variations in the B_0 magnetic field. Because these variations may exist in a variety of functional forms (linear, parabolic, etc.), shim coils are needed which can create a variety of opposing fields. By passing the appropriate amount of current through each coil a homogeneous B_0 magnetic field can be achieved. The optimum shim current settings are found by either maximizing the size of the FID, or maximizing the signal from the field lock.

1.4.4 Sample probe

The sample probe is the name given to that part of spectrometer which accepts the sample, sends RF energy into the sample, and detects the signal emanating from the sample. It contains the RF coil, sample spinner, temperature controlling circuitry, and gradient coils.
The purpose of the sample spinner is to rotate the NMR sample tube about its axis. In doing so, each spin experience the average magnetic field in the circle defined by the position along the Z axis and the radius from the Z axis. The net effect is a narrower spectral line

width. Figure 5 show two spectra for samples experiencing one a homogeneous field and an inhomogeneous field. Broadening of the spectrum is due to the presence of lines from the parts of sample experiencing different B_0 magnetic fields. When the sample is spun about its z-axis, variations in the X and Y directions are averaged out and NMR line width becomes narrower.

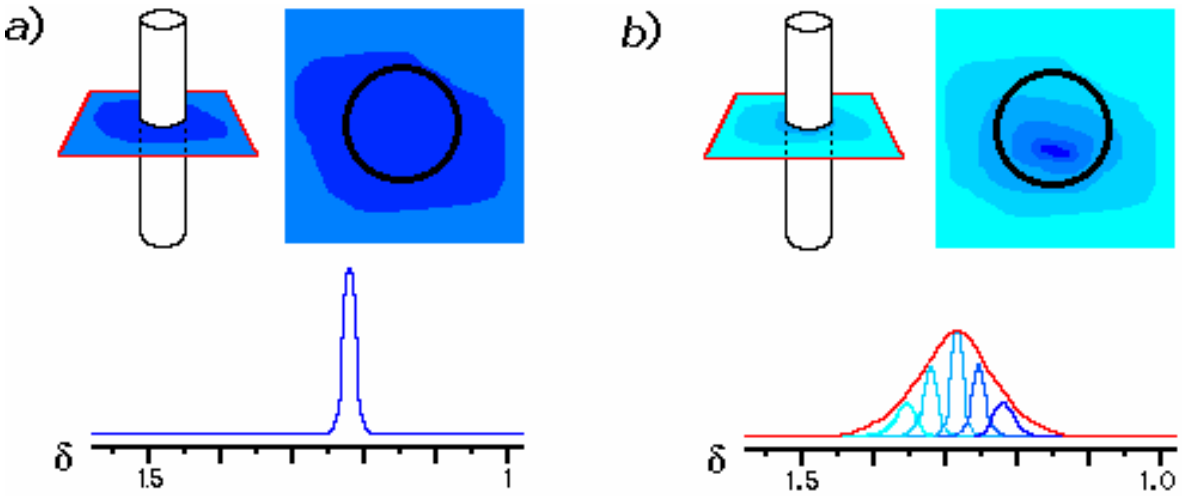

Figure 5 a) Spectrum of a sample embedded in a homogeneous field; b) Spectrum broadening due to an inhomogeneous field.

Some experiments need to examine properties of the sample as a function of temperature. As a result many instruments have the ability to pass air or nitrogen over the sample to heat or cool the sample. The temperature at the sample is monitored with the aid of a thermocouple and electronic circuitry maintains the temperature by increasing or decreasing the temperature of the gas passing over the sample.

1.4.5 RF coils

RF coils create the B_1 field which rotates the net magnetization in a pulse sequence. They also detect the transverse magnetization as it precesses in the XY plane. Most RF coils on NMR spectrometers are of the saddle coil design as shown in figure…

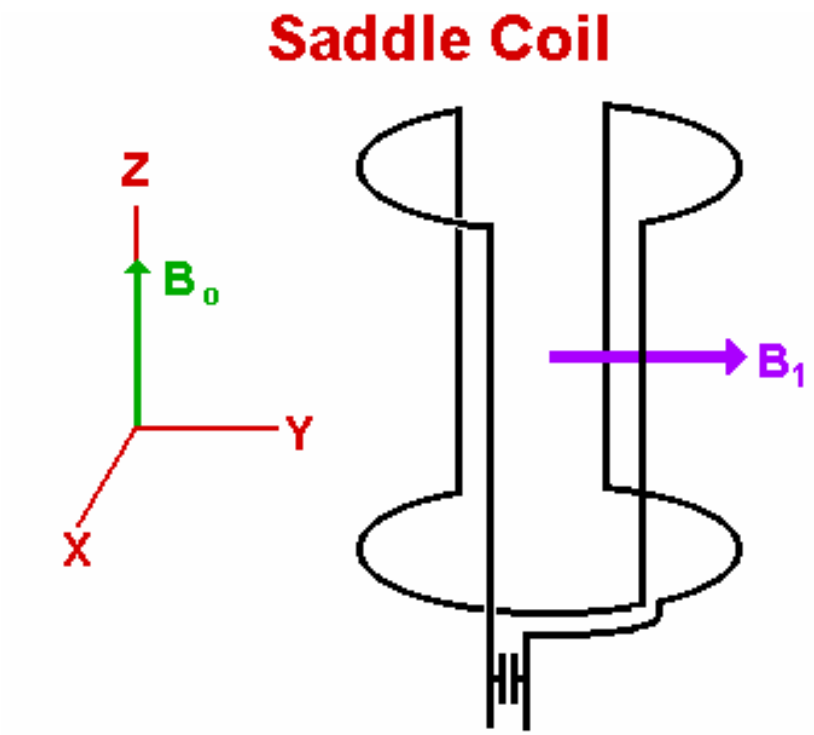

Figure 6 RF coils create the rotating B_1 field and sense the sample response.

Each of these coils must resonate at the Larmor frequency of the nucleus being examined. The resonant frequency is determined by the value of the inductance and capacitance of the circuit.
RF coils used in NMR spectrometer need to be tuned for the specific sample being studied. An RF coil has a bandwidth or a specific range of frequencies at which it resonates. The resonance frequency of a RF coil can be affected by the conductivity and dielectric constant of the sample. If this frequency is different from the resonance frequency of the nucleus under study, the coil will not efficiently set up the B_1 field nor efficiently detect the signal from the sample. The net magnetization will rotate by an angle smaller than expected, producing less transverse magnetization and less signal. Another requirement to be satisfied by an RF coil is that the B_1 field needs to be homogeneous over the volume of your sample.

1.4.6 Gradient coils

The gradient coils produce the gradients in the B_0 magnetic field needed for performing gradient enhanced spectroscopy, diffusion measurements, and NMR microscopy. The gradient coils are located inside the RF probe at room temperature. Assuming the standard magnetic resonance coordinate system, a gradient in B_0 in the Z direction is achieved with an antihelmoltz type of coil. Current in the two coils flow in opposite directions creating a magnetic field gradient between the two coils. The B field at the center of one coil adds to the B_0 field, while the B field at the center of the other coil subtracts from the B_0 field.

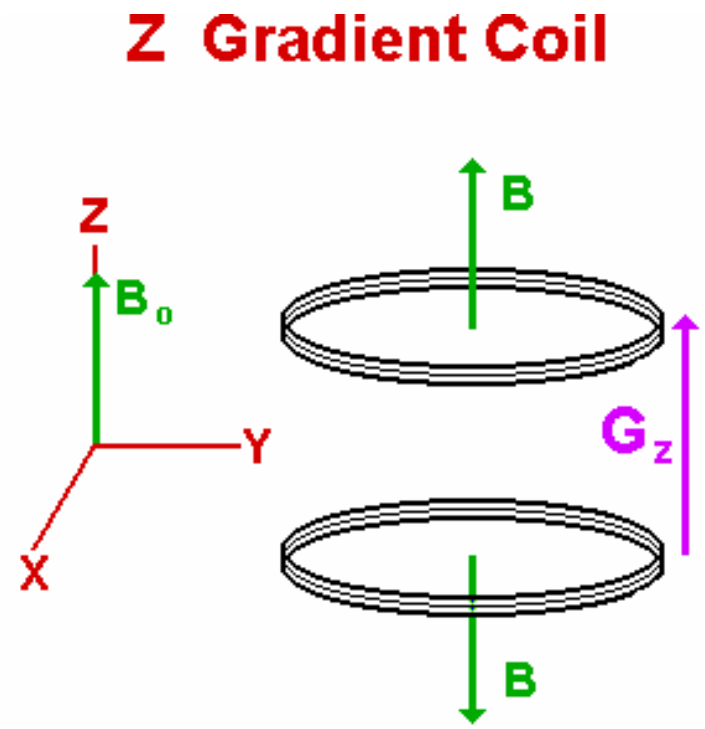

Figure 7 Gradient coils along the z direction are constituted by an antihelmoltz configuration.

In Figure 8 are shown the saddle coils used to create the gradients of the magnetic field along the transverse directions.

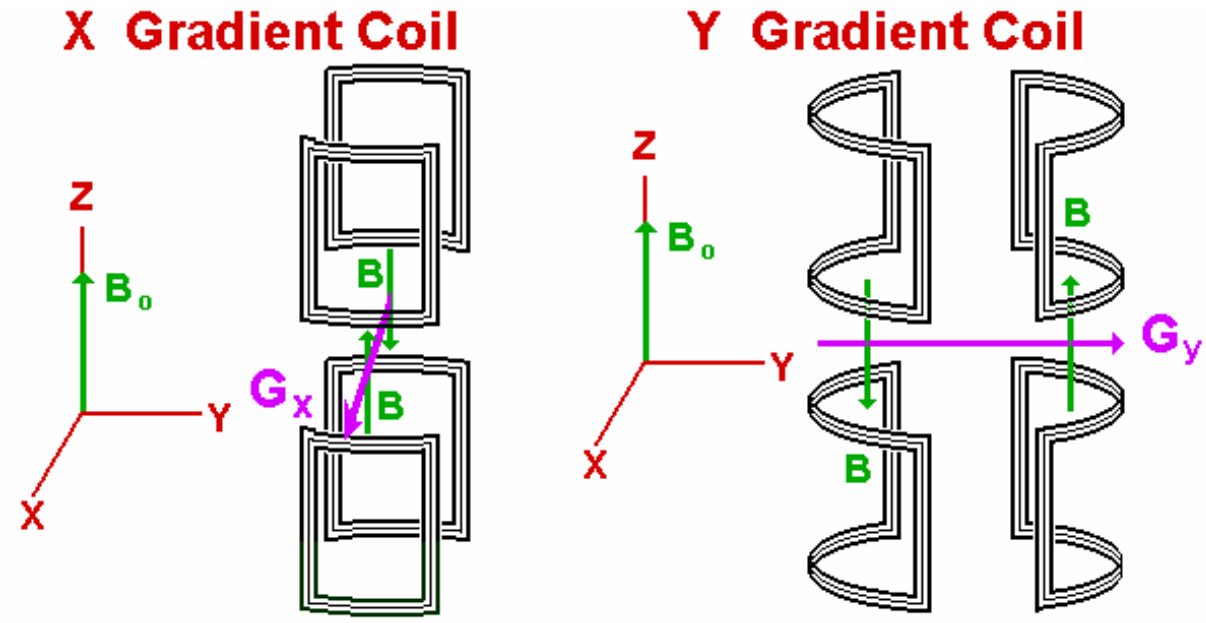

Figure 8 Coils creating the gradients along the x and y direction respectively.

1.4.7 Quadrature detector

The quadrature detector (Figure 9)is a device which separates out the two spatial components of the transverse magnetization from the signal from the RF coil. The heart of a quadrature detector is a device called a doubly balanced mixer.

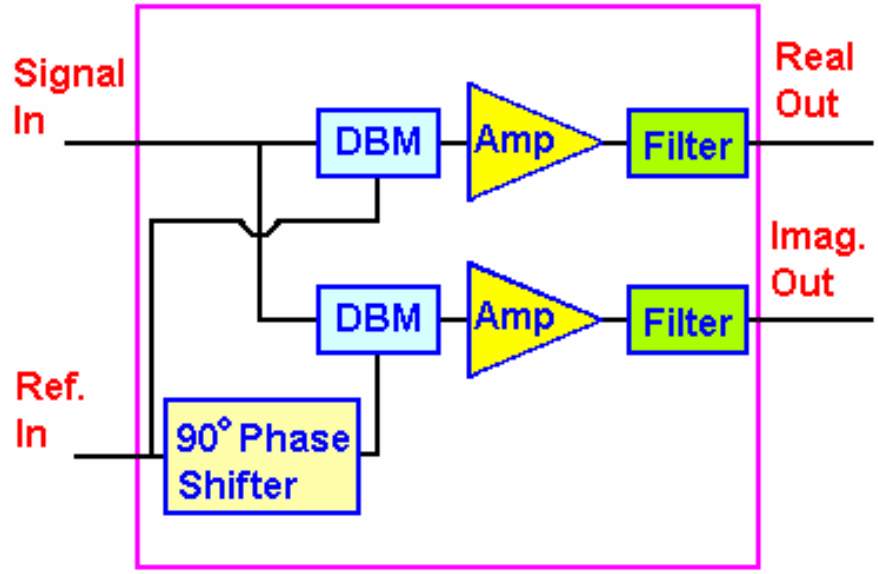

Figure 9 Scheme of a Quadrature detector.

The quadrature detector typically contains two doubly balanced mixers (DBM), two filters, two amplifiers, and a 90^{o} phase shifter.

2. The RFX experiment

Fusion research in Padua started in 1958 with a small University group that in the seventies became a CNR Research Center operating within the framework of the European Program.
From the initial theta pinch experiments the research moved towards the study of the Reversed Field Pinch configuration with Eta Beta I and Eta Beta II experiments in years 1972-1985.
The encouraging results obtained at the beginning of the eighties in Eta Beta II, in particular on "quiescent" plasma conditions, significantly contributed to prompt the research on the Reversed Field Pinch configuration, while the collaboration with the laboratories at that time operating in this field (Culham, Los Alamos, Padova and Tsukuba) was being consolidated. The advisability of constructing a machine of larger size was finally recognized.
RFX has been realized within the framework of the EURATOM-ENEA-CNR Association. The project was finally approved in January 1984, and the design was then carried out by the Padova Fusion Research Group. It was constructed from 1985 to 1991.The first plasma was obtained in November 1991.
The RFX Machine entered into operation in 1992 and since then it has produced a number of significant results in the understanding of unexplored phenomena, in the improvement of diagnostic systems, in the implementation of innovative technical solutions.
In 1999 Reversed Field Pinch experiments of RFX have been interrupted by a large fire which involved the power supplies but did not damage the machine.
During the reconstruction of the power supplies, the RFX machine was modified with the installation of 192 saddle coils, designed to allow the active control of MHD instabilities.

Reversed Field Pinch experiments resumed in December 2004 with the modified RFX device (RFX-mod). Due to the increased capability to control these instabilities, pulses length of 0.5 sec and 1.8MA have been reached.
Before showing the RFX machine is necessary to briefly review the physical basis of a Reversed Field Pinch experiment.

2.1 The Reversed Field Pinch [23, 8]

The RFP is an axisymmetric toroidal configuration characterized by a large toroidal current, a moderate sized toroidal magnetic field, and a relatively high β.
A schematic diagram of an RFP is shown in Figure 10.

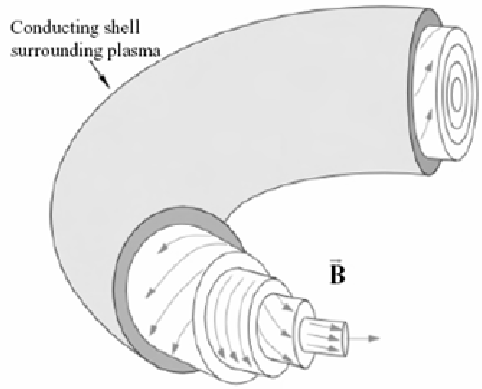

Figure 10 Schematic diagram of the RFP.

The device operates as follows. Initially a small toroidal bias field fills the vacuum chamber. A large toroidal current is then ramped up, and this compresses both the plasma and the toroidal bias field. In addition, the current raises the plasma temperature by means of ohmic heating. At the end of the current ramp, the toroidal and poloidal magnetic fields within the plasma are of comparable magnitude. However, since most of the toroidal magnetic flux has been trapped and compressed within the plasma, there remains only a small residual toroidal field at the plasma edge.
Typical equilibrium profiles are illustrated in Figure 11 for an equivalent cylindrical RFP.

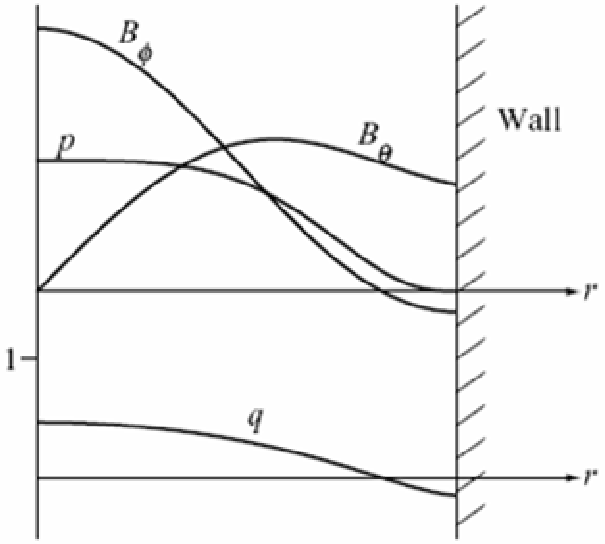

Figure 11 Typical Radial profiles for an RFP.

The flat central pressure profile and the B_φ reversal at the plasma edge are typical features of the RFP.

The theoretical analysis of Taylor has shown that the resulting field configuration always approaches that corresponding to a state of minimum energy, and therefore tends to be stable. While in a classical conductor the toroidal field in a steady state would reach, by diffusion, a uniform radial distribution, in an RFP the plasma relaxation processes maintain the configuration by a mechanism called the **dynamo effect** (by analogy with theories of the earth magnetic field generation).
The most significant difference between tokamak and RFP magnetic field configurations is that in the tokamak the toroidal field is much larger than the poloidal field, whereas in the RFP the toroidal and poloidal components are of the same order of magnitude and the toroidal field reverses in the plasma outer region.
Two parameters allow identification of an RFP configuration: the pinch parameter $\Theta=B_\vartheta(a)/\langle B_\varphi\rangle$, and the reversal parameter $F=B_\varphi(a)/\langle B_\varphi\rangle$, where a is the minor radius of the wall, $B_\vartheta(a)$ and $B_\varphi(a)$ are the poloidal and the toroidal field components at the wall and $\langle B_\varphi\rangle$ is the toroidal field averaged over the plasma cross-section. Taylor's theory states that, if the magnetic helicity and the toroidal flux are conserved, a plasma with $\beta=0$ spontaneously relaxes to a minimum energy force-free state described by the equation

$$\nabla \times \overline{B} = \mu \overline{B} \qquad (4)$$

Where μ is uniform and $\mu a=2\Theta$. In cylindrical geometry, the solution of equation (4) is given by Bessel functions and for $\Theta>1.2$ the toroidal field reverses at the wall. However, it is found experimentally that RFP plasmas have finite β and the current density tends to vanish at the wall, i.e. μ is not uniform, so that experimental profiles depart from the theoretical ones.

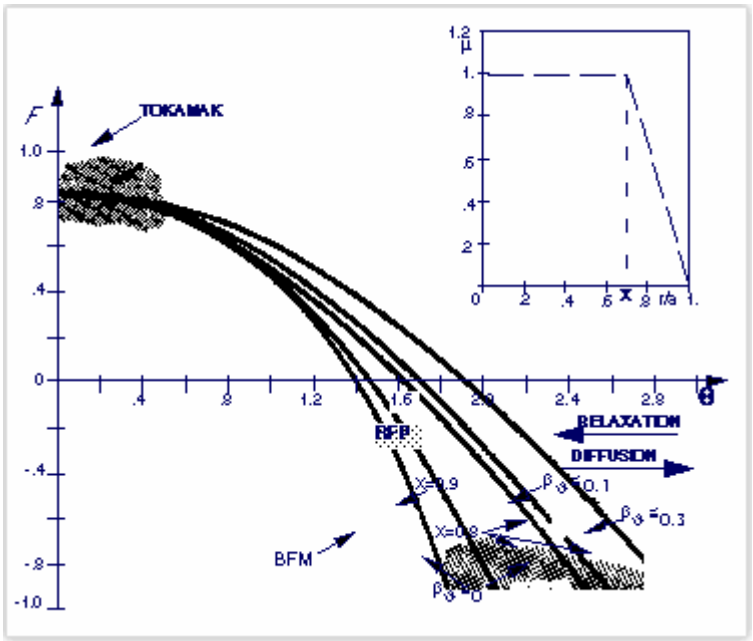

Figure 12 F-Θ diagram. The BFM curve refers to the Taylor minimum energy states, the other curves refer to a non-uniform μ and different β_ϑ, X represents the normalized radius where μ is truncated.

Figure 12 shows where the preferred classes of parameters of tokamak and RFP lie in the F-Θ diagram. The BFM (Bessel Function Model) curve corresponds to the theoretical Taylor's curve of force-free configurations; the other curves refer to a model which takes into account a non-uniform μ and a finiteβ. The tokamak is at left end of the diagram, with a large positive and almost uniform toroidal field and a comparatively small toroidal current (F~1 and Θ small). The RFP configurations lie at the other extreme (F<0 and Θ>1.2). As shown in the same figure, these configurations are the result of the dynamical balance of the counteracting actions of resistive diffusion and relaxation processes. The first tends to shrink the toroidal current distribution, whereas the second, driven by MHD modes destabilized by the resistive diffusion, tends to restore the previous state. As a consequence, an RFP configuration is continuously regenerated through magnetic fluctuations.

In an RFP several instabilities are simultaneously present leading to the characteristic turbulence of the configuration. The profile of q in this configuration is shown in Figure 13. It is quite different from the typical q profiles of a tokamak, so instead of the few modes allowed in a tokamak, in an RFP many modes are allowed and their resonant surfaces accumulate near the reversal surface. As a result, several instabilities can be excited contemporarily. These instabilities can overlap one another experiencing non-linear interactions; in such a case a wide stochastic region in the plasma is created which affects the energy transport. These instabilities also contribute to sustain the configuration, by the so-called dynamo effect. The plasma generates by itself the toroidal flux inside and therefore poloidal plasma currents are driven as a consequence of the poloidal flux variation produced by the voltage applied by the power supplies. Since the resistive diffusion timescales are much shorter than pulse duration, the diffusion processes are fully counteracted: the magnetic configuration is maintained as far as the current is maintained and it is lost only when the current drops.

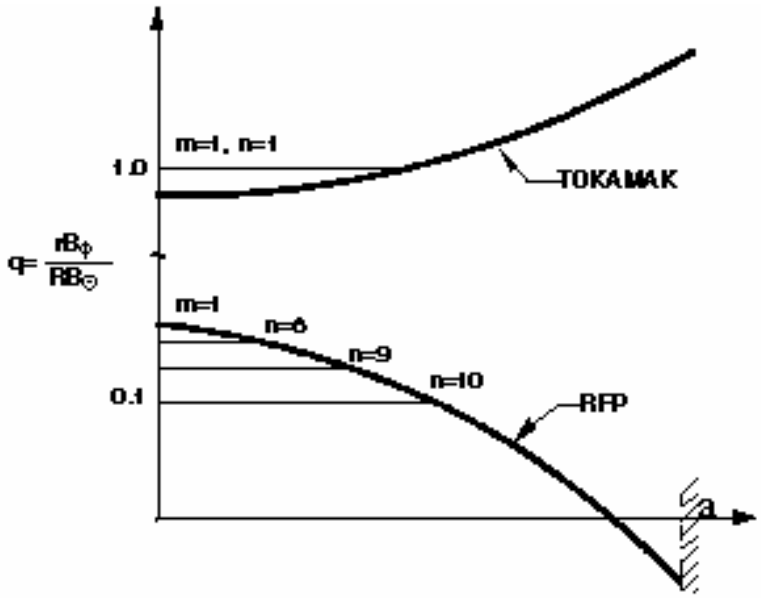

Figure 13 Radial profiles of the safety factor q for tokamaks and RFP configurations; resonating modes with m=1 are evinced.

2.2 The Reverse Field eXperiment [25, 26]

A brief review of the RFX machine is here presented, the next subsection is dedicated to the magnetic system of RFX paying particular attention on the Ohmic Heating winding individuated as the cause of the magnetic disturbance for the NMR instruments housed in the ICIS institute.
After the large fire of 1999, the RFX machine has been reviewed. A cross-sectional view of the RFX machine is shown in Figure 14 (left), in the right side of the same figure the coils making up the magnet systems are shown.
The vacuum vessel (Figure 14) is an all-welded rigid structure made of INCONEL 625, composed of 72 wedge-shaped elements, each of them consisting of a sandwich structure with a 2 mm thick inner wall and a 1 mm thick outer wall connected together by a 0.5 mm corrugated sheet and two poloidal stiffening end rings, welded to the inner and the outer walls. The toroidal loop resistance of vacuum vessel is 1.1 mΩ.
The plasma facing surface of the vessel is fully covered by 2016 graphite tiles, acting as armour against heat pulses coming from the plasma. The vacuum vessel is bakeable at a temperature beyond 350°C. Attached to the vacuum vessel are electromagnetic and piezoelectric gas valves and vacuum manifolds. The vacuum vessel of RFX is closely surrounded by a thin (3mm) Cu shell. Toroidal equilibrium is feedback controlled using the field shaping coil system. A set of 48x4 saddle coils outside the thin shell are controlled by a digital feedback system which allow a variety of operation modes to act both on field errors, radial field components due to dynamo modes and resistive wall modes (RWMs).

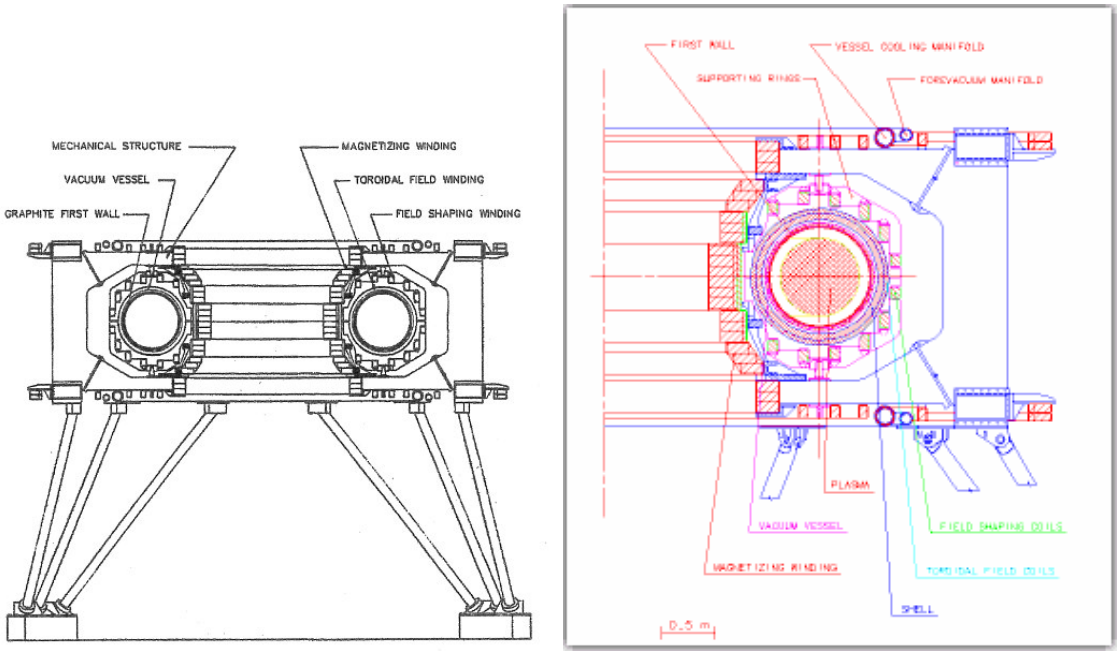

Figure 14 Left, RFX machine cross section; Right, Radial cross-section of RFX with the Ohmic Heating (OH) winding (coils M1-M20), the Field Shaping (FS) winding (coils F1-F8), a TF Coil, the stabilizing shell and the mechanical structure.

The main component of the RFX magnet system are the poloidal field (PF) windings (Figure 14, right side) and toroidal field (TF) winding (Figure 18**Errore. L'origine riferimento non è stata trovata.**).
PF windings are made up of the Ohmic Heating system (OH) and of the Field Shaping system (FS).
The flux swing of the Ohmic Heating system is 15 Vs and the maximum induced loop voltage is 700 V. The maximum peak power of an RFX pulse requires 200 MVA to be taken from the 400 kV 50 Hz Italian grid. The power received from the network is then transformed to 21.6 kV and distributed to various RFX loads.
The fulfilment of the previous function is obtained by means of a succession of operation of the components of the power supply system.
The electric scheme of the poloidal field circuit [27] is reported in Figure 15.
The following functions have to be provided by the poloidal field circuit:

- storage of the initial flux in the magnetizing winding;
- creation of the loop voltage and the flux variation which respectively ionise the gas and give rise to the plasma current;
- control of the level of the plasma current during the flat-top phase;
- control of the plasma position and avoidance of the mismatch between internal and external poloidal fields at the gaps of the shell.

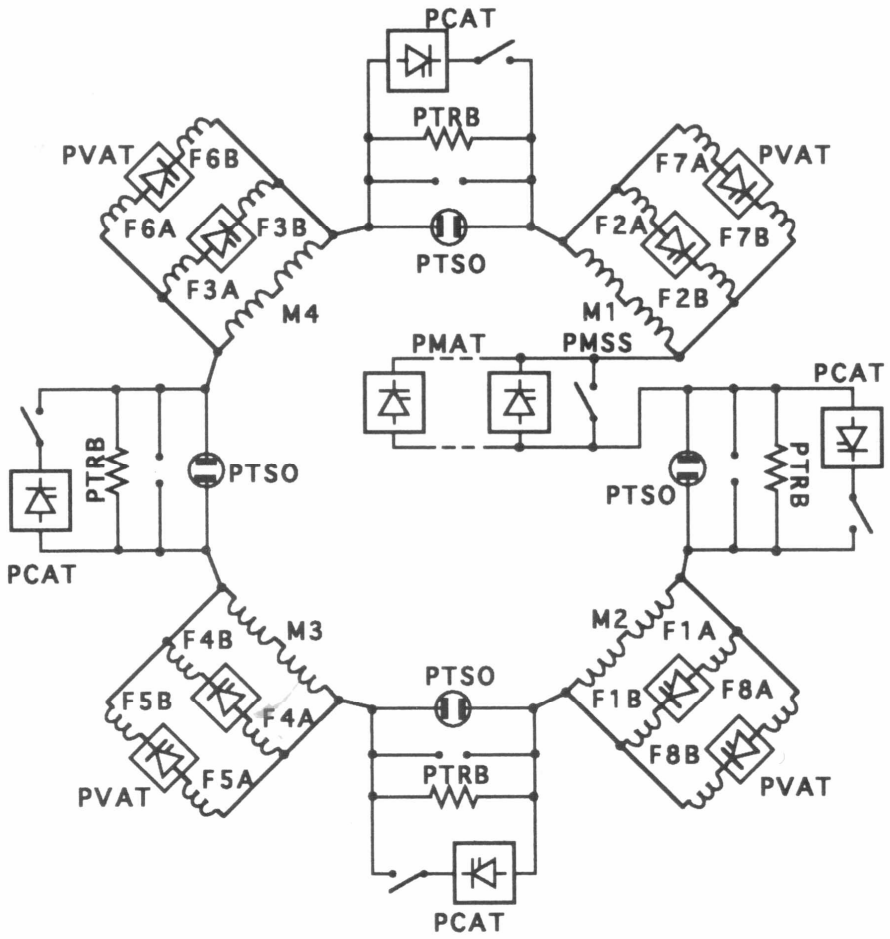

Figure 15 Scheme of the poloidal circuit with FS coils (F1-F8, A and B), their thyristor power supplies and the OH sectors (SM1-SM4).

The toroidal field circuit has to provide the following functions:

- establishment of the initial toroidal field and help in its reversal at the plasma boundary during the rise phase of the plasma current;
- control of the level of the reversed during the flat-top phase.

The fulfilment of the previous function is obtained by means of a distinct succession of operation of the components of the power supply system.

2.3 The RFX magnet system

The main magnetic system specification of RFX are a maximum toroidal field intensity of 0.7 T, provided by the TF (Toroidal Field) windings, and a poloidal flux swing of 15 Wb, provided by the PF (Poloidal Field) windings. The equilibrium and the shaping of the plasma is controlled by the PF windings.
At the pulse start-up, the OH winding creates a loop voltage of 730 V and stray field in the plasma region below 5 mT.
One shot every 600 s is the highest design repetition rate.
Thus the innermost region has become technologically critical, with highly stressed coils and mechanical structures, squeezed into narrow spaces (Figure 14). The above RFP characteristics framed the major constraints on the design of the RFX windings.
From a mechanical point of view, both the OH and the FS windings are subjected to working conditions similar to those experienced in tokamaks.
A comprehensive measuring system monitors both TF and PF systems, devoted to measurement of the following:

- all currents of the windings, by means of Hall effect compensated current transformer;
- all voltages to earth of each winding terminal, by means of compensated voltage dividers;
- more than 500 signals picked up by magnetic probes placed all around the vessel.

Mechanical measurement equipment is also provided to monitor the structural behavior of the magnetic system.
As faults can cause coil currents to rise quickly, leading to harmful conditions if allowed to evolve freely, a fast hard-wired high level logic system (RGM) has been installed that is able to start suitable fast protective actions according to fault severity.
The electrodynamic force acting on the OH winding are extremely large and have required a quite substantial engineering effort to design and to manufacture a sound mechanical structure, which also supports the whole torus assembly, that is the assembly of vacuum vessel, stabilizing shell, TF winding and FS winding.

2..3.1 Basic circuit operation [28,27]

The basic circuits for the TF and PF windings are shown in Figure 16; the waveforms of the magnetomotive force in each of the three windings during a typical full current operation are shown in fig. 3. the sequence of operation is as follows.

- initially, before time t_0, the OH winding is charged up to the operation current (and flux) by the power supply PMAT; the main capacitor bank C_p of the TF circuit is also

charged up to the operation voltage; at a suitable time the C_p is closed on the TF winding, forming an LCR circuit where a current oscillation starts.

- At time t_0 the TF swinging current reaches its first maximum. The circuit breaker I_T of the PF circuit is opened and the OH current quickly decreases through the transfer resistor R_T, producing a flux swing and a loop voltage suitable to start the plasma current; in this phase the TF current decreases to zero and reverses and the FS currents rise together with the plasma current. The winding arrangement causes these currents to be close to those supposed to give the ideal equilibrium;
- At t_1 time the plasma current reaches its flat-top value: the power supply PCAT is switched on, driving the OH current in order to sustain the plasma current, the power supply TFAT is switched on, driving the TF current in order to sustain the reversed toroidal field, and the power supplies PVAT control the FS currents providing the equilibrium field; this arrangement is maintained until the plasma current starts to decay.

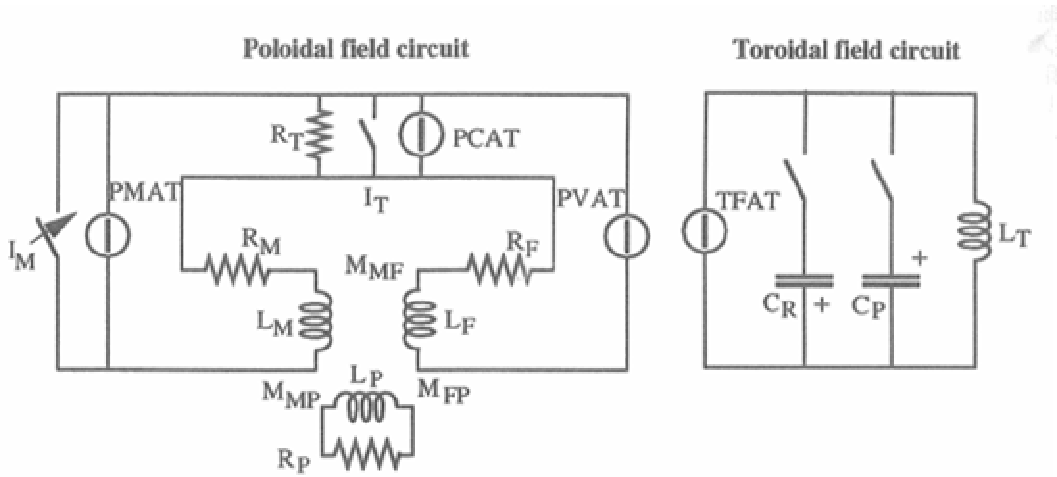

Figure 16. Basic PF and TF circuits.

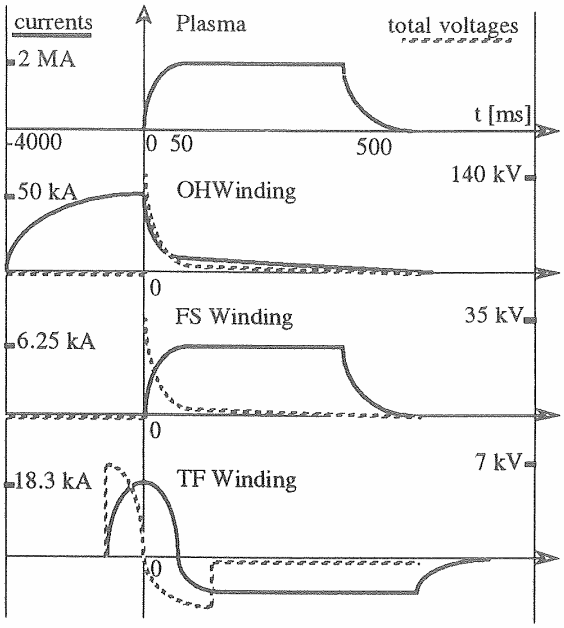

Figure 17 Magnetomotive force waveforms during a typical 2MA pulse.

2.3.2 Toroidal field winding

During normal operation the TF (Figure 18) winding current must produce a maximum toroidal bias field B_0= 0.7 T (at the beginning of the plasma pulse) and a reversed field B_w =0.44 T at the wall (during the plasma current flat-top). The winding is also used for pulsed discharge cleaning operation: in this case a lower toroidal field (27 mT) is continuously applied by a specific power supply.
The TF winding consists of 48 coils (with a diameter of 1.24 m), evenly distributed and partially inserted into grooves machined in the stabilizing shell. The magnetic field ripple, i.e. the ratio between the non-toroidal and the ideal components is below 4%.
Each coil is made with eight copper turns arranged in two layers, giving a total number of turns of 384. The maximum coil current is I_{T0}=18.3 kA (at the beginning of the plasma pulse) and I_{Tf} = -11.5 kA (during the plasma flat-top).
The TF winding are subdivided into twelve sectors, each consisting of four coils permanently connected in series by means of busbars close to the coil terminals. These sectors are cable connected to a collector system where six different arrangements of series-parallel connections can be quickly set.

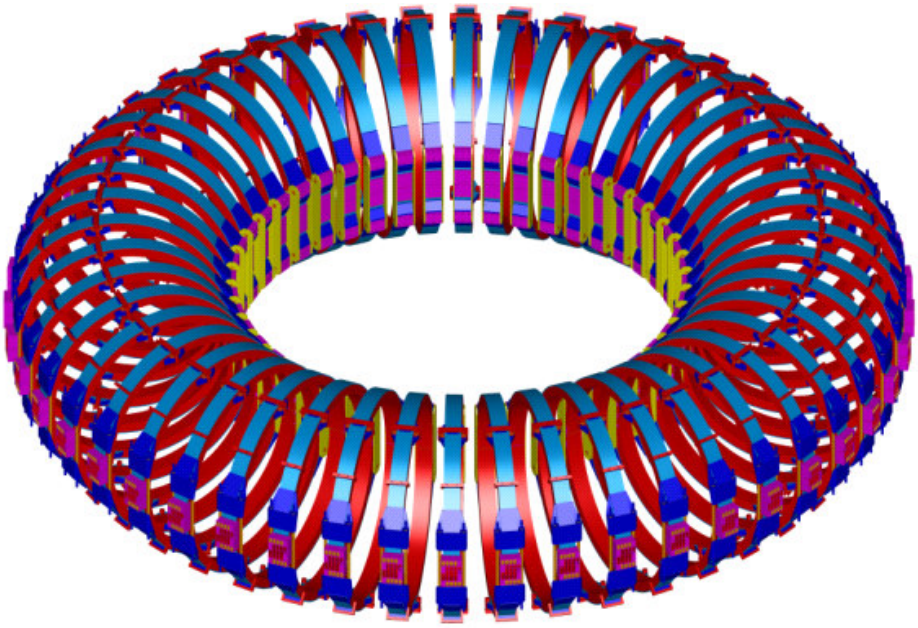

Figure 18 Toroidal field winding.

2.3.3 Field shaping winding

The FS winding (often referred to as primary winding, Figure 19) controls the plasma equilibrium, together with the stabilizing shell. More precisely it is required to provide three functions:

(i) in the early phases of the plasma pulse it controls the field on the shell outer surface in order to avoid error fields at the shell gaps and holes;

(ii) at longer times, when the shell is no longer effective, it produces an accurately shaped equilibrium field;

(iii) in both previous conditions it presents a magnetomotive force equal to the plasma current (up to 2 MA turns) in order to reduce the flux swing requirements.

The FS winding consists of eight couples of coils. Each couple is made of two equal coils symmetrically placed with respect to the equatorial plane and connected in series to form eight FS sectors. This number of coils provides a poloidal field configuration around the shell approaching that of an ideal continuous casing and leaves good accessibility to the vacuum vessel.

The two coils of each couple are connected in series and their current is controlled independently, by means of a thyristor power supply, so that a wide range of field configurations can be achieved while the total magnetomotive force of the winding is kept equal to the plasma current, thus providing the required high operational flexibility. This arrangement allows the proper coil currents to be naturally induced in the early phases of the pulse, when the power supplies are little effective due to their response time.

Each coil has 24 turns. This number gives the electromagnetic parameters L and M which provide a built-in balance of the voltage induced in the FS coils and in the OH sectors, which are connected in parallel (Figure 15). In this way the F currents naturally approach the required values, minimizing the voltage and power demand from the thyristor power supplies.

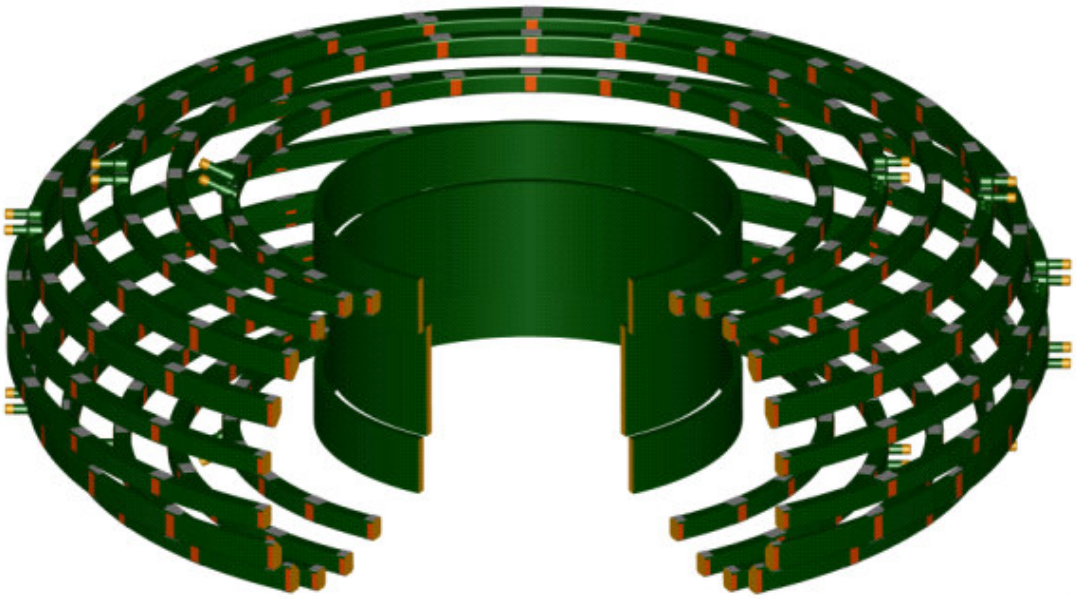

Figure 19 The Field Shaping winding.

2.3.4 Ohmic Heating winding

RFX requires a poloidal flux flux swing of 15 Wb and a peak loop voltage of 730 V, while the plasma current rise occurs in few tens of milliseconds. Such requirements demand a large flux consumption during setting up making the use of a bipolar flux swing operation almost useless. Thus 15 Wb also represents the flux to be stored before start-up to allow an unipolar flux swing. As a further requirement the stray field intensity in the plasma volume must never exceed 5 mT.
. The air core transformer requires a magnetomotive force of about 10 MA turns to create the 15 Wb flux, with a top field of about 4.5T in the central bore. It also requires the ampere turns to be suitably located to limit the stray field in the plasma region.

A specific OH winding (often referred to as magnetizing winding) provides all these functions. Its total number of turns was settled as a compromise between two opposite needs: to keep the voltage from coil terminals to ground within acceptable levels, and to have current and turn cross-section too large. A number of 200 turns was finally adopted, symmetrically placed above and below the equatorial plane.
The turns are wound to form 40 OH coils connected in series, to form four independent OH sectors. These sectors are arranged in the poloidal field circuit (Figure 15) in order to produce equal voltages between terminals and earth. In this way, the maximum total voltage at the winding terminals is 140 kV, while the voltage between an OH coil and earth is kept within ±17.5 kV.
The central solenoid, placed in the innermost part of the machine, is made with 156 turns, wound in 24 coils. It generates most of the OH flux, while the 16 outermost coils, with a total of 44 turns, are given primarily the function of shaping the field lines in order to limit the stray field in the plasma volume.
The 40 coils are impregnated together in groups, to constitute 17 solid OH blocks. The blocks above the equatorial plane are identical to the corresponding blocks below it, which

are installed turned upside down. Adjacent coils of a block do not belong to the same OH sector and full voltage is possibly present between their turns. A careful location of the coil terminal on the block surface was necessary to yield sufficient tracking distance between the electrical leads, complying with the symmetry conditions assumed for upper and lower blocks.
The final geometry of the OH coils has been adjusted in order to minimize the stray magnetic field intensity in the plasma. The final solution (Figure 20) achieves an even better performance than required, with stray field intensity below 1 mT, and present mechanical features able to cope with structural problems.

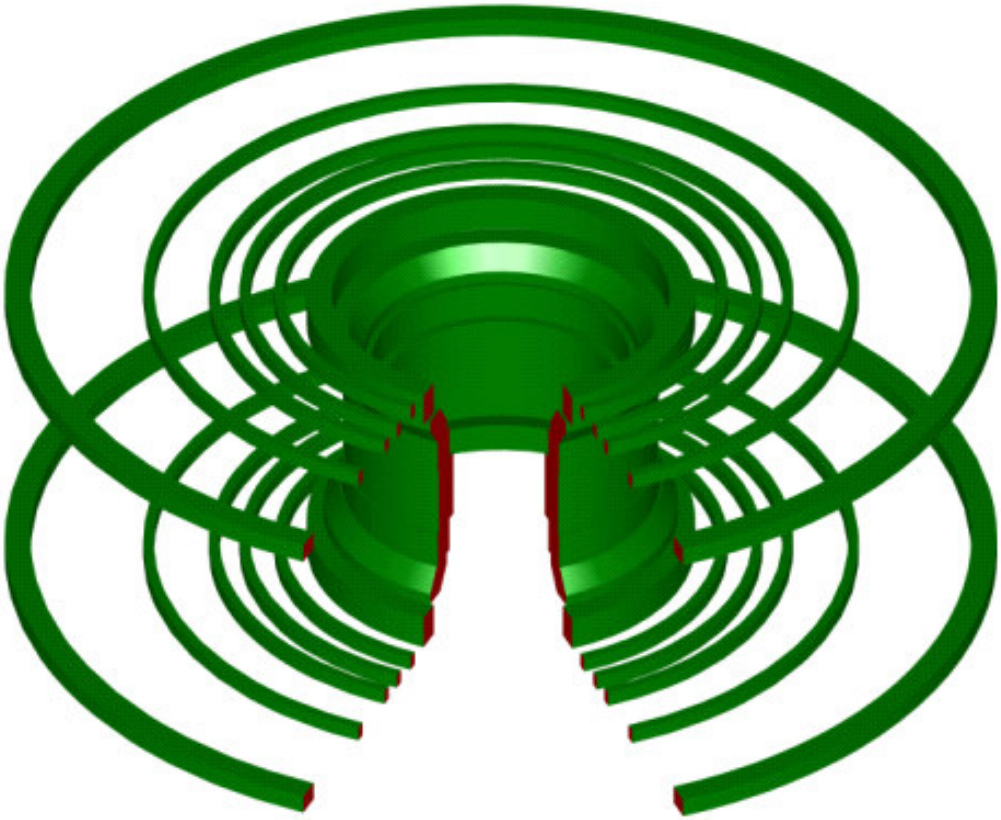

Figure 20 OH winding of RFX.

In order to minimize the flux requirement from the OH winding, the total ampere turns of the FS winding have to be equal and opposite to the plasma current, as previously stated. The two windings are arranged in order to obtain such a behaviour with minimized power requirement. This condition is achieved making equal the voltages induced by the OH flux swing in the FS and OH windings and connecting in parallel the two windings. As the OH winding is split into four OH sectors, the eight FS sectors are parallel in pairs to each OH sector, forming the four groups of Figure 15, where the balance of the voltages induced in the sectors of each group is ensured by a suitable choice of the self and mutual inductance of the coils.

2.3.5 Current sensors

24 current transducers measure the currents of all the winding sectors (+-20kA, +-7kA, +-50kA in the TF, FS and OH sectors respectively). These transducers are made with a special type of a zero-flux current transformer (CT), where the low frequency bandwidth limitation of conventional CTs has been overcome by means of a power supply feedback controlled by four Hall probes in order to maintain the zero-flux condition in the magnetic circuit. These transducers provide galvanic separation, are easy to install and have a competitive price. In the next chapter, these sensors will be called as LEM from the name of the factory house.
They were specified to ensure a precision better than 0.5% in a bandwidth from d.c. to 20 kHz. Extensive analyses and experimental tests were carried out in order to finalize the design and the layout, aiming for sound operation in a region with a strong and dishomogeneous magnetic field. The core cross-section and the magnetic material have been carefully defined in order to prevent local saturation in any working condition to minimize the errors coming from non-uniform external fields and to keep the residual magnetization as low as possible to minimize the offset.
As the power supply driven by the Hall probes must also face magnetic imbalance in any leg, the output stage of the amplifier has been designed to cope with a current demand of up to 40% beyond the maximum value required in normal operation.
A test facility has been set up to perform accurate measurements of the sensor error in several working conditions. An accuracy better than 0.1% in all the measuring ranges has been achieved, even with a 30% magnetic imbalance in the core legs.

3. Susceptibility of a NMR instrument

In the premises of the CNR research area of Padua, the IGI and ICIS institutes are located, are about 150m far from one another. The RFX machine is installed in the IGI institute, while the ICIS institute currently houses two NMR spectrometers.
In 1998, several anomalies were found during experiments with the NMR spectrometer installed in the ICIS institute. Such anomalies were correlated to the presence of the magnetic field created by the RFX magnetizing (OH) windings, necessary to initiate the hot plasma discharge.
The magnetic field induced by the magnetizing winding of RFX is shown in Figure 21 and Figure 22, for a current of 50 kA.

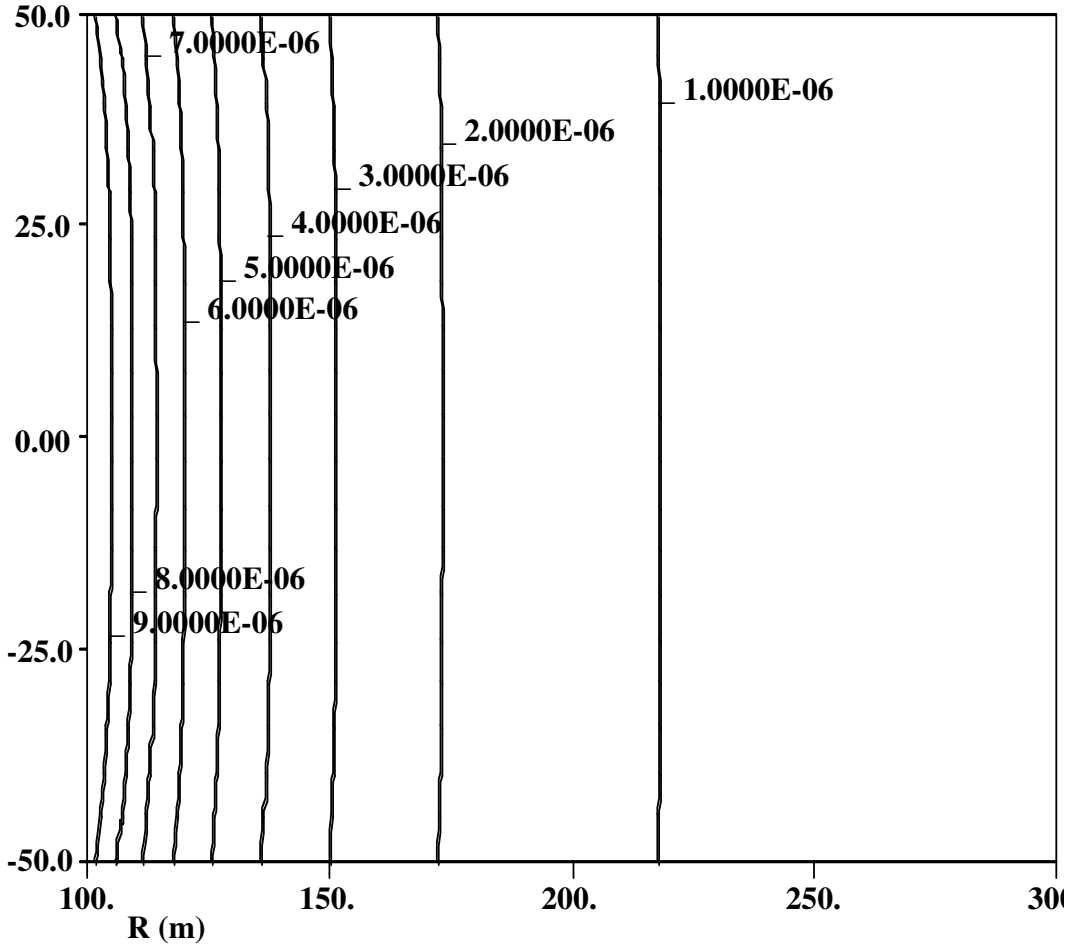

Figure 21 Map of the magnetic field produced by the magnetizing winding of RFX for the maximum current I_M=50 kA. Constant strength field lines [T].

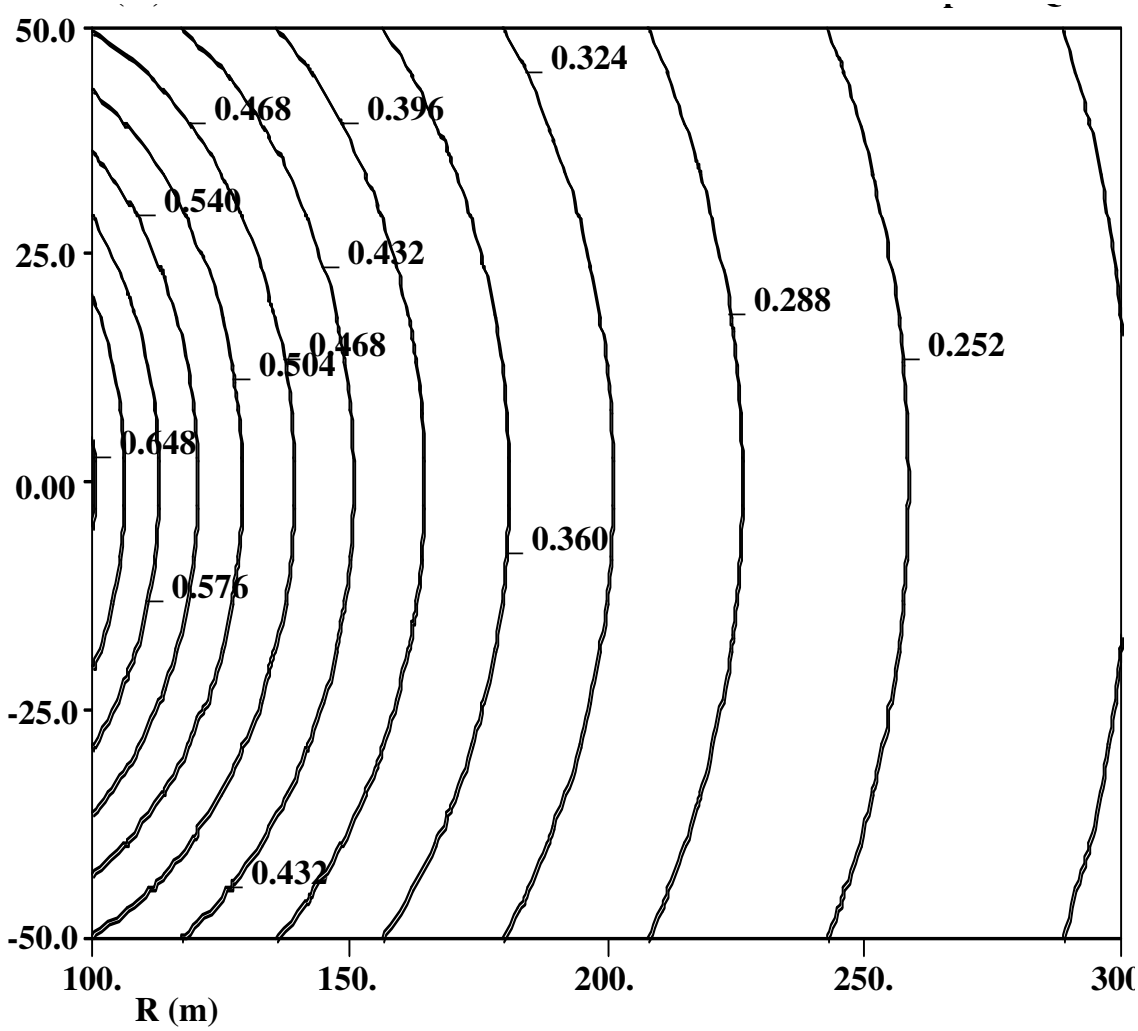

Figure 22 Map of the magnetic field produced by the magnetizing winding of RFX for the maximum current I_M=50 kA. Constant flux lines [Weber].

At approximately 150 m far from RFX, the strength of the induced magnetic field is of about 3 μT when the current flowing through the magnetizing winding reaches I_M= 50 kA, its foreseen maximum value.
Magnetizing current in RFX has the typical waveform shown in Figure 23. A slow raising slope lasts several seconds followed to a fast decay of the current, corresponding to the plasma discharge, which lasts about 0.2 seconds.

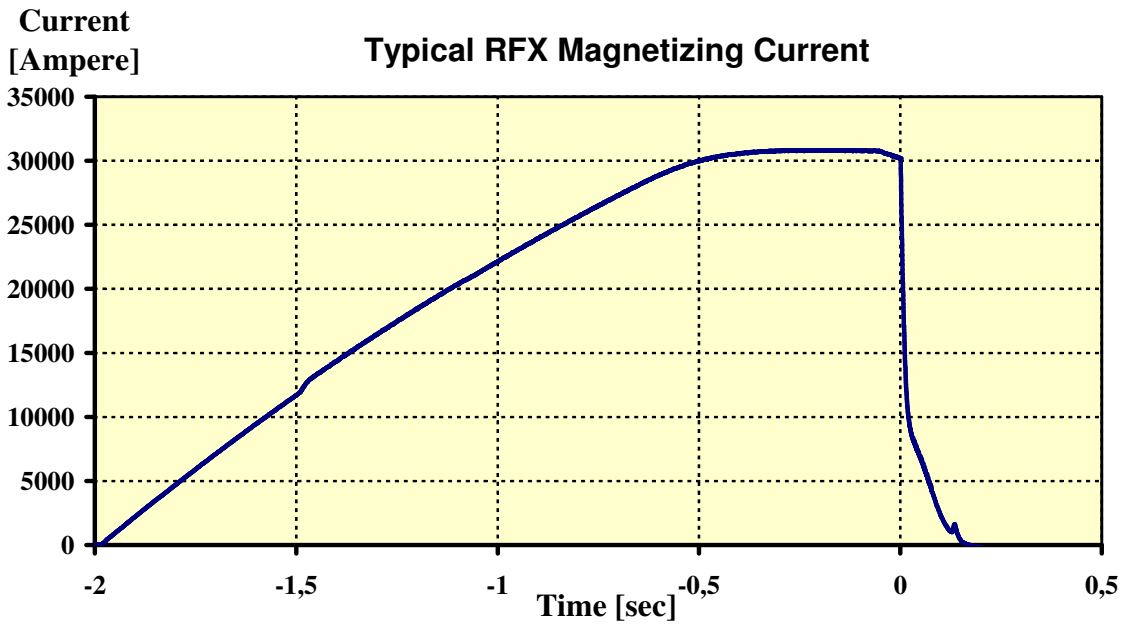

Figure 23 Magnetizing current during a typical RFX pulse.

The magnetic field produced by RFX in the area where the spectrometers are placed is approximately vertical and has the same time behaviour as the current. The repetition rate of RFX pulses is about one every ten minutes. Therefore, the disturbance field frequency is about 0.3-3 Hz.

First anomalies were observed with 30 kA pulses, corresponding to a field intensity of about 2 μT in the NMR spectrometer site.
Following these observations, researchers of the ICIS institute informed the researchers of RFX of the supposed interference. In such a way, it was decided to undertake a careful investigation in order to identify the source of interference and its mechanism. After measurements on the response to magnetic disturbances of many NMR instruments, it was shown that this kind of devices is susceptible to external magnetic fields with magnitude and spectra similar to the magnetic field induced by the magnetizing windings of RFX in the ICIS institute.
Experiments with dedicated pulses of RFX have shown the relationship with the observed failures on the NMR device housed in the ICIS Institute. Moreover, a careful investigation was undertaken on other NMR devices to individuate the best mitigating measure.

3.1 Experiments on a NMR BRUKER 200 MHz

In 1999, a NMR BRUKER 200 MHz instrumentation was housed in the ICIS institute. At that time, several NMR experiments have been carried out contemporarily to RFX pulses to investigate the relationship between the observed anomalies on the NMR experiments and the magnetic field induced during a RFX pulse. Three kinds of NMR experiments were carried out with this aim:

- $CHCl_3$ experiments, characterized by the high sensibility to an inhomogeneous magnetic field;
- H_2O experiments, with a low sensibility to an inhomogeneous field;
- 2D experiments with very high sensibility to an inhomogeneous field.

The Results obtained with $CHCl_3$ are shown in Figure 24, for different values of the magnetizing current I_M.

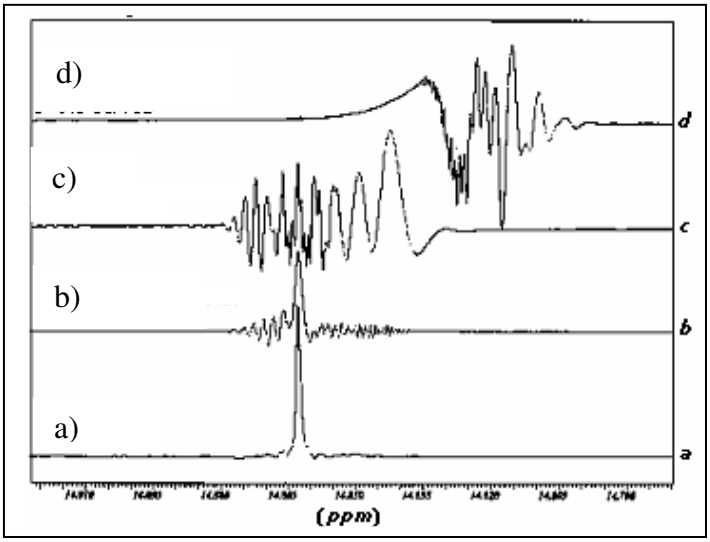

Figure 24 Results from $CHCl_3$. a) Spectra obtained in absence of disturbance. It is taken as reference; b) Spectra for a pulse with I_M=10 kA started 0.8 seconds before the FID acquisition by the NMR; c) I_M=10 kA pulse started contemporarily with the FID acquisition (-0.1 sec before); d) I_M= 15 kA pulse, -0.1 sec before the FID acquisition.

The temporal correlation between the two experiments has been investigated through the $CHCl_3$ experiment. It was found that major disturbances occur when the NMR starts the data acquisition contemporarily to a RFX pulse.

With the H_2O experiment, it was investigated the effect of the disturbance on a single proton. A broadening of the spectrum added to a shift in frequency was found, as shown in Figure 25 for both values of the magnetizing current I_M - b) I_M= 20kA; c) I_M= 25kA.

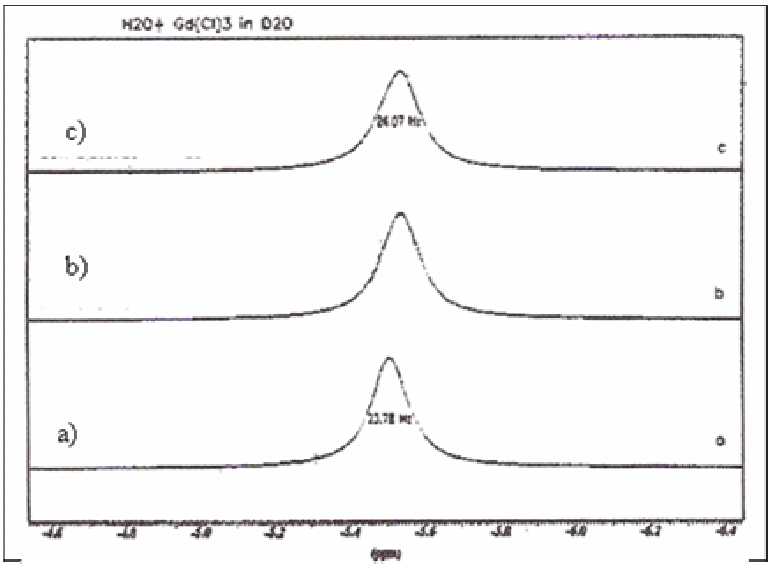

Figure 25 H_2O spectra: a) without disturbance; b) I_M=20 kA; c) I_M=25 kA.

The 2D experiment is a long term experiment lasting about 15 minutes, during the experiment many sampling occur. Two RFX pulses have been run with a current of I=25 kA, contemporarily to a 2D experiment. Also in this experiment great disturbance have been found, showing that is not possible to carry out long term experiment if any RFX pulse occurs.

3.2 Experiments on different NMR instrumentations

The tests above presented have confirmed the interference of the magnetic field induced by RFX with the NMR experiments in the ICIS institute.
Many other experiments have been carried out on different NMR instrumentations through the experimental set-up shown in Figure 26 [29].

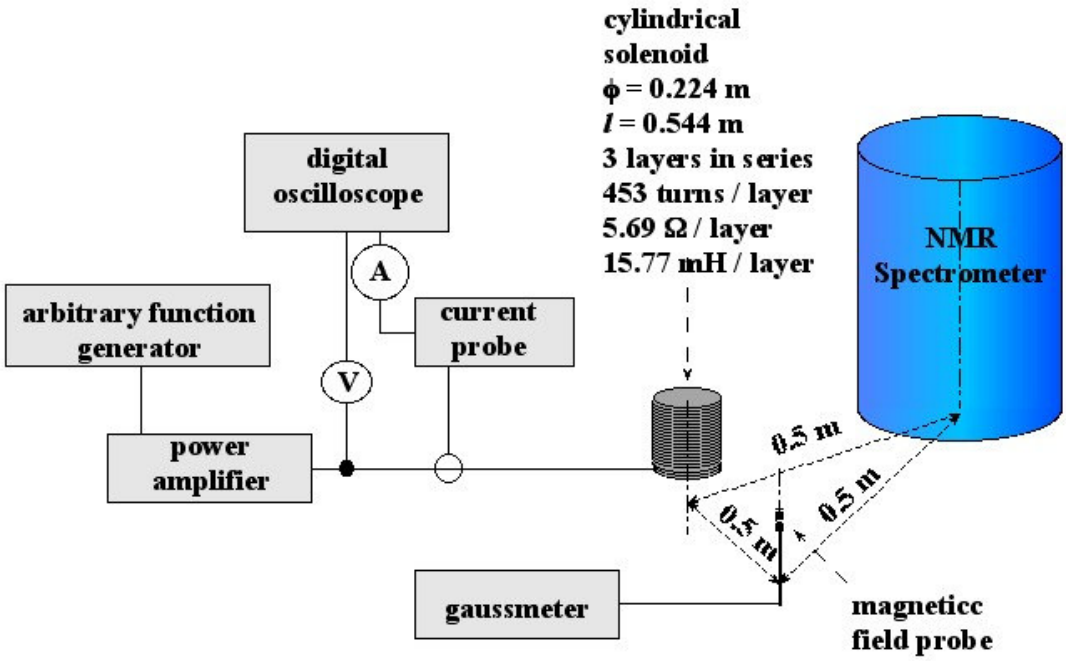

Figure 26 Experimental set-up for interference mechanism characterization. [29]

A solenoid, with well-known mechanical and electrical parameters, is placed 0.5 meter away from the NMR Spectrometer. A power amplifier, driven by a signal generator, so that any arbitrary field waveform can be generated, feeds the solenoid. Solenoid current is measured and visualized by a digital scope.
A Hall Probe, connected to a precision gaussmeter, is used to monitor the actual field value. The probe is placed in a position where the field is the same that the one experienced by the NMR spectrometer sample.
At the time of the experiments, a BRUKER AC 200 MHz NMR spectrometer was installed at the ICIS Institute.
The set-up above presented was used to investigate and characterize the susceptibility of this NMR device, defining the maximum magnitude of an external magnetic field which does not alter the NMR measurements and the spectra which both the magnetic shield and the Field lock circuitry of the NMR device can not compensate. To understand if the results depended on the particular spectrometer model or had a more general validity, it was decided to repeat all tests on different Brucker models. To this purpose, the experimental set-up was moved to the Bruker Italian headquarters in Milan where a more advanced spectrometer, model Avance 300, was available. This spectrometer had a more powerful digital field lock circuit, and a reinforced shielding called Ultrashield. Other tests have also been carried out on a

BRUKER AVANCE 300 without Ultrashield which was available at the "Istituto di Farmacia" of the University of Padua, also because the ICIS Institute had foreseen to purchase this NMR model in the following.
Different kinds of tests have been carried out in order to characterize the susceptibility of each device:

A. Static Field tests

A constant magnetic field ranging from 1 to 40 μT was produced. Spectrometer operation was not compromised, but field lock circuitry was not able to compensate totally the interference, so NMR measurement signal to noise ratio worsened as the perturbing field increased.

B. Sinusoidal Field tests

A sinusoidal magnetic field at 3 μT was produced, with frequency ranging from 0.01 to 50 Hz. A clear susceptibility frequency window was identified; in the range 0.1 to 3 Hz. Below 0.1 Hz Field lock circuit is able to compensate for interference. Above 3 Hz passive shields seem able to protect the spectrometer. Unfortunately, RFX pulse waveform frequency spectrum is just in the most sensitive range of frequencies.

C. Pulsed Field tests

By means of the waveform generator, a perturbing field with the same shape of RFX pulses was produced. It was observed that the field lock circuit was affected mostly in the fast decay phase, in accordance with the results of sinusoidal tests. When the maximum filed was greater than 2 μT, there was a system stop. For lower field data corruption was observed.

The results of the tests on the more advanced spectrometers were similar to the previous one, but with some significant differences:

1. A system stop was never observed: digital lock circuit was able to maintain the system operating also in presence of the perturbing field.
2. Also if system did not stop, data resulted corrupted if perturbing pulse occurred in coincidence with NMR measurement. In particular, it was identified a window of about 2-3 seconds around the NMR measurement in which the external pulse was able to corrupt data.
3. Only vertical perturbing fields resulted to have a negative influence on the spectrometer
4. The minimum field at which some disturbance was observed in NMR measurements resulted 0.1 μT.

It can be concluded that such type of spectrometer is unable to compensate for external field interferences if they have significant harmonics in a well-defined range, spanning from 0.1 and 3 Hz. Perturbing field compromises spectrometer results if it is present in critical phases of the measurement cycle. Depending on electronic implementation, the equipment can stop, go to an abnormal state, or not give any indication of the problem.
Natural or industrial magnetic field sources do not exist at these frequencies, so, in normal conditions, the NMR does not suffer of the anomalies here observed. Pulsed magnetic confinement fusion experiments, on the contrary, emit a field to which spectrometers are very sensitive, so it is a very rare and unfortunate case that a spectrometer happened to be near a so particular device.

4. Strategies to compensate a magnetic disturbance

The results given of different tests made in the 1999 (section 3) showed that the magnetic field induced by RFX produces great disturbances on NMR devices housed in the ICIS premises. So, the two experiments can not be run contemporarily.
In order to individuate the best strategies to compensate the magnetic disturbance induced by RFX, some solutions have been taken under consideration.

The safer and simpler solution would be relocating the spectrometer far from RFX plant. This would require a site at least 500 meters away from RFX, which was not available.

Another possible solution could be a passive ferromagnetic shield. This solution has several drawbacks which were noticed by the experts of the Bruker headquarter. First, the shield cannot be installed in the volume inside the superconducting magnet, where the sample is placed, because it would be completely saturated by the strong main field. So, it should be placed outside the cryostat, but at a distance where the residual field of the magnet is low enough to avoid shield saturation. This residual field is 5 mT at 1 meter from the magnet axis. In practice, to maintain an acceptable accessibility to the spectrometer, it would be necessary to shield the entire room where the spectrometer is placed. To obtain the required field attenuation, a very heavy and expensive shield would be required. Moreover, the possible interaction between shield and spectrometer must be investigated. Shield would present a residual magnetization, not constant in time, which should be compensated. Shield mechanical vibrations will modify the boundary conditions all around the NMR device, inducing change in the effective magnetic field inside the instrument. The overall effect would be to insert a new source of disturbance.

Another possible solution could be the realisation of an active shield, constituted by a couple of coils (in a Helmotz scheme) placed over the floor and below the ceiling of the room containing the spectrometer. To have enough field uniformity the coils must be quite large (at least 1 m diameter) but the very low correction field needed has the advantage that limited current is required, so the coils can be light and mechanically simple.
Two ways to drive the active shield have been taken into account.

4.1 Control of the active shield

4.1.1 Feedback scheme

A local sensing solution has been explored in 1999 [20], in which a measurement probe is present near the spectrometer and senses the perturbing field. The probe signal is then used to drive the correction coils.
With a careful chosen positioning, the control probe can be made insensitive to correction coils field in such a way to sense only the external perturbing field. A proper transfer function can be calculated in order to null the perturbing field in the sample region, taking into account the correction coils geometry and sample position inside them.
The critical point with this solution is the very low level of the field to be measured. It requires a very sensitive probe, with a suitable band-pass circuit able to select the RFX field

signal among all the other fields of various origins always present but not affecting the spectrometer.
To evaluate the obtainable performances, a reduced dimension version of the active field was realised, able to shield a CRT monitor, a typical device that is disturbed by the RFX pulses. It is shown in Figure 27.

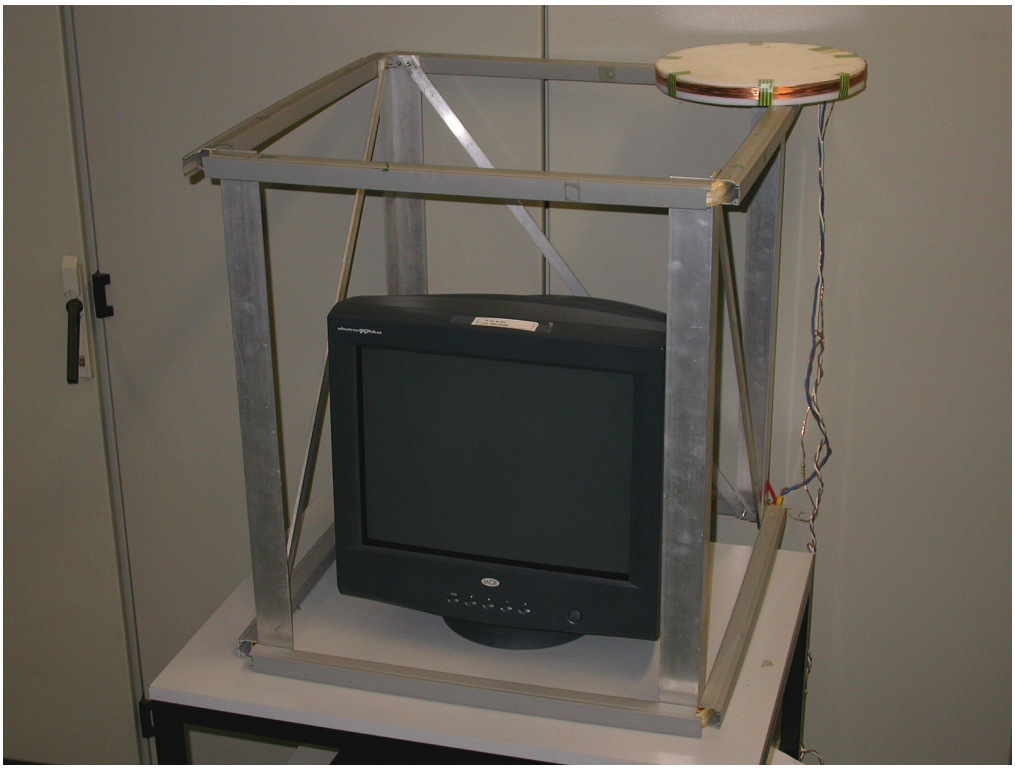

Figure 27 Photo of the reduced size active shield. On the top right it can be noted the probe used to control the shield current.

It is constituted by two equal square coils with a suitable supporting structure. A circular probe, visible on the top right angle of the photo, is used to measure the perturbing field. It is placed in a position were the field produced by the coils cancel itself in the area of the probe.
The prototype shield resulted very effective in protecting the monitor from interferences, but the first test has shown that this solution is not suitable to the purposed aims. Few drawbacks have been found:

- A huge noise (induced by the usual electric and electronic devices, such as the neon lamps) on the probe sensing could overcome the RFX signal;
- Two similar active shield operating on two NMR devices close one another could interfere;
- It could interfere with the usual operation during a NMR measurement because it can senses also the magnetic field induced by the RF coils stimulating the sample as well as the FID signal. So, a really complex circuitry, operating with the NMR signals, should be taken into account in order to avoid such a challenge.

4.1.2 Open loop scheme

At the end of 2004 RFX came back in operation after the stop due to the large fire in 1999. During 2005 the pulses energy has been increased and the interferences were observed again rising up the need of a definitive solution. Another possible approach was taken into account in order to correctly drive the active shield.
A signal proportional to the windings current can be sent to the spectrometer and used to drive a suitable power supply that feed the correction coils.
This "open loop" solution requires defining an accurate and reliable way of sending the RFX winding current signal in real-time to the spectrometer.
Its realization will be discussed in the next chapter.

4.2 Transmission of the driving signal

The driving signal, which has been individuated as the measurement of the I_M magnetizing current, has to be sent to the ICIS institute as soon as possible during a RFX pulse.
In order to achieve such a real time transmission, many systems have been taken under consideration:

- Transmission via dedicated cable;
- Via a telephone line;
- Via internet;
- Via wireless.

The first solution has not been taken under consideration for many disadvantages. The main disadvantage of a similar solution is its stiffness. In fact, if the NMR instrumentation is shifted from the present location, also the cable should be relocated.
The second and the third solution have not been taken under consideration, because they would require allocating specified resource to the present aim, without being able to furnish in each case a small transmission delay.
The last solution does not suffer of the disadvantages above presented, but it required to define the specifications which a transmission system should satisfy and, possibly, to find and buy such a transmission system.
At the end of the 2005, a RF transmission system, used for Telemetry purpose, has been found suitable to the transmission of the I_M measurement [21].

5. SUMMARY

Nuclei under a magnetic field are subjected to resonance effects, being able to absorb and emit electromagnetic radiation at a given frequency. The value of this frequency, called Larmor Frequency, is strictly related with the amplitude of the stray magnetic field where the nuclei are embedded. The NMR spectroscopy is based on these resonance effects. Into a NMR spectroscope, superconductive magnets are devoted to create a strong magnetic field (of about 5 T), and shim coils are provided to ensure a great homogeneity of this magnetic field. Moreover, the external structure, made up of the cryogenic dewar, and the field lock circuitry provide to shield the NMR sample against fast and slow magnetic field variation respectively.
However, several anomalies can be experienced by the NMR spectrometer housed in the ICIS institute if their measurements are carried out during a RFX pulse.
The interference mechanism between the RFX experiment and a NMR spectrometer has been described in this chapter. This depth comprehension of the mechanism was useful to define the requirements of a system aimed to compensate in real time the magnetic disturbance on NMR instrumentation by RFX.
Several mitigating measures have been taken under consideration as discussed in section 4.
An active shield seems to be the most promising solution.
The active shield has to compensate the magnetic field induced by RFX mainly in the frequency range of 0.1Hz to 3Hz (the susceptibility band of a typical NMR device), in order to reduce the strength of the vertical magnetic under the threshold of 0.1μT. Since the maximum amplitude of the magnetic field induced near the NMR devices by RFX is 3 μT, an attenuation factor of 1/30 is required to the system.
A feedback scheme was tested showing the effectiveness of the active shield, but rising up doubt about the driving system.
It was decided to project and realize a Open-loop active shield.
At the beginning of my PhD activity, a suitable system to transmit the signal was individuated in the SS 580e transceiver system produced by SRI/PMD. During the PhD, the performance of this telemetry system have been tested and improved to suit the aims of the project.
The coils composing the active shield have been designed and realized, and the power supply has been identified.
Finally, several tests have been carried out with different aims, such as a study on the performance of the transmission system, the electrical characterisation of the coils, the performances of the overall open loop system in compensating the magnetic field induced by RFX.

The overall scheme of this open loop solution will be shown in details on the next chapter. A brief overview of the tests of the system and their results will be given on the third chapter.

CHAPTER V

Design and Realization of the Magnetic Active Shield

In order to solve the incompatibility of the RFX experiment with the NMR spectrometer at the ICIS Institute, it was decided to realize a magnetic active shield. A pair of coils is located close to the NMR instrumentation to produce a B_A compensating magnetic field. The coils are driven by a measure of the I_M current flowing through the magnetizing windings of RFX. This current has been individuated to be the cause of the magnetic disturbance affecting the NMR instrumentation. The measure of I_M should be sent in real time, or with a transmission delay as little as possible.

The overall scheme block of this feed-forward magnetic active shield is described in the first section. In the next sections, details are given about the design of each block making up the shield and on their realization. Last section briefly reviewed the main contents of the present chapter.

1. Overall Block Scheme [21]

During a RFX pulse, the current flowing through the magnetizing windings generates a magnetic disturbance for the NMR devices housed in the ICIS institute located 150 m far from RFX, as described in the previous chapter.

With the aim of compensating this magnetic disturbance, it was decided to project and build a feed-forward magnetic active shield. In this way, the coils creating the compensating magnetic field are directly driven by transmission of a signal proportional to I_M, the current flowing through the magnetizing windings of RFX. No local magnetic measurements are necessary and the coils are driven directly by the signal proportional to I_M, so the scheme can be described also as an open loop active shield.

The sketch of the overall block scheme of the open loop active shield is shown in Figure 1.

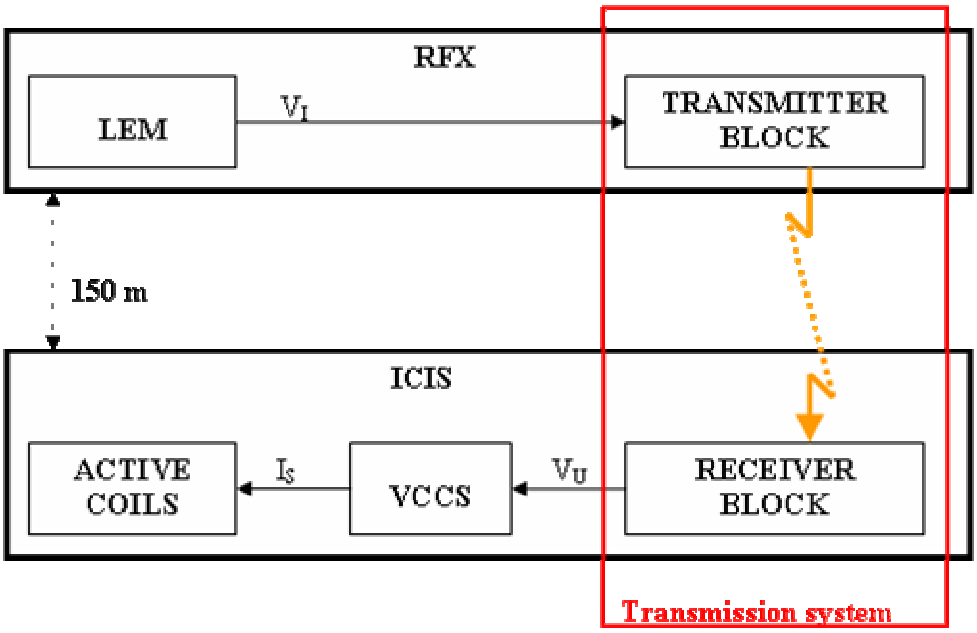

Figure 1 Sketch of the overall block scheme.

The blocks LEM and TRANSMITTER are located in the RFX building, while the blocks RECEIVER, VCCS and ACTIVE COILS are located into the ICIS institute.

The input voltage signal V_I is available from the LEM block. V_I is a measurement of the I_M current flowing through the magnetizing windings of RFX. V_I changes along the time as I_M and is directly proportional to the magnetic disturbance B_{RFX} induced on the NMR instrumentations housed at the ICIS Institute. The LEM block represents the measurement system described in chapter I section 2.2.3.5. The voltage signal V_I is sampled and sent in real time by the TRANSMITTER block to the RECEIVER block.

The RECEIVER block reconstructs the voltage signal V_U which is converted in a current signal I_S by the VCCS (Voltage Controlled Current Source) to drive the ACTIVE COILS. ACTIVE COILS create a magnetic field B_A directly proportional to the current I_M, hence also to the Magnetic disturbance interfering on the NMR spectrometer. The magnetic field B_A should have the same strength of the magnetic field induced by RFX but with opposite sign, in such a way to mitigate the magnetic disturbance by compensation.

The transmission system is made up of the TRANSMITTER and RECEIVER blocks, and they have been designed to correctly reconstruct the driving signal at the ICIS institute. The VCCS and ACTIVE COILS blocks have to generate a magnetic field B_A to correctly compensate the magnetic field induced.

The requirements on the design of the ACTIVE COILS and of the transmission system will be discussed on their respective sections.

The sample probe of a NMR device should be embedded on a highly uniform magnetic field. The sample probe should never sense a varying magnetic field with an amplitude larger than a given susceptibility threshold, as discussed on chapter I. The susceptibility threshold of such an instrumentation is almost 0,1 μT. The project of the overall block has been carried

out paying attention both on the project of the ACTIVE COILS, which have to create a magnetic field as uniform as possible close to the sample probe, and on the project of all the transmission line. In chapter I section 4.2 has been discussed the best way to send the driving signal V_I, a wireless transmission via RF has been individuated as the most promising to be reliable and accurate.

The next sections describe each block of the scheme shown in Figure 1. For each block, the requirements and the design are discussed. At the end of each section, the work done to realize the given block is reported.

2. LEM Block

The LEM block represents the measurement system of the current I_M flowing through the magnetizing winding of RFX. The maximum value of the current is I_M=50kA, which is related to a RFX pulse with plasma current I_P=2MA. The measurement system LEM was designed in such a way to measure a current up to 60 kA in case of failure.

The output impedance of this system is $R_{OUT} \cong 0.8\ \Omega$. The voltage signal supplied by this systems is the driving signal of the active shield system. This output signal usually has a spectrum between 0 and 4 kHz, while its dynamic range is within ±10V. The maximum value of the voltage is related to the maximum value of the I_M current foreseen. The voltage signal is proportional to the I_M current, the proportionality factor is:

(1) $$G_{LEM} = \frac{60 \quad kA}{10 \quad V} = 6000 \quad \Omega^{-1}$$

The signal V_I from the LEM is available on the diagnostic hall of RFX [26]. The TRANSMITTER block is located on a laboratory room, on the upper floor. A 10m long cable is used to connect the output of the LEM with the input of the TRANSMITTER block.

3. Transmission System

TRANSMITTER and RECEIVER blocks make up the TRANSMISSION SYSTEM. The overall chain of the transmission system is shown in Figure 2. The TRANSMITTER block is made up of a TX BUFFER, the ST 580e SRI/PMD transmitter and of a YAGI antenna. The RECEIVER block is made up of an antenna YAGI and the SR 580e SRI/PMD receiver.
The hearth of the transmission system is a commercial transceiver used for telemetry purposes: the SS 500e by the SRI/PMD [30].

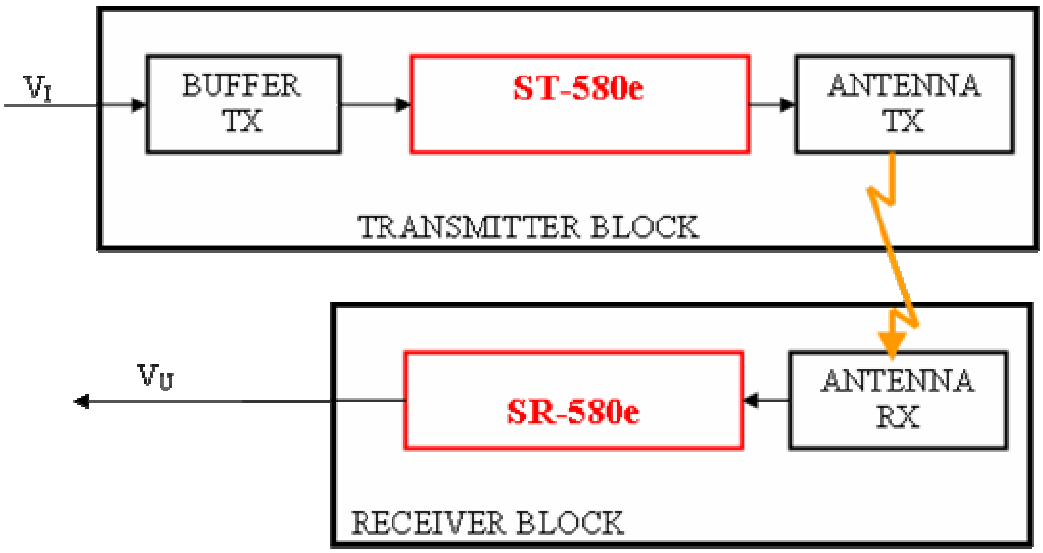

Figure 2 Block scheme of the entire transmission system.

The overall transmission system has been chosen according to the requirements exposed in section 3.1.
Section 3.2 is devoted to show the performance of the commercial transceiver utilized for this application. In section 3.3, the set-up of this transceiver is reported.

3.1. Requirements on the Transmission System

The main condition to be satisfied by the transmission system is that the error field has to be ever less than the susceptibility threshold. As discussed in chapter I section 4.3, it was chosen to send the signal via RF transmission with an A/D conversion at the transmitter and a D/A reconstruction at the receiver.
Several kinds of error can occur:

- error due to the limited bandwidth of the transmitted signal;
- Quantization error;
- Offset voltage at the output of the receiver;
- Errors due to a too large transmission delay.

The bandwidth of the input signal is 0-4 kHz.
The analog voltage signal V_I has to be converted in a digital one to be sent via RF. The sampling rate should be greater than 16 ksps (sps: samples per second) in order to correctly send all of the harmonic contents. However, a sample rate greater than 4 ksps could suffice to send the spectra up to 1 kHz.
In order to avoid errors due to the quantization, each sample should be sent with a resolution better than 7 bit. A resolution better than 11 bit could make the quantization error minor than the 0.1%.
The offset voltage at the output of the receiver should be adjustable or minimized. An offset voltage could feed the ACTIVE COILS with a stationary current also in absence of the disturbance. Moreover, also the gain of the receiver should be finely adjustable. In fact, the amplification factor of the overall transmission line has to be fixed in order to match the correct amplitude of the compensating magnetic field.
Finally, the signal has to be sent in real time to the ACTIVE COILS, i.e. with a transmission delay as little as possible. In Figure 3 is shown the error field (green) that a delay t_d could produce for a typical time behaviour of the I_M current, if any other source of error exists. Two spikes can be identified on the time behaviour of the error field for the typical time behaviour of a RFX pulse.

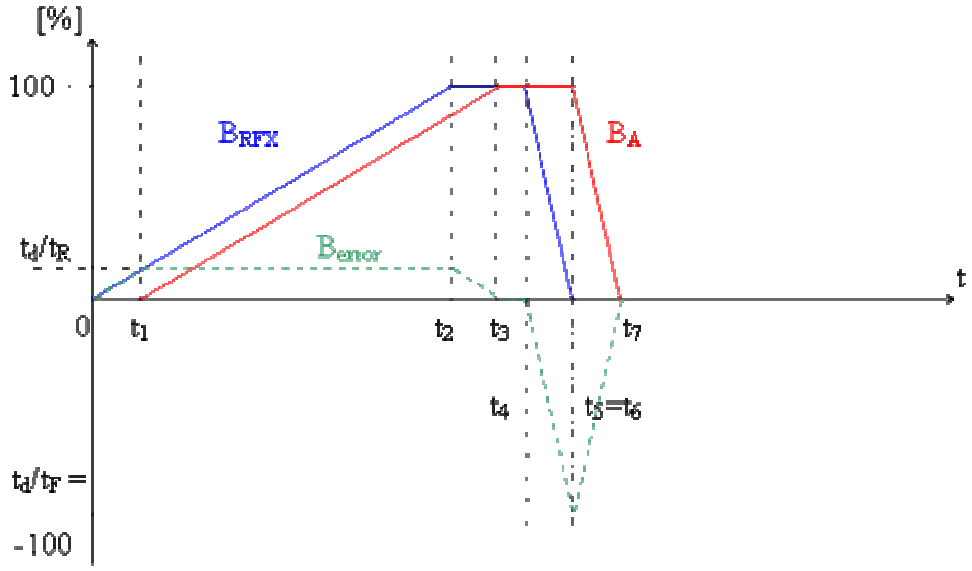

Figure 3 Error due to a transmission delay (green dashed lines). The B_A field (red) is the ideal reconstruction of the B_{RFX} (blue) magnetic disturbance, with a delay of t_1.

In order to ensure that the magnitude of the error field could never exceed the susceptibility threshold of 1μT, the maximum value of the errors should be less than the 1% of the maximum value of the flat-top uncompensated field which is about 3μT. With reference to the typical RFX waveform shown in Figure 3, for the ramp-up the delay time has to be

$t_d \leq 0.01*t_2=30$ ms.

Where **$t_2=3$s** is the ramp-up time of the RFX pulse. This condition is quite easy to be achieved.
The ramp-down would require:

$\mathbf{t_d \leq 0.01 * t_F = 100\ \mu s}$

where $\mathbf{t_F = t_6 - t_4 = 10ms}$ is the time in which the I_M current decays from the flat top to 0.
It is difficult to achieve the above condition.
It is worth noticing that for $\mathbf{t_d < 10ms}$ the spike has a period less than 20ms, corresponding to a spectrum with a fundamental frequency greater than 50 Hz. So, it shall not affect the NMR instrumentation.
So, the requirement for the transmission system is that the overall delay shall be:

$\mathbf{t_d \leq 10ms.}$

The definition of these requirements allowed to individuate a suitable commercial transmission system (SS 580e). This system is described on the next section.A TX BUFFER has been designed and realized to correctly provide the V_I signal to the ST-580e transmitter, as described in section 4, and two directional YAGI antennas have been installed to ensure a good reception of the signal at the ICIS Institute, as reported in section 5.

3.2. Overview of the SS 580e transceiver [30]

The SS580e transceiver is a Digital Telemetry Equipment produced by the SRI/PMD's Wireless Link.
Telemetry can encompass the entire process by which a measurement value is obtained, possibly quantified, qualified, or processed in other ways, and then transmitted via some mechanism to the "end user" for final processing or response actions. The "end user" may be a human for manual interpretation and analysis or, more often, a machine for automated processing functions. The phrase "Digital Telemetry" simply specifies that the methodology utilized to obtain, process and transmit the measurements data incorporates digital techniques, a highly efficient and more reliable means of handling data processing for transmission.
Typical measurements which telemetry can provide access to include: temperature, speed, direction, motion, location, distance, displacement, strain, torque, energy, power, pressure, humidity, density and so on. Furthermore, many applications require access to multiple and/or a variety of these measurements at the same time to allow for meaningful interpretation of the data.
The present application needs to transmit in real-time an analog differential voltage signal.
The following diagram (Figure 4) presents a simplified overview of the SRI/PMD Wireless Link system.

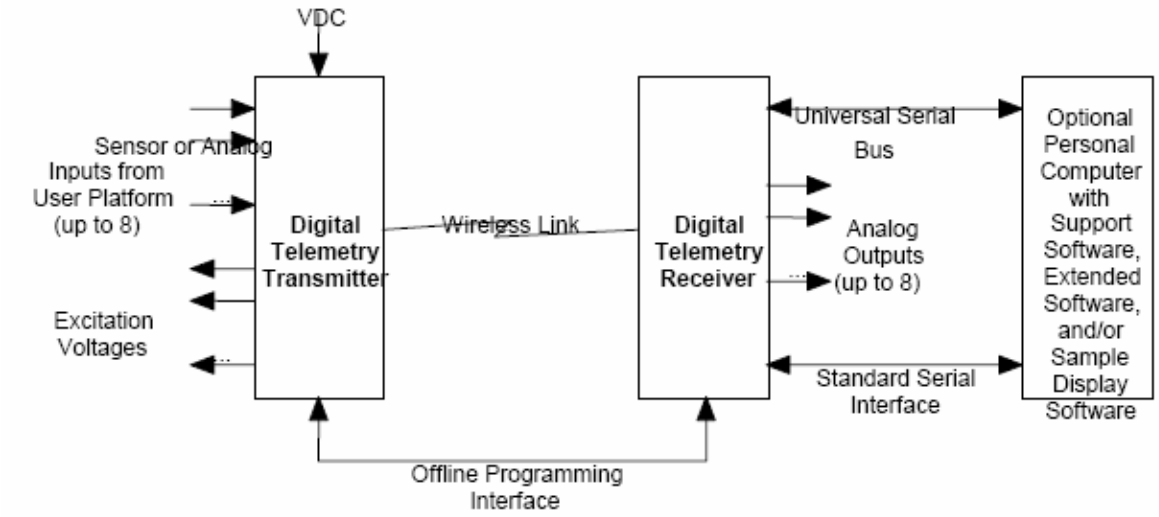

Figure 4 System Overview.

As shown in Figure 4, the system consists of the following major elements:

1) The Digital Telemetry Transmitter is a miniaturized and ruggedized radio frequency (RF) transmitter providing the interface circuitry to select and sample up to 8 sensor or analog inputs, condition the signals and transmit the detected readings in digital format over the Wireless Link.
2) The Digital Telemetry Receiver provides the logic to recover the transmitted data, detect and account for errors which might have been introduced via the transmission path, and output error free and digitally compensated samples of the sensor data in both analog and

digital output formats. The receive system also supports an optional interface to a standard personal computer for status, control and analysis functions.

3) The optional Personal Computer can be utilized to execute a support software package. The support software provides for:
   a) Monitoring general system health, communications performance, and sensor gain/offset calibration functions.
   b) Editing of sensor definitions including type, sampling frequency, filtering, measurements ranges, and so forth.
   c) Sample capture/display software for storing measurement data to the PC disk or displaying real time data in graphical/scope type formats.

In the July, 2007, the required SS-580e system has been delivered by the SRI/PMD. It is a Telemetry System working at 868 MHz, able to transmit up to 2 differential analog inputs, or up to 8 sensor inputs. The measurement resolution is of 16 bits and the Transmitter can reach a sampling rate up to the 17Ksps. The Receiver is able to dynamically compensate the Transmitter gain/offset temperature drift and also for sensor drift due to temperature, such as thermocouples. Factory calibration of above characteristics provides for better than 0.5% measurement accuracy, typical.
In the next sections, the details of both the Transmitter and the Receiver are reported, and an overview of the overall System Data Processing is given.

3.2.1. Transmitter Details

Figure 5 presents a more detailed overview of a Digital Telemetry Transmitter.

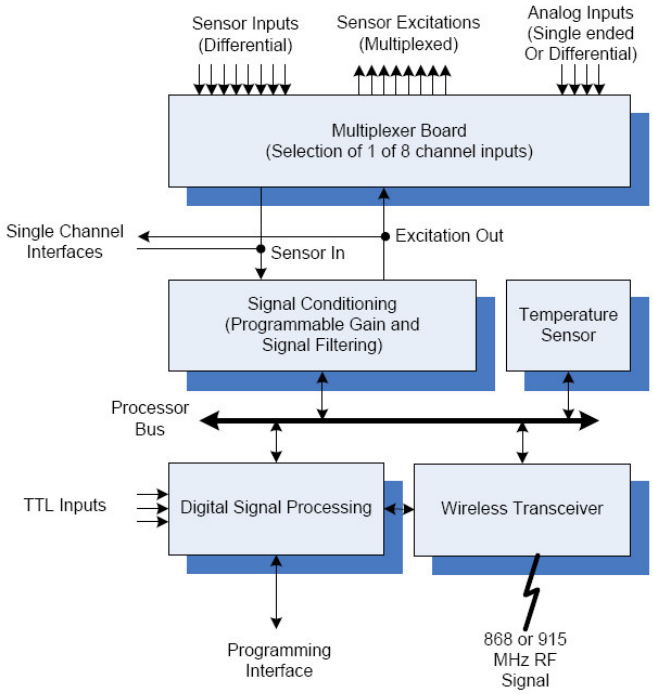

Figure 5. Transmitter Block Diagram

At the heart of the transmitter design is a high-speed processor with analog to digital conversion capabilities. Execution processing of the processing logic is determined via configuration data stored within electronically erasable programmable read-only-memory (EEPROM). The configuration tables contained within this memory dictates operational characteristics such as the number of input sensor channels, the type of each input, output RF frequency selection, and so forth. EEPROM memory space within the transmitter, including both configuration tables and executable program space, can be reprogrammed via the external programming interface to the Digital Telemetry Receiver. As such, all significant operational characteristics of the Transmitter can be readily modified or customized, even for fielded units.
For transmitters limited to a single input sensor channel, onboard circuitry is available to process the input measurement data through signal conditioning circuitry. All sensor-input logic also includes associated excitation voltage output circuitry that may be utilized to drive sensors requiring an input voltage, such as balanced bridges.
Operation of the signal conditioning logic is controlled via the processor to establish appropriate gain settings. This powerful feature of the design allows the same circuitry to be reprogrammed to support a wide variety of potential input sensor types. Furthermore, because the sensor type information is also included in the EEPROM configuration tables, these settings can be changed for various user requirements on a sensor by sensor basis.
A programmable filtering is also provided for the sensor inputs. This allows for configurable settings of the sensor input filtering based on sample rates through the ADC as well as signal multiplexing requirements for multiple channel systems.

In addition to sensor inputs, multiple channel systems also include analog channel inputs. These four inputs are typically pre-conditioned signals ranging up to 0-5 VDC for single ended inputs. Alternatively, the analog inputs can be paired to provide two differential inputs with range up to ±2.5 VDC. When activated, these channels replace the corresponding channels of the sensor inputs.

Data transmission across the wireless link is accomplished with dual data channels known as the primary and the background channels respectively. The primary data channel is allocated in excess of 90% of the transmit bandwidth and includes the input sensor data measurement information. The background channel is relatively low rate and contains information required for receive side frame synchronization and error detection. Another key feature to the design is that the background the background channel is also utilized to transmit data pertaining to the current transmitter operating temperature. This information is utilized to support real-time temperature based compensation of sensor data samples through the receive chain.

3.2.2. Receiver Details

Figure 6 presents a more detailed overview of the Series 550e Digital Telemetry Receivers.

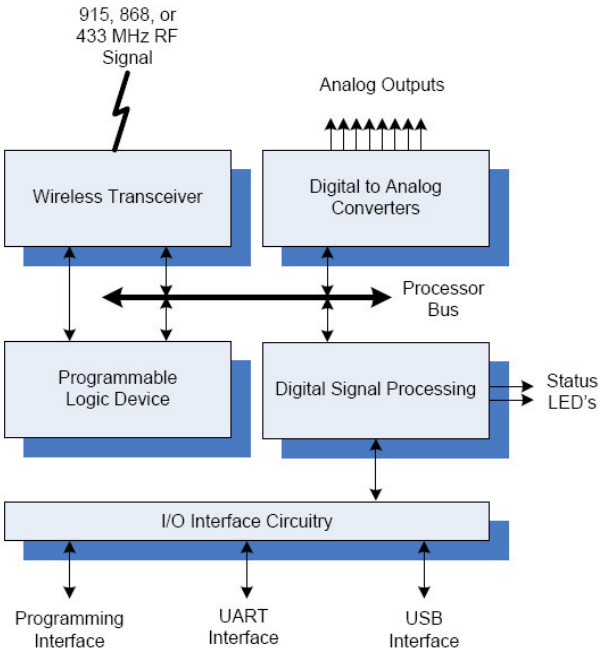

Figure 6 Receiver Block Diagram

The receiver incorporates a high-speed digital signal processor to provide for full real time processing of incoming measurement samples. Logic within the processor interfaces with the Wireless Link Receiver via a high speed programmable logic device (PLD) to recover bit, byte, word, and frame synchronization with the incoming data stream. The process of achieving this level of synchronization is known as the acquisition process.
After proper acquisition, the processor begins performing error detection functions via embedded checksums within the incoming data. All received data samples during a frame detected to have an error within it are flagged as error samples.
The data samples are processed through configurable data processing prior to outputting the data to analog and digital output channels. Data processing, in this case, may include standard gain adjustment multiplication, offset addition, transmitter temperature dependent data compensation, as well as alternate data averaging and or filtering functions.
Program execution of the processor is directed via code and configuration tables stored in EEPROM memory space resident within the device. The contents of this memory space can be loaded via a remote control RS-232 interface to a standard personal computer. This feature allows fielded Digital Telemetry Receiver systems to alter the processing characteristics of the signal received by the transmitter.
Digital Telemetry Receiver supports eight analog output channels. These onboard channels supports 16 bits of data resolution and can be programmed to cover an entire output voltage range of -10 to +10 VDC.

3.2.3 System Data Processing Overview

The Telemetry Transceiver here presented can be configured to process input sensor measuerements anywhere within the range of 0 to 5 VDC. Typically, instrumentation sensors do not utilize this entire measurement range, and can produce an amplitude of about one mV. These signal levels are not overly useful to most end-user processing equipment. To create a useful signal, the product lines has been provided of programmable gain, offset, and data filtering functions on the input sensor signals.
Several stages of gain are applied to the input signal such that the configured measurement input levels of sensor end corresponds to a specified output analog voltage range (e.g., -10 to +10 VDC). As an example, it implies a gain of x10000 in order to translate 1mVDC to 10VDC.
A gain of this magnitude is never 100% accurate. Furthermore, small errors introduced by the exact mechanical installation of the sensor, ground differentials, cabling losses, or transmitter sensor input to digital measurement processing circuitry end up causing additional errors. These errors are reflected as incorrect gain or variations in offset (i.e., where a 0 reading does not correspond to a 0 output).
In order to compensate for these factors, the Digital Telemetry System provides programmable gain and offset controls that are invoked at various stages within the system. Figure 7 provides a very simplistic overview of this process.

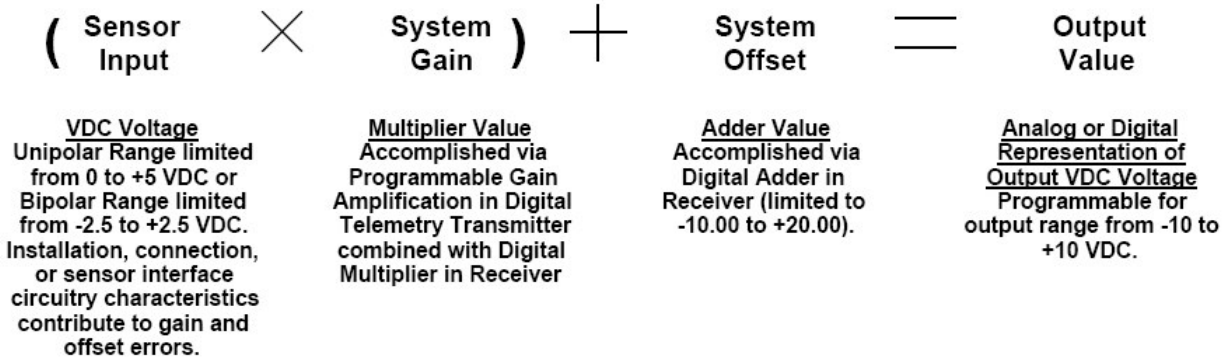

Figure 7 Data Processing Overview

The system gain and offset values are set to not only translate the input measurement signal range to the desired analog output voltage range, but are also utilized to account for the gain and offset errors discussed above.
Figure 8 presents a more detailed overview of the entire signal processing of the Digital Telemetry System.

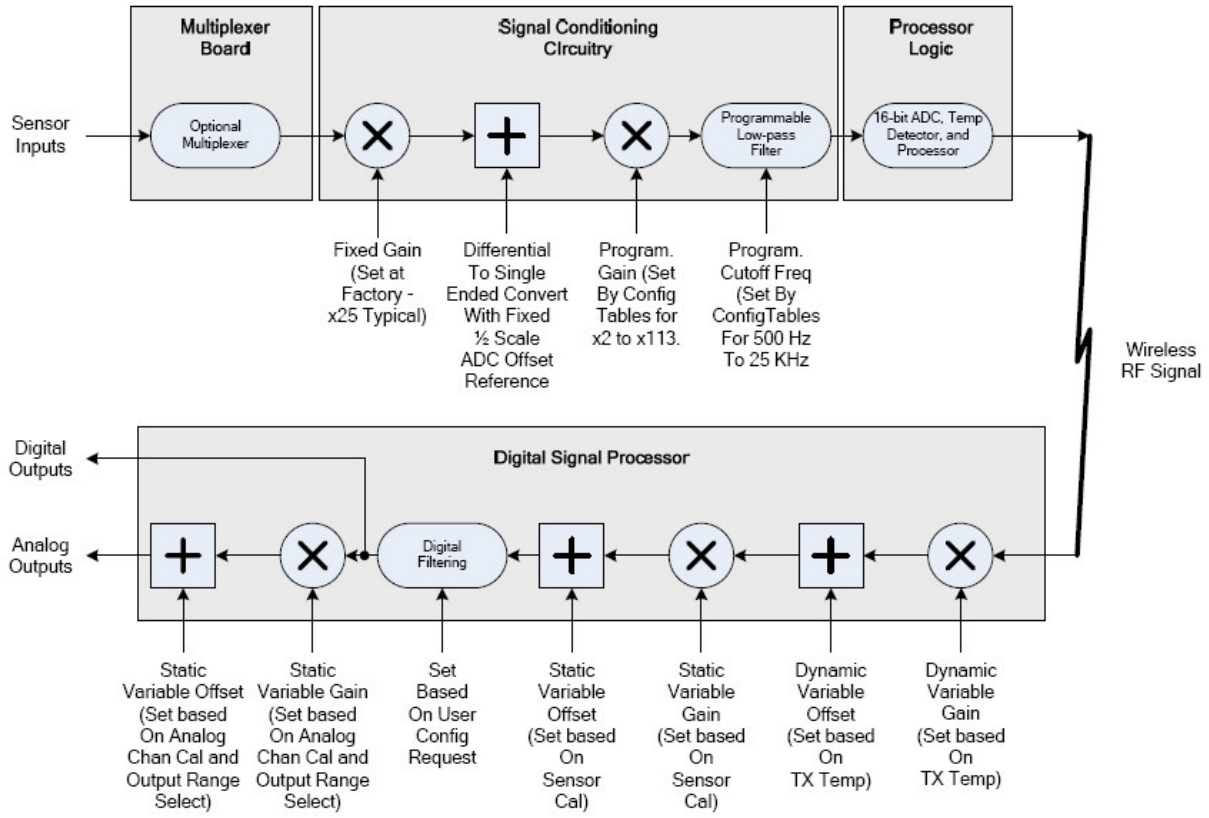

Figure 8 Data Processing Details.

Normal sensor inputs are processed through three stages of conditioning prior to digitization. All input signals through this path are treated as differential inputs. For sensor inputs with a grounded negative lead, the sensor ground must be left floating with respect to the transmitter ground.

The first stage applies a fixed gain, typically set for x25. The fixed gain is accomplished with a low noise, differential instrumentation amplifier, thus providing enhanced conditioning performance through the transmit system, including high common mode rejection.

The next stage establishes the offset to the input signal, bringing it to the center point of the analog to digital converter (ADC) range. This process also converts the differential signal to its single ended equivalent.

The next process provides a programmable gain stage. With a gain varying from x2 to x113, this stage provides the final amplification to the required input range for the ADC. Typically, transmit side gain is limited to cover 90% of the ADC range, which precludes sensor gain and offset errors from saturating the ADC.

All programmable logic on the transmit side may change in a per channel basis for multisensor channel systems. However, these settings are classified as static in that they are established by the PC control software and downloaded into the transmitters EEPROM space. While the transmit logic change these settings for each channel, they are not changed in response to any other dynamic conditions, such as transmitter temperature.

The receive side provides the final gain and offset processing of the system. This gain/offset is not only utilized to convert the signal to the selected output range of the digital to analog

conversion (DAC) for analog channels (0-5, 0-10, ±5, ±10 VDC), but also accounts for gain/offset errors of the input sensor signal, as well as dynamic characteristics of the transmitter system.
The first part of the processing through the receive side is dependent upon the transmitter operational temperature at the time of the measurement. The transmitter logic monitors its own temperature and periodically reports this value across the wireless link. This allows the receive side to dynamically compensate for gain/offset variations of the transmitter due to temperature. A highly accurate factory calibration of each transmitter product across temperature provides the means for precise measurements in the field.
For sensor data which varies with temperature (e.g., thermocouples), the dynamic gain/offset compensation feature is utilized to modify the receiver gain multiplier and offset added to compensate for these real time variations. Thus, the system automatically provides the 0 reference junction for these types of devices. This dynamic gain/offset processing is followed by additional static logic which is controlled by PC software sensor calibration processing logic. This feature is utilized to correct installation specific errors of the individual sensors. For example, an offset error in the installation of a strain gage would be compensated for by this level of static gain/offset corrections.
A final stage of static corrections is applied to account for analog channel output errors. This process is controlled by analog channel calibration logic of the PC control software combined with the operator selected output range of the channel (i.e. 0-5V, 0-10V, ±5V, ±10 V).
Processing of the analog signal is different from that of the sensor signal, because the analog signal have a dynamic range larger then the dynamic range fo the sensor signals. In fact, sensor signal can range up to ±45mV while analog signals can be single ended (0-5VDC) or differential (±2.5VDC). Analog input signals to the transmitter are processed directly into the ADC through a voltage divider, bypassing the entire discrete signal conditioning circuitry. Since these signals are not buffered, they exhibit high source impedance and typically require an external driver. The analog input signals can be grouped to form a pair of differential input analog inputs through the ADC. After digitization, all remaining gain/offset logic through the receive logic is identical to normal sensor inputs.

3.2.4. Digital Telemetry Control software

The Control software of the digital telemetry System runs on a standard PC operating under the Windows operating system. This software provides a number of critical functions for the system, including the following:

- Communications Analysis Functions
  - On-line monitoring of communications performance
  - Analysis of communications frequencies
- System Calibration
  - Modifications to system gain and offset settings
  - Calibration of output analog channels
- Table Control Functions
  - Edit functions of currently defined Digital Telemetry Systems
  - Download functions to update or restore EEPROM memory space

3.3. Set-up of the SS-580e Transceiver

The acquired Telemetry Transmission system can be utilized for a wide range of signal inputs. In particular, it can be used to accurately transmit the temperature sensed by thermocouples (types J or K). The data processing, as described in section 3.2.3, allows the compensation of thermal drifts in the region of the thermocouple. Moreover, the RF transmission allows to transmit the data from a transmit side with a given reference voltage to a receive side referred to ground. Therefore, such a data transmission system might be helpful to design the layout of the diagnostic system of the Neutral Beam Injector (NBI), where a great number of thermocouples are foreseen and several diagnostics are required on the High Voltage grids (1 MV).
For the present purposes, the SS 580e has been configured to transmit an analog signal from the IGI Institute to the ICIS institute. The transmitter samples an analog differential signal (±2.5VDC) with a sample rate of 8.5kHz for the chosen resolution of 16bit. In fact, the sample rate of the Transmitter is dependent upon:

a) Wireless link Transmit data rate (which has been choose as high as possible)
b) Configured Resolution of ADC Samples (i.e., 8,12, or 16)
c) Number of Active Sensor Channels

These same factors fix the system throughput delay (i.e. time from sensor sampling through corresponding output on the receivers digital or analog ports). With the actual configuration, the throughput delay of the Digital Telemetry System is about 4msec. Small improvements could be achieved lowering the resolution to 12 bit (Sample Rate of 9.5kHz, and a throughput delay of 3.5msec), so it was decided to send the signal as accurate as possible.
It is worth noticing that the Control Software allows the adjustment of the overall amplitude factor, acting on the gain of the receiver. This feature has been effectively used to match the correct amplitude of the compensating magnetic field with the amplitude of the disturbing magnetic field induced by RFX.
The Control Software has been useful to calibrate all of the transmission line and minimize the overall offset as well as to check the performance of the transmission line, as reported in chapter 3.
The mean characteristics of the actual configuration of the Digital Telemetry System are reported in Table 1.

Table 1 Actual set-up of the digital telemetry system SS 580e.

Input range	Output range	Number of channels	Transmission frequency	Transmitter data rate	ADC resolution	Sample rate	Throughput delay
±2.5V	±10V	1	868 MHz	1.523 kbps	16 bits	8.5kHz	4ms

4. TX BUFFER

As reported in the last section, the ST 580e Transmitter is configured to send a differential analog output voltage ranging within ±2.5VDC. The analog signal is digitalized with a sampling rate of about 8.5kHz. The range of the voltage signal exiting from the LEM block ranges within ±10VDC.
No processing is carried out by the transmitter to the input signal if it is analog. For these reasons a buffer circuitry has been designed and realized to process the input signal V_I and to provide a low impedance source to the ADC converter provided by the transmitter.
The aims of the circuitry are to attenuate the signal of a factor equal to 0.25 and to filter the signal in order to avoid aliasing errors due to the noise at the high frequencies.
The NMR spectrometer is susceptible to magnetic signal with a spectra within 0 to 3 Hz, the low frequency part of the signal needs to be sent with particular attention. The spectra of the input signal V_I is within 0-4kHz, so it may be provided to the ADC without requiring any filtering. However, to avoid error due to the aliasing, it has been preferred to filter the signal by a low-pass filter with a cut-off frequency of about 3kHz. Finally, a Butterworth's frequency response has been choose in order to not modify the low part of the signal. In Figure 9 is shown the scheme of the Multiple Feed Back stage (MFB) which furnish the processing of the signal. The resistance and capacitance of the present block have been dimensioned with the use of SPICE, and the characteristics of the circuit (cut-off frequency, time delay) have been evaluated.

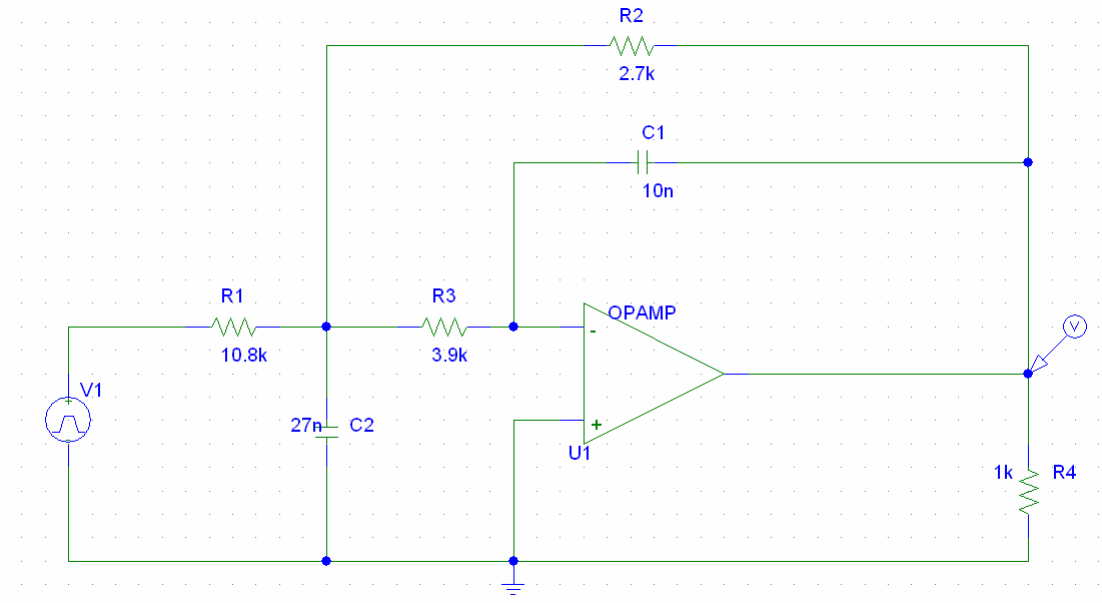

Figure 9 Electric scheme of the MFB stage of the TX BUFFER block.

The circuit shown in Figure 9 is a second order low-pass filter, that is with an attenuation of 40dB/decade over the cut-off frequency. The resistance and capacitance have been designed to achieve a cut-off frequency of about 3kHz and a DC attenuation factor of the -0.25. Resistance R1 has been realized as the series of a resistance of 10kΩ and a trimmer with a variable resistance from 0 up to 2kΩ. The ideal value of R1 has been evaluated to be 10.8kΩ using SPICE.

During the first test of the circuitry, the trimmer has been finely adjusted in order to match the attenuation desired. In fact, the frequency response has small change varying the trimmer from 0 to 2kΩ. That has been evidenced both with simulations carried out running SPICE and with experimental tests.
In Figure 10 is shown the overall scheme of the TX BUFFER circuitry. In addition to the MFB stage before presented, the circuitry is made up also of an input stage (INA114) and a DC/DC converter (TEN 122).

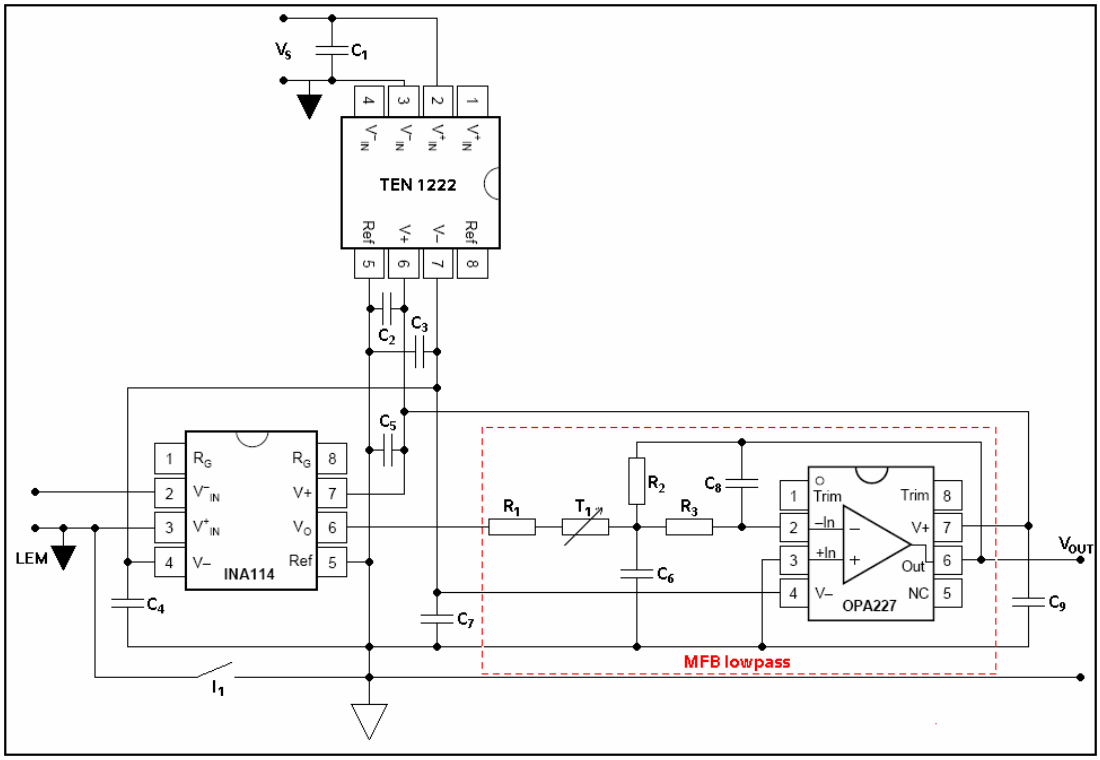

Figure 10 Electric scheme of the TX BUFFER block.

The input stage is a differential amplifier with unitary gain. The LEM block providing the input signal is located in a room of the IGI institute where the data acquisition equipment is installed. The Transmitter and the TX BUFFER circuitry are located in a Laboratory room on the upper floor. A long cable is used to connect the output of the LEM block with the input of the TX BUFFER block. The ground reference of the laboratory and of the LEM block could differ. The long connection cable can suffer by common mode noises. The input stage is aimed to eliminate these noises and to separate the ground reference of the input of this stage with the ground reference of the MFB stage. However, a switch I_1 has been inserted to reconnect the two ground references.
The power input of the circuitry is provided by an AC adapter with a voltage of 0-12VDC by the laboratory desk. The DC/DC converter TEN 122 converts this voltage to ±12VDC, it also provides an isolation from the ground reference of the laboratory to the ground reference of the room housing the LEM block. In such a way, it provides the power input voltage for the input stage and the MFB stage and also for the Transmitter. The ground reference of the Transmitter and the output of the Buffer circuitry are not directly connected. The chain of the entire transmission system has a tunable gain. In fact, the gain of the transceiver can be adjusted by means of the Control Software. Tuning the receiver with a gain g=1, the ratio between the input signal voltage V_I entering on the transmission system,

and it reconstruction V_U gives out by the transmission system is also unitary. In fact, both the signal range within ±10V. Varying the gain g of the receiver, the ratio between the input and the output signals is equal to g:

$$\frac{V_U}{V_I} = g \tag{2}$$

5. Antennas

The IGI buildings R4 and R5 are shielded by several metal Faraday cages [26]. In particular a metal cage screens each floor of the R4 building, where the laboratory room housing the transmitter is located. So, the signal transmission needs to install the antennas over the roof and out to the premises where the receiver and the transmitter are located. Moreover, in order to allow a good accessibility to the instrumentation, the transmitter should be pose into the laboratory room at IGI Institute where the connection cable to the LEM block is available, and the receiver should be pose into the room at the ICIS Institute where the NMR instrumentations are currently housed. Therefore, two long RF cable have to be used in order to connect both the receiver and the transmitter with the respective antennas. An 15m long RF cable is utilized to connect the transmitter with its antenna posed on the roof of RFX over the room where the transmitter is housed, and a 10m long cable is utilized to connect the receiver with the antenna posed on the ICIS Institute over the room where the receiver posed. The use of long connection cables from the receiver and the transmitter to the respective antennas causes an additional attenuation of the RF signal to be taken into account.
The SRI/PMD provided both the transmitter ST 580e and the receiver SR 580e with a quarter-wave stub antenna. Moreover, the roofs of the two premises have different heights from the ground and different obstacles can be found along the path from antenna TX to antenna RX.
The two premises, IGI and ICIS Institute, are far about 150 m from one another. A preliminary transmission test shown that, using the quarter-wave stub antennas, the transmission range of the SS 580e is sufficient to transmit a signal if the transmitter and the receiver are posed immediately out of the respective premises and at ground level. The distance between the two antennas increases, installing them over the roof of RFX and ICIS. For these reasons, the RF signal should be amplified or at least the attenuation due to the RF cables have to be compensated.
In order to improve the RF transmission, it was decided to acquire two YAGI antennas at 868 MHz. Quarter-wave stub antennas [32] have a low directionality. The quarter wave or unipole antenna is a single element antenna feed at one end, that behaves as a dipole antenna.. Since the fields above ground are the same as for the dipole, but only half the power is applied, the gain is twice (3dBd over) that for a half-wave dipole [33], that is 5.14 dBi with respect to an isotropic antenna.
A basic Yagi antenna [34,35] consists of some straight elements, each measuring approximately half electrical wavelength. The antenna can be balanced or unbalanced. The Yagi is inherently a balanced antenna, but it can be fed with coaxial cable and a device called a *balun* at the point where the feed line joins the *driven element*. The driven element of a Yagi antenna is the equivalent of a center-fed, half-wave dipole antenna. Parallel to the driven element, and approximately 0.2 to 0.5 wavelength on either side of it, are straight rods

or wires called *reflectors* and *directors*. A reflector is placed behind the driven element and is slightly longer than half wavelength; a director is placed in front of the driven element and is slightly shorter than half wavelength. A typical Yagi has one reflector and one or more directors. Due to its particular geometry, the antenna propagates electromagnetic field energy in the direction running from the driven element toward the directors, and is, by reciprocity, most sensitive to incoming electromagnetic field energy in this same direction.
Two 868MY08 Yagi antennas have been bought from the Linkit SRL [36] together with the H1000 connection cable. The characteristics of a 868MY08 YAGI antenna are reported in Table 2. Figure 11 shows the radiation diagrams for both the horizontal and the vertical planes.

Table 2. Main characteristics of a 868MY08 YAGI antenna.

Transmission frequency [*MHz*]	Element number	Gain [*dBi*]	Bandwidth [*MHz*]	Maximum Power [*W*]	Z [*Ω*]
868	8	12,4	40	120	50

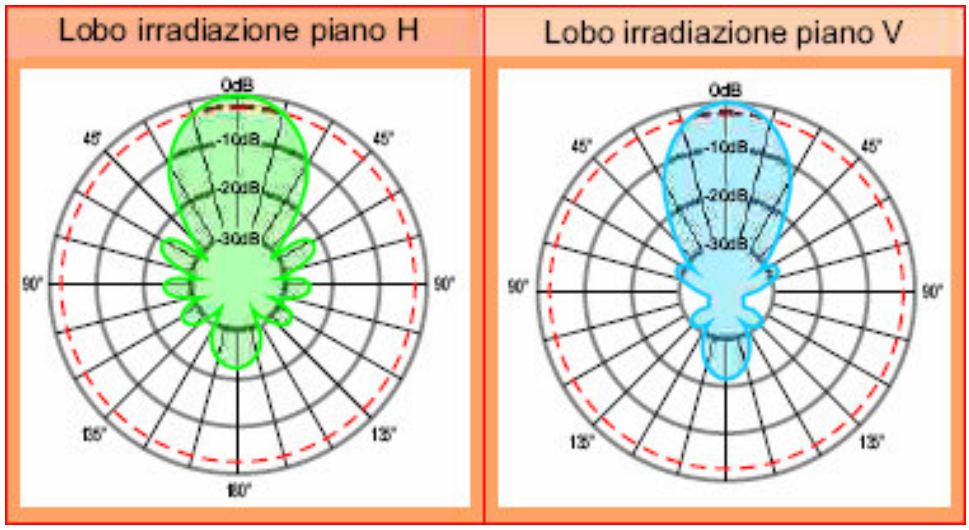

Figure 11 Radiation diagrams on the horizontal (left) and the vertical (right) planes.

The connection cable H1000 is a low-losses cable with 10.3 diameter, its attenuation is equal to 0.24 dB/m. The connection RF cable from the transmitter to the ANTENNA TX is less than 15 meters long. The connection RF cable from the ANTENNA RX to the receiver is less than 10 meters long. Therefore, it is expected that the cables cause an attenuation of the RF signal equals to:

(3) $$A_{cable} = -0.24 \cdot (15 + 10) = -6 \quad \text{dB}$$

Two connections are provided for each cable. Total Power losses due to these connections are estimated to be:

(4) $$A_{conn} = -0.1\sqrt{f \cdot 10^{-9}} \cdot n_{conn} = -0.1\sqrt{0.868} \cdot 4 = -0.37 \quad \text{dB}$$

As before described, a preliminary transmission tests showed that a transmission is possible if the receiver and the transmitter are located immediately out from the respective premises. With respect to the operating condition of this test, the minimum gain of each antenna has been evaluated. With respect to these conditions, the attenuation due to the increased distance can be evaluated referring to the case of transmission by an ideal isotropic antenna. The distance between the IGI and the ICIS premises is about r_1= 150m; the distance between the TX and RX antennas is less than r_2=250m. The power emitted by an isotropic antenna varies with the distance as 1/r. The free-air attenuation, due to the increased distance, is estimated to be:

(5) $$A_{free-air} = -10 \cdot \log_{10}\left(\frac{r_2}{r_1}\right)^2 = -10 \cdot \log_{10}\left(\frac{250}{150}\right)^2 = -4.44 \quad \text{dB}$$

In order to correctly estimate the minimum gain required to the antennas, the gain of the quarter-wave stub antennas (with respect to an isotropic antenna) should be subtracted. Therefore, the minimum gain required is:

(6)

$$G_{antenna} = -\frac{A_{cable} + A_{conn} + A_{free-air} - 2 \cdot G_{1/4}}{2} = -\frac{-6 - 0.37 - 4.44 - 10.28}{2} = 10.65 \quad \text{dBi}.$$

As shown in Table 2, the gain of the 868MY08 overcomes this value of 2dB. So, a small improvement on the transmission of the signal could be achieved.
It is worth noticing that during the preliminary transmission test the transmitter was configured to transmit with the maximum power transmission (+15dBm), and the receiver was configured to have the maximum sensibility.
As a conclusion, the choice of the 868MY08 antennas should allow a good transmission of the RF signal, with the helps of their better directionality. A small improvement should be achieved with the helps of this “passive” gain, which makes not necessary to insert along the transmission line a RF amplifier.
In chapter 3 are reported the final transmission tests showing the good performance obtained by the transmission system here described.

6. ACTIVE COILS block

The ACTIVE COILS block is driven by the current signal I_S produced by the VCCS block. Considering that this signal is a perfect reproduction of the I_M current of the magnetizing winding, and so, it is directly proportional to the magnetic disturbance B_{RFX}, the ACTIVE COILS should create a magnetic field B_A satisfying a uniformity criteria as discussed in the next section. Moreover, NMR instrumentation needs to be refuelled with Helium gas. The structure of the active coils should allow the refuelling of gas He. Starting from these needs, the design of the active coils has been carried out and realized as described in section 6.2 and 6.3. Finally, the equivalent electrical circuit of the coils has been designed starting from experimental measurements. This work is reported in section 6.4. Experimental measurements of the coils have been carried out with the aim to check the correspondence between the magnetic field produced by the coil as evaluated during the calculation and magnetic field actually produced by the real coil.

6.1 Uniformity Requirements

In correspondence to a RFX pulse, the active coils generate a compensating magnetic field B_A. Under this condition, without any other source of disturbance, the overall magnetic field close to the sample probe of the NMR spectrometer is the sum of three parts:

- the magnetic field produced by the permanent magnet of the NMR spectrometer, B_{MS}, which is spatially uniform in the volume where the probe containing the sample is located and with a magnitude of 4,7 T;
- the B_{RFX} field, which is also considered spatially uniform in the same volume and can have a maximum value of 3μT;
- the B_A compensating field.

Considering that the B_A field should have a maximum value equal to 3μT, it and its spatial variations will be ever less than a part of million of the B_{MS} field [21].
During a RFX pulse, the error field obtained subtracting B_A to B_{RFX} must never exceed the susceptibility threshold of the NMR spectrometer:

$$\left|B_{RFX,max} - B_A(x,y,z)\right| < 0.1\mu T \tag{7}$$

in any point close to the sample probe. The last condition has to be achieved in all of the volume. Assuming that the present condition is achieved in a point (x_0, y_0, z_0), the spatial variations have to be limited in order to ensure that the condition (7) is achieved for each other point (x_1, y_1, z_1) close to the sample probe of the NMR. This means that the conditions:

$$\frac{B_A(x1,y1,z1) - B_A(x0,y0,z0)}{B_A(x0,y0,z0)} < \frac{0,1}{3} = 3,3\% \tag{8}$$

Shall be verified at any point (x_1, y_1, z_1) in the volume of the sample.

In order to guarantee that the spatial variations of the magnetic field B_A around the sample probe are as little as possible, the design of the ACTIVE COILS has been carried out with the aim to create an ideal volume surrounding the sample probe as large as possible where the variations of B_A are under the 1% for each point inside this volume.
The compensation of the magnetic disturbance could be achieved using a single coil, but the required field homogeneity criteria could not be satisfied. A number of coils larger than two would guarantee a more uniform magnetic field, but a large number of coils would make the accessibility to the NMR more difficult. A good accessibility to the NMR devices is required in order to allow the refuelling of gas Helium. For this reason, a structure made up of two coils has been preferred. One of the coils is placed on the floor and the other one is fixed to the ceiling of the room in which the NMR are housed. So, a couple of Quasi-Helmholtz square-shaped coils has been chosen as the best solution.
The NMR devices can not be moved from their present location. So, the real dimensions of the room and the obstacle near to each NMR instrumentation have been taken into account. In Figure 12 a sketch of the room where the NMR instrumentations are housed at the ICIS institute is shown.

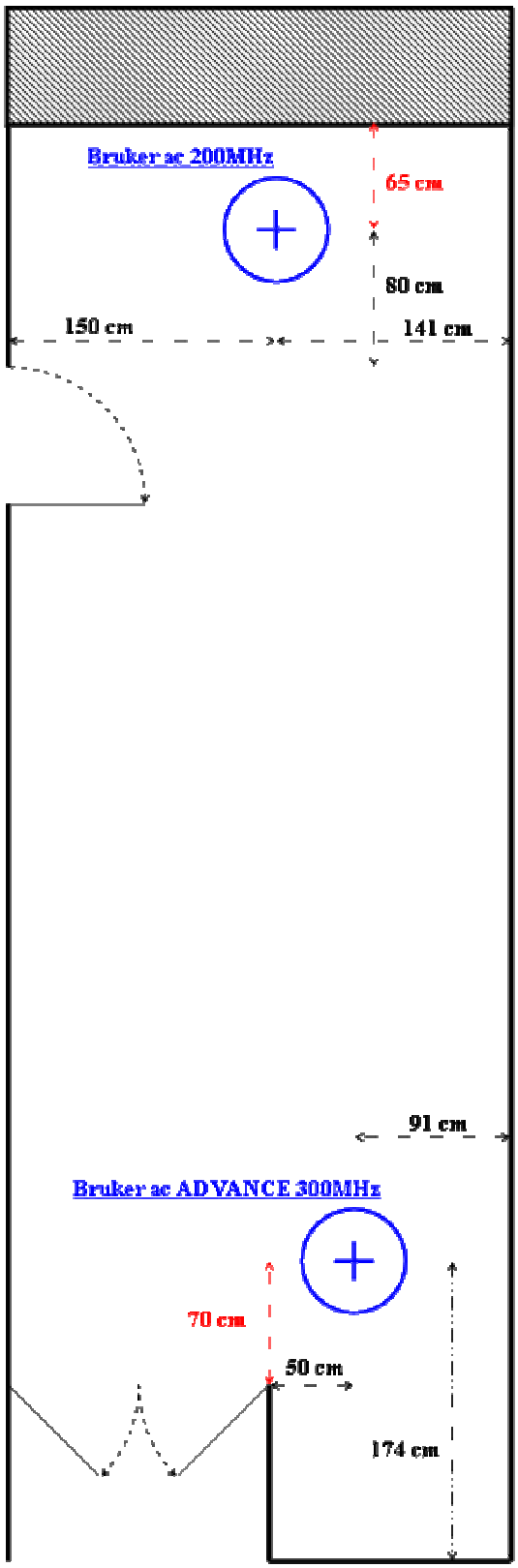

Figure 12. Sketch of the room where the NMR spectrometers are housed at the ICIS Institute.

The actual locations of the NMR spectrometers are shown in Figure 12 together with the distances from the main not removable obstacles. In Table 3 are reported the constraints to be respected for the project of the shield for both the NMR devices housed at the ICIS institute.

Table 3. Available dimensions for the active coils.

NMR instrument	Minimum Height required, H_{min}	Maximum Height available, H	Height of the sample probe, Z_{SP}	Distance from the nearest obstacle
BRUKER AC 200 MHz	2,8 m	3,18 m	94 cm	65 cm
BRUKER AC 300 MHz	2,8 m	3,18 m	96 cm	70 cm

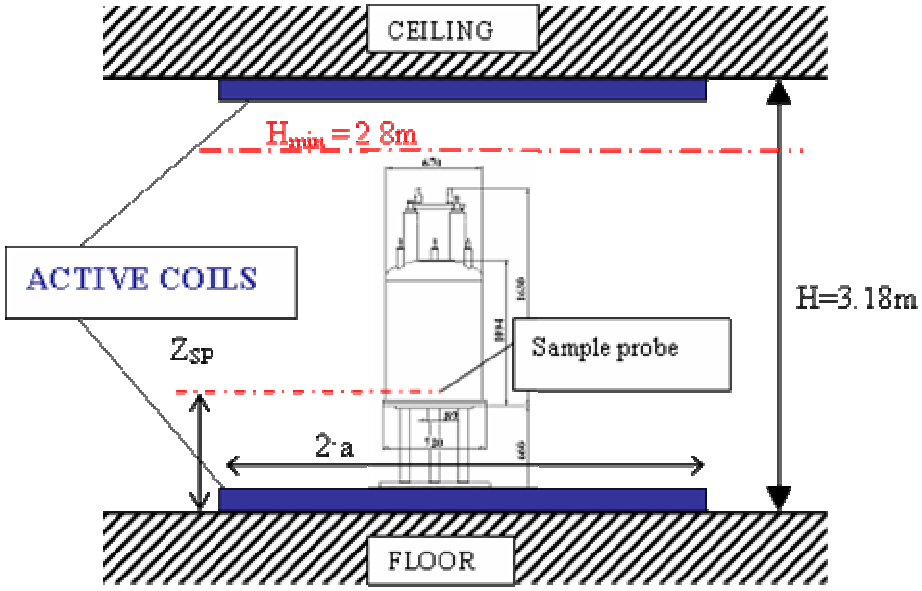

Figure 13. Sketch of a section of the room. The sample probe should be posed inside the active coils. Z_{sp} is the height of the sample probe.

6.2. Design

In order to guarantee a good accessibility to the NMR, it was decided to pose a coil (lower coil) on the floor and to fix the other (upper coil) at the ceiling (about 3m height, see Table 3) of the room.
Symmetric Helmoltz coils are usually used to create magnetic field with high uniformity in a small volume symmetrically located with respect to the coils. Due to the limited dimensions of the room and to the fact that Z_{SP} is 96cm only, a similar structure can not be utilized in any case for our purposes, because the height of the upper coil would be about 2 m, and the diameter of both the coils would be too large with respect to the dimensions of the room where the NMR devices are housed.

The use of two identical coils would create a field highly uniform only into a region near to half of the path between the two coils. As described by Figure 13, the sample probe is far from the half path between the two coils. A similar choice would require to pose the upper coil at 2m from the floor, or, fixing the upper coil to the ceiling, would create a magnetic field which is uniform in a region, of 1.5m height, far from the sample probe located at 0.95m height. So, it was decided to create two different coils in a Quasi-Helmoltz configuration. As Quasi-Helmoltz configuration we define a structure made up of two coaxial coils connected in series. This structure differs from an usual Helmoltz configuration by the ratio between the diameter of the coils and their mutual distance. Moreover, the two coils are realized with two different numbers of turns. The ratio N between the numbers of turns of each coil has been evaluated in order to pose the region where the field is uniform near to the sample probe.

$$N = \frac{N_{up}}{N_{low}} = \frac{\text{number of windings for the upper coil}}{\text{number of windings for the lower coil}} \tag{9}$$

A precise knowledge of the internal structure of the NMR was not available, that is the form and the position of the metal dewar surrounding the sample probe, so it was decided to design the magnetic active shield without taking into account the real structure of the NMR but a vacuum region into them.
Under the hypothesis of a vacuum region, preliminary calculations have been done in order to evaluate the feasibility of this kind of structure. These calculations have been carried out considering two coils having circular paths whose diameters are identical.

6.2.1 Circular coils

The magnetic shield is made up of two coaxial coils, preliminary calculations have been carried out considering two circular coils. The symmetry of this structure allows to simplify the design. In fact, under the vacuum hypothesis, it can be proved that all spatial derivates depend upon the spatial derivative of a single component, that is the $\partial B_z/\partial z$. If the coils are coaxial, it can be proved that all derivatives decrease to zero together with $\partial B_z/\partial z$. So, a single condition should be verified simplifying the design of the coils [21].

$$\left.\frac{\partial B_z}{\partial z}\right|_{z=0} = 0 \tag{10}$$

As well known, in case of two identical coaxial coils, a volume where the field is uniform is created near half to the path between the two coils. Varying the ratio N –see equation (9)-, this uniform volume can be shifted toward one of the coils. In particular the region will move to the coil with the minor number of windings.
In order to estimate the correct ratio, the number of turns for the lower coil has been fixed to 1. In this case, the following formula has been found:

$$N = \frac{z_{low}}{z_{up}}\left(\frac{a^2 + z_{up}^{\ 2}}{a^2 + z_{low}^{\ 2}}\right) \tag{11}$$

In equation (11), a is the radius of both the circular coils, z_{up} is the distance of the sample probe from the upper coil, and z_{low} is the distance of the sample probe from the lower coil.
The calculations done for circular coils showed the feasibility of the design maintaining the NMR instrumentations on their present locations [21].

6.2.2. Square-shaped coils

In order to make easy the construction of the supporting structure for the coils, it was decided to realize two coils having squared winding paths, a sketch is reported in Figure 14. Calculations have been carried out in order to correctly design coils with a similar winding path.
The magnetic field created by two coaxial square coils connected has a symmetry axis. As before described for circular coils, the symmetry allows to simplify the calculations, individuating the optimum design as that satisfies the condition:

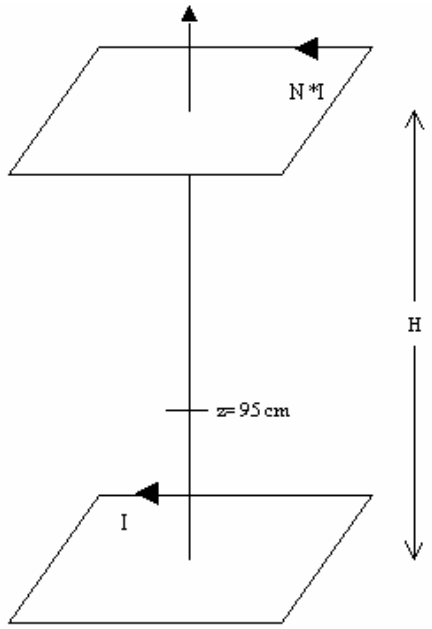

Figure 14 Sketch of the active magnetic shield made up of windings having square paths.

The two square coils should be connected in series and coaxially mounted. The magnetic field produced by this structure has a symmetry axis. As before described for circular coils, the symmetry allows to simplify the calculations, individuating the optimum design as that satisfies the condition expressed by equation (10) at sample probe height. In fact, also in the present case the above condition guarantees that all of the spatial derivatives of each field component are zero around the sample probe region.
A formula similar to (11) has been found to optimize the design of the square-shaped coils:

$$(12) \qquad N = \frac{z_{low}}{z_{up}} \cdot \frac{\int_{-a}^{a} \frac{1}{\left[s^2 + a^2 + z_{low}^{\ 2}\right]^{5/2}} ds}{\int_{-a}^{a} \frac{1}{\left[s^2 + a^2 + z_{up}^{\ 2}\right]^{5/2}} ds}$$

In equation (12), a is the half length of a side of the square path, and s is a curvilinear coordinate going along a side of the square-shaped coil.
The formulae utilized to evaluate the above condition and to perform the analytical calculations are reported in Appendix.
The correct ratio N has been evaluated for different values of the height H to have a minimum of the B_z field component at the center of the sample probe, at 0.95m height, see Figure 13. The B_x and the B_y components are null at the sample probe. In this case there is not a circular symmetry, so the changes of the magnetic field along the direction shown in Figure 15 have been investigated.

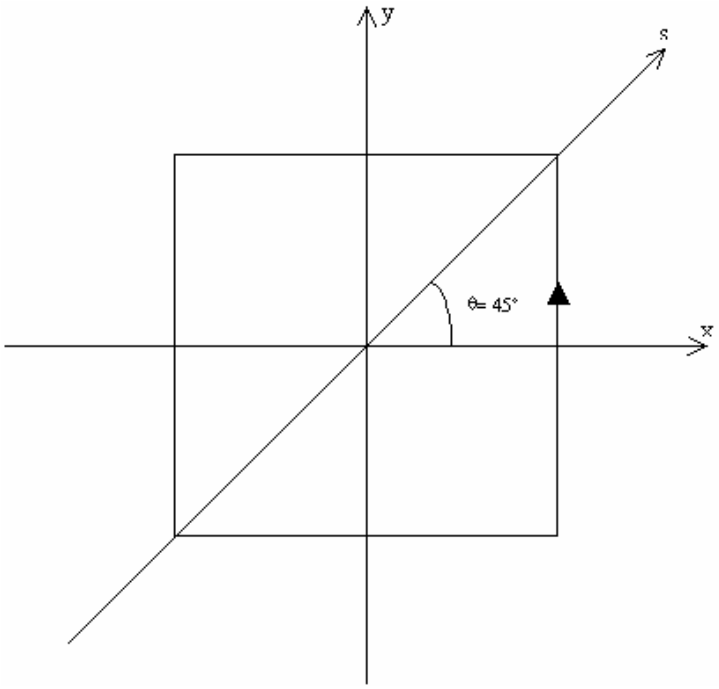

Figure 15. x, y and s directions with respect to the coil.

The symmetry of the structure implies that the B_y component changes along y as B_x changes along x. Moreover, B_y and B_x are zero along the x axis and the y axis respectively.
B_s is the component of the magnetic field evaluated along the s direction. Changes of this component along the s direction shown in Figure 15 can differ from changes of B_x along x.
In order to evaluate the dimensions of the volume surrounding the sample probe, the lengths Δz, Δx and Δs have been evaluated as the distances along z, x, and s respectively from the sample probe (z=0, s=0, x=0) where the field is uniform within the 1%. These lengths define the size of this volume.
In .Figure 16 are shown the variations of Δz, Δx and Δs with the height H of the upper coil.

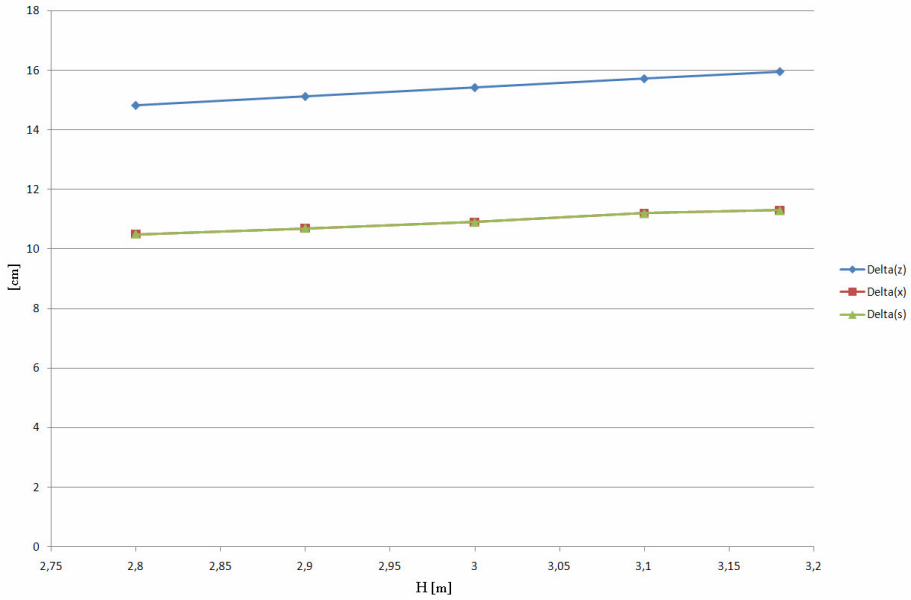

Figure 16. Δz, Δx and Δs values against the height H of the upper coil. Δz, Δx and Δs values are the size of the volume in which the field is uniform within the 1%.

The Δz, Δx and Δs values have a limited dependence upon H. Moreover, Δs is almost equal to Δx. So, the chosen structure creates a magnetic field uniform until the 1% in a cylindrical region of almost Δz= 15cm height and r=11cm radius for each value of H considered. . That shows a great tolerance on H which means to a great feasibility of such a structure. The shape of the vertical component of the magnetic field B_z against the height z is shown in Figure 17. In Figure 17, z is equal to zero at the sample probe.

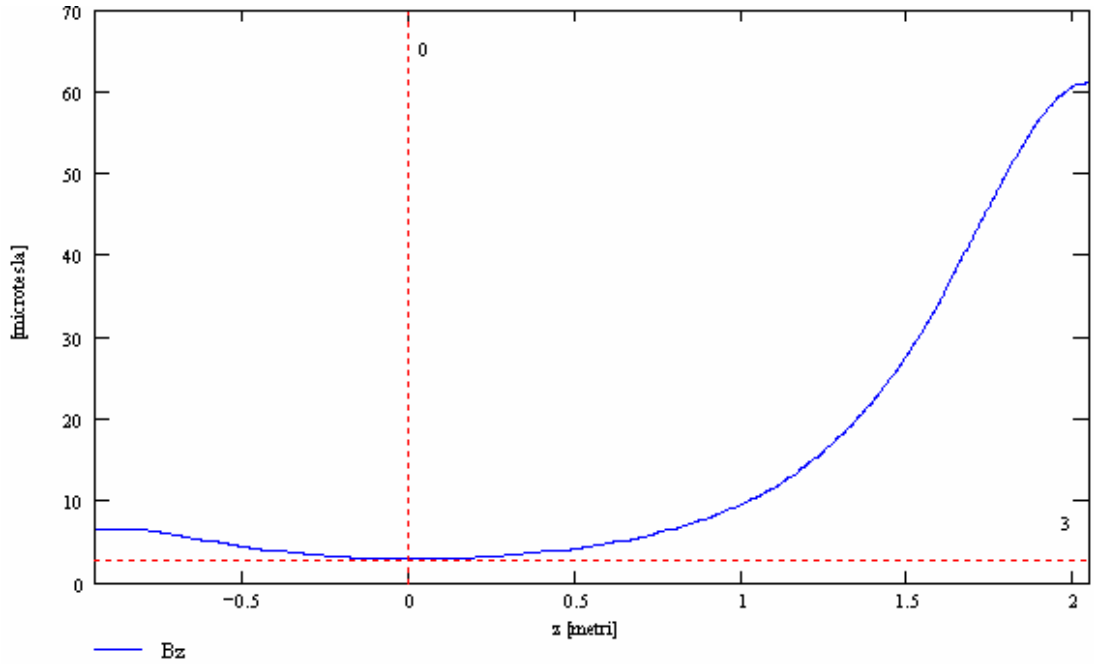

Figure 17. B_z behavior on the z-axis against the z coordinate. For two square-shaped coils with L=1.2m long side and H=3.0m height. The sample probe is located at z=0, where the minimum of B_z is found. B_z=3μT at z=0.

The behavior of the B_x, B_y, and B_s components along x, y, and s respectively is shown in Figure 18 for two coils designed as in Figure 17.

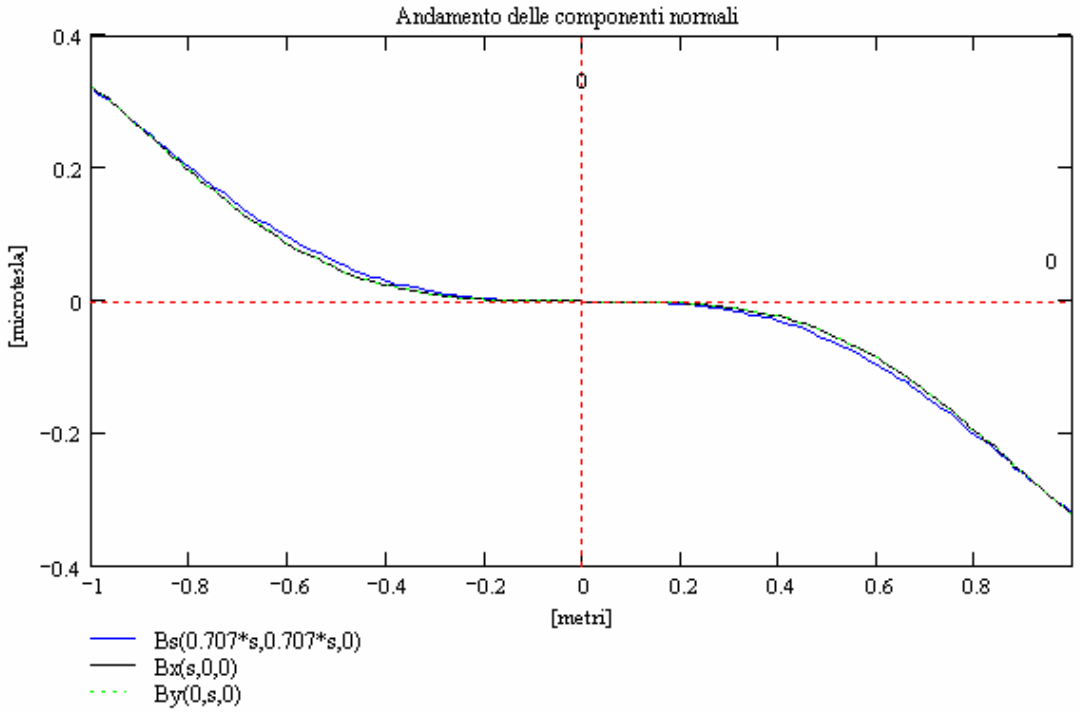

Figure 18. Behavior of B_x, B_y, and B_s against x, y, and s respectively, for the same structure studied in Figure 17.

Results here reported have been calculated by some worksheets developed with MathCad. The worksheet worked on the basis of the analytical model described by the formulae reported in Appendix. These results have been confirmed by other codes, as ANSYS or ADAMM. Figure 19 and Figure 20 show the results obtained with a 2D code. A circular approximation of the coils have been taken, the lower coil has 10 windings, and the upper coil has 120 windings, this is designed for H=3.13m. Figure 19 shows the locus where the magnetic field has the same amplitude, and Figure 20 reports the equiflux lines.

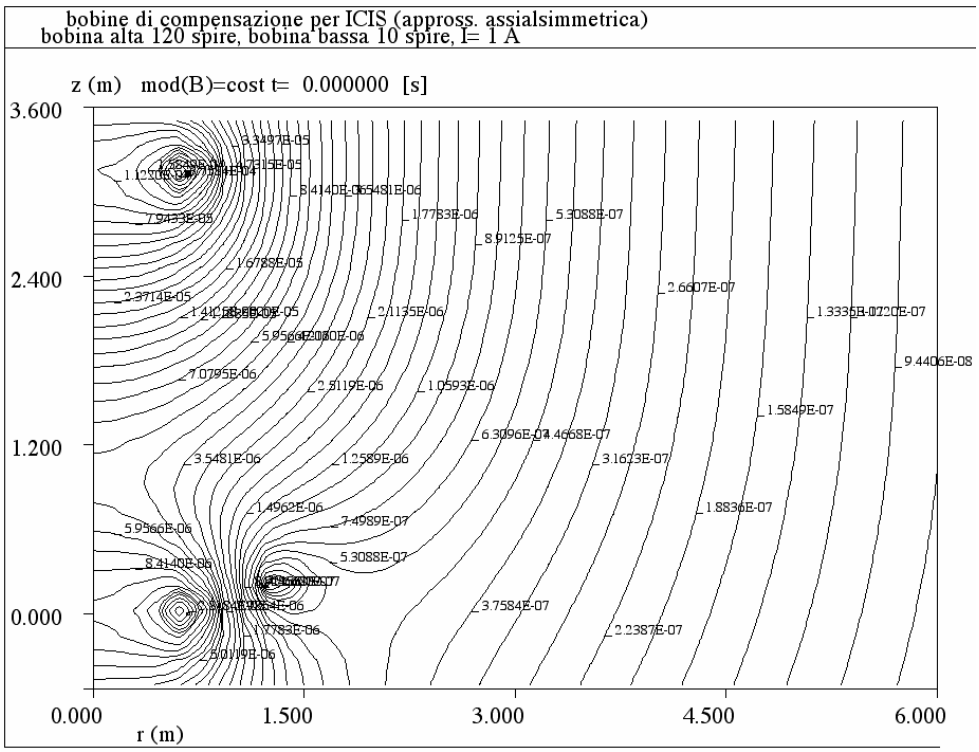

Figure 19 Map of the constant strength field lines [T] of the magnetic field produced by a structure made up of a 10 windings lower coil, and a 120 windings upper coil. The upper coil is at H=3.13m.

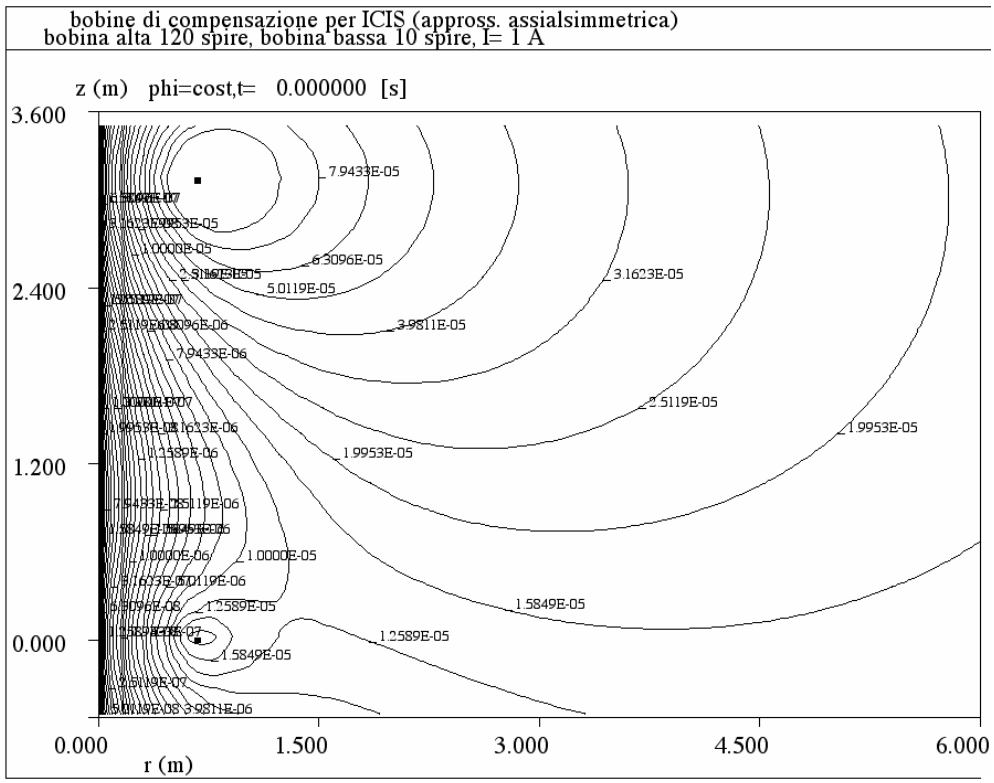

Figure 20 Map of the constant flux lines [Weber] of the magnetic field produced by the same structure of Figure 19.

The final designs for the two pairs of active coils (a pair of coils for each NMR instrumentation housed at ICIS) are reported in Table 4 and Table 5. It was decided to realize the lower coil by tenturns. In this case, the current I_{MAX} need to have a magnetic field strength of 3μT at the sample probe height z_{SP} and the maximum amplitude B_{MAX} of the field at the centre of the upper coil are also reported in the tables.

Table 4 Design and main characteristics of the active coils for the BRUKER NMR AC 200 MHz.

L [m]	H [m]	N_{low}	N_{up}	$I_{S,MAX}$ [A]	B_{MAX} [μT]	z_{sp} [m]	Δz [m]	Δr [m]
1.2	3.133	10	130	0.611	74.5	0.94	0.16	0.11

Table 5 Design and main characteristics of the active coils for the BRUKER NMR AC ADVANCE 300 MHz.

L [m]	H [m]	N_{low}	N_{up}	$I_{S,MAX}$ [A]	B_{MAX} [μT]	z_{sp} [m]	Δz [m]	Δr [m]
1.2	3.134	10	120	0.643	72.8	96	0.16	0.11

6.3. Realization of the coils

In order to experiment the performance of the present open-loop active magnetic shield, it was decided to realize the pair of active coils devoted to compensate the magnetic disturbance sensed by the BRUKER NMR ADVANCE 300 MHz. The NMR experiments at ICIS Institute are often carried out with this instrumentation.
Active coils have been realized using a copper wire with 1.5mm^2 section. With the use of this wire, the resistance of the two coils connected in series has estimated to be equal to 7.4 Ω. A theoretical value of the two coils has been estimated as L= 92 mH, with the use of a Math cad worksheet.

6.3.1. Supporting structure

The wire has been wound around two supporting structures made in aluminium. The supporting structures have both an U section as depicted in Figure 21 (left).

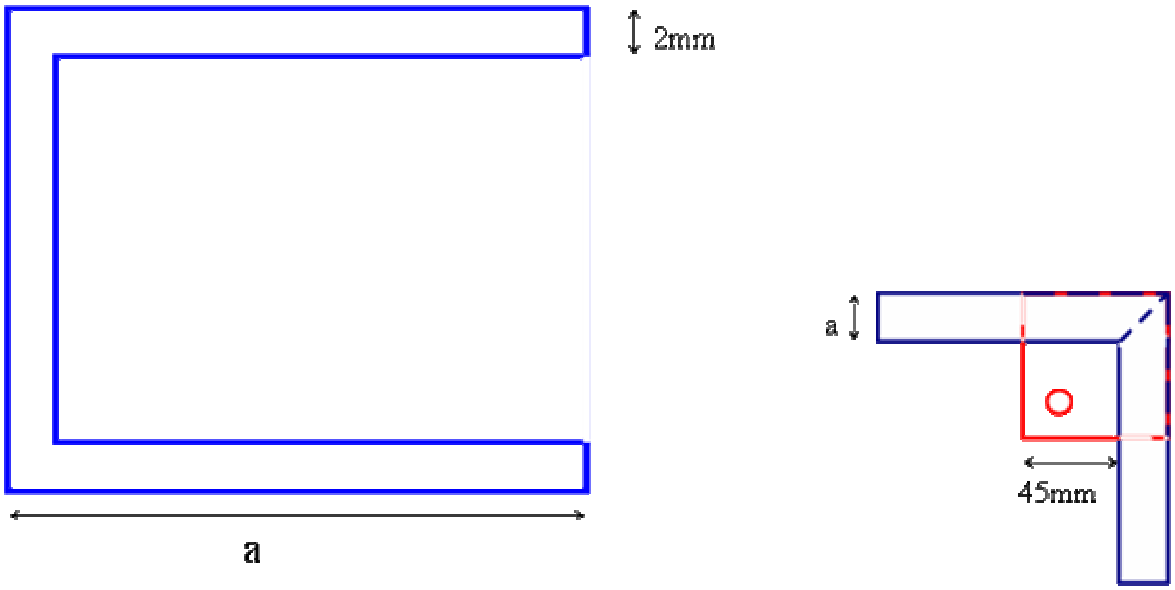

Figure 21. (left) The U section of the frame constituting the supporting structure. The length a of each side is 25mm for the lower coil, and is 35mm for the upper coil. (Right) Zoom of a corner of the supporting structure. An aluminium layer has been welded with an hole at the inner corner. Each holes of the upper coil corresponds to a given hole of the lower coil.

The supporting structures are made with aluminium. They can interact with the magnetic field created by the windings. Under the hypothesis that the B_A field induced by the windings is proportional to the current I_M, during the fast decay of the current the supporting structure can create a reacting magnetic field affecting the performance of the shield.
The response to this rapid variation of the magnetic flux has been evaluated for the upper supporting structure.
The total magnetic field created by the upper coil results as the sum of the B_A field, created by the windings only, plus the magnetic field created by the supporting structure. It has been evaluated that the supporting structure have a constant time equal to 10ms. The effect of such a structure has been evaluated for an exponential decay of the I_M current of with time constant of 2ms, the result is shown in Figure 22.

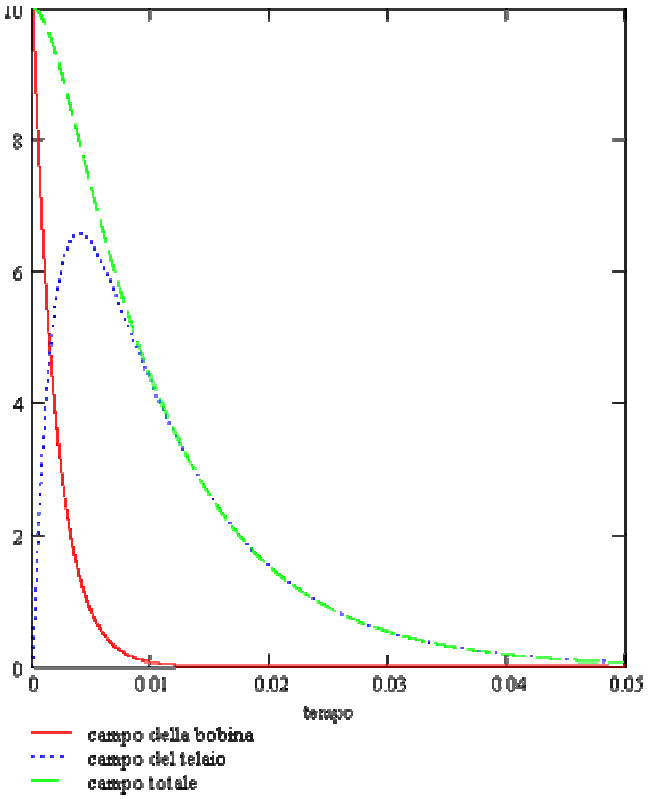

Figure 22 The total field induced by the upper coil (green) results the sum of the B_A field (red), due to the winding, and the field due to the reaction of the supporting structure (dashed blue) to the fast decay of the current. So, this reaction affects the response of the shield, slowing down the decay of the total field which should compensate a magnetic disturbance ideally varying as the B_A field.

The supporting structure acts as a single coil, and a reaction field is produced which slows down the total response of the shield, as depicted in Figure 22. Under this condition, considering B_A as a perfectly compensating field equal and opposite to the magnetic disturbance B_{RFX}, the magnetic shield made up of this pair of coil should create an error field equal to the reaction field. In order to avoid this failure, it was decided to vertically cut a side of each supporting structure. The cut is almost 5mm large. In this way, the supporting structure can not interact with the fast variation of the magnetic flux.
Finally, the copper wire has been coiled up around each supporting structure. The lower coil has been realized with 10 windings posed on a single layer. The upper coil has been realized with 119 windings placed on 8 layers. It has been verified that this difference from the design causes negligible changes on the expected performances of the shield.

6.4. Equivalent electric scheme of the coils

In order to verify the correctness of the design, the ratio B_{MAX}/I_S has been measured for the upper coil. B_{MAX} is the amplitude of the magnetic field induced by the coil at the centre of the upper coil, and I_S is the current flowing through the coil. Moreover, the electric characteristics of the upper coils have been measured to develop an equivalent electric circuit of the shield and to define the power supply VCCS.

The equivalent electric circuit has been measured by a HP-4194A IMPEDANCE/GAIN-PHASE Analyzer, on the range from 100 Hz to 100 KHz. Results of the present measurement are shown in Figure 23.

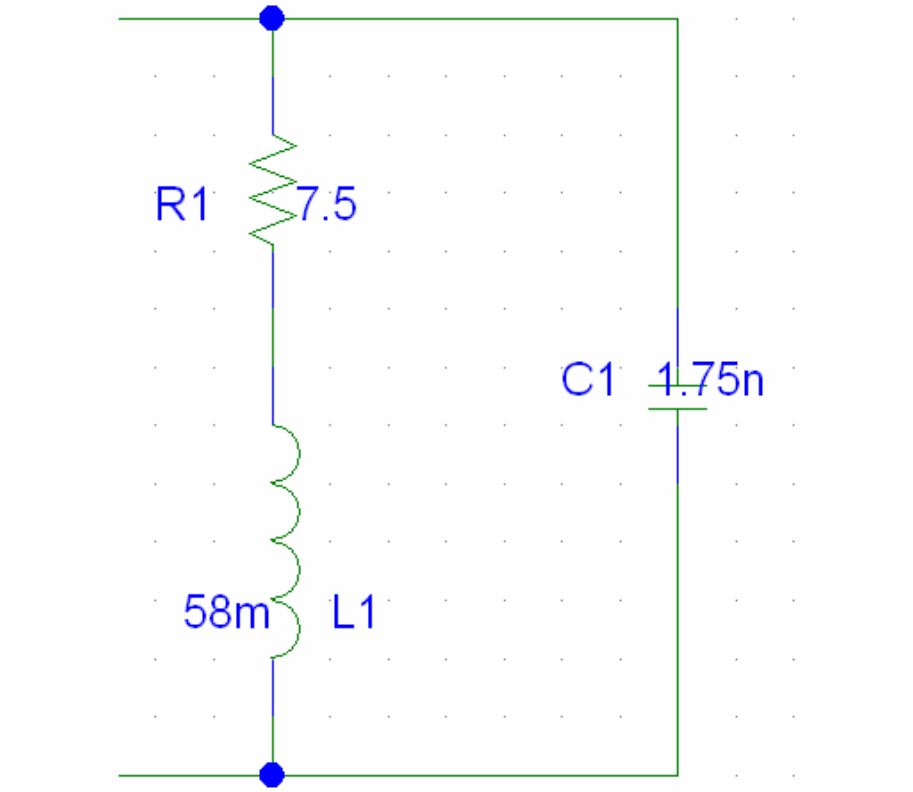

Figure 23. Equivalent electric scheme for the upper coil.

A great parasitic capacitance is present on the equivalent scheme of the upper coil, as shown in Figure 23. This huge value is probably due to the thin insulation layer of the wire making up the windings, and to the close proximity of each winding with the others.
In Figure 24 is shown the frequency response of this coil. A resonance is present at 15.8 kHz.

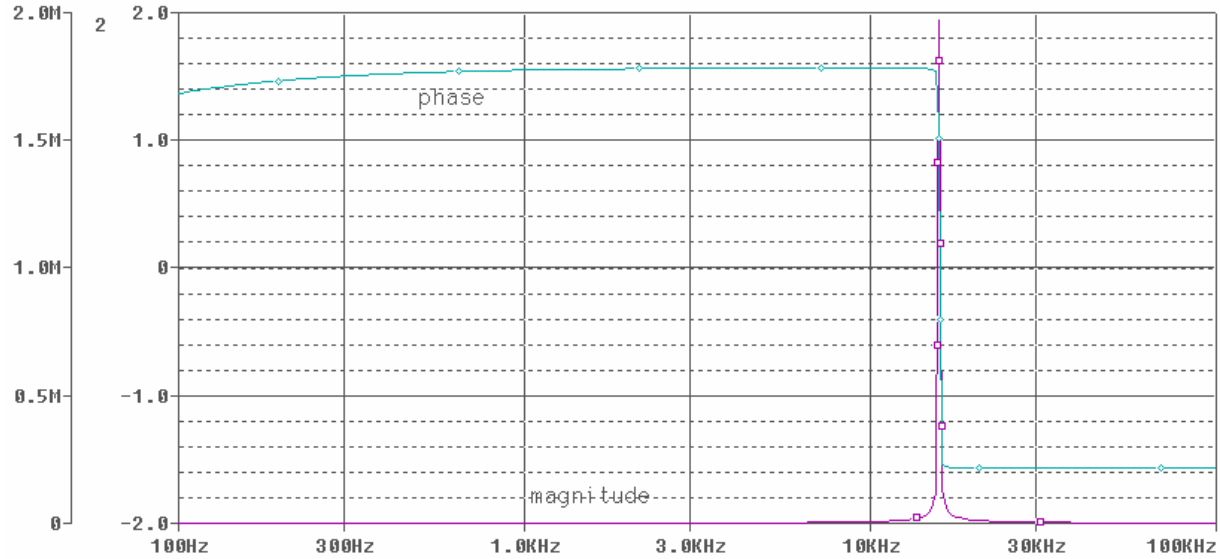

Figure 24. Transfer function V/I (impedance) of the coil as a function of frequency.

The measurements of the magnetic field have been carried out using the following instrumentation:

- LeCroy wavesurfer 44Xs 400 MHz oscilloscope
- FW Bell series 9950 Gaussmeter
- Current Probe Amplifier Tektronix AM 503
- KEPCO BOP 100-4M power supply

The KEPCO BOP 100-4M has been utilized as a constant voltage source.
A ratio B_{MAX}/I_S of 115μT/A has been evaluated from the measurements. This value agrees with that of 113.4μT/A evaluated from the results exposed in Table 5. The ratio between the magnetic field close to the sample probe and the current can be evaluated from Table 5 as equal to:

(13) $$\frac{B_A}{I_S} = \frac{3\mu T}{0.64A} = 4.68\frac{\mu T}{A}$$

7. VCCS block

The power supply making up the VCCS block should act as a transconductance transforming the voltage signal input V_U in a current signal I_S. The current signal I_S should drive the active coils in order to create the compensating magnetic field B_S.
Active coils electrically act as an inductance, as shown in Figure 23. The power supply should be able to furnish also an high level of voltage to drive the fast variation of the I_S current flowing through the coils. The maximum voltage required by the coils has been evaluated both using the estimates reported in section 6.3 and using the measured values as reported in Figure 23.
A maximum value of about 40V has been evaluated from the results reported in section 6.3. With this voltage level the power supply should be able to drive the current I_S from I_S=0.64 A to 0A with a exponentially decay with a time constant of 2ms.
Several calculations have been carried out with SPICE. The circuit is shown in Figure 25 it is driven by two different type of current sources, I1 and I2, in order to produce a shape of the current similar to typical shape of I_M during a pulse of RFX. The current sources are connected in parallel one another, with the equivalent circuit of the coils, and with a resistance R_2 aimed to minimize the oscillation given by resonance frequency. The calculations have been carried out for different values of R_2.
In each case a current source able to supply a maximum current of 1A and a maximum voltage of 50V should be able to correctly drive the active coils.

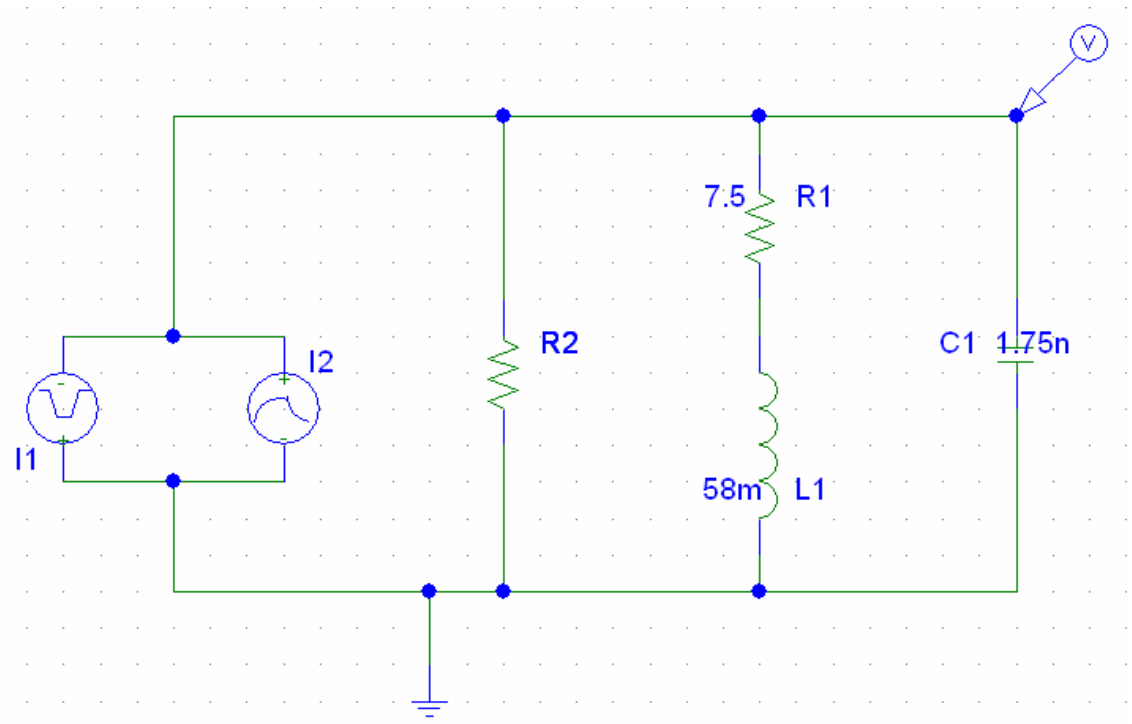

Figure 25. Scheme of the circuit utilized to define the power supply making up the VCCS block. I1 and I2 are two current sources. The right part of the circuit (R1, L1, and C1) is the circuital approximation of the active coils. R2 is a slaking resistance act to minimize the resonating behavior of the active coils.

It was decided to purchase a KEPCO BOP 100-2M power supply, able to supply a maximum current of 2A and a maximum voltage of 100V.
At the time of the first experiments, which are reported in chapter III, a KEPCO BOP 10-4M was available at RFX. It is able to give out a maximum current of 4A and a maximum voltage of 100V.
Major details about this power supply, on the oscillations observed when it joins the active coils, and on the adopted solutions to this unexpected challenge are given in chapter III.
The KEPCO BOP 100-4M gives out a current signal ranging within ±4A, that is directly proportional to the input voltage signal ranging within ±10V. So, the G_{VCCS} transconductance of the power supply is equal to:

(14) $$G_{VCCS} = 0.4 \ {}^{A}\!/_{V}$$

8. Gain of the receiver

The B_A compensating field should have the same amplitude of the magnetic disturbance B_{RFX}, but with opposite sign. As described in section 3.3, the gain of the SR 580e receiver is adjustable, and the gain of the overall transmission system is equal to this value for the set-up of the transceiver used during the experiment. A preliminary estimate of the gain g of the receiver can be carried out as follows. For a given value of I_M, B_A and B_{RFX} should be equal. For a current I_M=50KA, a magnetic disturbance with amplitude B_{RFX}= 3μT is sensed by the NMR instrumentations housed at the ICIS institute. The amplitude of B_A is equal to:

(15) $$B_A = \frac{B_A}{I_S} \cdot G_{VCCS} \cdot \frac{V_U}{V_I} \cdot \frac{1}{G_{LEM}} \cdot I_M = B_{RFX}$$

An estimate of B_A/I_S can be found by the value of $I_{S,max}$ (see table…) need to have B_A=3μT close to the sample probe. The transconductance G_{VCCS} of the power supply is given in section 7, equation (14). The G_{LEM} factor of the LEM is given in section 2, equation (1). The ratio V_U/V_I is equal to the gain g of the SR 580e receiver, as reported in section 4, equation (2). Therefore, an estimate of g is given by:

(16) $$g = \frac{V_U}{V_I} = \frac{B_{RFX}}{I_M} \cdot \frac{G_{LEM}}{G_{VCCS}} \cdot \frac{I_S}{B_A} = \frac{3\mu T}{50kA} \cdot \frac{6000\Omega^{-1}}{0.4\Omega^{-1}} \cdot \frac{1}{4.67 \ {}^{\mu T}\!/_{A}} = 0.19 \frac{V}{V}$$

9. SUMMARY

The design of the present system has been carried out paying attention especially on the design of the two main blocks: the transmission system and the active coils.
The transmission system should satisfy the need of a transmission delay as little as possible without losing in precision and in the fidelity of the reconstruction of the signal.
A suitable commercial Digital Telemetry transceiver has been found , see section 3 [21]. This transceiver suits all of the most important need of the design, such as the resolution and the transmission delay, making possible the transmission via RF of the driving signal V_I, see section 1. However, the SS-580e is not able to process the analog input signal V_I, and the transmission via RF is not possible if the transmitter and the receiver are posed into the RFX building and the ICIS Institute, respectively. In order to solve these additional challenge, a buffer circuitry has been designed (section 4), and two YAGI antennas (section 5) have been bought and installed over the roof of both RFX and ICIS. With the help of these additional components, the transmission system seems suit the requirements on the transmission, as defined in section 3.1.
On the other hand, the active coils should produce an uniform magnetic field surrounding the sample probe of the NMR instrumentation, section 6.1. Moreover, the size of the active coils should suit the dimensions of the room where the NMR instrumentations are housed. A suitable structure has been designed (section 6.2)and realized (section 6.3) made up of two coaxial coils with a different number of windings. A coil is posed over the floor, and the other one is fixed to the ceiling around the NMR instrumentation.
The coils have been electrically characterized by analytical calculations and with the measurement of the electrical response (section 6.4). An equivalent electric scheme has been drawn out. The electric scheme has been used to design the power supply aimed to drive the coils (section 7).
Finally, it is worth noticing that the gain of the SR-580e can be adjusted. Varying this gain the amplitude of the compensating magnetic field, produced by the system, can be controlled in order to match the amplitude of the magnetic disturbance B_{RFX} (section 8).
The present system seems to be suitable to compensate the magnetic disturbance induced by the magnetizing windings of RFX. The preliminary tests, aimed to set-up the instrumentation, and the experiments of compensation are reported in chapter III.

CHAPTER VI

Set-up of the instrumentation and experimental results

Several tests have been carried out on each block making up the open loop active magnetic shield and on the complete system with the aims of verifying its performances and correctly setting-up the system before its application to the NMR instrumentation housed at the ICIS institute. In this chapter the tests on the equipment are described together with the set-up of the overall gain of the system and the final experimental tests. During the applications, some unexpected challenges have been encountered and solved before a complete compensation of the magnetic disturbance on the NMR could be achieved. Brief discussions about the encountered challenges and their solutions are reported in this chapter.

1. Introduction

In chapter V, figure 1, the overall block scheme of the open loop active magnetic shield is presented. Each block has been realized as reported in chapter V. The suitability of the instrumentations has been checked by several tests before to mount the active coils and to connect together the control chain.
The strategy of driving the active coils by the transmission of a signal proportional to the disturbance has been verified. Several experiments have been carried out at RFX, with the aims of compensating the magnetic field induced by RFX in a laboratory room located into the RFX building and about 10m far from the RFX experimental machine.
Section 2.1 describes the preliminary tests aimed to check the performance of the transceiver SS-580e, and to verify the capability of the Control Software (chapter V, section 3.2.4) in varying the gain of the receiver SR-580e.
Section 2.2 describes the characteristics of the prototype of the active coils [Baggio], and of the power supply KEPCO BOP 100-4M utilized during the experiments at RFX. The active coils have been connected to the KEPCO BOP 100-4M power supply and once the KEPCO has been set as a current source then the instabilities have been observed. Instabilities often occur when an inductive load is driven by a current source.A simple solution for such instabilities was to connect in parallel with the active coils a damping resistor, and preliminary experiments at RFX have been performed, as described in section 3.
Some differences have been noted between the input signal V_I driving the system and the magnetic disturbance actually sensed at RFX. However, the experiments show that a good compensation can be achieved and the system seems promising to compensate the magnetic disturbance a ICIS. Some doubt raised up on the differences shown between the input signal V_I and the magnetic disturbance, but a deeper investigation on that would not give out any useful information on the actual differences which could be experienced at the ICIS institute. Therefore, it was decided to mount the active coils at ICIS and to undertake some preliminary tests before to apply the system to the NMR instrumentation. The YAGI antennas (chapter V, section 5) have been installed on the roofs of the RFX and ICISI buildings.

Section 5 describes the preliminary tests carried out on the overall system near to the NMR instrumentation. Active coils have been posed few meters far from the NMR instrumentation in order to measure the residual error field obtained by compensation.
Differences between the input signal V_I and the magnetic disturbance at ICIS have been noted and a simple solution has been found as described in section 5.2.
These preliminary experiments show that the system suits the global requirements required to compensate the magnetic disturbance. Therefore, the active coils have been installed near the NMR instrumentation and final experiments have been carried out. The experimental results are reported in section 7.

2. Preliminary tests at RFX

Several preliminary tests have been carried out in a laboratory room located on the floor above the diagnostics hall about 10m from the machine axis [FED2]. The transmitter ST-580e is located here, because it is possible to connect the input of the transmitter with the output of the LEM diagnostics through a long screened cable.
In this laboratory room the amplitude of the magnetic field is about 100μT, i.e. two orders of magnitude larger) than the magnetic disturbance affecting the NMR instrumentation at ICIS institute, see the magnetic field maps reported in section 2.3. Therefore, the magnetic field can be measured by a gaussmeter.
During the tests, the following equipment has been used:

LeCroy wavesurfer 44Xs 400 MHz Oscilloscope
FW Bell series 9950 Gaussmeter
Current Probe Amplifier Tektronix AM 503
HP-34401A Multimeter
Wavetek 185 Waveform generator
KEPCO BOP 100 4M power supply

Firstly, the performance of the transmission system have been checked, as described in section 2.1.
A prototype of the active coils [Baggio] has been used to compensate the magnetic field induced by RFX. The KEPCO BOP 100-4M power supply is used as a VCCS current source to drive the active coils. An unstable behavior has been observed once connected the active coils with the VCCS. The instabilities observed are reported in section 2.2, and a solution to avoid the instability is given.
The experimental results are reported in section 2.3.

2.1 Tests on the transmission system

Some tests have been carried out in order to verify with which resolution the characteristics of the signal outputting from the receiver SR-580e can be modified by the Digital Telemetry

Control Software (section 3.2.4, chapter V)of the transceiver SS-580e in order to fix the offset and to set the optimum gain required to compensate the magnetic disturbance.
The delay time of the overall transmission line, made up of the transceiver plus the buffer tx circuitry, has been measured.
The buffer TX circuitry (section 4, chapter V) has been adjusted in order to attenuate the input signal V_I by the 0.25.
A **delay time** equals to 90μs and a cut frequency of 2.796kHz have been measured for the buffer TX board. An offset of about 0.4mV is present at the output of the board.
Some anomalies have been observed at the output of the receiver SR-580e. When the receiver is switched on, the output voltage V_U suddenly becomes +10 or -10V, until the receiver does sense a signal from the transmitter ST-580e. This behavior is not acceptable because it could produce an additional disturbance to the NMR instrumentation when the receiver is connected to the active coils, and a solution shall be found before the definitive installation of the system. However, this was not a problem during the tests, taking care that the power supply was switched off until the receiver works properly.
The analog output channel of the receiver can be adjusted using the Control Software, independently of the digital output data. During this calibration, the offset has been measured equal to 3mV. During the first transmission tests, the transmitter was switched on with a zero signal at the input. In this case, an offset of 20mV has been measured. As described in section 3.2.3, chapter V, the offset can be adjusted varying the Static Variable Offset (Figure 7 section 3.2.3, chapter V) with a resolution of 5mV.
The overall offset from the LEM output to the receiver output has been reduced to 0.9mV.
Change along the time of the overall offset has been noted [NM]. However, the offset never overcome a level of 20mV. An offset of 20mV should not affect the NMR. In fact, it is foreseen to use a VCCS with a transconductance of $0.1\Omega^{-1}$, thus the offset should drive a current of 2mA through the active coils. The active coils have to be driven by a maximum current equal to about 1A to compensate the maximum magnetic disturbance. So, the overall offset should create a magnetic field with an amplitude less than the 0.5% of the maximum disturbance which does not affect the NMR. In fact, the susceptibility threshold of the NMR is over about the 1% of the maximum magnetic field to compensate (3μT).
The overall delay time has been measured from the input of the buffer TX to the output the receiver. The system has been driven with a square wave with a period of 50ms. The overall delay time has been measured equal to 4.25ms. This value is in good agreement with the delay time measured for the buffer TX and the throughput delay time of the transceiver, see sections 3.3 and 4, chapter V.

2.2 Prototype shield and power supply

To carry out the experiments aimed to compensate the magnetic disturbance at RFX, a prototype of the active coils has been used. In Figure 1 is shown a picture of the prototype, its main characteristics are reported in Table 1.

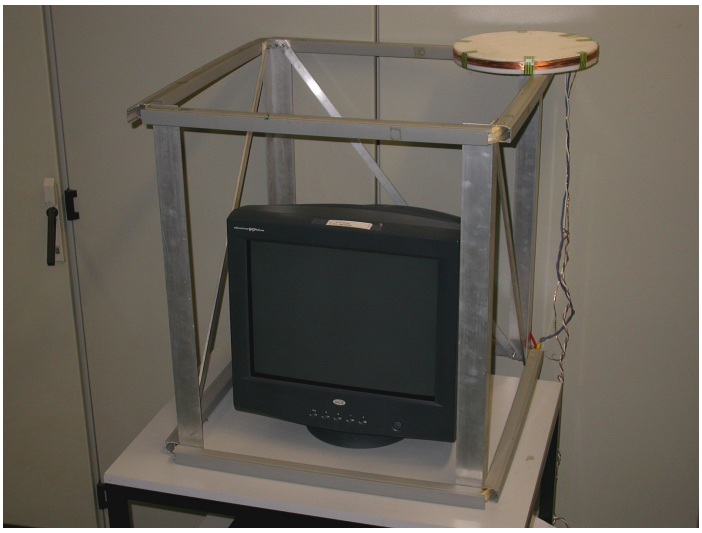

Figure 1 Picture of the prototype shield [Baggio].

Table 1 Characteristics of the prototype shield.(Measured values [NM])

Side length[cm]	Height [cm]	$N_{windings}$ per coil	R_c [Ω]	L_c [mH]
60	70	150	13.36	86.01

A KEPCO POWER BOP 100-4M has been used as VCCS current source, as reported in section 7 chapter V.
The shield has been connected to the KEPCO, as current source. Switching on the KEPCO and in absence of an input signal, the output current flowing through the shield oscillates. At the oscilloscope a behavior of the current similar to saw-teeth has been observed. The oscillations have a period of about 800μs (f= 1.25 kHz).
If the KEPCO is used as current source, its output behaves as a capacitor-resistor parallel, whose frequency response is shown in

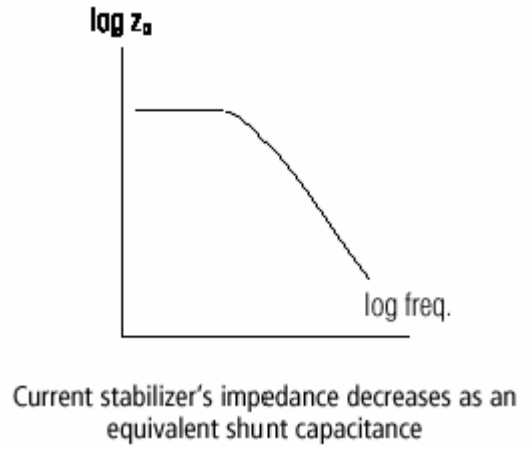

Figure 2 Frequency response of the resistor-capacitor parallel equivalent with the output of the KEPCO BOP used as current source [BOP].

The nominal value of the equivalent resistor is R_a= 100kΩ, the equivalent capacitor is C_a= 0.1μF.
In order to avoid the instability, it was decided to connect a damping resistor in parallel with the prototype shield. The value of this damping resistor has been evaluated with the help of the measured value of the fundamental of the oscillations. The prototype shield shows an impedance of 7kΩ at f=1.25kHz. In order to minimize the inductive behavior of the load seen from the KEPCO output, a resistor of 1kΩ (P_{MAX}=20W) has been inserted.
The oscillations have been completely damped by this simple solution.
It is worth noticing that the ratio V_I/I_S between the input voltage and the current flowing in the shield is not constant along the spectra of V_I, but it varies with the frequency. However, this ratio is constant at low frequencies, i.e.in the band of susceptibility of the NMR instrumentation.
Simulation with SPICE can help to describe the efficiency of the damping resistor adopted.
In Figure 3 the electrical equivalent schemes of the loads seen from the current source are shown in two cases: left, without the damping resistor (unstable circuit); right, with the damping resistor (stable circuit). Subscripts "c" refer to the equivalent inductor and resistor of the coils, while subscripts "o" refer to the equivalent capacitor and resistor of the output impedance of the KEPCO.

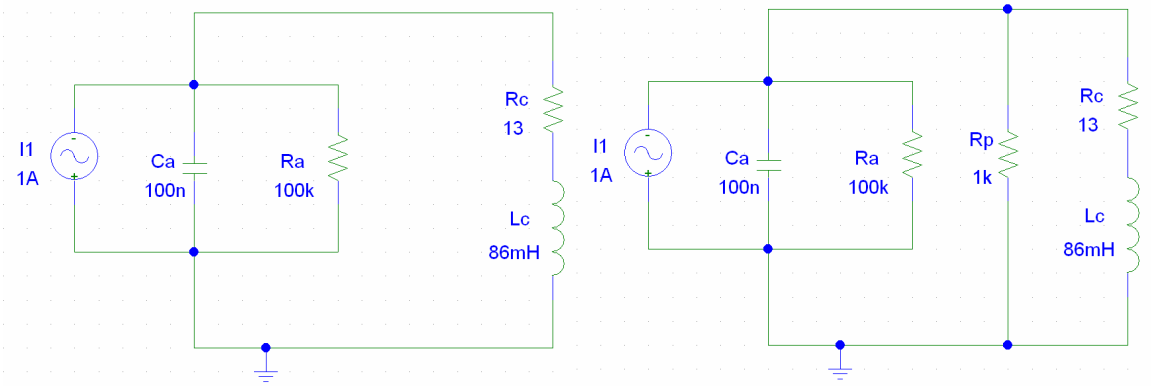

Figure 3 Equivalent schemes with (right) and without (left) damping resistor R_P.

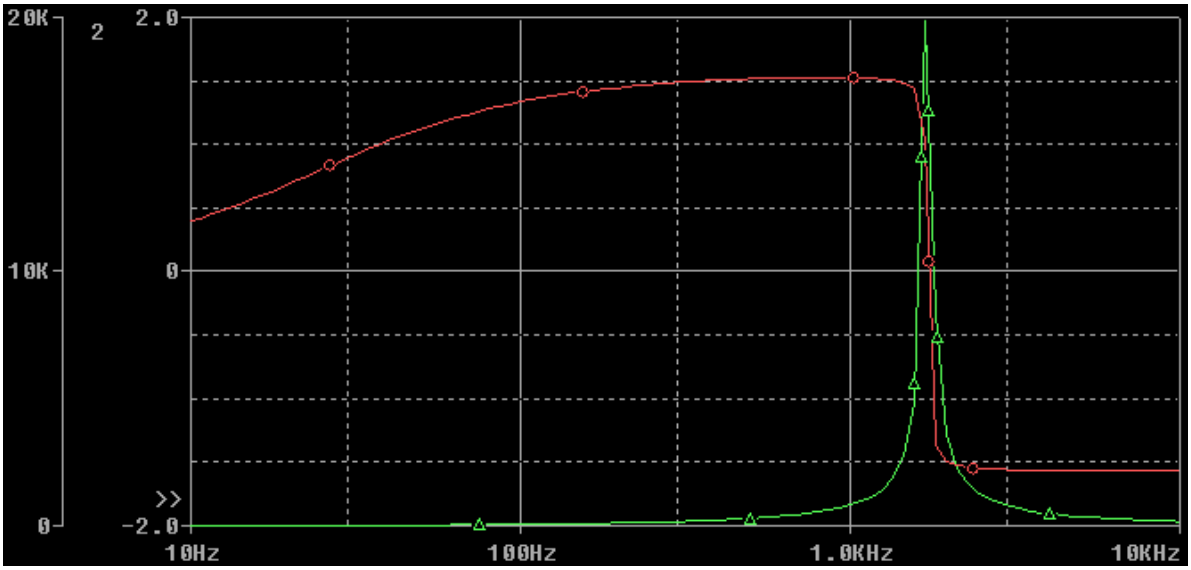

Figure 4 Impedance (green) and phase of the equivalent scheme shown in Figure 3 (left).

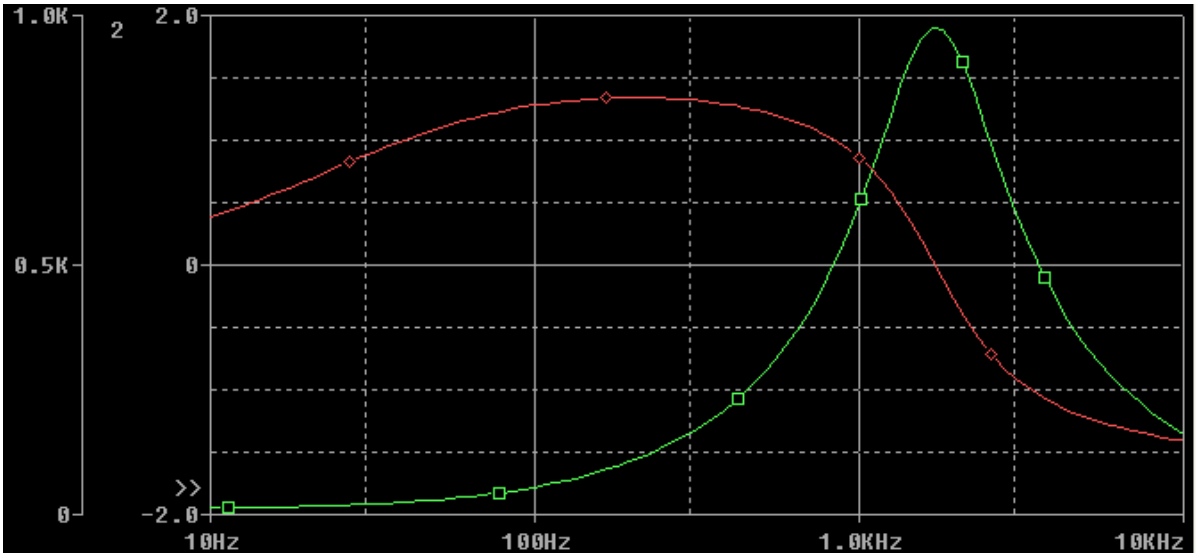

Figure 5 Impedance (green) and phase of the equivalent scheme shown in Figure 3 (right).

Figure 4 shows that a resonance occurs at f=1.68kHz. This value is in reasonable agreement with the measured value of f=1.25kHz. The maximum amplitude of the impedance is about 20kΩ. In Figure 5 the effect of the damping resistor is shown. The value of the maximum amplitude of the impedance is reduced to less than 1kΩ, but the resonance at f=1.68kHz is still present.

The behavior of the KEPCO connected with an inductive load is only qualitatively described by the C_a and R_a values provided from the manual [BOP]. A prior evaluation of the best solution to adopt need a deeper knowledge on how the KEPCO exactly works. C_a and R_a values make us able to define a range of values or strategy to adopt, but the exact value of a damping resistor, as an example, has to be defined by experiment.

In each case, the value of R_p=1kΩ has shown to be sufficient in damping all the observed oscillations.

In section 8, chapter V, a formula (16) has been found to set the receiver gain g in order to match the amplitude of the magnetic field B_A produced by the active coils with the magnetic disturbance B_{RFX}. The gain g of the receiver can be adjusted step by step, with steps of less than 10^{-3}.

The equation (16) in section 8, chapter V, has to be rewritten in terms of measurable values:

$$(1) \qquad g = \frac{V_U}{V_I} = \frac{B_{RFX}}{V_I} \cdot \frac{1}{G_{VCCS}} \cdot \frac{I_S}{B_A}$$

The ratio B_A/I_S, that is to say the magnetic field B_A created by the prototype shield divided by the I_S current flowing through the coils making up the shield, has been measured using the KEPCO as constant voltage source. So, the current I_S was controlled by the applied voltage of the KEPCO (no oscillations have been observed with the KEPCO in voltage mode), and the current was measured also with the Current probe. The magnetic field B_A has been measured by two Hall probes connected to the Gaussmeter, as shown in Figure 6. Measurements are reported in Table 2.

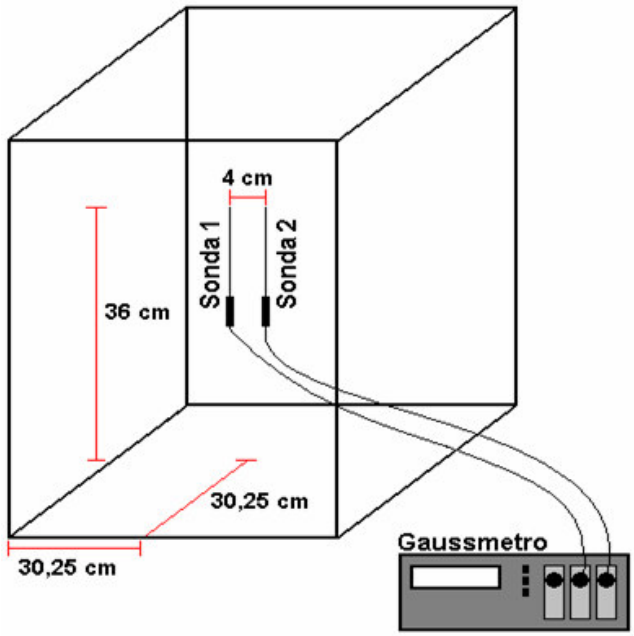

Figure 6 Measure of the magnetic field B_A created by the shield. The Hall probes are located near to the centre of the shield.

Table 2 DC measurements of the magnetic field B_A and the current I_S.

V [V]	*I [A]*	*sonda 1 [μT]*	*sonda 2 [μT]*
1,342	*0,1*	*19*	*19*
2,676	*0,2*	*42*	*41*
6,95	*0,5*	*111*	*110*
14,23	*1*	*226*	*227*
27,79	*2*	*444*	*444*

So, it was estimated that:

$$\frac{B_A}{I_S} = 213 \quad \frac{\mu T}{A} \tag{2}$$

2.3 Set-up of the system [NM]

The laboratory room housing the equipment is located about 10m far from the RFX machine axis [FED2]. The B_{RFX} magnetic field induced by RFX in the laboratory room is vertical and about 100 times the magnetic field sensed by the NMR instrumentations at ICIS. It also strongly depends upon the distance, as shown in Figure 7.

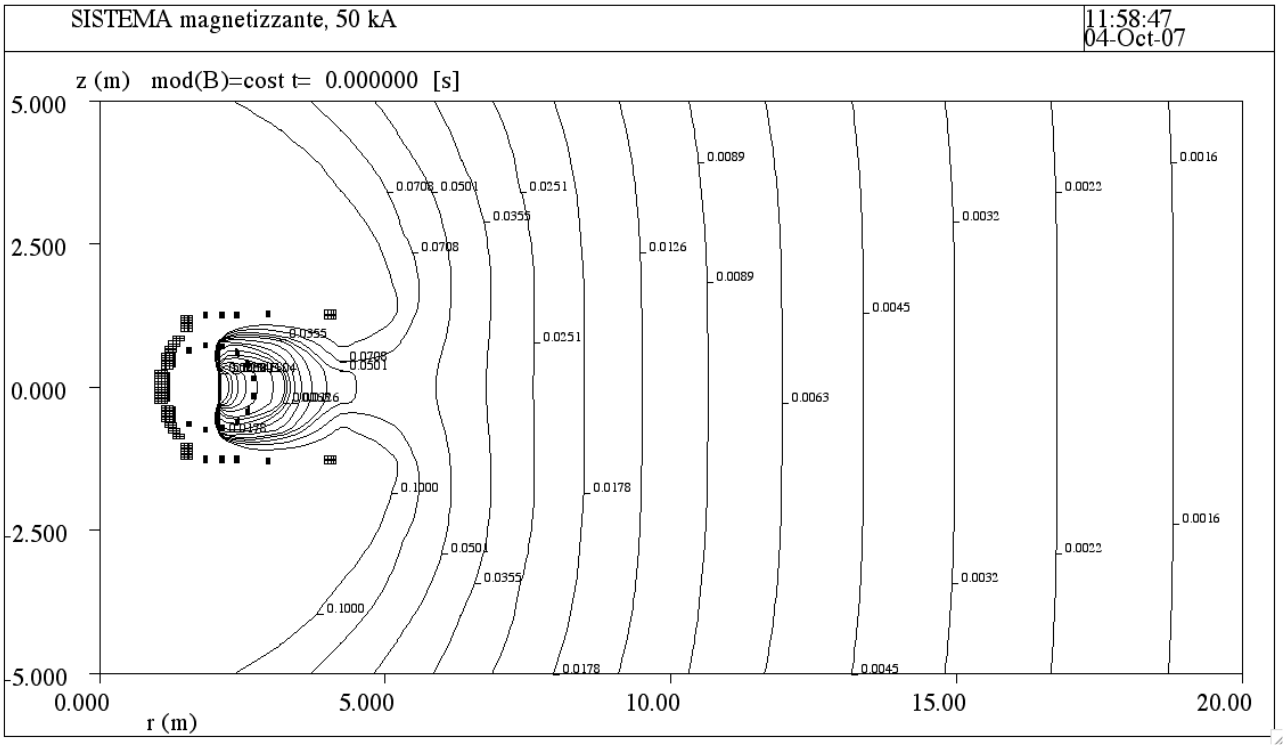

Figure 7 Magnetic field map for the magnetizing windings of RFX with I_M=50kA.

In the laboratory room, the amplitude of the magnetic field can be of 800μT for I_M=50kA. The Hall probes have been posed as shown in Figure 8 to measure the ratio B_A/V_I and to test the configuration to use during the experiments for the compensation.

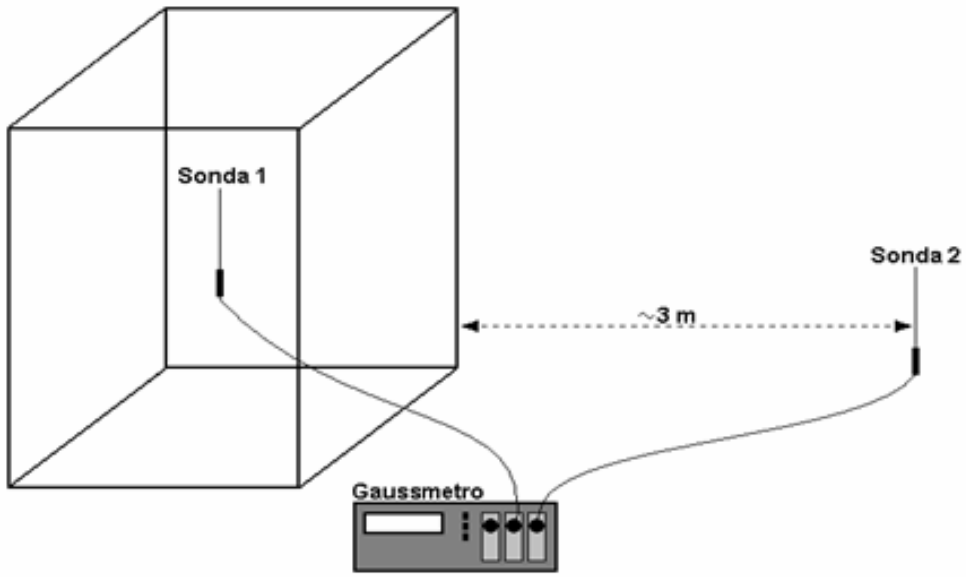

Figure 8 Measure of the magnetic field created by RFX. The Hall probe are located 3m far from one another.

The Hall probes have been placed 3m far from one another. In this way the probe 2 should not sense the compensating magnetic field created by the shield.

These measurements have been carried out without driving the shield. In Figure 9 the magnetic fields measured by the two Hall probes are shown.

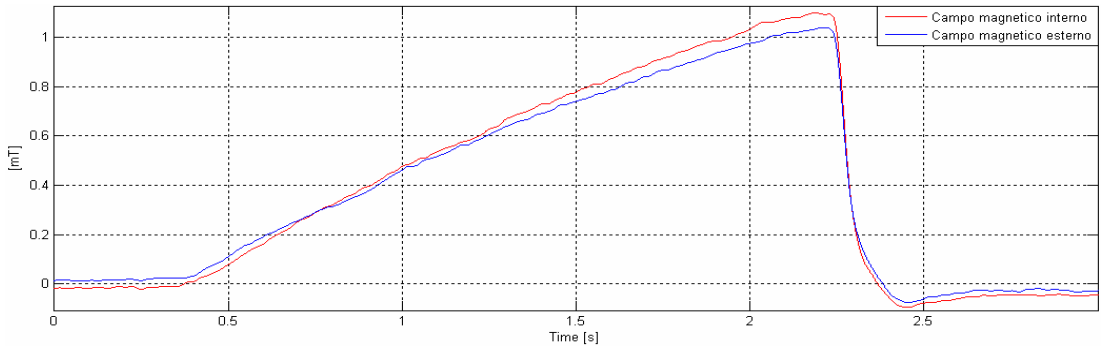

Figure 9 Magnetic field measured by the internal probe (red) and by the external one (blue) for a pulse with $I_M \approx 40kA$.

The magnetic field measured by the two Hall probes seems different. There can be many causes affecting the magnetic measurement:

- The magnetic field depends upon the distance from RFX;
- The internal probe is located near to a cubicle for electrical equipment;
- There are many ferromagnetic objects inside the laboratory room.

It is worth noticing that the Hall probes as well as the prototype shield have not been fixed during the experiments. So, both the B_{RFX}/V_I ratio and the B_A/I_S ratio need to be verified day by day.
Several measurements, as that shown in Figure 9, have been carried out, but only an estimate has been found for the B_A/V_I ratio:

(3) $$\frac{B_{RFX}}{V_I} = 173.3 \frac{\mu T}{V}$$

An estimate of the gain receiver g can be evaluated with the measured values above presented and the values given in chapter V:

(4) $$g = 173.3 \frac{\mu T}{V} \cdot \frac{1}{0.4 \Omega^{-1}} \cdot \frac{1}{213 \mu T / A} = 2.03 \frac{V}{V}$$

The estimated value of g means that the voltage signal V_U output from the receiver has to be twice than the input voltage signal V_I. However, the maximum current in the RFX machine winding I_M is 50kA, which corresponds to a LEM output signal of 8.33V. This voltage exceeds the operating range of the radio link, which is ±5V. So, the system is able to compensate the RFX field B_{RFX} only for a magnetizing current I_M<30kA. In Figure 10 is shown what happens for current higher than 30kA.

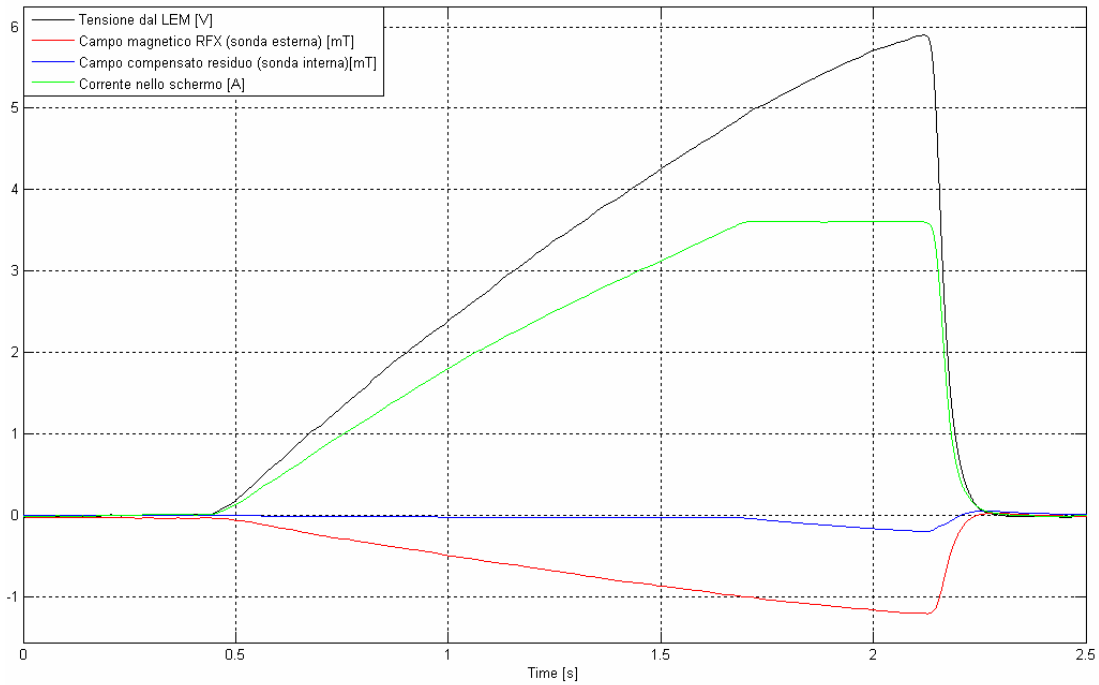

Figure 10 Compensation of the magnetic field for a RFX pulse with I_M>30kA.Black: voltage input V_I (proportional to I_M); Green: current I_A flowing through the prototype shield; Blue: magnetic field error sensed by the internal probe; Red: magnetic field induced by RFX sensed by the external probe.

The saturation of the current I_S (green line) due to the dynamic limits of the system is visible in Figure 10. This saturation affects the residual magnetic field (blue) measured by the internal Hall probe 1.
This saturation is a problem only relevant to the tests carried out in the RFX diagnostic hall; for the compensation of the NMR spectrometer the value of the gain of g estimated in (4) is about ten times the value estimated in (16), section 8, chapter V. So, there would not be a similar challenge when the system would be installed at the ICIS institute.

3. Compensation experiments at RFX

Several experiments have been carried out during RFX dry runs. RFX dry runs are daily performed at RFX at the start and at the end of operations. This kind of pulse require a magnetizing current I_M of about 10kA, and the saturation challenges at the output of the receiver are not present.
Figure 11 shows the compensation obtained during a vacuum discharge, setting the receiver gain g=2.

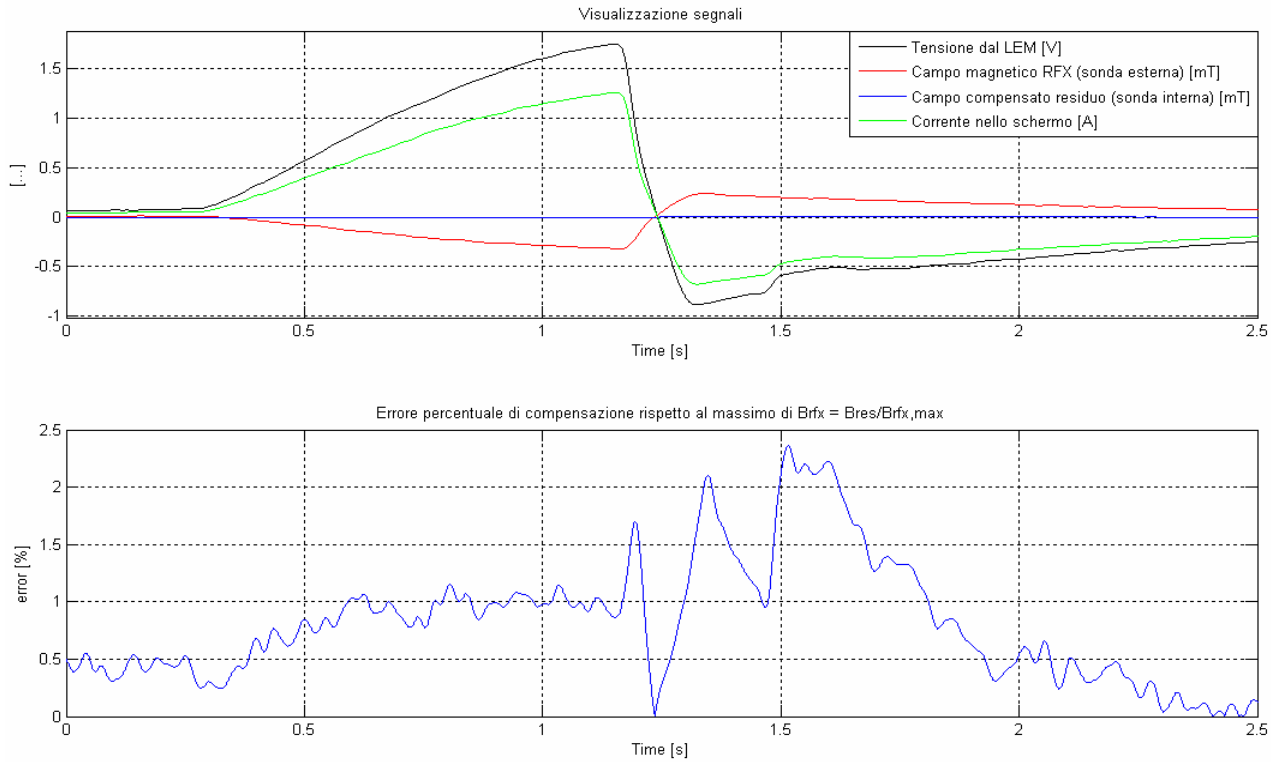

Figure 11 Compensation of the magnetic field obtained contemporarily to a RFX vacuum discharge with I_M=10kA. Top: behavior of V_I [V] (black), I_M [A] (green), B_{RFX} [mT] (red), residual magnetic field [mT] (blue). Bottom: behavior of the residual magnetic field normalized to the maximum value of B_{RFX}.

In Figure 11 (top), all measured signals are shown. The overall system seems able to correctly reproduce a magnetic field B_A which behaves as the input signal V_I (black).
In Figure 11 (bottom), the residual magnetic field B_{err} is reported, as measured by the internal Hall probe. It was divided by $B_{RFX,max}$ the maximum value of magnetic field sensed by the external Hall probe. In order to extend present results with I_M=10kA to cases with higher values of current, the results are reported in percentile. The residual error never exceeds the threshold of 3%. The compensation obtained suits our purposes.
However, the time behavior of the I_M current during a vacuum discharge differs from that one during a typical RFX pulse. Other tests have been performed during RFX pulses with I_M=25kA. The measured signals during a typical RFX pulse with I_M=25kA are shown in Figure 12.

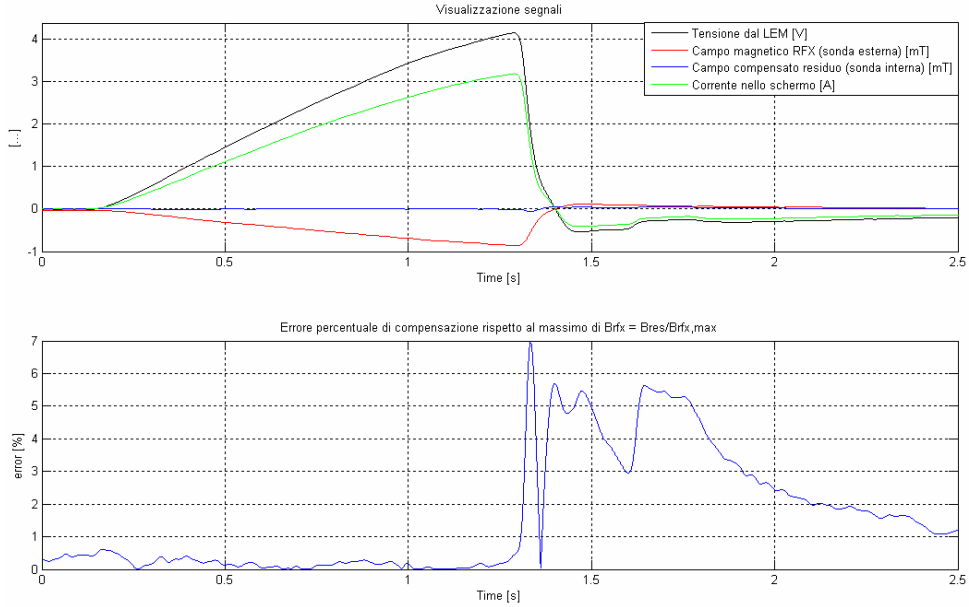

Figure 12 Compensation of the magnetic field obtained contemporarily to a typical RFX pulse with I_M=25kA. Top: time behavior of V_I [V] (black), I_M [A] (green), B_{RFX} [mT] (red), residual magnetic field [mT] (blue). Bottom: time behavior of the residual magnetic field normalized to the maximum value of B_{RFX}.

The residual magnetic field obtained in the case reported in Figure 12 differs from the residual magnetic field obtained in the case of a dry run, Figure 11. The 7% peak can be due to the delay time of the transmission system as foreseen in section 3.1, chapter V. This peak does not appear in Figure 11 because the ramp-down time of a dry run is larger than that one of a typical pulse. After the 7% peak at t=1.3s, the residual magnetic field decreases to acceptable values after a time (about 1s) longer that the time (8ms) foreseen in section 3.1, chapter V. In Figure 13, the input signal V_I and the magnetic field sensed by the two Hall probes are divided by their maximum value with the aims of comparing their time behavior.

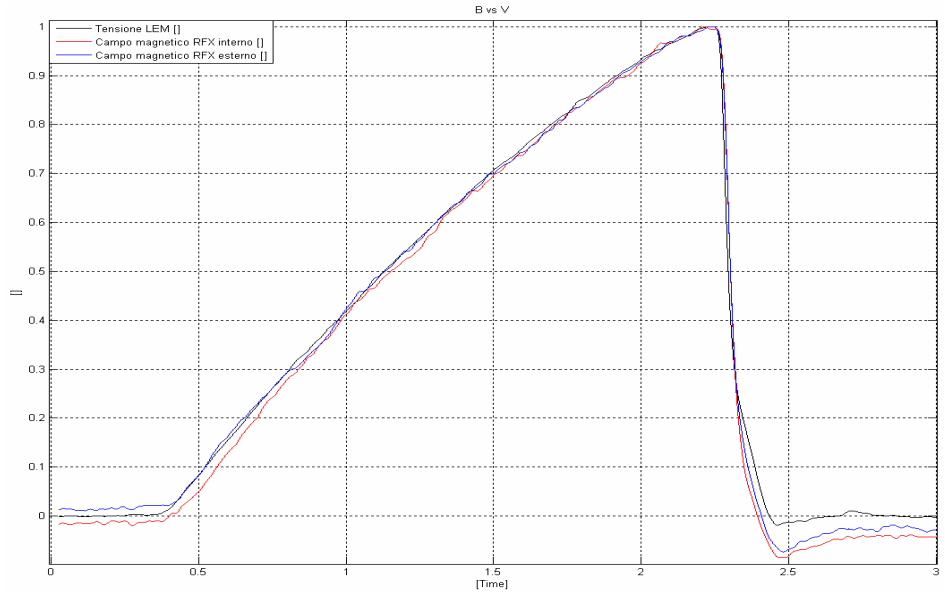

Figure 13 Time behavior of V_I (black), and of the magnetic field sensed by the internal (red) and the external Hall probe (blue

Each signal in Figure 13 has been divided by its maximum value in order to compare the different time behavior of the signals. At t≈2.5s, the magnetic fields sensed by the two Hall probe are similar one another (less than an offset and the noise), but their time behavior sensibly differ with the time behavior of the V_I signal used to drive the prototype shield. So, the long tail shown in Figure 12 seems due to the difference between the actual magnetic disturbance and the driving signal V_I. The V_I signal is a measure of the I_M current flowing through the magnetizing winding of RFX, I_M has been individuated as the main cause of the magnetic disturbance at the ICIS institute, section 3, chapter I. There is not a clear explanation of these differences. It seems likely than an additional source of the magnetic field is present during the last phase of a RFX pulse. This additional source should be due to the Field Shaping winding of RFX as well as the screening ferromagnetic structure of the building. In any case, the effect of this additional source are not predictable and preliminary tests at the ICIS institute have to be carried out in order to evaluate if differences between the driving signal V_I and the actual magnetic disturbance occur, and the solution to adopt.

4. Test on the transmission of the RF signal from RFX to ICIS

The two YAGI antennas, presented in section 5, chapter V, have been installed one over the ceiling of RFX, and the other over the ceiling of the ICIS institute. In Figure 14, a picture is shown of the two YAGI antennas once installed.

Figure 14 Pictures of the YAGI antenna installed at ICIS (right) and of that one installed at RFX (left).

The Digital Telemetry Control Software has been useful during the installation and the pointing of the antennas.
Once the antenna RX has been installed at ICIS, it was verified that no noise were present into the RF bandwidth of the receiver, 868 to 870 MHz. The transmitter was turned off, and the bandwidth of the receiver was scanned using the receiver and the control software. No signals have been sensed by the receiver. Therefore, the the noise is below -102dBm at any frequencies from 868 to 870MHz. -102dBm is the minimum level of the signal sensed by the receiver. Finally, the two antennas have been fixed and pointed in such a way to obtain the maximum power received. The antennas were pointed step by step keeping the transmitter and the receiver turned on and overlooking the received power with the help of the control software.
The power of the signal sensed by the receiver is shown in Figure 15.

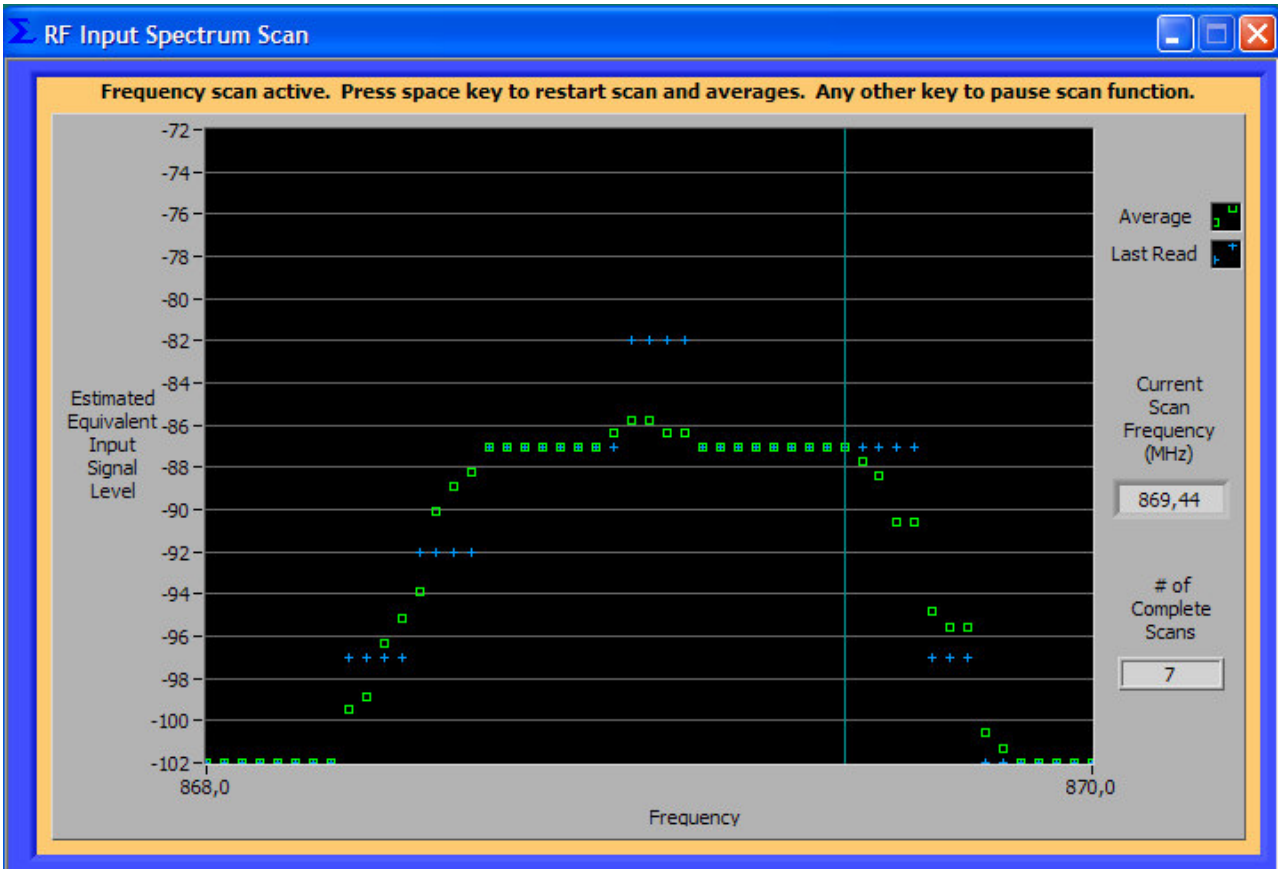

Figure 15 Screenshot of the Control software. It shows the spectrum of the RF signal sensed by the receiver.

The power of the RF signal sensed by the receiver varies from -87 to -82dBm. Typically any reading above -90dBm is considered a high quality signal, although reception can typically be to as low as -100 dBm input level [SRI].
A definitive transmission test has been carried out in order to verify if the voltage signal V_I is correctly reconstructed at ICIS during a RFX pulse. Two oscilloscopes have been used [NM], one located in the diagnostic Hall at RFX to measure the input signal V_I, and the other

located at ICIS to measure the output signal V_U giving out from the receiver. The receiver gain was set equal to g=1.
In Figure 16 the two signals are compared.

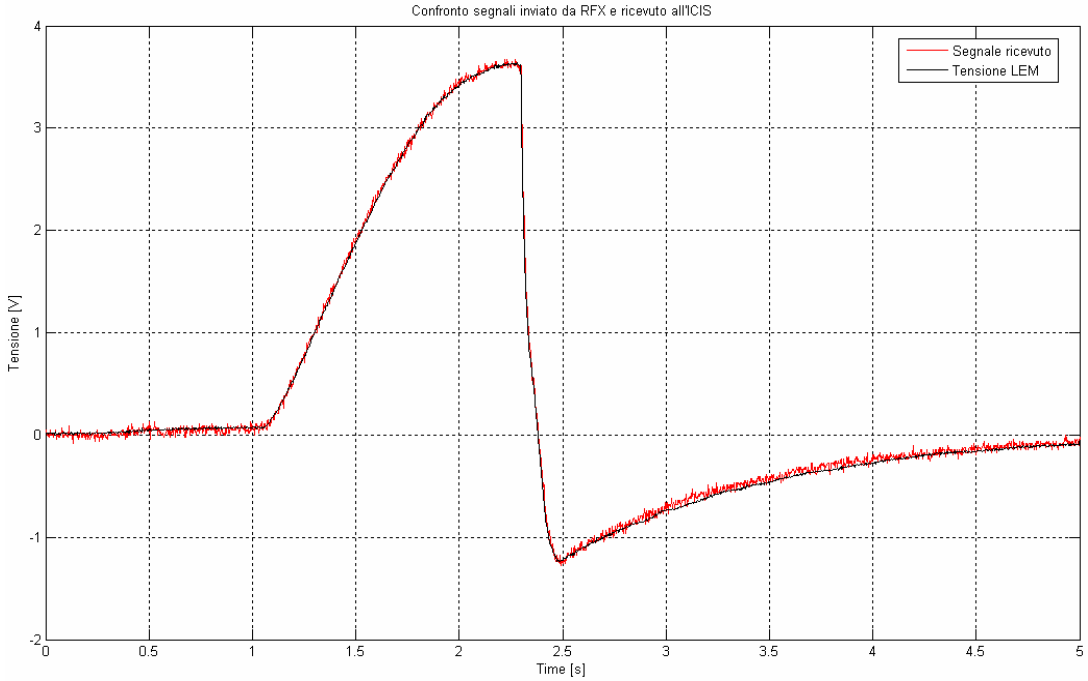

Figure 16 Transmitted V_I (black) and received V_U (red) signals, with a receiver gain of g=1.

In Figure 16 the received signal (red) is shown to be a good reproduction of the input signal V_I (black).

5. Preliminary experiments at ICIS [NM]

Preliminary tests have been carried out installing the active coils few meters far from the NMR BRUKER ac ADVANCE 300 MHz in order to check the equipment and to set-up the receiver gain.
In order to measure the low magnetic field induced by RFX and the residual magnetic field, a magnetic sensor has been realized [NM]. The maximum amplitude of the magnetic field induced by RFX is of 3μT. This low magnetic field can not be measured by the gaussmeter reported in section 2.
The magnetic sensor has been realized by a copper wire, 0.24mm diameter, wound 10000 times around the supporting structure shown in Figure 17.

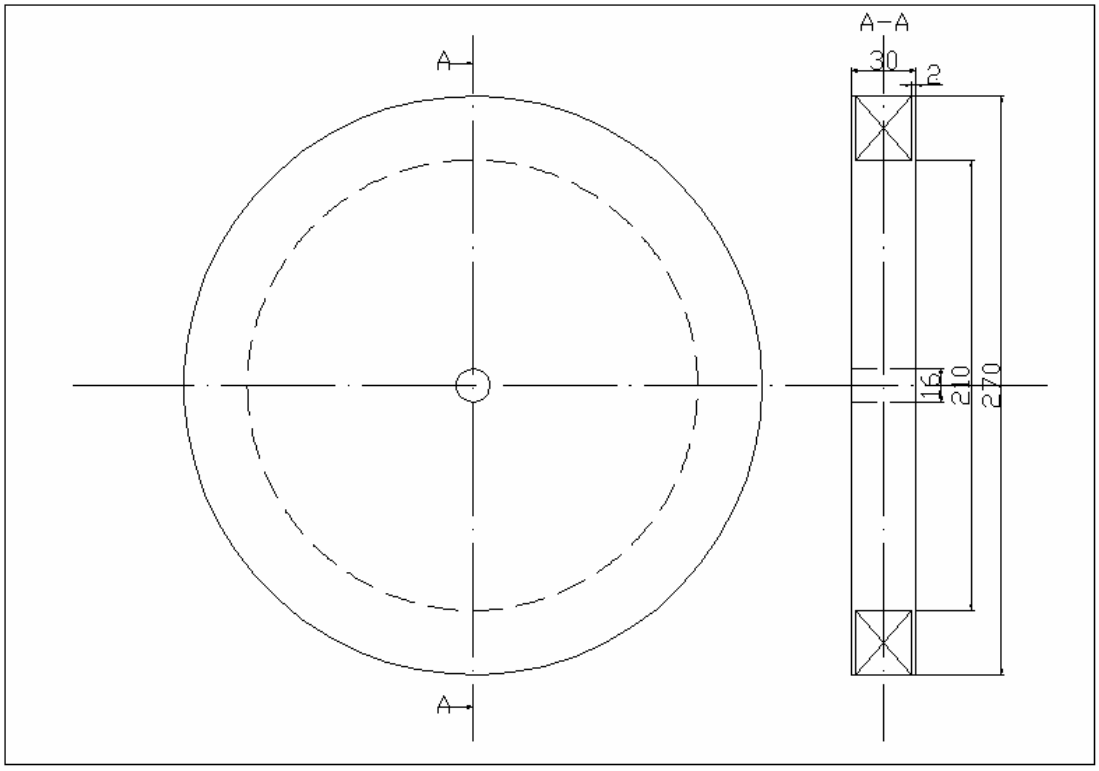

Figure 17 Supporting structure for the magnetic sensor. Dimensions in mm. [NM]

The supporting structure, Figure 17, has been realized with a Ketron PEEK-CA130 disk of 21cm diameter and 3cm thick. The medium diameter of the windings is of 24mm, the equivalent surface is 450m^2. The coil has been connected in parallel with a damping resistor of R_{PS}=10kΩ. The damping resistor has been experimentally adjusted in order to give a constant impedance equivalent to the parallel resistor-coil on the bandwidth of the signal (f<1kHz) and to avoid the resonance of the coil due to the parasitic capacitor of the coil itself. This parallel is after connected with an integrator yet available at RFX. The complete magnetic sensor is shown in

Figure 18 Picture of the sensor magnetic realized to measure the low magnetic field induced by RFX at ICIS. [NM]

5.1. First set-up of the system

The KEPCO BOP 100-4M has been used in current mode as a VCCS to drive the active coils presented in section 6, chapter V. As above discussed in section 2.2, oscillations can occur when the KEPCO works in current mode on an inductive load. Moreover, the active coils are characterized (section 6.4, chapter V) by an high parasitic capacitance, therefore the active coils have a resonant behavior at f= 15.8kHz. In order to reduce the oscillations, a damping resistor of R_P=575Ω is connected in parallel with the active coils. This value has been experimentally adjusted [NM] has a compromise between the oscillation damping and the fidelity of the response. This value of R_P allows a sufficient damping and a response I_S/V_U of the KEPCO-active coils system constant up to f=100Hz. In this way the magnetic field B_A created by the active coils should correctly reproduce the V_U signal along the NMR susceptibility band (0-10Hz).
In Figure 19 is shown the comparison of the current signal I_S (flowing through the active coils) and the voltage signal V_U (driving the KEPCO VCCS).

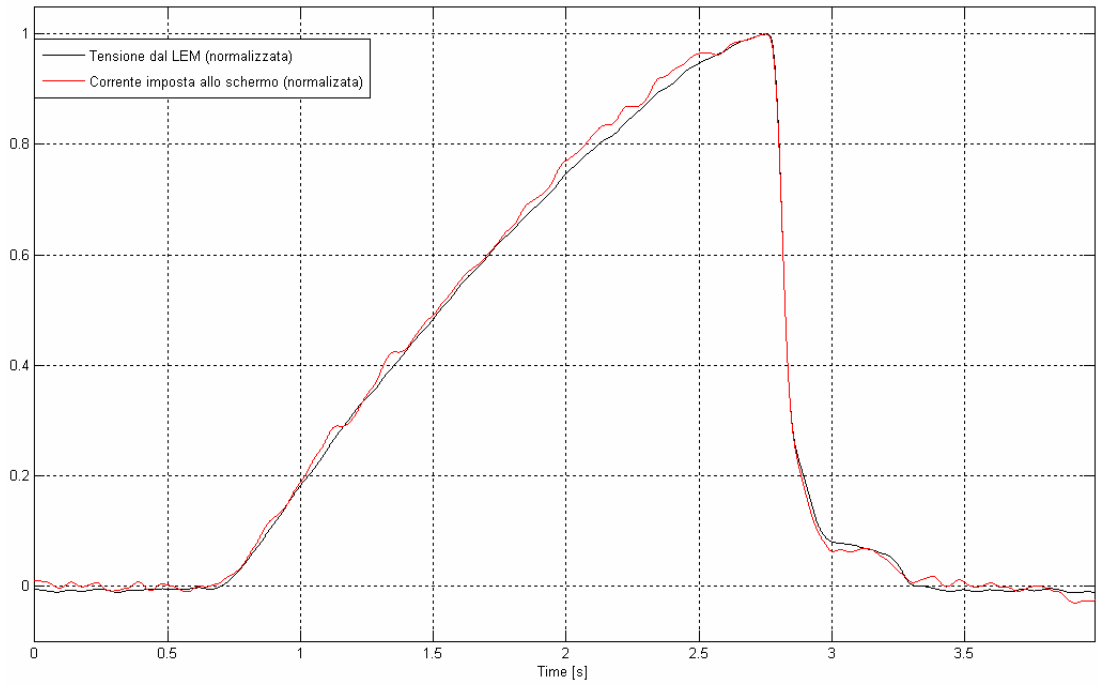

Figure 19 Comparison between the current signal I_S (red) flowing through the active coils and the voltage signal V_U (black) driving the signal.

Once the system above described was set_up, several compensation tests have been performed varying the receiver gain. In Figure 20 the measured V_U, I_S and $B_{err}=B_{RFX}-B_A$ signals are reported for a RFX pulse with $I_M \approx 30$kA and g=0.201.

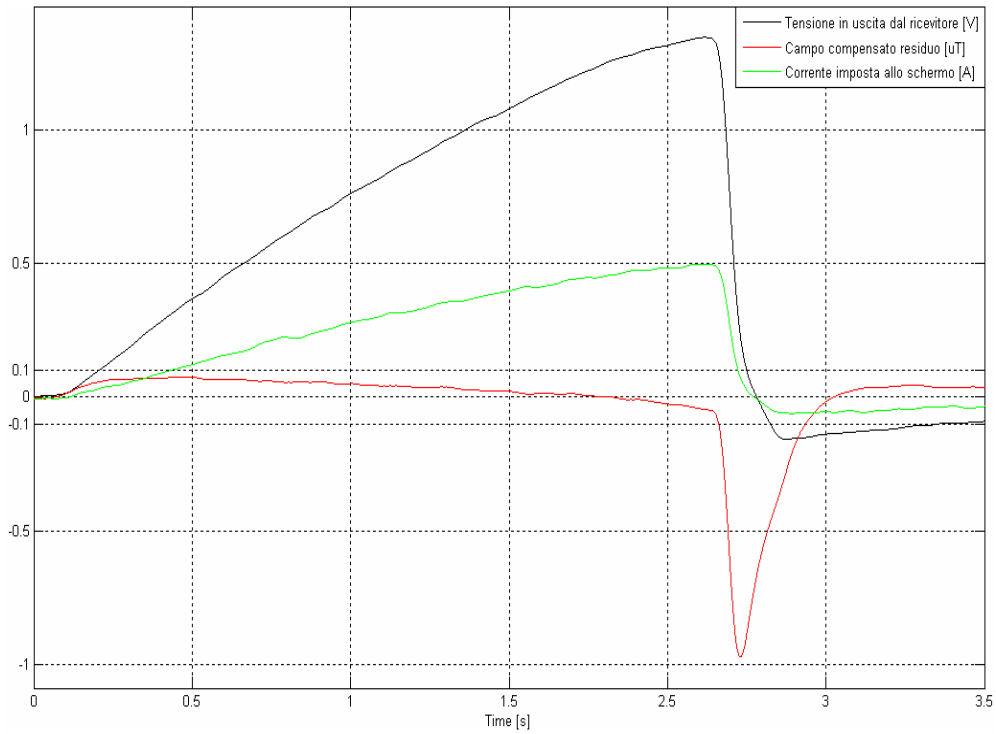

Figure 20 V_U (black) [V], I_S (green) [A] and B_{err} (red) [μT] signals with I_M=30kA and g=0.201.

As shown in Figure 20, the compensated B_{err} magnetic field exceeds the susceptibility threshold of 0.1μT during the pulse, reaching aboutb1μT and 0.2s duration. The maximum value of this spike agrees with the error predicted in section 3.1, chapter V. So, it seems due to the time delay of the transmission, but the duration of this spike is larger than the duration foreseen (about 8ms). It could be caused also by differences between the V_U signal and the time behavior of the magnetic disturbance B_{RFX}. The signals V_U and B_{RFX} have been measured turning off the KEPCO. The spectra of these signals have been normalized and then compared as shown in Figure 21.

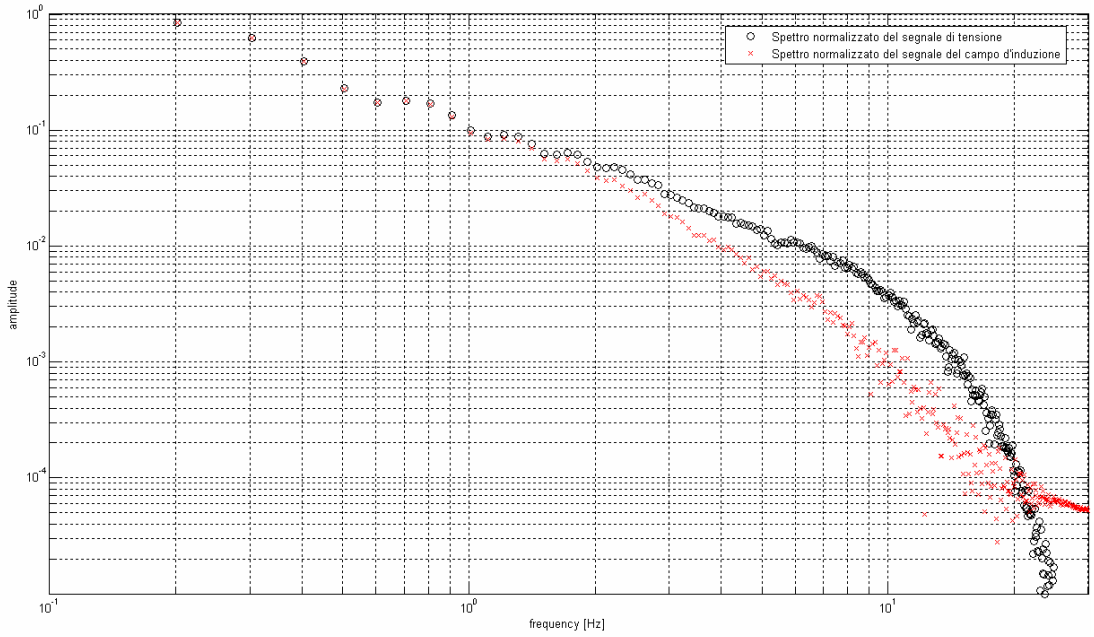

Figure 21 Spectra of the V_U (black) and B_{RFX} (red) signals. The spectra have been normalized.

As shown in Figure 21, the spectra of V_U and B_{RFX} are similar up to a frequency of about 2Hz. At higher frequencies than 2Hz, the harmonics of the B_{RFX} spectrum are smaller than that ones of the V_U spectrum.
It seems reasonable that the metallic iron cage surrounding the RFX building should affect the induction of the magnetic field acting as a low-pass filter.

5.2 Second set-up of the system

It was decided to insert a low-pass filter between the output of the receiver and the inut of the KEPCO. The low-pass filter is made up of two resistor R_S and R_P, and a capacitor C. The resistor R_S=100Ω is connected in series to the output receiver and the parallel R_P and C. In parallel with the input of the KEPCO has been inserted the resistor R_P=400Ω and the capacitor C=0.5mF. With this second set-up, further compensation experiments have been performed, results for a RFX pulse with I_M=16kA are reported in Figure 22.

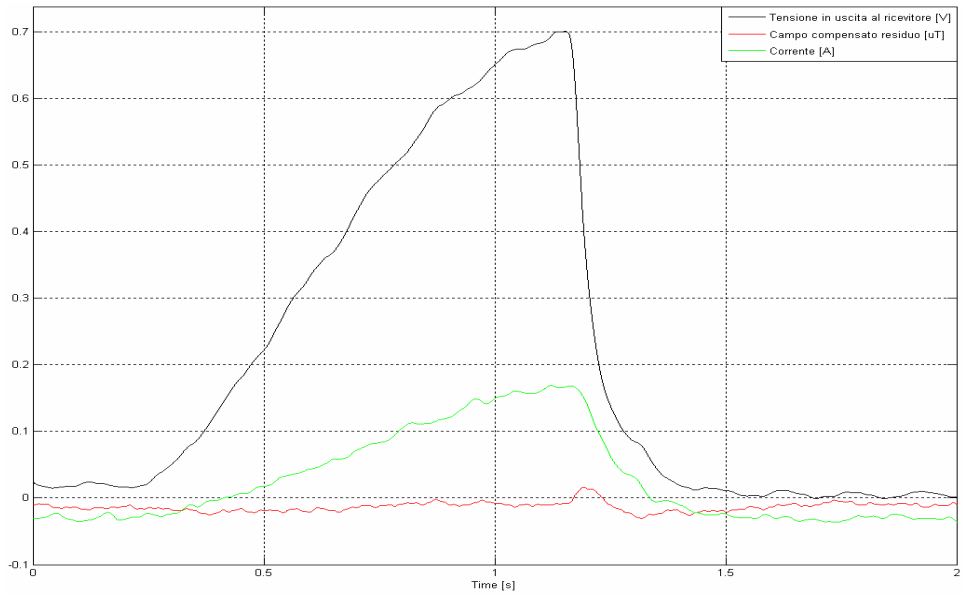

Figure 22 V_U (black) [V], I_S (green) [A] and B_{err} (red) [μT] signals with I_M=16kA .

Signals shown in Figure 22 have been measured for a RFX pulse with I_M=16kA. A general estimate of the performance of the compensating system can be given considering the time behavior of the normalized B_{err} magnetic field. In Figure 23 the normalized time behavior of B_{err} is shown. An estimate of $B_{RFX,max}$ has been found measuring the magnetic field induced by a RFX pulse similar to that exposed in Figure 22.

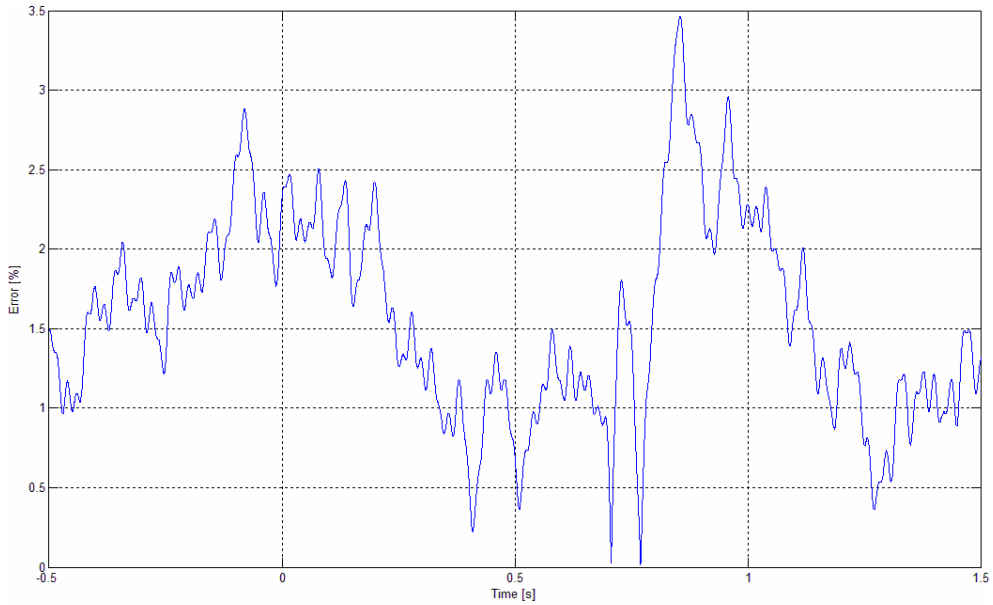

Figure 23 Time behavior of the residual magnetic field B_{err} [%] normalized by an estimate of $B_{RFX,max}$ for the same case shown in Figure 22.

An optimum compensation has been achieved, as shown in Figure 23. In fact, the percentile residual B_{err} magnetic field is all under the susceptibility threshold of the NMR (3%), less than a peak of 3.5% with a small duration. The system seems to suit all the requirements.

6. Compensation of the magnetic disturbance on the NMR ac ADVANCE 300 MHz

At present, the active coils are installed around the NMR BRUKER ac ADVANCE 300 MHz. The lower coil (10 windings) is installed over the floor around the NMR device. The upper coil (119) is fixed to the ceiling just over the NMR device. The two coils are coaxial and the symmetry axis pass through the sample probe of the NMR.
The system has been configured as follows. The magnetic sensor has been posed near to NMR in such a way to sense the same magnetic field sensed by the sample probe. The correct positioning of the magnetic sensor has been evaluated with the help of the magnetic field maps as shown in Figure 24 and Figure 25.

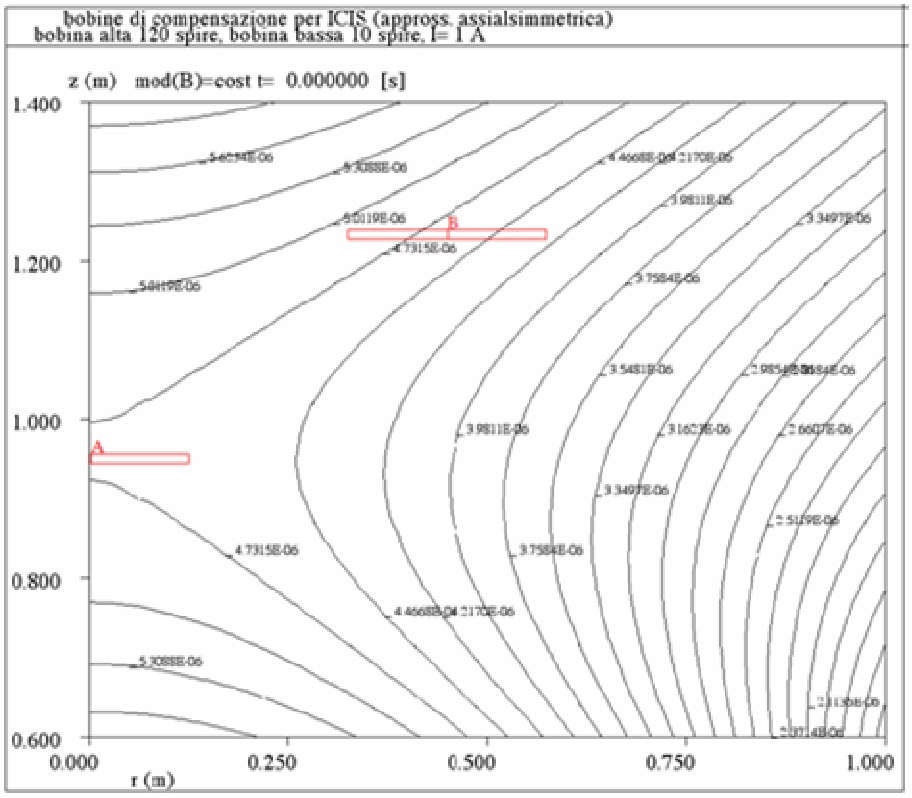

Figure 24 Map of the constant strength field lines [T] of the magnetic field produced by the active coils. The magnetic sensor has been placed in B, in such a way to sense the same magnetic field sensed on A (sample probe location). [NM]

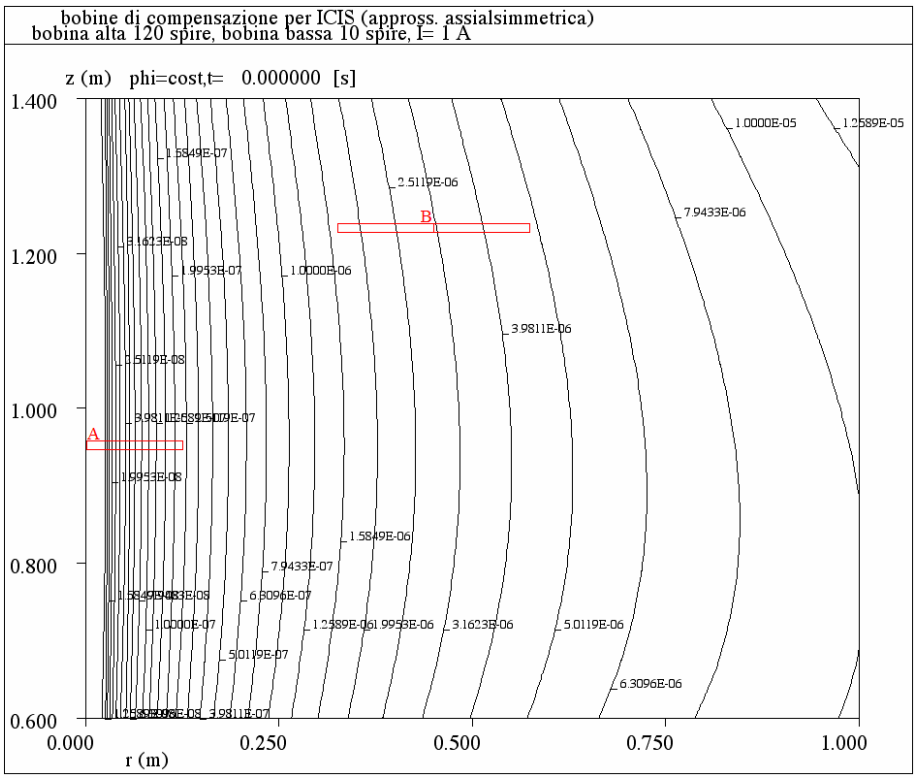

Figure 25 Map of the constant flux lines [Weber] of the magnetic field produced by the active coils. The magnetic sensor has been placed in B, in such a way to sense the same magnetic field sensed on A (sample probe location). [NM]

Experiments have been carried out with the power supply VCCS switched off, in order to provide a first set-up of the receiver gain g [NM].

6.1 $CHCl_3$ experiments

The NMR $CHCl_3$ experiments are the most sensitive to the magnetic disturbance induced by RFX. The experimental results are reported in Figure 26 for three different cases. In order to evaluate the effect of the compensation one $CHCl_3$ experiment has been carried out contemporarily to the rapid decay of the magnetizing current I_M (bottom in Figure 26), and a second $CHCl_3$ experiment has been carried out in absence of the disturbance (middle in Figure 26). The results of the compensation is shown at the top of the Figure 26.

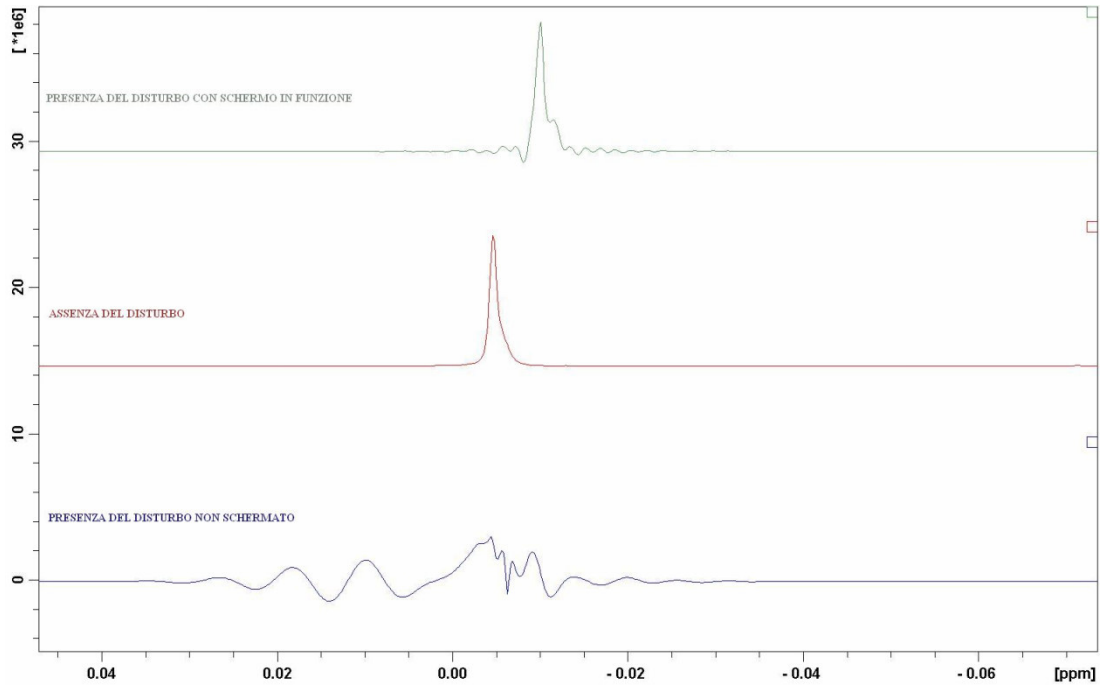

Figure 26 Measurement obtained by the NMR for the $CHCl_3$ experiment. Compensated measurement (top); Measurement in absence of the disturbance (middle); Corrupted measurement (bottom).

By comparison of the three measurements shown in Figure 26, the compensation of the magnetic disturbance makes the NMR signal readable even though if some errors occur. The main peak is shifted of about 0.01 ppm and the shape of the signal is quite deformed.
Several experiments have been further carried out to adjust the R_P, R_S, and C values of the low-pass filter discussed in section 5.2. These values are been varied in order to obtain a deformation as little as possible. The parallel resistor R_P has been removed while the capacitor C=0.5mF is maintained. The series resistor R_S has been decreased to R_S=75Ω.

6.2 Organic compound experiments

Last compensation experiments have been carried out using an organic compound into the sample probe. Such experiment is often performed at the ICIS institute. Results are shown in Figure 27 and Figure 28.

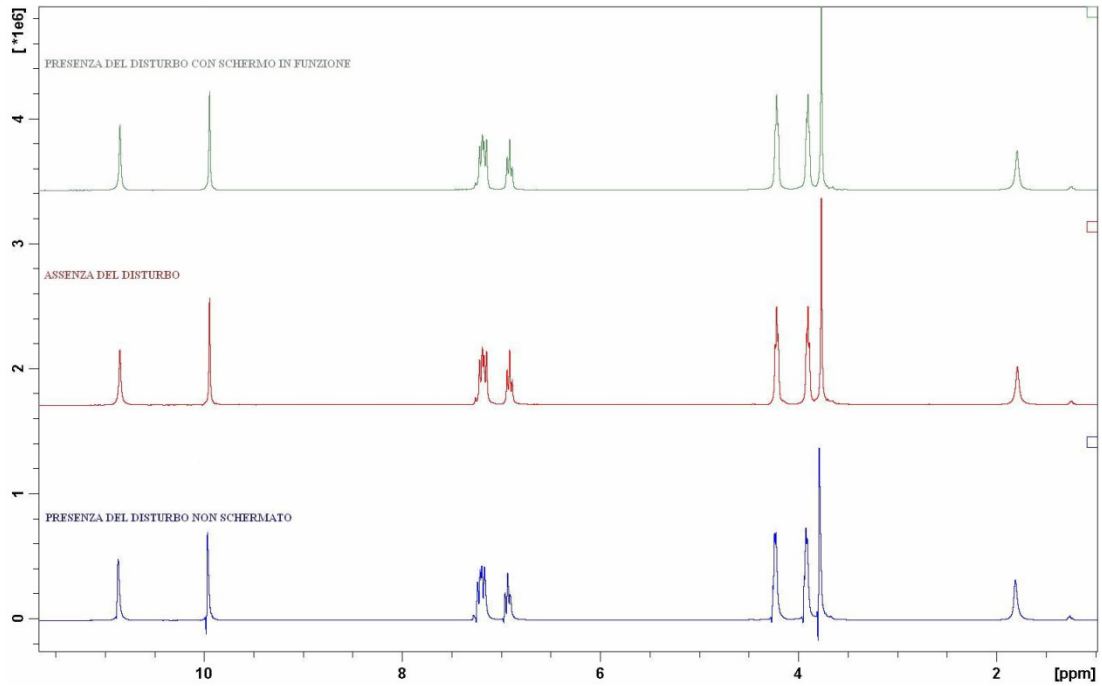

Figure 27 Measurement obtained by the NMR for the Organic compound experiment. Compensated measurement (top); Measurement in absence of the disturbance (middle); Corrupted measurement (bottom).

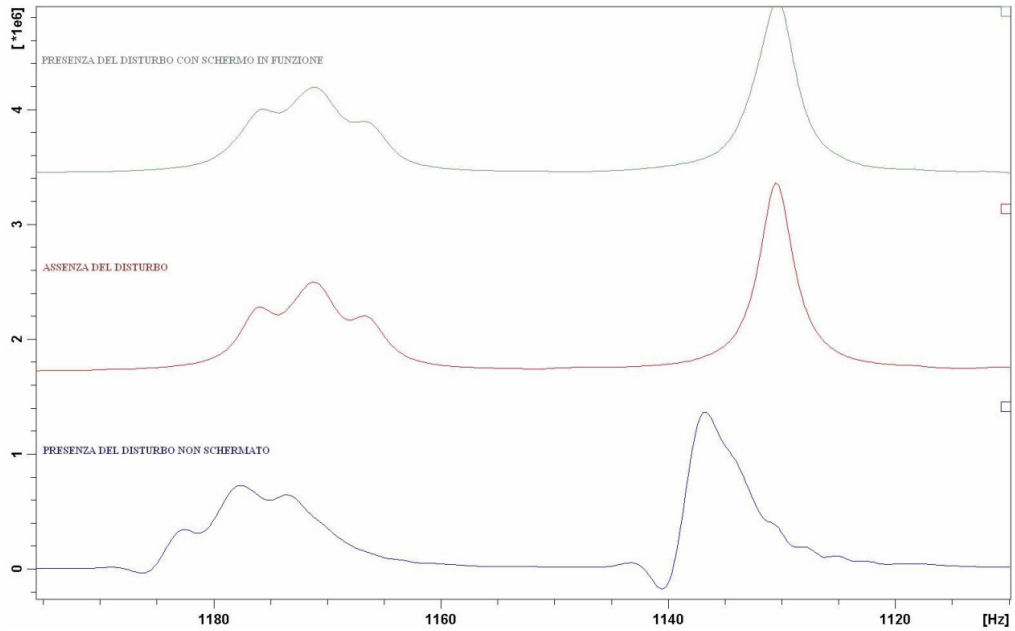

Figure 28 Zoom of Figure 27 (against Hz instead of ppm) to evidence the differences between the measurements..

A huge shift of the spectra is evident in the uncompensated measurement. Such a shift makes hard to interpret the measurements. The compensation obtained shows that the measurement is practically un-affected by any deformation or shift.

Present experiments are so proved that the open loop active magnetic shield is able to perfectly compensate the magnetic disturbance induced by RFX, or, at least, to improve the readability of the NMR measurements.

7. SUMMARY

First tests carried out at RFX (section 2) allowed us to verify that each block of the system is working as expected. The experiments performed at RFX (section 3) with the prototype shield [Baggio] showed that compensation is achievable with the adopted strategy. However, some differences have been noted between the V_I driving signal and the actual magnetic disturbance during the experiments. A deeper analysis of the causes of these differences has not been undertaken, because these anomalies could differ or not appear at ICIS.
The transmission system is able to send the RF signal from RFX to ICIS. The signal V_U received at ICIS is a good reproduction of the V_I signal sent from RFX (section 4).
Several tests were performed installing the active coils few meters far from the NMR instrumentation (section 5). In this way, different kinds of differences between the VI signal and the BRFX magnetic disturbance have been observed. Here, the analysis of the spectra allowed individuating a suitable solution. So, the system showed the capability to compensate the magnetic disturbance and to reduce the magnetic field under the threshold susceptibility of the NMR.
The active coils have been finally installed in their final location near to the NMR. Several NMR experiments have been carried out in order to verify the capability of the active shield in compensating the magnetic disturbance (section 6).
Compensation experiments carried out on the NMR devices have shown that a good compensation is achieved for the most common NMR experiments (section 6.2). A partial compensation is achieved for the most sensitive NMR experiments (section 6.1), which makes the NMR measurements readable.

Therefore, the project here presented suits all the requirements.

CONCLUSIONS

The activity here presented was aimed to solve the electro-magnetic compatibility problem observed in the research area of the CNR, at Padua, between a NMR spectrometer and the RFX experiment.
Accurate measurements of the magnetic disturbance aimed to drive an active magnetic shield are not achievable, due to the low amplitude and the frequency spectrum of the magnetic field induced by RFX. For these reasons it was decided to control the active magnetic shield by a signal transmitted in real time. The system works in accordance with an open-loop (or feed-forward) scheme.
The activity concerning the design of the overall compensating system is described in chapter V.
Both the control strategy and the sensitivity of the NMR spectrometer required to accurately design and test each part of the system.
The system has been realized building some parts at RFX or buying suitable devices in accordance to the design developed during my activity. The entire control chain and the coils making up the active shield have been realized and installed. The first experimental test, described in chapter VI, verified the performances of the system and the feasibility of such a control strategy to compensate a magnetic disturbance. A second series of tests, carried out at RFX and at ICIS, have shown that the system suits to the purposed aims and performs a good compensation of the magnetic disturbance induced by RFX. The compensating system allows carrying out NMR experiments obtaining readable measurements.
At present, a last challenge shall be solved regarding the unexpected behavior of the analog output stage of the receiver. Once the receiver is turned on, it suddenly changes its output voltage from 0V to +10V or -10V. The output voltage decays to acceptable levels once the receiver senses a signal by the transmitter. This behavior could create an additional magnetic disturbance to the NMR, if the power supply of the active shield is already working. This problem can be overcome inserting a control circuitry between the output of the receiver and the input of the power supply. This circuitry shall work as a Schmitt's trigger and provide a digital signal to turn off the power supply, if the output voltage at the receiver is over +9V or -9V, avoiding to drive the active shield with a huge current signal, and hence to create an huge magnetic disturbance for the NMR. In fact the output voltage signal should range within ±8V, so this solution seems feasible

Finally, this activity showed that the transmission via Radio of experimental measurements with a high precision is feasible. The possibility of sending a measurement via radio could be useful for those applications requiring a large amount of diagnostics and for those in which it is difficult to connect the sensors to the data acquisition system via cable.
As an example, the diagnostics system for the *Neutral Beam Injector* (NBI) needs a large number of thermocouples and other diagnostics. Some diagnostics will be located on the high voltage grids (1MV). The electrical connections between these diagnostics and the data acquisition systems shall be carefully designed in order to avoid failure due to this large difference of electrical potential. A wireless transmission system, similar to that utilized in the present activity, could simplify the lay-out of the connection, reducing the complexity of the design.

BIBLIOGRAPHY

[1] Y. Neyatani et al, *Nucl. Fusion* **39**, 559 (1999)

[2] G. Pautasso and O. Gruber, *Fusion Science and Techn*. **44**, 716 (2003)

[3] D. A. Humphrey, A. G. Kellman, *Physics of Plasmas* **6**, 2742 (1999)

[4] V. Riccardo et al, *Plasma Phys. and Control. Fusion* **46**, 925 (2004)

[5] N. Pomphrey, J. M. Bialek, W. Park, *Nucl. Fus.* **38**, 449 (1998)

[6] www.fusion-magnetique.cea.fr/gb

[7] www.iter.org

[8] J. Freidberg, *Plasma Physics and Fusion Energy*, Cambrideg University Press, 2007.

[9] P.Helander, *Notes on MHD equilibrium*, Culham, Plasma Physics Summer School, 2008

[10] J. Wesson, *Tokamaks*, Oxford, Clarendon Press, 1997.

[11] T.C: Hender, *Nucl. Fusion* **47,** S128(2007)

[12] G. Chitarin, T. Bolzonella, M. Cavinato, *Re-evaluation and optimization of the sub-system for measuring halo currents in ITER* (Association Euratom-ENEA, Consorzio RFX Padova, Italy), in Final Report of EFDA Contract 02-1000, (2004).

[13] E.Alessi, M.Cavinato, G.Chitarin, *Rev. Sci. Instrum***. 79**, 10F332 (2008)

[14] J. Haw (editor) *ITER Project Integration Document* ver. 3.0, ITER Organisation (2007)

[15] H. Stark, Y. Yang, *Vector space Projections*, J. Wiley and Sons (1998)

[16] G. Chitarin, E. Alessi et Al., *Design Study of the ITER magnetic diagnostic: in-Vessel pick-up coils, Blanket Halo sensors and Divertor Halo sensors, numerical*

model of Halo currenst, (Association Euratom-ENEA, Consorzio RFX Padova, Italy), in Final Report of EFDA Contract 05-1247, (2007)

[17] M.Preindl, *Simulation tool for the Halo current patterns on the first wall of a fusion reactor*, bachelor thesys, University of Padua, 2008.

[18] P. Bettini, M. Cavinato and G. Marchiori, *Nucl. Fusion* **43**, 119 (2003)

[19] R.R. Khayrutdinov, V.E. Lukash, *Journal of Comp. Physics* **2**, 106 (1993)

[20] G. Baggio, *Problemi di compatibilità elettromagnetica relativi ad una strumentazione NMR*, Tesi di Laurea, Università degli Studi di Padova, a.a. 1998-1999.

[21] E. Alessi, *Sviluppo di un sistema per la trasmissione di misure elettriche in RFX*, Tesi di Master in Ingegneria e Fisica dei Plasmi, Università degli Studi di Padova, a.a. 2004-2005.

[22] http://www.cis.rit.edu/htbooks/nmr/

[23] http://www.igi.pd.cnr.it/wwwexp/index.html

[24] G.Rostagni, *Fus. Eng. And Design*, **25**, 301 (1995)

[25] F. Gnesotto et Al., *Fus. Eng. And Design*, **25**, 335 (1995)

[26] L. Fellin, P. Kusstatscher, G.Rostagni, *Fus. Eng. And Design*, **25**, 315 (1995)

[27] A. Maschio et Al., *Fus. Eng. And Design*, **25**, 401 (1995)

[28] A.Stella, M.Guarneri, F.Bellina, P:P: Campostrini, G. Chitarin, F.Trevisan, P. Zaccaria*, Fus. Eng. And Design*, **25**, 373 (1995)

[29] G. Chitarin, S. Peruzzo, N. Pomaro, *Susceptibility of NMR instrumentation to ELF fields,* Proceeding of EMC EUROPE Workshop, Roma, settembre 2005.

[30] http://www.summationresearch.com/pages/sister/pmd.htm

[31] A. Paraboni, *Antenne*, McGraw-Hill, Milano, 1999

[32] http://en.wikipedia.org/wiki/Antenna_(radio)

[33] http://en.wikipedia.org/wiki/Dipole_antenna

[34] http://searchmobilecomputing.techtarget.com/sDefinition/0,,sid40_gci214378,00.html

[35] http://en.wikipedia.org/wiki/Yagi_antenna

[36] http://www.linkit.it/pages/home/1.htm

[37] N. Marconato, *Realizzazione e messa in uso di un sistema wireless per la compensazione del campo magnetico lentamente variabile prodotto dalla macchina RFX sulle apparecchiature NMR del centro ICIS*, Tesi di Laurea, Università degli Studi di Padova, a.a. 2007-2008.

[38] http://www.kepcopower.com/hbkanlg.htm#A1

[39] E. Durand, *Magnétostatique*, Masson et C^{ie}, Paris, 1968

APPENDIX

FORMULAE FOR SQUARE SHAPED COILS [39]

The formulae used to evaluate the magnetic field created by two coaxial square shaped coils and to optimize the design of the active shield (described in section 6, chapter IV) are discussed in this appendix. Present calculations are carried out considering two square coils in vacuum.

A sketch of the structure together with the Cartesian system used in the following is shown in figure A.1. The z-axis is an axis of symmetry for the structure. The distance between the two coils is of H. The origin of the coordinate system is far $-Z_{inf}$ to the lower coil and Z_{sup} from the upper coil.

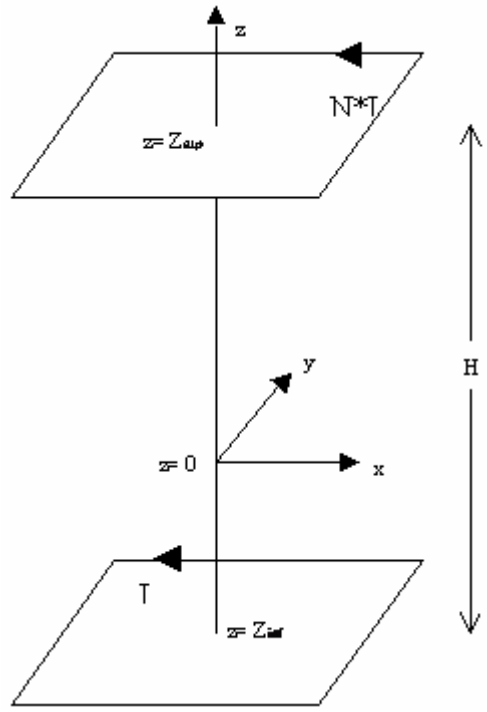

Figure A.1 Sketch of two square shaped coils.

The optimization of the design of the coils is aimed to find a structure able to generate a magnetic field whose spatial derivatives are all zero in the origin of the coordinate system. To this aim, the current flowing through the upper coil is N times the current I flowing through the lower coil. Therefore, the ratio N between the currents flowing through the two coils is the unknown of the present problem.

The magnetic field generated by a square shaped coil is calculated as follows. The Laplace's first law (figure A.1) states that:

$$d\mathbf{B} = \frac{\mu_0 \cdot I}{4\pi} \cdot \frac{d\mathbf{s} \times (\mathbf{r} - \mathbf{r}')}{|\mathbf{r} - \mathbf{r}'|^3} \qquad \text{(A.1)}$$

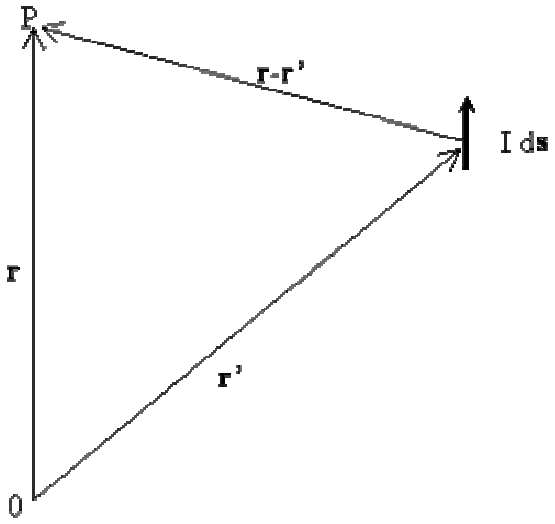

Figure A.2 Laplace's first law.

Applying equation (A.1) on each side of a square shaped coil at z=Z', (figure A.2), the magnetic field generated by each side (labeled with I, II, III, and IV as in figure A.2) can be easily calculated:

$$\mathbf{B_I} = \frac{\mu_0 \cdot I}{4\pi} \int_{-a}^{a} \frac{1}{\left[(Y-y)^2 + (X-a)^2 + (Z-Z')^2\right]^{3/2}} dy \cdot \begin{bmatrix} Z-Z' \\ 0 \\ -(X-a) \end{bmatrix} \tag{A.2}$$

$$\mathbf{B_{II}} = \frac{\mu_0 \cdot I}{4\pi} \int_{-a}^{a} \frac{1}{\left[(Y-a)^2 + (X-x)^2 + (Z-Z')^2\right]^{3/2}} dx \cdot \begin{bmatrix} 0 \\ Z-Z' \\ -(Y-a) \end{bmatrix} \tag{A.3}$$

$$\mathbf{B_{III}} = \frac{\mu_0 \cdot I}{4\pi} \int_{-a}^{a} \frac{1}{\left[(Y-y)^2 + (X+a)^2 + (Z-Z')^2\right]^{3/2}} dy \cdot \begin{bmatrix} -(Z-Z') \\ 0 \\ (X+a) \end{bmatrix} \tag{A.4}$$

$$\mathbf{B_{IV}} = \frac{\mu_0 \cdot I}{4\pi} \int_{-a}^{a} \frac{1}{\left[(Y+a)^2 + (X-x)^2 + (Z-Z')^2\right]^{3/2}} dx \cdot \begin{bmatrix} 0 \\ -(Z-Z') \\ (Y+a) \end{bmatrix} \tag{A.5}$$

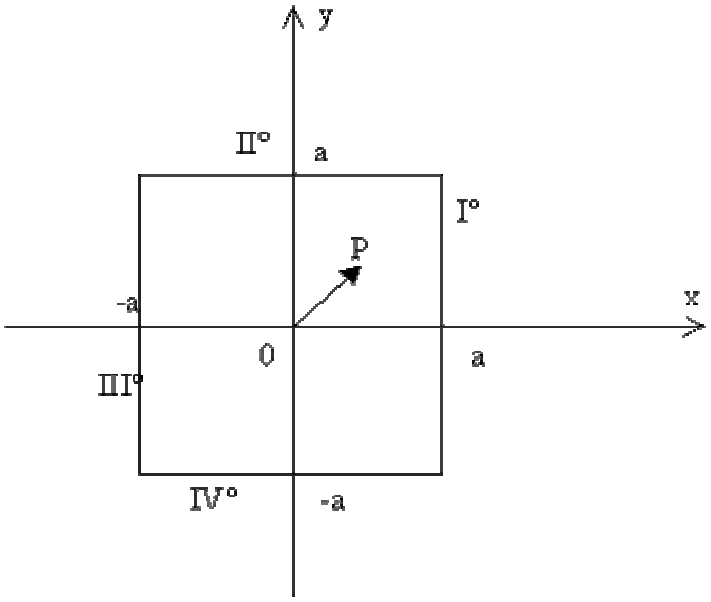

Figure A.3 Sketch of a square shaped coil, position of each side on the (x,y) plane.

The magnetic field is calculated as the sum of the equations (A.2) to (A.5).
From equations (A.2) and (A.4) results that the magnetic field component along x does not depend upon the y coordinate. Therefore, it is found that:

(A.6) $$\frac{\partial B_x}{\partial y} = \frac{\partial B_y}{\partial x} = 0$$

From equations (A.3) and (A.5), we found that the component along y does not depend upon y.
The symmetry of the structure leads to:

(A.7) $$B_x(x = 0, y = 0, z) = B_y(x = 0, y = 0, z) = 0$$

Therefore, the spatial derivative of the x and y component of the magnetic field against z along the axis of symmetry are equal to zero:

(A.8) $$\frac{\partial B_x}{\partial z} = \frac{\partial B_y}{\partial z} = 0$$

Along the axis of symmetry z, the magnetic field component along z is:

(A.9) $$B_z(x = 0, y = 0, z) = \frac{\mu_0 \cdot I \cdot a}{\pi} \int_{-a}^{a} \frac{1}{\left[s^2 + a^2 + (Z - Z')^2\right]^{3/2}} ds$$

The z-component of the magnetic field along the axis of symmetry generated by the two square shaped coils is:

$$B_z(x=0, y=0, z=Z) =$$

(A.10) $$\frac{\mu_0 \cdot I \cdot a}{\pi} \int_{-a}^{a} \frac{1}{\left[s^2 + a^2 + (Z - Z\,inf)^2\right]^{3/2}} ds + \frac{\mu_0 \cdot NI \cdot a}{\pi} \int_{-a}^{a} \frac{1}{\left[s^2 + a^2 + (Z - Z\,sup)^2\right]^{3/2}} ds$$

Considering a vacuum region surrounding the two coils, the Maxwell's equations state that:

(A.11) $$\nabla \times B = 0$$

(A.12) $$\nabla \cdot B = 0$$

Equation (A.11) applied at x=0, y=0 leads to:

(A.13) $$\nabla \times \mathbf{B} = \begin{bmatrix} \frac{\partial B_y}{\partial z} - \frac{\partial B_z}{\partial y} \\ \frac{\partial B_z}{\partial x} - \frac{\partial B_x}{\partial z} \\ \frac{\partial B_x}{\partial y} - \frac{\partial B_y}{\partial x} \end{bmatrix} = \begin{bmatrix} -\frac{\partial B_z}{\partial y} \\ \frac{\partial B_z}{\partial x} \\ \frac{\partial B_x}{\partial y} - \frac{\partial B_y}{\partial x} \end{bmatrix} = 0$$

The symmetry at x=0, y=0, leads to:

(A.14) $$\frac{\partial B_x}{\partial x} = \frac{\partial B_y}{\partial y}$$

In the axis of symmetry the equations (A.14) and (A.12) lead to:

(A.15) $$\frac{\partial B_z}{\partial z} + \frac{\partial B_x}{\partial x} + \frac{\partial B_y}{\partial y} = \frac{\partial B_z}{\partial z} + 2 \cdot \frac{\partial B_x}{\partial x} = 0$$

and then:

(A.16) $$\frac{\partial B_x}{\partial x} = \frac{\partial B_y}{\partial y} = -\frac{1}{2} \cdot \frac{\partial B_z}{\partial z}$$

So, posing:

(A.17) $$\frac{\partial B_z}{\partial z} = 0$$

all spatial derivatives of each component of the magnetic field result to be equal to zero.
By the application of equation (A.17) to equation (A.10), the optimum ratio between the current flowing through the two square shaped coils is found equal to:

(A.18) $$N = -\frac{Z_{inf}}{Z_{sup}} \cdot \frac{\int_{-a}^{a} \frac{1}{\left[s^2 + a^2 + Z_{inf}{}^2\right]^{5/2}} ds}{\int_{-a}^{a} \frac{1}{\left[s^2 + a^2 + Z_{sup}{}^2\right]^{5/2}} ds}$$